
science
NAC-CPC'08
Humboldt-Kolleg
North African Conference on Computational Physics and Chemistry 2008
University Of Sidi-Bel-Abbes
November 23rd-25th, 2008
University Of Sidi Bel Abbes
Sidi Bel Abbès
PHOENIX-EDEN Airport Hotel, Oran

DEDICACE

To the memory of our dear collegue and friend misses RABIA MENEZLA, deceased in the beginning of this year 2008

Conference Objectives

This African Conference on Computational Physics and Chemistry 2008, organized by the L2MSM laboratory of the Faculty of Sciences, University Djillali Liabes of Sidi Bel Abbes, Algeria, will bring together an international network of chemists and physicists interested in computational physics and chemistry methods in molecular, nano and material sciences. Since it is organized with the collaboration of the Alexander von Humboldt foundation (Bonn, Germany), the Conference in this field should attract participation of a number of Humboldtians from neighbouring countries and of researchers from various application areas who are pioneering advanced application of computational methods to sciences such as physics and chemistry, to discuss problems and solutions in the area, to identify new issues, and to shape future directions for research, as well as to help industrial users to apply various advanced computational techniques.
The emphasis will be on innovative theory, computational realization, and applications

Technical Topics Area

NAC-CPC'08 covers the following major thematic sessions:

* Material Science (Condensed matter, electronic structure, ab initio calculations, Molecular Dynamics, nanostructure, material characterization)
* Theoretical physics
* Theoretical chemistry
* Simulation and molecular modelling methods
* Molecular Structure and Spectroscopy
* Electrochemistry
* Biological physics, Drug design, bioinformatics, QSAR
* Computational Physics and Chemistry Education
* Other fields more or less related to the main orientation of the conference (especially for Humboldtians as poster contributions)

Scientific Committee

International Members
Prof. Philippe Derreumaux (Univ. Paris VII, France)
Prof. Michael Springborg (Univ. Sarrlandes, Saarbruechen, Germany)
Prof. Manuel Dauchez (Univ. Reims, France)
Prof. Abdou Boucekkine (Univ. Rennes1, France)
Prof. Hassan Ameri (Univ. El Manar, Tunisia)
Prof. Hassan Oulyadi (Univ. Rouen, France)
Prof. Nacer IDr.issi (USTL - Lille1, France)
Prof. Christian Mathieu (Univ. d'Artois, France)
Dr. Adlane Sayed (Univ. d'Artois, France)
Dr. Amal Maurady (Univ. Tanger, Morrocco

National Members
Prof. Ali Rahmouni (Centre Univ . Saida)
Prof. Djamila. Hammoutène (USTBH, Alger)
Prof. Noureddine Chabane-Sari (Univ. Tlemcen)
Prof. Abdelouaheb. Zaanoun (ENSET Oran)
Prof. Nourredine Zekri (USTO, Oran)
Prof. Boumediène Benyoucef (Univ. Tlemven)
Dr. Abdelhakim Benosmane (Univ . Tlemcen)
Dr. Okacha. Ouardi (Centre Univ. Saida)

Local Members
Prof. Majda Sakkal-Rahal
Prof. Abd-Ed-Daim Kadoun
Prof. Kadour Guemra
Prof. Zineb. Benamara
Prof. Guaouti Bassou
Prof. Bachir Bouhafs
Prof. Boucif Abbar
Dr. Ilhem .N.Taleb-Mokhtari

Organizing Committee
Prof. K Guemra
Dr. G. Bassou
Dr. I.N. Taleb-Mokhtari
Dr. Z. Bengharez
Dr. M. Brahami
Dr. A. Lazreg
Mr. N. Yousfi
Mr. M. Bouterfas
Mr. M.H. Gaffour
Mr. M. Sellam
Mr. Y. Mahmoud
Mr. O. Mansour

Table of Content

Plenary Lectures

1.

Coarse-grained protein simulations aimed at understanding the early steps of amyloid-fibril formation and disassembly.

P. Derreumaux[1]

[1] Laboratoire de Biochimie Théorique, UPR9080 CNRS, IBPC et Université Paris 7, 13 rue Pierre et Marie Curie, 75005 Paris, France, philippe.derreumaux@ibpc.fr

More than 20 human diseases are associated with the pathological self-assembly of soluble proteins into transient oligomers and eventually amyloid fibrils. Alzheimer's disease, affecting today more than 15 million people world-wide, is characterized by the aggregation of the Abeta40/Abeta42 peptides. There is strong evidence that the soluble oligomers, forming in the early steps of aggregation, are the most cytotoxic species.

Structural characterization of these species is difficult, however, experimentally, because they are unstable and span a time-scale of several days in vitro. One numerical challenge in characterizing these transient species is the development of coarse-grained models and sampling methods able to explore, at an appropriate atomic resolution, large time and spatial scales. Similarly, though N-methylated Abeta16-22 peptides inhibit the fibrillogenesis of full-length Abeta and disassemble fibrils in vitro, there is little information about their mechanism of action.

Here, I first review recent simulations aimed at understanding the dynamics and free energy surface of the oligomerisation of amyloid-forming peptides using a coarse-grained protein force field (OPEP) coupled to the activation-relaxation technique (ART), and molecular dynamics (MD) and replica exchange MD (REMD) simulations. We emphasize that the OPEP force field is generic and can be used to study the structural and thermodynamical properties of any amino acid sequence using MD and REMD, or explore the low energy conformations using ART.

Based on ART-OPEP and MD-OPEP simulations of various oligomeric sizes ranging from dimers to 16-mers, we can for instance extract a generic aggregation picture starting from random orientations and conformations of the peptides. Of importance in the late steps of aggregation is the observation of reptation moves of the chains, mechanism confirmed later experimentally. Application of this coarse-grained protein simulation package to amyloid peptides also can complement experiments by pointing to the non-negligible Boltzmann probability of unexpected topologies, such as the beta-barrel.

Then I present coarse-grained MD and REMD simulations of oligomers with multiple copies of an N-methylated inhibitor. While MD simulations do not point to any significant information within 100 ns time scale, REMD simulations help identity three modes for destabilising protofibrils.

Acknowledgement

I acknowledge financial support from CNRS, University of Paris 7 Denis Diderot, Alzheimer Society of Canada and "ImmunoPrion, FP6-Food-023144, 2006-2009". Most of the work was done contribution in collaboration with Prof. Normand Mousseau (University of Montréal, Canada), Prof. Guanghong Wei (University of Fudan, Shanghai University, China) and Yassmine Chebaro (Ph.D student, IBPC, France).

2.

Etude DFT et TDDFT de propriétés spectroscopiques et d'optique non linéaire de composés organométalliques

Abdou Boucekkine

Equipe de Chimie Théorique Inorganique, UMR CNRS 6226 Sciences Chimiques de Rennes, Université de Rennes 1, campus de Beaulieu, 35042 Rennes cedex (France) ; abdou.boucekkine@univ-rennes1.fr

Le domaine des propriétés spectroscopiques, de luminescence ou d'Optique Non Linéaire (ONL) constitue un champ d'application des complexes organométalliques. Plusieurs méthodes quantiques permettent d'étudier ces systèmes et d'interpréter ces propriétés. Parmi les techniques les plus utilisées actuellement figurent celles basées sur la Théorie de la Fonctionnelle de la Densité (DFT) et la DFT dépendante du temps (TDDFT).

Après un bref rappel sur ces techniques, il sera présenté plusieurs exemples d'application relatifs:

- au ligand 4,4''dimethyl,4'-(*N,N*dimethylaminophenyl)2,2',6',2''terpyridine et de ses complexes de métaux de transition et de lanthanides (figure 1) qui ont révélé des propriétés spectroscopiques et d'ONL intéressantes [1].

- à des complexes neutres monométalliques, de degré d'oxydation deux, dichlorés avec un ligand 2,2'-bipyridyle substitué en 4,4' (figure 2) pour leurs propriétés d'ONL.

- aux propriétés spectroscopiques d'absorption, mais aussi d'émission (phosphorescence) de plusieurs complexes du platine de formule R-styryl-C^N-ppy)Pt-O^O-acac (R= H, OMe, NMe_2, NO_2) dérivant de la structure de base C^N-ppy-Pt-O^O-acac (figure 3) [2].

- à des composés photochromes, composés qui sous irradiation lumineuse subissent une transformation réversible entre deux formes ayant des caractéristiques d'absorption différentes. Le phénomène de photochromisme impliquant le dithiényléthène (DTE, figure 4) est dû à une interconversion réversible sous irradiation (photocyclisation) entre deux formes isomères: une forme ouverte et une forme fermée [3].

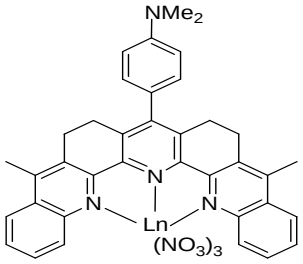

Fig. 1

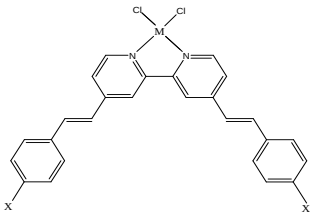

Fig. 2

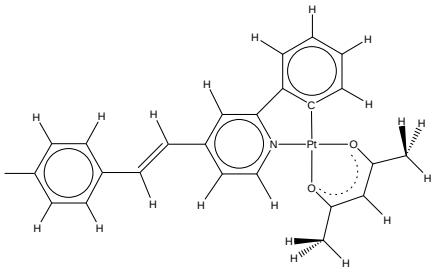

Fig. 3

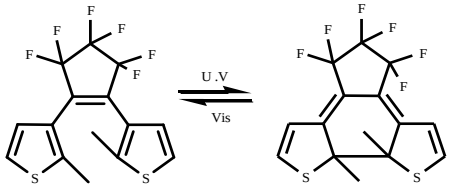

Fig. 4

La combinaison de ligands DTE diversement fonctionnalisés et de métaux de transition peut donner lieu à des complexes présentant des propriétés remarquables de luminescence ou d'ONL, le photochromisme servant d'interrupteur pour déclencher une ou l'autre de ces propriétés.

Nous présentons ici les résultats obtenus pour deux ligands à base de DTE : pour le premier, appelé ligand « original », chaque thiophène est fonctionnalisé en position 2 par un groupement phénylamino (groupement donneur d'électrons) et par un groupement pyridile (accepteur) en position 5. Dans le second ligand, appelé ligand « classique » les deux groupements donneur (D) et accepteur (A) sont fixés aux deux thiophènes du DTE (figure 5).

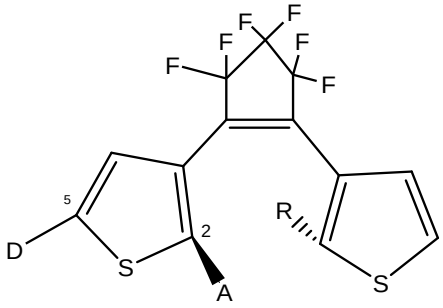

fig.5: ligand "original"

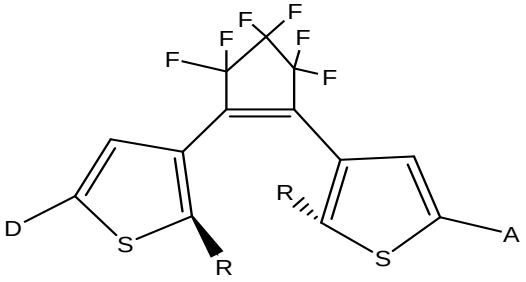

fig. 6 : ligand "classique"

Des complexes de Zn(II) bipyridile dérivés de ces ligands ont également été étudiés

(la figure 6 présente la forme fermée d'un de ces complexes).

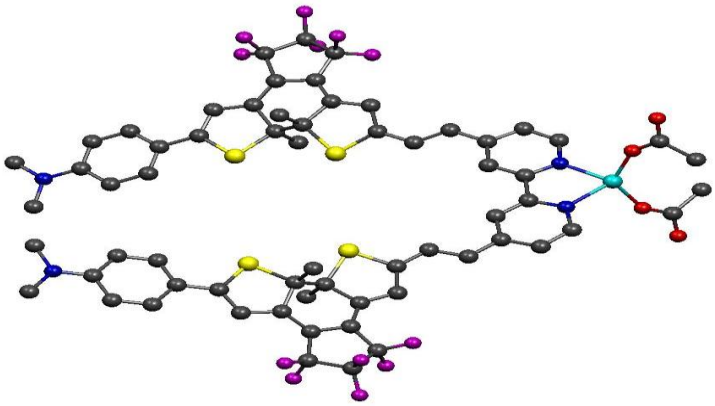

Fig. 6

Les différents calculs effectués, qui ont fait appel aux fonctionnelles hybrides B3LYP et surtout PBE0 et à une base LANL2DZ polarisée, ont permis de caractériser complètement les systèmes étudiés, et d'interpréter leurs propriétés spectroscopiques et d'ONL éventuelles. Les applications éventuelles de ces études sont discutées.

References:

[1] K. Sénéchal-David, A. Hemeryck, N. Tancrez, L. Toupet, J. A. Gareth Williams, I. Ledoux, J. Zyss, A. Boucekkine, J-P. Guégan, H. Le Bozec, O. Maury, J. Am. Chem. Soc. 128 (2006) 12243

[2] B. Yin, F. Niemeyer, J. A. Gareth Williams, J. Jiang, A. Boucekkine, L. Toupet, H. Le Bozec, V. Guerchais, Inorg. Chem. 45 (2006) 8584

[3] a- H. Bouas-Laurent, H. Durr, Pure Appl. Chem. 73 (2001) 639.
b- M. Irie Chem. Rev. 100 (2000) 1685.
c- V. W. W.Yam, C.C. Ko, N.Y. Zhu, J. Am. Chem. Soc. 126 (2004) 12734.
d- V. Aubert, thèse de l'Université de Rennes 1 (2007).

3.

Classification et Etude théorique de nouvelles formes allotropiques du carbone

Bahoueddine Tangour, Anis Gannouni

Université de Tunis-El Manar, Tunisie. baha.tangour@laposte.net

L'élément chimique carbone présente une grande variété de composés formés uniquement par des atomes de carbone hormis ceux des bords. Cette grande variété impose une nouvelle lecture de la notion d'allotropie. Ce vocable est souvent utilisé pour décrire des formes moléculaires ou cristallographiques d'une même composition chimique mais présentant des caractéristiques géométriques différentes et par conséquent exhibant des propriétés physicochimiques spécifiques. Il est nécessaire de mettre à côté ce type de différences pour l'atome de carbone et de nous limiter à une propriété chimique pour distinguer de manière univoque les différentes formes allotropiques avant de subir les simples modifications structurales pour les composés d'essence cristalline.

L'hybridation de l'atome de carbone est souvent citée pour interpréter les grandes différences de comportement entre ses deux principales formes qui sont le diamant et le graphite. Le premier est hybridé sp3 et le second sp2. En nous basant sur cette propriété et en tenant compte de la valence 4 du carbone nous retrouvons une autre forme dont la découverte est clamée depuis les années 60 qui est le carbone acétylénique linéaire (LAC) [1], nommé aussi carbyne (Russe: карбин) ou polyyne linéaire infini, qui est formé par un ensemble de carbone hybridé en sp et dont la structure chimique [2] s'écrit -(C::: C)-n. Ce type de carbone est d'un intérêt considérable pour les nanotechnologies comme son module de Young est quarante fois supérieur à celle du diamant [3]. Il semble être un semi-conducteur qui est très sensible à la lumière, donc il a été suggéré de l'utiliser dans les photodiodes et les dispositifs similaires. Nous avons effectués des calculs avec les logiciels Gaussian et Vasp qui mettent en évidence un écart de près de 0.18Å entre deux liaisons voisines en compétition avec une forme polycumulènes où toutes les liaisons sont égales à presque 1.3Å. Nous avons aussi déterminés les spectres de vibration et le gap évalué à 1.3 eV caractéristique d'un semi-conducteur.

On peut aussi parler de la molécule de dicarbone C2 comme une autre forme allotropique du carbone mais dans l'état de valence 2, celui définissant la famille des carbènes.

Le tableau 1 présente un classement des différentes formes allotropiques connues du carbone dans ses deux états de valence 2 et 4. Ce tableau est à deux entrées. Les lignes représentent le nombre de doublets libres de l'élément chimique et les colonnes indiquent la coordinance définie par le nombre d'atomes voisins à un atome donné. Cette classification montre une certaine périodicité. Le carbone tétravalent d'hybridation sp3 occupe la case (0,4) la plus à droite de la première ligne. Le passage à la case adjacente à gauche (0,3) exclut la participation d'une orbitale 2p à l'hybridation amenant au graphite où le carbone est hybridé sp2. Le même procédé fait passer au LAC présenté dans la case (0,2) avec l'hybridation sp.

Une diminution de la valence du carbone se répercute par le passage à la ligne en dessous avec un décalage de deux colonnes à gauche. Ainsi la molécule C2 est présente dans la case (1,2) avec la

configuration non hybridé p2. On peut prévoir une polymérisation de cette molécule pour former un fil de carbone zigzagant avec des angles de 120° caractérisé par l'hybridation sp2.

D'autre part, les fullerènes |4] et les nanotubes de carbone [5] ont donné une nouvelle notoriété aux différentes formes allotropiques du carbone. Dès sa découverte, le fullerène sous sa forme la plus symétrique C60 a été appelé la 3ème forme allotropique du carbone. Cette grosse molécule est représentative d'un grand nombre d'homologues moins symétriques et présentant un nombre d'atome de carbone allant d'une vingtaine à quelques centaines, certains d'entre eux ont aussi été désignés par leurs auteurs comme des nouvelles formes allotropiques. Les nanotubes de carbone sont considérés aussi comme une variante cylindrique des fullerènes. Très tôt cette affiliation a été mise à épreuve à cause des particularités structurales des nanotubes. Les atomes des fullerènes sont tous compatibles avec une hybridation classique soit sp2 soit sp3 selon le nombre d'atomes dans les cycles (5, 6, 7…) alors que tous les atomes d'un nanotube appartiennent à des cycles à 6 chainons qui ne sont paradoxalement pas plans. L'allongement des longueurs des liaisons par rapport à celles du graphite ainsi que les écarts à la planéité ont été pris en compte sous le vocable re-hybridation sp2/sp3. Malheureusement l'application des concepts usuels d'hybridation à la valence 4 du carbone ne permet pas de proposer un nouveau type d'hybridation. Une approche qui pousse à définir une nouvelle forme d'hybridation a été proposée qui consiste à supposer l'intervention de 5 orbitales dans une hybridation sp3s*[6]. Cette manière d'opérer implique implicitement l'intervention de la valence 6 du carbone. Nos calculs théoriques montrent sans ambigüité l'intervention des fonctions représentant les orbitales 1s dans les orbitales moléculaires. Les coefficients relatifs à l'orbitale 1s se situent entre 0.3 et 0.7 selon la base utilisée.

Table 1: Classement des formes allotropiques du carbone II et IV.

	1	2	3	4
0		sp/AX2 LAC	sp^2 /AX3 Graphite	sp^3/AX4 Diamant
1	p^2/AXE Dicarbone	sp^2/AX2E VShaped C		

Table 2: Classement des formes allotropiques hypothétiques du carbone VI

	1	2	3	4	5	6
0		s^2/AX2 Squaryne	s^2p/AX3 Cubene	s^2p^2/AX4 Diamonyne	s^3p^2/AX5 diamonène	s^3p^3/AX6 Hexadiamant
1		s^2p/AX2E Zallène	s^2p^2/AX3E Nanotube	s^3p^2/AX4E Graphitubène		
2	s^2p /AXE2 Superdicarbone	s^2p^2/AX2E2 SuperVShaped C				

L'application de la manière utilisée dans le tableau 1 à la valence 6 du carbone est indiquée dans le tableau 2. Dix nouvelles formes allotropiques sont ainsi proposées dont le nanotube de carbone. Nous avons entamé dans notre laboratoire l'étude des autres formes et en particulier l'hexadiamant.

References

[1] A.E. Goresy et al, Science , 1968, 161, 363
[2] Richard J. Lagow et al, Science, 1995, 267, 362 – 367
[3] Lior Itzhaki et al, Angew. Chem. Int. Ed. , 2005, 44, 7432-7435.
[4] H. W. Kroto et al, Nature, 1985, 318, 162.
[5] S. Iijima, Nature, 1991, 354,56-58
[6] J X Cao et al, J. Phys. Condens. Matter, 2001, 13, L271

4.

Random-Matrix Theory within Superstatistics

A.Y. Abul-Magd

Faculty of Engineering, Sinai University, El Arish, Egypt

Superstatistics is a technique that allows modeling thermally non-equilibrated systems in terms of a canonical Gibbs distribution in which an intensive parameter (the inverse temperature) fluctuates. In analogy to superstatistics, we connect the canonical Gaussian ensembles of the random-matrix theory (RMT), which models quantum chaotic systems, to their superstatistical generalizations through the fluctuation of an intensive parameter, the local density of states. On one hand, the superstatistical RMT, seen from the present perspective, may bear interest per se because of the additional nontrivial fluctuations introduced in a simple model. On the other hand, it may constitute a useful statistical paradigm for the analysis of the spectral fluctuations of systems with mixed regular-chaotic dynamics. In contrast to other proposals for applying RMT to mixed dynamics, the superstatistical approach yields ensemble of matrices, which are invariant with respect to base transformation. The formalism has been checked by the analysis of experimental resonance spectra of mixed microwave billiards. The spectra for each billiard are represented as time series in which the level order plays the role of time. Each series is shown to have two relaxation times as required by superstatistics, which involves the folding of two distribution functions. Analysis of the time series suggests that the superstatistical-parameter has an inverse-chi-square distribution. The experimental distribution nearest-neighbor level spacings and strength functions agree with the corresponding predicted distributions

5.

Thrombosis Modeling in Stented Intracranial Aneurysms using a Lattice Boltzmann Numerical Method

R. Ouared[1], B. Chopard[2] and D. Rufenacht[3]

[1] Université de Genève, Centre Universitaire d'Informatique, Battelle A, 7 route de Drize, Genève, 1227, Switzerland, *rafik.ouared@unige.ch*
[2] Université de Genève, Centre Universitaire d'Informatique, Battelle A, 7 route de Drize, Genève, 1227, Switzerland, *bastien.chopard@unige.ch*
[3] Hopital Universitaire de Genève , Service de Neuro-Interventionel, 24 rue Micheli-du-Crest, Genève, 1211, Switzerland, *daniel.rufenacht@hcuge.ch*

Numerical modeling of thrombogenesis in intracranial aneurysms (Fig. 1) is important from both the fundamental and clinical point of views. Fundamentally, it will help in explaining why spontaneous thrombosis often occurs in unruptured giant aneurysms and rarely in smaller ones. Clinically, it will provide an assessment tool for the clotting capability of flow-diverter stents deployed within the intracranial arterial structures. The aim of such an implant is to induce an occluding thrombosis in the aneurysm, hence re-establishing the normal course of blood flow circulation in the vascular tree. Thrombosis is the first phase of vascular remodelling before subsequent biological processes take over to achieve full resorption of the aneurysm.

Intracranial aneurysms may rupture and cause death or disability of the patients. Studies have shown that in average 5% of the world wide population is a "positive" intracranial aneurysm carrier.

Thrombosis can be modeled in either way: 1/ by describing the time evolution of thrombin concentration through the numerical resolution of several reaction-diffusion equations involving tens of clotting factors in the clotting pathway. Thrombin is the most important ingredient which transforms soluble fibrinogen contained in blood into fibrin strings to consolidate the thrombus. This microscopic description is not self-consistent to explain the inhibition mechanism in aneurysms which is responsible for partial aneurysm occlusions. 2/by describing spatial and temporal evolution of thrombus in the aneuryms through mesoscopic modeling of the adhesion and aggregation of the platelets to the aneurysm wall and to fibrin (Fig. 3). This scheme captures geometrical variations of the anatomy and pulsatiliy of flow that both influence blood flow conditions for thrombogenesis. It applies to intracranial aneurysms to a large extend.

We present in this conference the main guidelines of the numerical model developed at university of Geneva. The objectives and justifications have been fully described in [1-2] and the qualitative (visual) validations in [3]. We present here the first quantitative validation of one of the main hypothesis of the model. The mathematical modeling of thrombogenesis in the framework of lattice Boltzmann is described in [4].

In this model, thrombosis is locally driven by the shear stress of blood near the aneurysm wall, and controlled by a shear stress threshold. In intracranial aneurysms, thrombosis reaction occurs at low shear rates (less than 100 s-1), the level at which platelet adhesion and aggregation is enhanced.

Two phases of blood flow are described within the lattice Boltzmann method (LBM): 1/ the plasma motion is described as an idealized newtonian fluid particles moving and colliding on a discrete space-time space (grid). The fluis is described in terms of discretized density distribution functions from which hydrodynamic moments (pressure, shear stress, velocity fields) are extracted. In a 2-dimension grid, the so-called D2Q9 model (8 directions) is used. The dynamics used to describe time and space evolution of the density distribution functions is the so-called BGK [5]. 2/ the platelet

motion is added on top of the flow model to characterize its transport and the adhesion and aggregation as well. Platelets are assumed to be point particles passive scalars.
Assuming an oscillating flow, the correlation of the clotting surface fraction with size of the aneurysm and shear stress threshold in a sidewall configuration, has been studied. The results are qualitatively matching clinical observations in which conditions of no, partial (Fig. 2) or full occlusion of aneurysms have been fulfilled. Recently on, the first indirect validation of the shear stress threshold hypothesis has been established. This has opened the way further for future experimental validations to calibrate the model and improve its assessment capability.

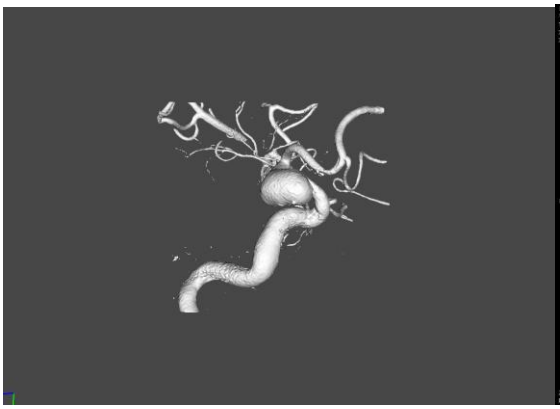

Fig. 1. Patient-specific intracranial aneurysm

Fig. 2. Partially thrombosed aneurysm.

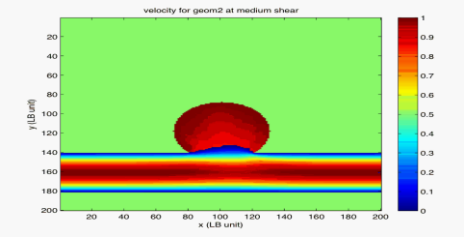

Fig. 3. Simulated thrombosis in sidewall aneurysm.

Acknowledgement
We acknowledge and thank Ernest Boninchi foundation, the Swiss National Science Foundation and @neurIST European collaboration for their financial support.. We also thank Alexander von Humboldt Foundation for the invitation to NAC-CPC'08 held in the city of Sidi BelAbbes in Algeria.

References

[1] B. Chopard, R. Ouared, D.A. Ruefenacht, Mathematics and Computers in Simulation **72** (2006), 108-112
[2] R. Ouared, B. Chopard, Journal of Stat. Physics **121** (2005), 209-221
[3] B. Chopard, R. Ouared, D.A. Ruefenacht, H. Yilmaz, Int. Jour. of Mod. Phys. C **18** (2007), 712-721
[4] R. Ouared, B. Chopard, B. Stahl, D.A. Ruefenacht, H. Yilmaz, G. Courbebaisse, Computer Physics Communicaitons **179** (2008), 922-930
[5] S. Succi, The lattice Boltzmann Equation for Fluid Dynamics and Beyond, Oxford University Press, 2001

6.

The Monte Carlo simulation: an interesting tool for the understanding of high pressure scanning electron microscopy

C. Mathieu[1], L. Khouchaf[2] and O Mansour [3] and A. Kadoun[3]

[1] Université d'Artois , Faculté des Sciences Jean Perrin., Lens, 62300, France, christian.mathieu@univ-artois.fr
[2] Ecole des Mines de Doiau, Douai.,59500, France
[3] LECM., Sidi bel abbes, 22000, Algéerie

The use of elevated gas pressures in the sample chamber of a scanning electron microscope (i.e., High pressure SEM, or HPSEM) together with specialized electron detectors create imaging conditions that allow samples to be examined without any preparation [1]. Specific operating conditions of elevated pressures combined with sample cooling can allow hydrated samples to be maintained in a pristine state for long periods of time. Dynamic processes also can be easily observed. A wider range of detector options and imaging parameters introduce greater complexity to the HPSEM operation than is present in routine SEM. The Fig 1 shows for example the image of a same sample obtained under different gases in the same excitation conditions [2]. It is easy to see that the gas nature induces modifications in the sample response and more generally in the image contrast.

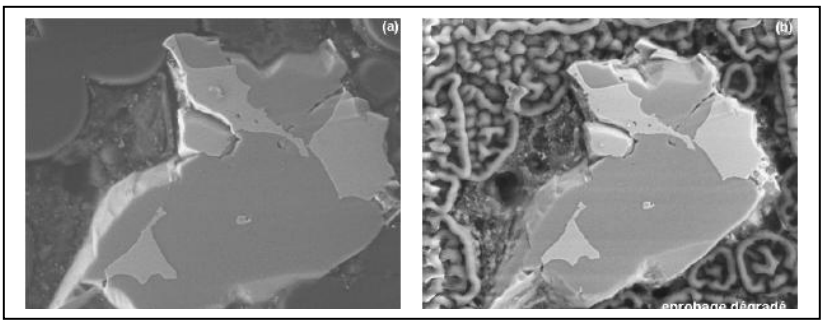

Fig. 1. Image at 266 Pa and 20kV in (a) water vapour (b) helium

Characterization of chemical microstructure is one of the most important applications of the conventional scanning electron microscope (SEM) equipped with an energy dispersive x-ray spectrometer (EDS).). Interest in electron-excited x-ray microanalysis is potentially even greater in the High pressure (HPSEM) where dynamic chemical experiments can be conducted. Figure 2 shows the effects of elastic and inelastic scattering of the beam electrons by the gas atoms . The consequences of elastic scattering are the reduction of beam current within the focused probe and redistribution of this current to form a wide "skirt" around the beam, significantly degrading the spatial resolution of x-ray microanalysis. These gas-scattering effects can greatly alter the results achieved with x-ray microanalysis in the HPSEM compared to performing a similar x-ray measurement in a conventional SEM under high vacuum conditions. The major consequence of inelastic scattering is the generation of characteristic and continuum (bremsstrahlung) x rays from the gas atoms that contribute to the measured Si-EDS spectrum. X-ray production is a relatively rare event, suffered by one in 10^6 electrons or fewer. Most electrons do not suffer significant energy loss from inelastic interactions.

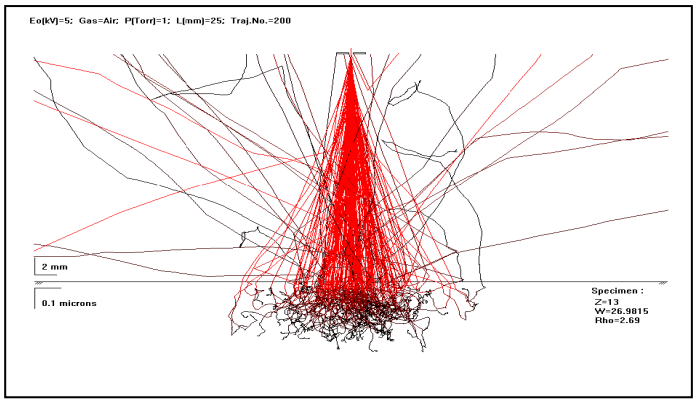

Fig. 2 Beam broadening under air gas at 5 kV

So, it is of fundamental importance to know the details of the new electron distribution resulting from the collisions with the gas. Monte Carlo computations have been extensively used for solid targets, but much less for gases . A Monte Carlo simulation has been developed in order to answer the question of beam distribution under high pressure conditions. In order to quantify the beam spreading, r0,9 is defined as the radius in the plane of the electron impact that contains 90%of the scattered electrons [1-2]. The unscattered fraction belonging to the primary beam is first subtracted from the total current and it is the remaining component that is characterized by the broadening measured.

The understanding of the operating parameters (beam energy, gas nature (monoatomic, molecular gas, and mixture), pressure, working distance) are investigated. Previously[3], it has been clearly established that scattering with helium is much lower than with air, water or argon. Together with air, Fig. 3 reports on the r0,9 radius vs. pressure for helium. It appears that at a pressure of 1 Pa, helium behaves like air and scatters strongly, leading to a wide skirt of about 1450 mm, slightly lower than that of air. The difference between the two gases does appear only at higher pressures where the radius for helium is about 30% lower than for air at 100 Pa. Note that for helium, at pressures in the (1–100 Pa) range, the skirt radius remains almost constant and hence does not dependent on the pressure. Contrary to air, it seems that there is no skirt at high vacuum conditions (10-3 Pa) in helium.

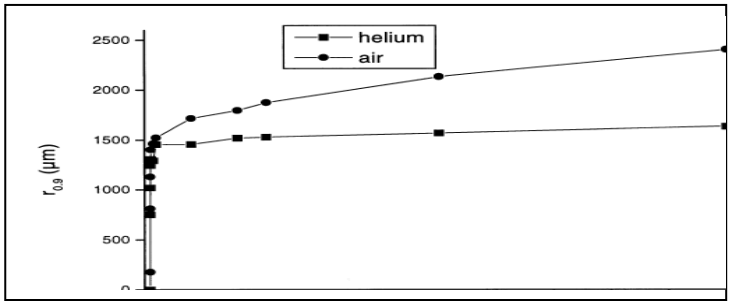

Fig3. Skirt radius vs gas pressure for air and helium (Wd =25 mm and U =15kV)

An another example deals with the variation of the skirt radius when the analytical distance is gradually lowered. This variation is shown for air in Fig. 4 where r0,9 vs. pressure curves are plotted for various analytical distances between 25mm and 2 mm. For a distance of 15mm that is the minimum usually used in classical HP-SEM, the skirt radius is obviously still too high, of around 1000 mm at 100 Pa. On the other hand, the skirt extent is drastically reduced for a distance of 5 mm. The

better result is obtained for an analytical distance of 2mm where the relative deviation from the 25mm corresponding radius at 100 Pa is of about 90%. However, this very thin distance could generate difficulties in X-ray
detection in such a way that appropriate experimental geometry are needed to accomplish XRMA under this extreme HP-SEM condition.

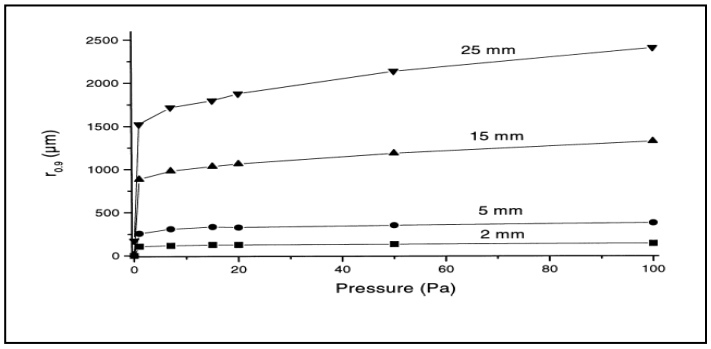

Fig. 4. Skirt radius versus pressure and for various Working distance

A combination of modelling and experiments will help high pressure scanning electron microscope operators. The Monte Carlo modelling can be used to determine the optimum conditions for minimizing the effect of the spreading of the electron primary beam on X-ray microanalysis.

References

[1] G.D Danilatos,.Advances in Electronics and Electron Physics **71** (1988), 71, 109–250.
[2] C Mathieu, L Khouchaf, A Kadoun , In Modern Research and Educational Topics in Microscopy; (Eds.), A. Méndez-Vilas and J. Díaz Sons: Chichester (2007), 779-786
[3] Adamiak, B.; Mathieu, C. Scanning 22 (2000) 178–181.

Oral Contributions

1.

Theoretical study of protonated hydrate clusters by combined Monte Carlo and quantum chemistry methods

Ariche Berkane, Sellaoui Wafa, Rahmouni Ali

Laboratoire de Modélisation et de Méthodes de Calcul, Centre Universitaire docteur Moulay Taher de

Saida, B.P. 138, Cité En-nasr, route de Mascara, 20002 Saida, Algérie. Fax : +21348471508.
E-mail : ariche_mc@yahoo.fr

The study of structures and energies of protonated hydrate H3O+(H2O)n were the object of a lot of theoretical and experimental investigations(1-25). The general objective of these researches is to supply precise information which can be used in very different domains such as the atmospheric chemistry (10,11), biochemistry(12), the chemistry of solutions(13), catalysis(14)…etc.

In the statistical physics, the simulations of aggregates H3O+(H2O)n requires the knowledge of these various dominating terms contributing to the energy. The knowledge of these terms is an important stage during the modelling but is not the end it self. The majority of Monte Carlo simulations of such systems depend on tow main approximations made for the total interaction energy calculation of a given configuration: the first concerns the decomposition of the total interaction energy. Generally this energy is calculated as the sum of the pair-wise interaction energies of the constituents. In the case of a protonated hydrate clusters; we have tow types of interaction, ion-water interactions, and water-water interactions. The multi-body effects are enclosed some times in the representation of the total interaction energy. According to the level of the approximation, we can obtain completely different results. The second approximation concerns how the interactions energies are represented. The choice of the shape of the potential used to represent each of the terms of the energy is not easy. It remains then to find parameters having a theoretical or experimental justification. These parameters are generally fitted from empirical data, and or ab initio. Independently of their origins, these potentials can give values of the energy far from the reality.

The main motivation of our work is to reduce the source of indistinctness and to improve the quality of results of Monte Carlo simulations of H3O+(H2O)n=1, 6 systems. The idea is to estimate by quantum calculations the total energies of generated configurations during the simulation. To make it, we write a program of calculation in which we have combined the quantum mechanics to the statistical mechanics. This program allowed us to replace the use of analytical potentials by a quantum estimation of the energy.

Our program of calculation works under the operating system UNIX, and that is going to assure us the combination of the statistical mechanics to the quantum mechanics. From a computer point of view, the major difficulty is to integrate quantum calculations, made by the Gaussian software (28) in a set of programs written with FORTRAN language which execute sequentially a great number of spots. The Program so developed is a script file written in a shell language, which allows to organize alternately the totality of spots stemming from Metropolis's (29) algorithm. This program is actually adapted to the simulation of protonated hydrates clusters, and it allows obtaining the energetic and structural properties of equilibrium at given temperature. To observe the effect of the geometry of

hydronium ion on the energetic and structural characteristics of ionic clusters H3O+(H2O)n=1, 6 at 300K, tow series of Monte Carlo simulations were done: the first one with a planar geometry for the hydronium ion (ROH=0.965Å and HOH=120°)(1), the second one with a slightly pyramidal geometry (ROH=0.969Å and HOH=113.1°)(2), the geometry of water molecules is the same for the two series (ROH=0.9572Å and HOH=104.52°)(30). These geometries are fixed during simulations. The notation CPYRn and CPLNn corresponds to the cluster containing an ion of pyramidal and planar geometry respectively. n represent the number of water molecules present in the cluster. For every simulation the number of sampling is 25000, except for CPYR3 and CPYR6 systems it is about 50000, in these last cases convergence was pushed to observe the behaviour of clusters beyond 25000 iterations. The energies of configurations are calculated by the DFT method using the functional B3LYP and the base 6-31G*.

Our tools of analyses allow us to know the water molecules distribution according to the distance R which separates them from the ion, and know their orientations with regard to the ion. We shall study two types of radial distributions noted (OI-OW) and (OI-HW). In the first one the distances R are evaluated between the oxygen atom of the hydronium ion and the oxygen atoms of the water molecules. In the second the distances are evaluated between the oxygen atom of the hydronium ion and the hydrogen atom of the water molecules.

The integration of radial distribution curves according to R allows us to know the number of water molecules around the ion for a given distance.

Maximal intensities for the (OI-OW) distribution of the first solvation shell are the same for the two systems CPYR and CPLN. These maximums are founded for clusters containing one and two water molecules at 2.50Å. This distance is exactly the same as the values stemming from simulations with analytical potentials **(1, 2, 5, 6, 7)**. This distance will be larger about 0.1Å when we introduce the third and fourth water molecules. This difference can be due to the multi-body effects. This distributions was observed in the results stemming from Monte Carlo simulations using the analytical potential RK for the system $H_3O^+(H_2O)_3$ **(5)**. The molecules of the first solvation shell of the clusters containing five and six water molecules will occupy a position corresponding in average to 2.50Å again. This situation can be due to the interaction between the molecules of the second solvation shell and the ion, and consequently they obliged the molecules of the first shell to be closer to the ion, this allows to find a better compromise of interaction between the water molecules and the ion and the repulsion due the multi-body effect. These distances are in good agreement with experimental values found for the liquid which are 2.52Å **(3)**, and those found in the crystals that are included between 2.48Å and 2.68Å **(4)**. The privileged positions for the second solvation shell differ according to the geometry of the hydronium ion and the number of water molecules. The most important difference is observed in the case of systems containing four water molecules; it is 5.10Å in CPYR and 4.40Å in CPLN. In the case of clusters containing five and six water molecules the second shell places itself between 4.50Å and 4.70Å. These distances are comparable with the results of references **(1.2.5.6.7)** that are included between 4.60Å and 4.85Å. The maxima corresponding to the first shell in the (OI-HW) distribution is at a distance larger about 0.7Å than the maxima of (OI-OW) distribution; so we conclude that all the molecules of the first solvation shell orient their hydrogen atoms in the opposite direction of the ion. This molecules orientation allows the formation of hydrogen bonds as strong as possible between the oxygen atoms of water molecules and the ion hydrogen atoms. This spatial organization observed for the first solvation shell molecules disappears for the second shell molecules. The maxima of the hydrogen atoms for the aggregate

CPYR are moved with regard to the distributions of oxygen atoms by 0.2Å to 0.3Å, while for the aggregate CPLN the gap is 0.5Å. This orientation is may be due to the geometry of the ion which obliged the water molecules to occupied well defined positions in the space. The main conclusion that one can pull from the coordination numbers values is that the solvation shells are well identified and the first solvation shell contains only three water molecules for the aggregates containing more than three water molecules, and we can say that the results giving four molecules in the first solvation shell **(1.2.7)**, are due to an uncertainty in the description of the interaction energy of the system.

The energetic data stemming from our simulation are either global (average interaction energies), or punctual (energy of every configuration, energetic minima). To study the energetic aspect of our system in a global way, our calculation program estimates the average energy of interaction every macro-step. This tool allows us to verify our energy convergence.

It is noted that we have used adequate initial configuration to accelerate the convergence. The energetic behaviour of our systems finds explanation in nature of the spatial distributions of water molecules around the ion, as well as the type of hydrogen's bonds formed during simulations. For the tow systems

CPYR3 and CPLN6 particular behaviour beyond 25000 steps was not observed and we noticed that the energy is well stabilized around the value of equilibrium. Now we will compare our results with experimental available values and those of Monte Carlo simulations using analytical potentials.

Due to a bad description of energetic components, an important disagreement is obtained with results stemming from simulation using analytical potentials for the aggregates containing more than three water molecules. It is noted that the main advantage of our program is the fact that it takes into account all energetic terms and so estimate the energies of configurations with a good precisions. The average interaction energies obtained for aggregates containing the planar ion are always lower; this result is due essentially to the distribution of the water molecules around the ion and to the nature of hydrogens bond formed in each system. If we compare the energy values according to the structure of the hydronium ion, we notices that for the CPYR system values obtained with the AR potential are very far to our results, however values obtained with the RK potential are in very good agreement with our results, and this can be explain by the fact that the RK potential and contrary to the AR potential takes into account non- additive terms like the three body effect. For the CPLN system, our results are close to values obtained with the NT potential, and are far from values obtained with the AR potential, which can be explain also by the nature of the used potential. The NT potential takes into account non-additive terms, and it describes them with a formula restricted to the induction energy which is the main non-additive term. It is noticed that the main advantage of our calculation program is in the fact that it takes into account all the energetic terms.

Provided with a tool of precise calculation, we were able to begin the investigation of protonated hydrates clusters $H_3O^+(H_2O)_{(n=1,6)}$ and of their behaviour. We began tow simulations series with tow geometries of hydronium ion, to observe the ion structure effect on the energy and structural characteristics. The two series reproduce correctly experimental distributions. The aggregates containing three and four water molecules have a first solvation shell placed at 2.60Å , this distance confirm the results obtained with RK potential, which is among the best current potential**(5)**. Besides, taking into consideration the all of energetic terms of the system

show that the presence of four molecules in the first solvation shell can be due to an artefact of analytical potential. We have shown the simulation space dimensions, and conclude that the molecules exchange between tow solvation shells are forbidden. The aggregation energies are better described, and the series which use a pyramidal geometry of the hydronium ion reproduced these energies with a very good precision.

References

[1] E. Kochanski, Nouv. J. Chim.1984, 8, 605.
[2] R. Kelterbaum, N. Turki, A. Rahmouni, E. Kochanski, J. Chem. Phys.1994, 100, 1589.
[3] R. Triolo, A. H. Narten, J. Chem. Phys.1975,63, 3624.
[4] J. O. Lundgren, I. Olovsson, in "the Hydrogen Bond", Eds. P. Schuster, G. Zundel,C. Sandorfy ; North Holland, Amsterdam.1976, 2, 471.
[5] R. Kelterbaum, thèse Université Louis Pasteur. 1995.
[6] N. Turki, Rapport de D.E.A. Université Louis Pasteur. 1991.
[7] A. Rahmouni, Thèse Université Louis Pasteur. 1990.
[8] Y. K. Lau, S. Ikuta, P. Kebarle. J. Am. Chem. Soc.1982, 100, 1462.
[9] C. A. Deakyne, M. Meot-Ner, C. L. Campbell, M. G. Hughes, S. P. Murphy, J.Cbem.Phys 1986, 84, 4958.
[10] Castleman Jr. A. W. Nucleation processes and aerosol chemistry. Space Sci. Rev. 1974, 15, 547-589.
[11] Castleman A. W. Nucleation and molecular clustering about ions. Adv. Colloid Interface Sci.1979,10, 73-128 .
[12] K. Drukker, S.W. de Leeuw, S. Hammes-Schiffer, J. Chem. Phys. 1998,108, 6799.
[13] Kebarle P. Ion thermochemistry and salvation from gas phase ion equilibriums. Ann. Rev. Phys.Chem. 1977,28, 445-476 .
[14] Robinson A. L. Heterogeneous catalysis: can surface science contribute. Science 1974,185,772-774 .
[15] C. Chaudhuri, Y.-S. Wang, J.C. Jiang, Y.T. Lee, H.-C. Chang, G. Niedner-Schatteburg. Mol. Phys. 2001,99, 116 .
[16] J.-C. Jiang, Y.-S. Wang, S.H. Lin, Y.T. Lee, G. Niedner-Schatteburg, H.-C. Chang, J. Am. Chem. Soc. 2000,122, 1398.
[17] Y. Xie, R.B. Remington, H.F. Scheafer III, J. Chem. Phys.1994,101, 4878 .
[18] D. Wei, D.R. Salahub, J. Chem. Phys. 1994,101, 7633.
[19] M. Tuckerman, K. Laasonen, M. Sprik, M. Parrinello, J. Phys. Chem.1995,99, 5749.
[20] M. Tuckerman, K. Laasonen, M. Sprik, M. Parrinello, J. Chem. Phys.1995,103, 150 .
[21] R. Vuilleumier, D. Borgis, J. Phys. Chem.1998,B 102, 4261.
[22] R. Vuilleumier, D. Borgis, J. Chem. Phys.1999,111, 4251.
[23] U.W. Schmitt, G.A. Voth, J. Phys. Chem.1998,B 102, 5547.
[24] U.W. Schmitt, G.A. Voth, J. Chem. Phys.1999,111, 9361.
[25] T.J.F. Day, U.W. Schmitt, G.A. Voth, J. Am. Chem. Soc.2000,122,12027.

2.

Solar Energy Conversion in North Africa and Universal Energy Situation

Waheed A. Badawy

Chemistry Department, Faculty of Science, Cairo University,12613 Giza–Egypt

E-mail: wbadawy@cu.edueg, wbadawy@chem-sci.cu.edu.eg;, wbadawy50@hotmail.com

Our universal energy problems can be solved if we concentrate on the ultimate source of energy of all kinds i.e. the Sun. The North African territory represents the best and most suitable positions for solar farms based on photovoltaic and photoelectrochemical cells. The concentration of sun light and the use of photovoltaic systems can provide not only the African countries but also the whole European countries with enough and environmentally safe energy.

Photovoltaic and photoelectrochemical systems were prepared by the formation of a thin porous film on silicon. The porous silicon layer was formed on the top of a clean oxide free silicon wafer surface by anodic etching in HF/H2O/C2H5OH mixture (2:1:1) [1]. The silicon was then covered by an oxide film (tin oxide, ITO or titanium oxide) by the spray/pyrolysis technique which enables the incorporation of foreign atoms like In, Ru or Sb in the oxide film matrix during the spray process [2]. The incorporation of foreign atoms improves the surface characteristics of the oxide film which leads to the improvement of the fill factor and higher solar conversion efficiency [3].

The prepared solar cells are stable against environmental attack due to the presence of the stable oxide film. It gives relatively high short circuit currents (Isc) compared to our previously improved silicon solar cells. Although the open-circuit potential (Voc) was not affected by the porous silicon film, the short circuit current was found to be sensitive to this layer and its thickness. An optimum thickness of the porous film and also the oxide layer is important for the application of porous silicon layers in solar energy converters [4]. The use of porous silicon instead of silicon single crystals in solar cell fabrication and the optimization of the solar conversion efficiency reduce the cost of solar modules and also increase the solar conversion efficiency through the large area of the porous structures.

References:

[1].Modern Trends in Physics Research; American Institute of Physics (AIP [Conference Proceedings, Volume 888, Melville, New York, 2007, Pages 29-36.
[2].W. A. Badawy , F. Decker and K. Doblhofer; Solar Energy Materials , 8 (1983) 363.[
[3] W. A. Badawy; J. Electroanal. Chem. , 281 (1990) 85.
[4] W. A. Badawy, J. Alloys and Compounds; (2008) In press.

3.

ETUDE THEORIQUE DU MECANISME, DE LA CHEMO- ET STEREO SELECTIVITE EXPERIMENTALE DE LA CYCLOADDITION DIPLAIRE-1,3 DU CARBONYL YLIDE DE PADWA AVEC LE α-METHYLENE CETONE

W. Benchouk[1], S. M. Mekelleche[1] et L. R. Domingo[2]

1 Département de Chimie, Faculté des Sciences, Université A. Belkaïd, B. P. 119, Tlemcen, 13000.
E-mail: benchouk_wafaa@mail.univ-tlemcen.dz & sm_mekelleche@mail.univ-tlemcen.dz)
2 Departamento de Química Orgánica, Universidad de Valencia, Dr. Moliner 50, 46100 Burjassot,
E-mail: domingo@utopia.uv.es

Les réactions de cycloaddition dipolaires-1,3 (13DC) sont largement utilisées dans la synthèse des composés cycliques et hétérocycliques pentagonaux d'intérêt pharmacologique et industriel et également dans la synthèse des substances naturelles. Dans ce travail, on se propose d'étudier théoriquement le mécanisme et la stéreosélectivité de la réaction de 13DC entre le carbonyle ylide de Padwa 1 et le α-méthylène cétone 2 (figure 1). L'analyse des indices globaux et locaux nous a permis de rationaliser la formation du stéréoisomère majoritaire formé expérimentalement. La localisation des états de transition, le calcul IRC (Intrinsic Reaction Coordinate), le calcul des degrés de synchronicité et des ordres de liaisons et l'analyse de la surface d'énergie potentielle (PES) ont été menés pour l'étude du mécanisme de cette réaction. Les calculs ont été effectués au niveau B3LYP/6-31G* et les résultats obtenus sont en accord avec les constatations expérimentales.

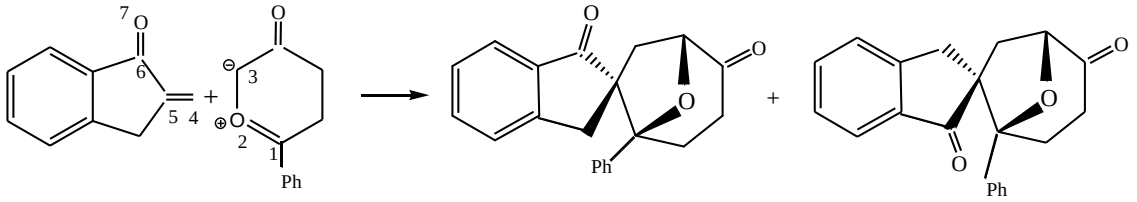

2 **1** **3 (endo)** **4 (exo)**

igure 1

Références

[1] A. Padwa, , Ed.; In 1,3-Dipolar Cycloaddition Chemistry, Wiley-Interscience: New York, 1984; Vol 1,2
[2] S. Muthusamy, J. Krishnamurthi, M. Nethaj, Chem. Commun., 2005, 3862.
[3] L. R. Domingo, E. Chamorro, P. Perez, J. Phys. Chem. A. 2008, 112, 4046.
[4] L. R. Domingo, M. J. Aurell, P. Pérez, R. Contreras, J. Phys. Chem. A. 2002, 106, 6871.
[5] L. R. Domingo, W.Benchouk, S. M. Mekelleche, Tetrahedron 2007, 63, 4464.
[6] W. Benchouk, S. M. Mekelleche, J. Mol. Struct.: THEOCHEM 2008, 852, 46.

4.

Homogénéisation et caractérisation mécanique de multicouches à base de carbone époxyde

M.H. Ben Ghozlen et M. Ben Amor

Lab. de Phy. des Matériaux, Dépnt. de Phy. Fac. Des Sc. De Sfax BP 1171 Sfax 3000 Tunisie

La propagation des ondes élastiques dans les systèmes multicouches, est de nos jours l'objet de plusieurs travaux de recherche dans plusieurs domaines comme l'aéronautique, la géophysique ou encore la télécommunication. Dans le présent travail on s'intéresse à des composites de type carbone époxyde, ces systèmes sont périodiques et ils résultent de la stratification de couches ayant les fibres de carbone orientées suivant deux séquences 0/90 et 0/45/90/135. Les fibres positionnées à l'angle 0, définissent l'axe X1 et celles à 90 l'axe X2, ainsi la base de travail est définie par le plan (X1,X2) et l'axe X3 normal aux interfaces entre les couches. Ces multicouches immergés dans l'eau, sont soumis à un rayonnement ultrasonore décrit par une onde plane contenue dans le plan (X1,X3) appelé plan sagittal.

Dans le domaine de faibles incidences et à des fréquences suffisamment basses, le comportement de ces structures est rapproché à celui d'un matériau homogène. Et de ce point de vue, il est possible de leurs associer une symétrie et des caractéristiques mécaniques. Ces matériaux composites auxquels on associe une forte anisotropie ainsi qu'un caractère dispersif, peuvent être homogénéisés. La procédure consiste à développer pour chaque couche une matrice dynamique reliant les contraintes et les déplacements au niveau des surfaces limitant la couche. Une méthode récursive basée sur la continuité de la contrainte et du déplacement de part et d'autre de chaque interface, est élaborée. Elle permet de relier la contrainte et le déplacement au niveau de la première et la dernière interface du système multicouche. Le résultat se représente par une matrice globale de rigidité, qui est à la base du calcul des coefficients de réflexion et de transmission ainsi que la description du champ de déplacement en fonction de la profondeur.

L'analyse spectrale du champ de déplacement en un point du diagramme (incidence,fréquence) permet d'obtenir les angles critiques et les nombres d'onde de Floquet traduisant le caractère périodique et homogène de ces systèmes stratifiés.

L'application de la méthode d'affinement de Newton Raphson à l'équation de Christoffel a permis de remonter aux constantes mécaniques des deux multicouches dans le domaine d'homogénéisation, et en dégager une légère dépendance en fonction de la fréquence. En fait une collecte de la vitesse de phase en fonction de l'orientation est utilisée, dans la résolution du système d'équations non linéaires relatif à chaque multicouche. L'étude et la présentation des deux systèmes permet de faire une comparaison des résultats et une meilleure compréhension des étapes de l'homogénéisation.

Le présent travail apporte des éclaircissements sur l'homogénéisation de multicouches en y incluant des diagrammes de bandes d'arrêt et de passage, des courbes de dispersion et des analyses du champ de déplacement en fonction de la profondeur. Cette contribution est de nature à apporter un complément d'informations permettant une meilleure compréhension du comportement mécanique de systèmes stratifiés.

5.

Influence of Size and Chain Form Factor on the Phase Behavior and Structural Properties of Polyelectrolyte Solutions

F. Benmouna[1], S. Zemmour[2], Y. Kazi-Bouayed[2] and M. Benmouna[2]

[1] Macromolecular Research Laboratory, University of Tlemcen, BP119, Algeria, fbenmouna@mail.com
[2] Faculty of Sciences, University Aboubakr Belkaid, Tlemcen BP119, Algeria

A correlative study of structural properties and phase behavior of polyelectrolyte solutions in the presence of added salt is reported. Partial structure factors are derived from the Random Phase Approximation and the lines of instability related with micro and macrophase separations are determined from their q-dependences. This work is an extension of the one reported by Châtellier and Joanny including the entropic effects due to chain length finiteness. An improved description of the internal chain form factor is also included. It is shown that as the polymer chain length decreases, the lines of instability shift to lower temperatures inducing an enhanced stability towards both micro and macrophase separations. The internal structure of the polymer chain has important effects on the microphase separation. Position of the peaks in the monomer structure factor is weakly dependent on the total mass of the polymer but depends quite strongly on its internal structure represented by the form factor P(q). While using the Edwards approximation for P(q) does not change the position of Lifshitz point, an improved P(q) taking into account the internal structure of the chain with more detail produces a change in the Lifshitz point and hence a displacement of the microphase instability line.

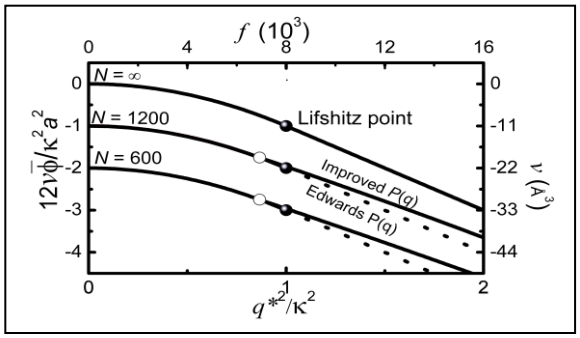

Fig. 1. Phase diagram of the polylectrolyte system

Acknowledgement
The first author thanks the AvH foundation for provinding the opportunity to do research at the MPI-P (Mainz, Germany) during one year (september 02 until august 03)

References

[1] J. F. Joanny, X. Châtellier, J. Phys. France II **6**, (1996), 1669-1675.
[2] F. Benmouna, Y. Kazi-Bouayed, A. Boussaid, M. Benmouna, Euro. Polym. J,.Accepted.

6.

Monte Carlo calculation of velocity-field characteristics of wurtzite GaN

B.Bouazza[1], C.Sayah, A.Guen Bouazza, N.E.Chabane-Sari, C.Gontrand

[1]Laboratoire des matériaux et énergies renouvelables, Faculté des sciences de l'ingénieur, Université Abou-Bekr Belkaïd de Tlemcen.BP 230, Tlemcen 13000, Algérie.corespending author.
E-mail: bouaguen@yahoo.fr
b_bouazza@mail.univ-tlemcen.dz
chou28dz@yahoo.fr

Abstract- present the velocity-field characteristics of wurtzite gallium nitride, determined using Single particle Monte Carlo simulation. A three valley model with nonparabolicity for the conduction band is employed and polar and non-polar optical phonon, acoustic phonon, piezoelectric, intervalley and ionized impurity scatterings mechanisms are considered. It is found that gallium nitride exhibits an extremely high peak drift velocity at room temperature, 2.9 x107 cm s-1, at a doping concentration of 1.0 × 1016 cm – 3. We also demonstrate that the saturation drift velocity of indium nitride, 2.2 × 107 cm s-1, is much larger than that of gallium arsenide. Our results suggest that the transport characteristics of gallium nitride are superior to those of gallium arsenide, over a wide range of temperatures, from 150 to 1000 K, and doping concentrations, up to 1.0 × 1018 cm – 3. We compared our results with the literature.

The III–V nitrides have recently attracted considerable attention for their application in short wavelength optoelectronic devices. They are also very appealing because their thermal stability, their high breakdown voltage due to a wide band gap and their high electron velocities make these materials suitable for high power and high temperature electronic devices. Wurtzite is the natural crystal phase for III–V nitrides, especially on sapphire or SiC substrates but, when grown on Si or GaAs substrates the zinc blende phase can be obtained which exhibits better electronic transport properties [1-4]. Recently, microwave heterojunction field effect transistors (HFET) in the wurtzite form have been demonstrated, exhibiting interesting performances in terms of current densities, ransconductance and current gain cut-off frequency [2-3-4]

In this work, we further study electron transport in wurtzite GaN. We employ a Single particle Monte Carlo simulation to determine the corresponding steady-state velocity-field and low field mobilities characteristics at different temperatures and ionized impurity concentrations. The Monte Carlo technique we have employed has been described in detail before [5-6]. Three valley model of the conduction band using parameters for wurtzite GaN is used. Nonparabolicity is considered in three valleys. Material parameters have been taken from literature. The scattering mechanisms included in the simulations are polar and non-polar optical phonons, acoustic phonons, piezoelectric and intervalley and ionized impurity.

In Figure 1, the simulated electron drift velocity is plotted as function of applied electric field in w-GaN. Lattice temperature is 300K, and electron concentration is equal to 1016 cm-3. We find that wurtzite GaN achieves a peak drift velocity of about 2.9 x107 cm s-1 at an electric field of around 170 kV cm-1.

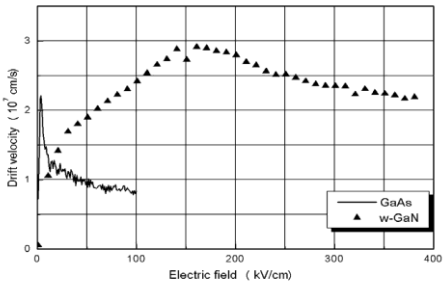

Fig. 1. Steady state electron velocity as a function of electric field in wurtzite GaN and GaAs.

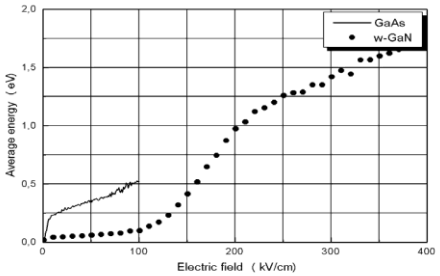

Fig. 2. Average Energy as a Function of Field for Electrons in wurtzite GaN and GaAs

The dependencies of the average electron energy on the applied electric field are shown in Fig. 2. In connection with the velocity-field curves, these characteristics provide some physical insight into the transport processes. Average energy versus electric field dependence shows a typical behavior for compound semiconductor materials. For low applied electric field, the average electron energy is equal to the electron thermal equilibrium energy. As the applied electric field is above the threshold electric field, the electron energy increases abruptly with increasing applied electric field.

The drift velocity is plotted in Figures 3 a function of applied electric field in w-GaN with temperature as a parameter. For the calculations a fixed doping concentration of 1 x 1017 cm-3 was used. We note that the form of the velocity-field characteristic changes substantially as the temperature is increased.

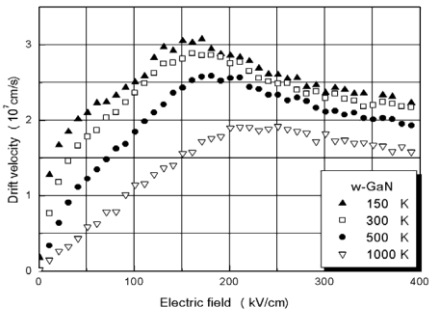

Fig. 3. The dependence of the velocity-field characteristic associated with wurtzite GaN on the temperature

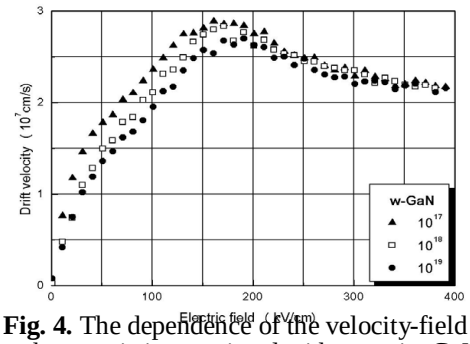

Fig. 4. The dependence of the velocity-field characteristic associated with wurtzite GaN on the doping concentration

the position of the peak velocity moves and decreases from about 3.0 x 107 cms-1 at 150K to about 1.9 x 107 cm s-1 at 1000 K. Increased temperatures are also seen to soften the sharpness of the peak, in addition to decreasing the saturation drift velocity, the saturation drift velocity ranging from about 2.2 x 107 cm s-l at 150 K to about 1.5 x 107 cm s-1 at 1000 K. The high field transport, on the other hand, is dominated by polar optical phonon and intervalley scatterings that have weak lattice temperature dependence. However, just as in the case of GaN and InN, these effects are mild when contrasted with the case of GaAs; in the case of GaAs, for a doping concentration of 1 x 1017cm-3 , our Monte Carlo simulations show that the peak drift velocity decreases from about 2.2 x 107 cm s-1 at 150 K to about
2.5 x 106 cm s-1 at 1000 K, the corresponding saturation drift velocity decreasing from 1.4 x 107 cm s-1 at 150 K to about 2.2 x 106 cm s-l at 1000 K. This is due to the fact that AlN, GaN and InN, have relatively large polar optical phonon energies, 99.2, 91.2 and 89.0 meV, respectively, when compared with GaAs, 35 meV, as well as relatively large intervalley energy separations [7].

Figure 4 shows the variation of the steady-state drift velocity as a function of the applied electric field for three different ionized impurity concentrations at room temperature for wurtzite GaN. The influence of doping becomes particularly noticeable for doping concentrations in excess of 1 x1018 cm-3; the peak and saturation drift velocities decreasing markedly with further doping.

The velocity-field characteristic remains essentially unchanged for doping concentrations less than 1 x 1017 cm-3. the position of the peak velocity moves and decreases from about 2.88 x 107 cm s-1 at 1 x 1017 cm-3 to about 2.67 x 107 cm s-1 at 1 x 1019 cm-3. A corresponding decrease in the saturation drift velocity is also noted, this velocity decreasing from about 1.95 x 107 cm s-1 at 1 x1017 cm-3 to about
1.87 x 107 cm s-1 at 1 x 1019 cm-3.
We have studied electron transport in wurtzite GaN using single particle Monte Carlo simulation. We find that aluminum nitride exhibits a room temperature, steady-state peak drift velocity of around 2.9 x107 cm s-1, at a doping concentration of 1.0 × 1016 cm – 3, the corresponding saturation drift velocity being around .2 × 107 cm s-1. The sensitivity of these steady-state results to variations in temperature and doping concentration is examined and found to be much less than that which occurs in GaAs. Preliminary results show that it is only the saturation drift velocity that is affected by these variations in parameters.All these results are in very good agreement with Monte Carlo results obtained using Dessenne [4], Brennan [8-9] and Foutz [7-10] only recently.

References

[1] J. Kolnik, I.H. Oguzman, K.F. Brennan, R. Wang, P.P. Ruden, W. Wang, "Monte Carlo Calculation of Electron Initiated Impact Ionization in Bulk Zincblende and Wurtzite GaN" J. Appl. Phys. 78 (1995) 1033.
[2] S.N. Mohammad, A.A. Salvador, H. Morkoc, "Emerging galluim nitride besed devices" Proc. IEEE 83 (1995) 1306.
[3] Y.F. Wu, B.P. Keller, D. Kapolnek, S.P. Denbaars, U.K. Mishra, "Measured microwave power performance of AlGaN/GaN MODFET " IEEE Elect. Dev. Lett. 17 (9) (1996) 455.
[4] F. Dessenne, D. Cichocka, P. Desplanques, R. Fauquembergue, "Comparison of wurtzite and zinc blend III-V nitrides fields field effect ransistors: a 2D Monte Carlo device simulation" Materials Science and Engineering B50 (1997) 315–318.
[5] C. Jacoboni and L. Reggiani, , "The Monte Carlo method for the solution of charge transport in semiconductors with applications to covalent materials"Rev. Mod. Phys., 55 (3), 645 - 705 (1983).
[6] C. Moglestue, "Monte Carlo Simulation of Semiconductor Devices " Chapman &Hall, 1993.
[7] S. K. O'Leary, B. E. Foutz, M. S. Shur, U. V. Bhapkar, and L. F. Eastman, "Monte Carlo Simulation of Electron Transport in Wurtzite Aluminum Nitride" Solid State Communications, Vol. 105, pp. 621-626, 1998.
[8] J. Kolnik, I.H. Oguzman, K.F. Brennan, R. Wang, P.P. Ruden, W. Wang, "Monte Carlo Calculation of Electron Initiated Impact Ionization in Bulk Zincblende and Wurtzite GaN" J. Appl. Phys. 78 (1995) 1033.
[9] M. Farahmand, C. Garetto, E. Bellotti, K.F. Brennan, M. Goano, E. Ghillino, G. Ghione, "Monte Carlo simulations of electron transport in III-Nitride wurtzite phase materials system: binaries and ternaries" J.D. Albrecht and P.P. Ruden IEEE Trans. Electron Devices 48, 535, 2001.
[10] B. Foutz, S.K. O'Leary, M. Shur, "Electron Transport in GaN and Related Materials" 2nd Annual Report, September 1998.

*

7.

Ethanol oxidation at noble metal/zeolite modified electrodes in alkaline medium

A.A. El-Shafei*, A.M.A Ouf and Amira M.Abd Elhafeez

Department of Chemistry, Faculty of Science, El-Mansoura University, ET-35516 El-Mansoura, Egypt

Noble metal/zeolite modified graphite (NZG) electrodes show higher catalytic activity for ethanol oxidation in alkaline medium compared with massive noble metal or noble metal modified graphite (N/G) electrodes. The noble metals incorporated in the zeolite layer are Au or Pd. The activity of this electrode depends on the amount of zeolite loaded on the graphite surface and on the soaking time in noble metal solution. The effects of both scan rate and ethanol concentration on the anodic peak height are indicatives of a diffusion controlled process. Current decay measurements indicate that the activity of studied electrodes towards poisoning tolerance decreases in the following order: NZG > N/G > N. Simultaneous immersion of zeolite modified graphite electrode in Au and Pd solution indicates that Pd can easily replace Au than Au can do.

Among all studied NZG electrodes, Au-PdZG electrode exhibits the highest catalytic activity towards ethanol oxidation.

8.

Élaboration et caractérisation de nanomatériau d'oxyde de manganite

W. Cherif[1], M. ELLOUZE[1], M. Ben Amar[2], F. Halouani[2]

[1] Laboratoire de Physique Appliquée, Faculté des Sciences de Sfax, B.P. 1171-3000 Sfax, Tunisie, e-mail : Mohamed.Ellouze@fss.rnu.tn
[2] Laboratoire d'analyse des systèmes électromécanique, École Nationale des Ingénieurs de Sfax, TUNISIE

Le broyage mécanique, inclus dans la métallurgie des poudres, est une technique très utile pour préparer des poudres à grains nanométriques, à cause du taux de déformations très élevés qu'on peut introduire dans la structure. Il permet aussi d'élaborer des alliages nanostructurés à partir des poudres élémentaires. L'étude des propriétés microstructurales de ce type de matériaux, détermine l'intérêt majeur de cette technique. En effet, nous espérons obtenir une résistance mécanique importante, par affinement des grains.

Les oxydes magnétiques de formule générale LnMnO3 où Ln est une terre rare (Ln = La, Pr, Nd, etc…) cristallisent dans la structure pérovskite. La substitution de la terre rare par un alcalino-terreux tel que le strontium, le baryum, le calcium ou par un alcalin tel que le sodium, le potassium, l'argent, entraîne l'oxydation de l'ion Mn3+en Mn4+ et donne lieu à des divers propriétés physiques et le composé résultant de la substitution pourrait être écrit, dans le cas du calcium, sous la forme de $La^{3+}_{1-x}Ca^{2+}_{x}Mn^{3+}_{1-x}Mn^{4+}_{x}O^{2-}_{3}$. On dit que le manganèse présente une valence mixte Mn3+/Mn4+.

Dans notre travail, nous nous sommes intéressés dans un premier temps à la réparation et l'amélioration d'un broyeur mécanique, ainsi que la préparation des échantillons de type La0,7Ca0,3MnO3. Ces derniers ont été élaborés à différentes vitesses et temps de broyage. Nous avons utilisés différentes méthodes de caractérisation, à savoir la microscopie électronique à balayage (MEB), l'analyse thermogravimétrique (ATG), la calorimétrie différentielle à balayage (DSC), la spectroscopie d'absorption infrarouge (IR), la diffraction des rayons X suivi par l'affinement par la méthode de Reitveld pour déterminer la structure des composés et enfin la mesure de l'aimantation pour savoir les propriétés magnétique du matériau sont en cours. L'étude par diffraction des rayons X montre que tous les échantillons élaborés cristallisent dans la structure pérovskite. L'étude par microanalyse X par l'intermédiaire du microscope électronique à balayage confirme la présence de tous les éléments chimiques dans les échantillons élaborés. La spectroscopie d'absorption infrarouge confirme les résultats cristallographiques.

9.

How do electronic properties of conventional III-V semiconductors hold for the III-Bismuth (BBi, AlBi, GaBi, InBi, and TlBi) compounds?

M. Ferhat[1], D. Madouri[2], N. Saidi-Haout[3], A. Belabbes[1], L. Kahal[1],

A. Boukra[4], and A. Zaoui[5]

1. Département de Physique, Université des Sciences et de la Technologie d'Oran. Oran. Algeria
2. Faculté des Sciences. Université d'Oran Es Senia. Oran. Algeria
3. Faculté des Sciences. Université de Mostaganem. Mostaganem. Algeria
4. Département d'Electronique. Université de Mostaganem. Mostaganem. Algeria
5. LML, Ecole Polytechnique de Lille. Université des Sciences et de la Technologie de Lille. France

We have performed ab initio self-consistent calculations using the stat of the art, the full potentiel augmented plane wave (FLAPW) method to investigate structural, electronic, bonding and dynamical properties of the less know bismuth III-V compounds: BBi, AlBi, GaBi, InBi, and TlBi.
The zinc-blende(ZB) phase is found to be the most stable for BBi, AlBi, and GaBi, however heavier III-Bi: InBi, and TlBi prefers the tetragonal (PbO) phases. Moreover our total energy calculations demonstrates clearly, the importance of the relativistic(RL) effects on the relative stability of the ZB and the PbO phases, particularly we found for the most heavier III-Bi : InBi and TlBi, that without the RL effects, the ZB phase is found the most stable. The origin behind these relativistic effects is explained in terms of stabilization (destabilization) of s, and p1/2 (p3/2, and d) orbital energies.
The relativistic contraction of the 6s orbital of Bi has strong effect on the band structure of III-Bi compounds, which exhibits some features that differ considerably from those of typical III-V semiconductors. In particular, we found an inverted band gap, which reflects a semimetallic character of these systems.
The bonding nature of III-V Bismuth compounds is analyzed in terms of valence charge density. BBi shows an anomalous bonding behaviour characterized by a charge transfer toward the 'cation' B atom, while others III-Bi behave as typical III-V comppund with a relatively small charge transfer to the anion bismuth atom.
Lattice dynamics study is performed for III-Bi compound, the most prominent features are:
(i) The transverse optical (TO) phonon modes show flatness along high symmetry direction, and a very sharp peak in the phonon DOS.
(ii) Strong flatness of the transverse acoustic (TA) mode over a large part of the Brillouin zone, which is not typical for other III-V compounds, giving a pronounced peak in the phonon DOS.
(iii) The LO and TO branches are separated in all Bismuth compounds, this feature was never seen in typical III-V compounds.
(iiii) In contrast to AlBi, GaBi, and other III-V semiconductors, the born effective charge and the LO-TO splitting of BBi increases with rising pressure.
We investigate the structural and electronic properties of GaAsBi alloys. We found a strong deviation from the Vegard's law for the variation of the lattice parameter. The calculated optical band gap bowing is found strong, and composition dependent. The result suggests the bowing parameter has a marked contribution from structural effects.
Finally we performed electronic and magnetic properties of VBi, CrBi, and MnBi.

10.

Molecular dynamics simulation of the effect of urea and acetone solutes on the structure of water

A. Idrissi[1], P. Damay[1], Pál Jedlovszky[2]

[1]Laboratoire de Spectrochimie Infrarouge et Raman (UMR CNRS A8516), Centre d'Etudes et de Recherches Lasers et Applications, Université des Sciences et Technologies de Lille, 59655 Villeneuve d'Ascq Cedex, France
[2]Laboratory of Interfaces and Nanosize Systems, Institute of Chemistry, Eötvös Loránd University, Pázmány P. Stny 1/A, H-1117 Budapest, Hungary

When theoretical interpretations are sought for the macroscopic properties of aqueous solutions, one must consider the solute-solute, solute-solvent and solvent-solvent interactions. The last term addresses the manner in which a given solute may alter the structure of water. This question has led many workers to use the terms "structure making and structure breaking" to describe the effect of the solute on the structure of the hydrogen-bond network of water. This concept becomes essential to describe phenomena of fundamental and practical importance in aqueous solutions ranging from the change in the conformation of proteins (denaturisation process), the bio-protection in drying and freezing processes, to hydrophobic/hydrophilic interactions and intermolecular forces.

The aim of this communication is present detailed investigation using both the radial/orientation nearest neighbour distributions of water molecules, their tetrahedral structures and the method of Voronoi polyhedra to analyze the effect of these solutes on bulk water, as well as on the structure of water molecules in the solvation shell of these solutes. The changes in the parameters associated with these distributions, such as the average values and the corresponding fluctuations, are analyzed in order to address unambiguously this effect

11.

Modelling and computation of the anodic dissolution of silicon electrode in HF solution

R. Cheggou[1] A. Kadoun[2] N. Gabouze[2] F. Ozanam[3] J.-N. Chazalviel[3]

[1] L2MSM, Faculté des Sciences, Université Djilali Liabès,
B.P. 89, 22000 Sidi Bel-Abbès, Algeria
[2]UDTS, 2 Bd Frantz Fanon, B.P. 399, Alger-Gare, Algeria
[3]Physique de la Matière Condensée, École Polytechnique, CNRS, 91128 Palaiseau, France

In 1990, the discovery of Canham that microporous silicon exhibits a bright photoluminescence at room temperature [1] has triggered renewed interest for the basic electrochemistry of silicon in fluoride medium. Anodic polarization of Si yields a formation of porous silicon, silicon anodic oxides and results in Si electropolishing, depending on the experimental conditions. Each process finds important practical applications while their scientific backgrounds still remain to be well established.

The shape of the voltammograms available in the literature invariably exhibit two maxima (characteristic currents usually termed J1 and J3) and two plateaus (characteristic currents J2 and J4). The region of potential preceding the first current maximum J1 corresponds to the formation of porous silicon, the rest of the curve corresponds to the electropolishing region [2-6]. It was suggested that this complex shape arises from the presence of two types of oxide: a "wet" oxide at potentials below the second maximum J3, plus a "dry" suboxide layer at higher potentials [7].

It has been shown theoretically that oxide begins to form at potentials just below J1 [8, 9]. On the other hand, semi-phenomenological models were developed to understand the phenomenon of oscillations in the region of potentials >3 V [10, 11]. Finally, a model has been outlined to account for the extreme anodic regime (V>10 V), where porous silica is formed [12]. However, to our knowledge, no theoretical effort has been made so far to understand the transport phenomena which are involved between the first current maximum (J1) and the region of oscillations (J4). In this work we are interested in the region of the voltammogram usually called the first electropolishing plateau, i.e., the potential region between the minimum of the current (J2) located beyond the first current maximum (J1), and second current maximum (J3). This region will be theoretically modelled by considering that a wet oxide layer is present between the electrolyte and the silicon surface. This layer is described as a composite medium [SiO2]1□ h [H2O]h where the h function represents the local volume fraction of water (Figure 1).

Our theoretical approach based on the resolution of coupled non-linear differential equations involving the h function and the local fluoride concentration allows for a quantitative explanation of the shape of the experimental voltammograms of p-type Si, as well as for a quantitative estimate of the oxide thickness in the J2-J3 region. Our model well agrees with the experimental results up to the potential corresponding to the second current maximum J3 (Figure 2). Beyond J3, the model even predicts a decrease of the current in agreement with experiment, but fails to accurately fit the oxide thickness variation as a function of potential as can be seen in Figure 3. We have also drawn, in the same figure, the variation of the effective oxide thickness defined as deff=∫0d[1□ h(x)]dx. This quantity is precisely the oxide thickness which can be determined by using in situ infrared spectroscopy [7]. It increases as expected with increasing potential for low potentials but decreases, unlike experiment, for higher potentials (beyond J3). We foresee that associating a dry oxide layer with the wet one will give the right behaviour for the oxide thickness and will lead to the correct modelling of the second electropolishing plateau J4.

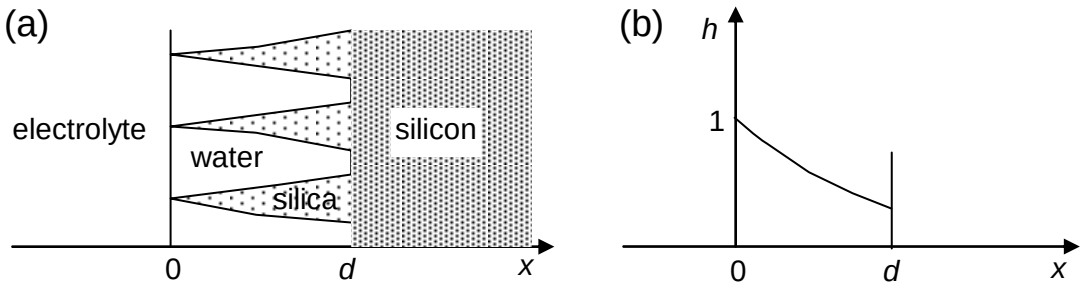

Fig. 1. Schematic representation of the wet oxide layer (a) and the h(x) variation (b).

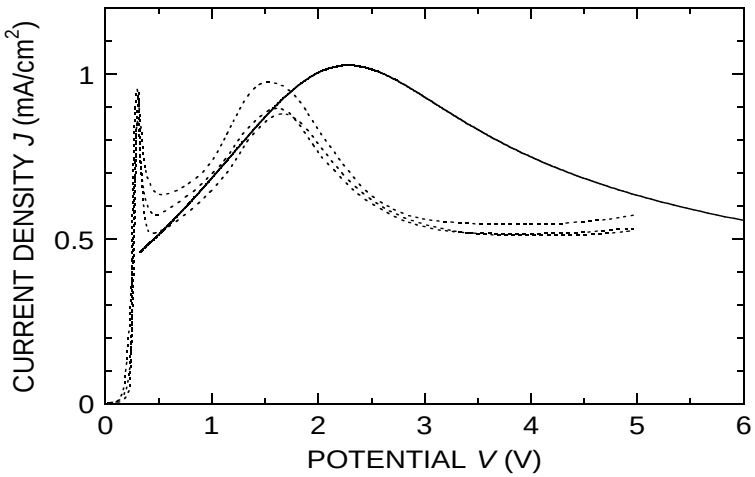

Fig. 2. Theoretical J(V) curve. The dotted lines are experimental data from Ref. [9]: p-Si/(0.05M, pH 3) for the (100), (110) and (111) orientations.

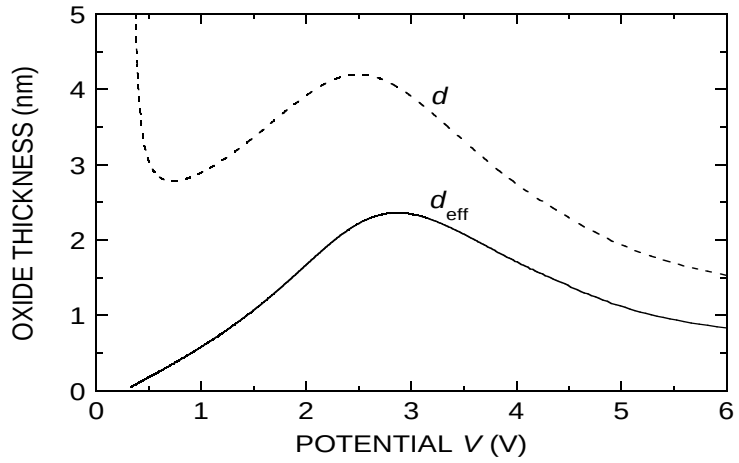

Fig. 3. Theoretical curves for the oxide layer thickness d (broken line) and effective thickness deff (solid line) versus potential.

References

[1]L.T. Canham, Appl. Phys. Lett. 57 (1990) 1046.
[2]J.-N. Chazalviel, M. Etman, F. Ozanam. J. Electroanal. Chem. 297 (1991) 533.
[3]H.H.Hassan, J.L.Sculfort,M. Etman, F. Ozanam, and J.-N. Chazalviel, J. Electroanal. Chem. 380 (1995) 55.
[4]S. Cattarin, I. Frateur, M. Musiani, R. Tribollet, J. Electrochem. Soc. 147 (2000) 3277.
[5]J.E.A.M van den Meerakker, M.R.L. Mellier, J. Electrochem. Soc. 148 (2001) G166.
[6]H.H.Hassan, B. Fotouhi, J.-L. Sculfort, S.S. Abdel-Rehim, M. Etman, F. Ozanam, J.-N. Chazalviel, J. Electroanal. Chem. 407 (1996) 105.
[7]C. da Fonseca, F. Ozanam, J.-N. Chazalviel, Surf. Sci. 365 (1996) 1.
[8]A.Belaïdi, M. Safi, F. Ozanam, J.-N. Chazalviel, O. Gorochov, J. Electrochem. Soc. 146 (1999) 2659.
[9]R.Outemzabet, M. Cherkaoui, N. Gabouze, F. Ozanam, N. Kesri, J.-N. Chazalviel J. Electrochem. Soc. 153 (2006) C108.
[10]E. Foca, J. Carstensen, H. Föll, J. Electroanal. Chem. 603 (2007) 175.
[11]J. Grzanna, H. Jungblut, H. J. Lewerenz , J. Electroanal. Chem. 486 (2000) 190.
[12]S. FreyS.Keipert, J.-N.Chazalviel, F. Ozanam, J. Carstensen,H Föll,Phys.Status Solidi (a) 204 (2007) 1250.

12.

Propriétés rhéologiques de nanocomposites à matrice polymère Approche expérimentale et modélisation

S. Chaoui[2], A. Mehamha[1]

[1]Laboartoire des matériaux polymériques multiphasiques LMPMP), Université de Sétif, Algérie
[2]Laboratoire de Structure et Propriétés de l'Etat Solide (LSPES), Université de Lille1, France

Des nanocomposites polypropylène/montmorillonite modifiés ont été préparés par mélange à l'état fondu au moyen d'un mélangeur interne. La matrice polymérique utilisée est le polypropylène (PP). Le choix du PP comme matrice polymérique a été motivé par le fait que celui-ci utilisé à grand tonnage, comporte certaines imperfections liées principalement à sa basse dureté ainsi que la température de service. La nonotechnologie constitue un des moyens d'améliorer les imperfections déjà citées. En utilisant l'intercalation à l'état fondu, un silicate lamellaire approprié peut être ajouté au PP pour obtenir un nanocomposite. La Montmorillonite, qui constitue la partie inorganique la plus utilisé dans ce domaine, est modifiée par un échange cationique à l'état liquide. Le tensioactif utilisé est l'octadécylammonium qui est un tensioactif cationique préparé à partir de l'octadecylamine par une réaction de protonation. Un polypropylène fonctionnalisé anhydride maléique (PP-g-MA) a été utilisé comme agent compatibilisant afin d'améliorer la qualité de la dispersion de la nanocharge modifiée dans la matrice polypropylène. Le degré de dispersion a été caractérisé par la diffraction des rayons X, l'analyse calorimétrique, la microscopie électronique en transmission et les mesures rhéologiques en régime dynamique et l'analyse mécanique dynamique. L'effet du rapport PP-g-MA / Mmt-C18 sur la qualité de la dispersion a été examiné. Les résultats obtenus montrent que le degré de dispersion dépend de la concentration en PP-g-MA. Le mélange dont le rapport de PP-g-MA / Mmt-C18 est de 3/1 semble avoir une dispersion meilleure par rapport aux autres. Les résultas obtenus ont montré qu'il ya formation d'un mélange de structure intercalé et microcomposite pour tous les mélanges compatibilisés.

13.

On some passive and active motion in biology: a physicist point of view

Chaouqi Misbah

[1] Laboratoire de Spectrom´etrie Physique, UMR, 140 avenue de la physique, Universit´e Joseph Fourier, and CNRS, 38402 Saint Martin d'Heres, France.

This contribution focuses on two main questions inspired by biology: (i) passive motion under flow, like advection of red blood cells in the circulatory system, and (ii) active motion generated by actin polymerization, as encountered in cells of the immune system and some micro-organisms (e.g. some bacteria and viruses). The first part is dedicated to the dynamics and rheology of vesicles
(a simple model for red blood cells) under flow. Some results obtained on red blood cells are also presented and compared to vesicles. Vesicles and red blood cells under flow exhibit several interesting dynamics: tank-treading, tumbling, vacillating-breathing, and so on. These dynamics have a direct impact on rheology, as will be discussed both from the theoretical and experimental point of views. The second part addresses active motion. Some Bacteria (like Listeria) are known to transfect cells thanks to the polymerization on their surface of an actin gel. Monomeric actin proteins are recruited from the transfected cell when the bacteria get in contact with the cell surface. It has been found that the bacteria propulsion into the cell occurs in the absence of molecular motors. Biomimetic experiments on beads and droplets have revealed that motion is a consequence of a spontaneous symmetry breaking that is accompanied with force generation. A simple basic model taking into account growth of actin and elasticity is sufficient to capture the essence of symmetry breaking and force generation, as will be presented in this contribution.

In the realm of biology cell motion can be broadly clas- sified into two important categories: (i) passive motion, and (ii) active motion. Passive motion refers to a sit- uation where a cell is subject to the action of a force from outside. A typical example is the motion of blood cells (red blood cells, leucocytes, and platelets) in the blood circulatory system. The cells are simply advected by the flow. Active motion, in contrast, refers to the fact that motion may occur due to building of a force inside the cell itself. It must be kept in mind, however, that this motion is initially triggered by an external signal. A typical situation is cell motility of the immune sys- tem (leucocytes or white blood cells): due to a chemical signal (for example detection by membrane receptors of trails of diverse molecules derived from microorganisms or damaged tissues) the cell builds internally a traction force that enables it to move forward. Active motion is also present within a variety of microorganisms (some viruses, bacteria and so on).

This contribution focuses on some aspects of these two motions. More precisely in the first part we shall study the dynamics of an individual biological red blood cell

(RBC), or its biomimetic counterpart represented by a vesicle. A vesicle is a closed membrane made of a bilayer of phospholipid molecules (Fig.1). These molecules have a polar hyrdophilic head which points towards the sol- vent, and hyrophobic tails which are directed inward in the bi-layer (Fig.1). Unlike vesicles, which are present in the cell cytoplasm which have a few nm of radius, the vesicles we refer too here are significantly bigger (their radius range typically between 10 and 100 μm), and thus sometimes called giant vesicles, or giant liposomes. Their large size allows for a direct observation under an optical

(Phase contrast) microscope. Both at room and physio- logical temperatures the bilayer is a two dimensional in- compressible fluid (at lower temperature they are known to exhibit gel-like transition). We consider only their study in the fluid state. Human RBCs constitute one of the

simplest cells in biology. Indeed the RBC is made, like a vesicle, of a phospholipid bi-layer, plus a protein network (spectrin), known also under the name of cy- toskeleton (2). Its cytoplasm is devoid of a nucleus and organella; the internal content of a RBC is made of a hemoglobin solution, which is a simple newtonian fluid. It is thus hoped that vesicles may represent a simplistic staring point to understand viscoelastic properties, dy- namics and rheology of bio-fluids, like blood.

We shall see that several dynamical and rheological features are common to RBC and vesicles. The study of vesicles offer a certain advantage. Indeed, unlike RBCs,

Fig. 1. A schematic view of a vesicle (left) made of a bi-layer of phospholipid molecules (right)

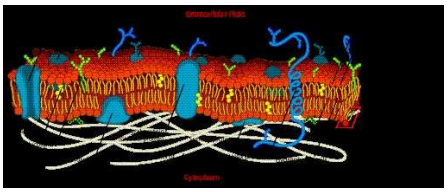

Fig. 2: A schematic view of a red blood cell membrane. Besides the bi-layer of phospholipids, there is a network of proteins (called also cytoskeleton, shown in white) and other proteins (shown in blue and green).

they lend themselves to exploration of various param- eters without affecting their structural properties. For example, their size can be varied over a decade at least. Furthermore, they can be swollen or deflated by osmosis

(and heating), so that one can get more or less deformable shapes. Finally, their internal content can be modified: one can change the internal solution in order to vary the internal viscosity, mechanical and viscoelastic properties, and so on... The ability to act on these parameters is es- sential with regard to scientific progress. For example, scanning a large parameter space offers the possibility to explore potential new phenomena. Another benefit is that this also allows to guide modeling (like checking some scaling relations which often requires exploration of parameter ranges over decades or more). Studies on vesicles under shear flow have revealed several dynamical features that will be reported on: (i) tank-treading (the vesicles orients itself with a certain angle with respect to the flow, while the membrane makes a tankreading mo- tion), (ii) tumbling (which occurs beyond a certain vis- cosity contrast between the internal and external fluids),

(iii) vacillating-breathing (the long axis of the vesicle os- cillates around the flow direction, while the shape shows a breathing like dynamics)[1?]. These motions impact on the global rheological properties of the suspension[2]. Recent comparison with experiments on a dilue vesicle and erythrocyte suspension wills be discussed[3].

The second part will be dedicated to the active mo- tion mediated by actin polymerization. Inside many bi- ological cells there exists a reservoir of proteins, called actin monomers. When the membrane receptors detect a chemical signal (originating, for example, from surround- ing pathogens) this elicits a series of chemical reactions inside the cell, which ultimately lead to polymerization of the actin monomers into a cross-linked gel. Polymeriza- tion occurs at the front of the cell, while depolymeriza- tion takes place at the rare (Fig.3), so that the polymer-

ized volume remains about constant during the motility. Molecular motors (myosin molecules) intercalate between the actin filaments in the gel and are able to convert the ATP (Adenosine Tri-Phosphate) into mechanical work. This conversion is used by the cell to move itself forward in response to an infection or a tissue injury, and so on. It has been concluded quite recently that some organisms

(e.g. the bacteria Listeria monocytogenes) move forward by using the actin gel assembly, in which no molecular motor has been found [4]. It has been further demon- strated that even simplified systems, and artificial beads or droplets (quoted with an enzyme in order to trigger polymerization) and put in a solution containing actin monomers, can be propelled to the sole effect of poly- merization of the actin gel (which is free of molecular motors) on their surface [4–8]. This has pointed to the fact that motion (i.e. force generation) is produced with-out the intervention of molecular motors.

Here we shall introduce a simple model [9] based on growth and elastic stress that is built in the gel in order to show (i) that the growth of a symmetric gel is unstable against a spontaneous symmetry-breaking, and (ii) that this symmetry breaking results in a force generation that is capable of pushing the bead forward. It is also shown that the symmetry breaking leads to the formation of an actin comet, as is observed for the bacteria Listeria monocytogenes.

Studies on blood flow together with active motion are two major questions in biological and medical sciences. Several issues are now accessible to physical and mathe- matical modeling. Some basic results are now beginning to emerge with both fundamental and technological im-portances.

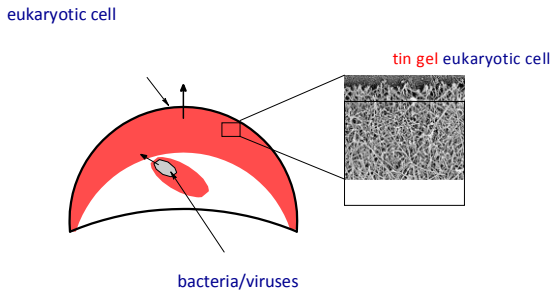

Fig. 3. A schematic view of an actin network (in red) that develops inside the cell during active motion. Also shown is a schematic view of bacteria, or a virus, which has transfected a cell. The cross-linked gel is shown on the right

References

[1] C. Misbah, Physical Review Letters 96, 028104 (pages 4) (2006), URL http://link.aps.org/abstract/PRL/v96/e028104.
[2] G. Danker, T. Biben, T. Podgorski, C. Verdier, and C. Misbah, Physical Review E (Statistical, Nonlinear, andSoft Matter Physics) 76, 041905 (pages 10) (2007), URL http://link.aps.org/abstract /PRE /v76/e041905.
[3] V. Vitkova, M.-A. Mader, B. Polack, C. Misbah, andT. Podgorski, Biophys. J. Letters 95, ?? (2008).
[4] D. Yarar, W. To, A. Abo, and M. D. Welch, Curr. Biol 9, 555 (1999).
[5] T. P. Loisel, R. Boujemaa, D. Pantaloni, and M.-F. Calier, Nature 401, 613 (1999).
[6] F. Gerbal, V. Laurent, A. Ott, M.-F. Carlier, P. Chaikin,and J. Prost, Eur. Biophys. J. 29, 134 (2000).
[7] A. Bernheim-Groswasser, S. Wiesner, R. M. Golsteyn, MF. Carlier, and C. Sykes, Nature 417, 308 (2002).
[8] S. Wiesner, E. Helfer, D. Didry, G. Ducouret, F. Lafuma, M.-F. Carlier, and D. Pantaloni, J. Cell Biol. 160, 387(2003).
[9] K. John, P. Peyla, K. Kassner, J. Prost, and C. Misbah, Physical Review Letters 100, 068101 (pages 4) (2008), URL http://link.aps.org/abstract/PRL/v100/e068101.

14.

Electrophilicities of α,β-Unsaturated Iminium Ions

Sami Lakhdar and Herbert Mayr

Department Chemie und Biochemie, Ludwig-Maximilians-Universität, Butenandtstr. 5–13 (Haus F), 81377 München, Germany sami.lakhdar@cup.uni-muenchen.de

Iminium ions are among the most important intermediates in organic chemistry. They play a significant role in a range of enzyme-catalyzed processes and synthetic transformations.[1] In the growing field of organocatalysis, numerous enantioselective methods have been achieved that rely on the use of chiral iminium ions.[2] On the other hand, there is a lack of kinetic data which are necessary for the rational design of organocatalytic processes.

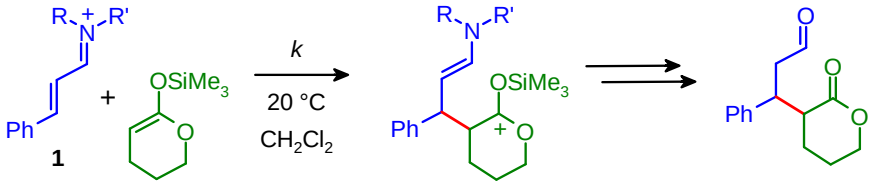

In this communication we report on the determination of the rate constants for the reactions of the iminium ions 1 with nucleophiles that possess known nucleophilicity parameters N and s.[3] We will discuss how these parameters can be employed for the quantification of their electrophilic reactivities on the basis of equation [1,4]

$$\log k2(20\ °C) = s(N + E) \qquad (1)$$

E = electrophilicity parameter,
N = nucleophilicity parameter,
s = nucleophile-specific slope parameter.

15.

[1] (a) Wong, C. H.; Whitesides G. M. Enzymes in Synthetic Organic Chemistry; Pergamon: Oxford, 1994. (b) Jencks, W. P. Catalysis in Chemistry and Enzymology; Dover: New York, 1987. (c) Böhme, H.; Haake, M. In Iminium Salts in Organic Chemistry; Advances in Organic Chemistry; Taylor, E. C., Ed.; John Wiley and Sons: Weinheim, 1976; p 145.
[2]Berkessel, A.; Gröger, H. Asymmetric Organocatalysis: From Biomimetic Concepts to Applications in Asymmetric Synthesis; Wiley-VCH: Weinheim 2005.
[3] S. Lakhdar, T. Takayasu, H. Mayr. Angew. Chem., Int. Ed. 2008, 47, Early View.
[4] (a) Mayr, H.; Patz, M. Angew. Chem., Int. Ed. Engl. 1994, 33, 938, (b) Mayr, H.; Kempf, B.; Ofial, A. R. Acc. Chem. Res. 2003, 36, 66-77; (c) Mayr, H.; Ofial, A. R. Pure Appl. Chem. 2005, 77, 1807- 1821.

Acknowledgements: We thank the Alexander von Humboldt Foundation (research fellowship to S. L) and the Deutsche Forschungsgemeinschaft for support of this work.

How to Avoid the Interaction of Water-Soluble Phenyl Phosphane with Cyclodextrin? A quantum chemical calculation answer.

A. D. Sayede and E. Monflier

Université d'Artois, Unité de Catalyse et de Chimie du Solide -UMR CNRS 8181, rue Jean Souvraz, S.P.18, 62307 Lens Cédex (France), adlane.sayede@univ-artois.fr

One of the most widespread ligands in biphasic organometallic catalysis is the sodium salt of metatrisulfonated triphenylphosphane (TPPTS). Nevertheless, this ligand forms an inclusion complex with cyclodextrins (CDs) that are used as mass transfer promoters. The formation of such inclusion complexes alters notably the catalytic behaviour of the catalyst and must be avoided.
To circumvent these disadvantages, different approaches have been related to the use of modified TPPTS which do not interact with CDs. Accordingly, we have undertaken, by mean of quantum mechanical calculation, the study of water-soluble phenyl phosphanes bearing one or two methyl (or methoxy) groups on each aromatic cycle to elucidate the influence of the group position and/or the group number on the inclusion phenomenon with β-CD.
The geometrical structures of β-CD and water-soluble phosphanes have been optimized at the PM3 level of the theory. According to the symmetry of the optimized structures, the water-soluble phosphanes have been classified in three groups. The first one includes TPPTS and the para substituted phosphanes (owning a pseudo C2 symmetry), the second one includes the ortho substituted phosphanes (owning a pseudo C3 symmetry), and the third one includes phosphane which do not have any symmetry due to the lack of methyl or sulfonate group at one of their aryls (see Fig. 1). Docking energy profiles of the different water-soluble phosphanes with β-CD showed a complexation of the phosphane of the group 1 and 3, suggesting hence that presence of one methyl or methoxy group in ortho position on each aromatic cycle is sufficient to hamper the formation of an inclusion complex with the β-CD. This result was confirmed by spectroscopic studies [1].

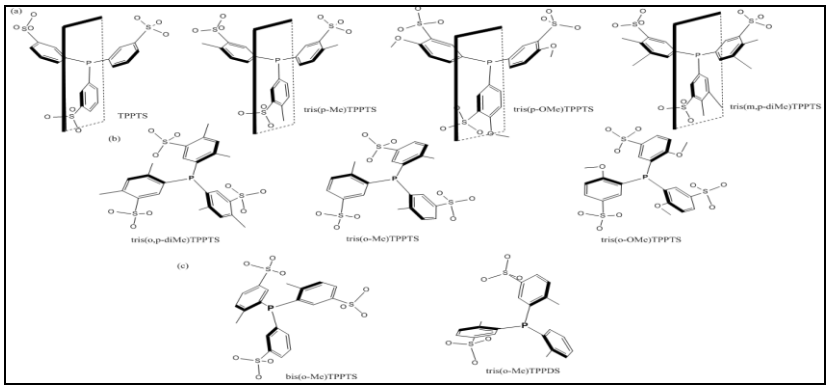

Fig. 1. Optimized structure of the different water-soluble Phosphanes.

Acknowledgement
I .D.R.I.S., C.I.N.E.S. and C.R.I.L. computing centres are acknowledged for the CPU time donated.

References
[1] M. Ferreira, H. Bricout, A. Sayede, A. Ponchel, S. Fourmentin, S. Tilloy, E. Monflier. Adv. Synth. Catal. 2008, 350, 609-618.

16.

Zeolite based catalysts for the methanol oxidation for direct methanol fuel cells.

W. Khalil

Department of chemistry, Cairo University, Giza. Egypty
Email: the_egyptian4@yahoo.com

Nickel impregnated zeolite-modified electrodes were prepared by mixing Ni–silicalite-1 with conducting carbon black in different rations.Using the cyclic voltammetric technique the electrochemical oxidation of methanol at such electrodes was investigated. Experiments on silicalite-1 (S-1) and nickel–silicalite-1 (Ni–S-1) show that they are not electrochemically active towards methanol oxidation in KOH solution. The presence of nickel ions in the zeolite matrix, by soaking the electrode in an aqueous NiSO4 solution, markedly enhances the electrocatalytic activity which was found to depend on the nickel content. On the other hand, the presence of zeolite and/or Ni metals in the catalyst is essential, however, the electro-catalytic activity depends on the Ni–S-1:carbon black ratio. Electrodes with Ni–S-1:carbon black ratio of 1:3, show the maximum electro-catalytic activity. The importance of impregnated Ni metal in the zeolite matrix is discussed on the basis of the experimental results. A weak dependence on bulk methanol concentration was observed. SEM analysis was used to characterize the Ni–S-1 catalyst. Dependence of methanol electro-oxidation on methanol concentration was discussed.

17.

Electronic Structure and magnetism of cubic Ga1-xEuxN and Al1-xEuxN using the LSDA+U approach

Z. Dridi[1], A. Lazreg, and B. Bouhafs

[1]Modelling and Simulation in Materials Science Laboratory, Physics Department, University of Sidi Bel-Abbes, 22000 Sidi Bel-Abbes, Algeria.

First-principles calculations of the electronic structure and magnetic interaction of substitutional europium rare-earth impurity in cubic GaN and AlN have been performed using density functional theory within the LSDA+U approach (local spin density approximation with Hubbard-U corrections). The LSDA+U method is applied to the rare-earth 4*f* states. The Ga1-xEuxN and Al1-xEuxN are shown to be semiconductors, where the filled *f* states are located in the valence bands and the empty ones in the conduction bands. The magnetic interaction of the rare-earth ion with the host states at the valence and conduction band edges has been investigated and found to be relatively weak in comparison with Mn impurities.

The diluted ferromagnetic semiconductors are considered as promising materials for spintronic applications, due to their unique combination of magnetic, semiconducting and optical properties. Most of the materials that have been studied are III-V and II-VI semiconductors doped with Mn and other 3d transition metal (TMs), which have been predicted and, in some cases, observed to show hole mediated ferromagnetic behaviour above room temperature [1-3]. However, ferromagnetism has been also observed in GdxGa1-xN, with Curie temperature larger than 400 K [4-6], meaning that rare-earth (RE) ions can become an interesting alternative to transition metals for spintronic applications. In optoelectronics, it has been reported that in contrast to Er-doped Si, the intra-*f* luminescence in Er-doped GaN is not drastically quenched at room temperature [7] and both electroluminescence as well as photoluminescence (PL) in the visible have been observed [8]. RE doped GaN and AlN lead to red, green, and infrared, and blue light emission for use as primary colors in screen displays for optoelectronic applications [9-11].

An accurate description of the electronic structure of solid containing rare-earths is a challenging problem because of the correlated nature of the *f* electrons in the filled 4*f* shell [12]. Calculations based on local spin density approximation (LSDA) invoked in the frame work of density-functional theory, place the *f* derived states which appear as a set of narrow bands at the Fermi level, while experiments reveal their localized nature as atomic multiplets over a broad energy range [13]. To overcome these failures, a variety of strategies to extend the LDA have been developed, among them the self-interaction correction SIC [14], and the LSDA+U [15, 16].

In this work, the electronic structure and magnetic interaction of europium substituting in cubic GaN and AlN are studied. The strong correlation of the Eu *f*-electrons was taken into account using an LSDA + U-like potential. We have reported the density of states and have calculated the exchange splitting parameters.

The present paper is organized as followed: Section 2 presents details of our calculations. Results and discussion are presented in Sec. 3, and Sec. 4 summarizes our conclusion.

The calculations are based on the density-functional theory in the local spin-density approximation (LSDA) with additional Hubbard correlation terms describing on-site electron-electron repulsion associated with the 4*f* narrow bands (LSDA + U approach) [15, 16]. The first-principles band-structure approach applied in this work is the scalar relativistic full-potential linear-augmented-plane-wave plus local orbital (FPLAPW+lo) method (Wien2k implementation [17]). Basis functions were expanded as combinations of spherical harmonic functions inside non-overlapping spheres around the atomic sites (muffin-tin spheres) and in Fourier series in the interstitial region. In the muffin-tin (MT) spheres, the l-expansion of the non-spherical potential and charge density was carried out up to lmax=10. In order to achieve energy eingenvalues convergence, the wavefunctions in the interstitial region were expanded in plane waves with a cutoff of kmax = 7/Rmt (where Rmt is the average radius of the MT spheres). Our calculations were performed in

the zinc-blende ferromagnetic phase, at the concentration x = 0.25. The Brillouin-zone integration were performed using 2 × 2 × 2 Mokhorst-Pack special k-points [18].
For GaEuN and AlEuN alloys, we have calculated the total and partial density of states (DOS) at the equilibrium lattice constant. The spin direction (↑ and ↓) is taken as the direction of the rare-earth spin (majority ↑ and minority spin ↓ direction).
The partial densities of states shown in fig. 1 for Ga0.75Eu0.25N and fig. 2 for Al0.75Eu0.25N are given for Eu-4*f*, Eu-5d, and N-2p states. For majority spin, we note two peaks corresponding to the filled *f*-states in the valence band and to empty ones which constitute the CBM. For minority spin, the Eu-4*f* states are unoccupied and located for Ga0.75Eu0.25N and Al0.75Eu0.25N above the CBM. For majority and minority spin, the valence band maximum shows a highest contribution of the N-2p states, which hybridize with Eu-5d states. The latter are high in energy in the conduction band, and thus are fully unoccupied for both spin directions.
To study the magnetic interaction of the rare-earth with the host band states, we have calculated the exchange splitting of the band states at the VBM and CBM. The sign of the spin-splitting at the top of the valence band is positive for Ga0.75Eu0.25N and Al0.75Eu0.25N, and is estimated, respectively, to 0.114 and 0.142 eV. So for both alloys, the VBM states tend to align with europium spin. At the conduction band minimum, the spin-splitting has been estimated to 0.111 eV for Ga0.75Eu0.25N and 0.261eV for Al0.75Eu0.25N. The spin-splittings obtained in the present work for europium are weak in comparison to those of Mn-doped GaN [19]. So, for GaN:Eu and AlN:Eu, it is unlikely that the rare-earth dopant by itself may induce room temperature ferromagnetism, perhaps by introducing defects as the case of GaN:Gd in which high temperature ferromagnetism and giant magnetization amplifications have been observed. Electronic and magnetic properties of europium substituting in cubic GaN and AlN have been investigated by taking into account the strong correlation of the Eu *f*-electrons using the LSDA+U approach. It is pointed out that the filled *f* states are located in the valence bands for majority spin, and the empty ones in the conduction bands for both spin directions. The magnetic behaviour of Eu in GaN and AlN appears to be different from that of Mn: the effect of the exchange interaction of the europium ion with the host states at the valence band maximum and conduction band minimum is weaker.

Reference

[1] I. Zutic, J. Fabian, S. Das Sarma, Rev. Mod. Phys. 76 (2004) 323.
[2] D. D. Awschalom and R. K. Kawakami, Nature (London) 408 (2000) 923.
[3] T. Dietl, H. Ohno, F. Matsukura, J. Cibert, and D. Ferrand, Science 287 (2000) 1019.
[4] N. Teraguchi, A. Suzuki, Y. Nanishi, Y.-K. Zhou, M. Hashimoto and H. Asahi, Sol. State Comm. 122 (2002) 651.
[5] S. Dhar, O. Brandt, M. Ramsteiner, V. F. Sapega, and K. H. Ploog, Phys. Rev. Lett. 94 (2005) 037205.
[6] H. Asahi, Y. K. Zhou, M. Hashimoto, M. S. Kim, X. J. Li, S. Emura, and S. Hasegawa, J. Phys. Condens. Matter 16 (2004) S5555.
[7] P. N. Favennec, H. L. Harridon, M. Salvi, D. Moutonnet, and Y. L. Cuillo, Electron. Lett. 25 (1989) 718.
[8] Y. Q. Wang and A. J. Steckl, Appl. Phys. Lett. 82 (2003) 402.
[9] A. J. Steckl, J. Heikenfeld, M. Garter, R. Birkhahn, and D. S. Lee, Compound Semicond. 6 (2000) 48; U. Hömmerich, E. E. Nyein, J. Heikenfeld, A. J. Steckl, and J. M. Zavada, Mater. Sci. Eng. B 105 (2003) 91.
[10] A. J. Steckl and J. M. Zavada, Mat. Res. Soc. 24 (1999) 33.
[11] L. C. Chao, B. K. Lee, C. J. Chi, J. Cheng, T. Chyr, and A. J. Steckl, Appl. Phys. Lett. 75 (1999) 1833; L. C. Chao, B. K. Lee, C. J. Chi, J. Cheng, T. Chyr, and A. J. Steckl, J. Vac. Sci. Technol. B 17 (1999) 2791.
[12] I. N. Yakovkin, Takashi Komesu, and P. A. Dowben, Phys. Rev. B 66 (2002) 035406.

Posters

Material Science

P1.

Near Field Analysis of Silver Nanoparticles Placed on Various Substrates for Precise Nanostructuring

M. Youcef Mahmoud[1], G, Bassou[1]

1Laboratory of Microscopy and Microanalysis and Molecular Spectroscopy, Department of Physics, Faculty of Sciences, University of Djillali Liabes , Sidi Bel-Abbes 22000. Algeria, ,mahmoudhamoud@yahoo.com

We present theoretical results on the near field distribution in the vicinity of silver nanoparticles placed on various substrate materials. The numerical calculations have been carried out using the Differential Formalism. We investigate a 2D-PSTM configuration with a metallic rectangular particle. Metal (Ag), semiconductor (Si) and dielectric (SiO2*)* substrate materials are investigated. The enhancement factor strongly depends on the polarization state of illumination, the nature of the substrate, the wavelength of incident light and the particle size. The results show that the electric field is localized in the vicinity of the contact point. A large field enhancement observed in transverse magnetic (TM) polarization when the substrate is silver metal. The enhanced electric fields are confined within a few nanometers near the surface of nanoparticles. By reducing the particle symmetry, both the field enhancement and the spatial confinement increases which offers a good opportunity for further decreases in the size of the produced structures. The present results make the nanometal particle template method suitable and flexible for precise nanostructuring of thin films.

Silver nanoparticles; Field enhancement; Near-field; Differential Formalism.

Metallic nanoparticles are of interest for various optical based studies, including surface enhanced Raman spectroscopy, single molecule spectroscopy, chemical sensors, photonic bandgap structures, etc. Their ability to show dramatic local field enhancement of the incident electromagnetic field due to the coherent resonant electron plasma excitation, as well as the sensitivity of this behavior to the particle shape and surrounding physico-chemical properties, make them particularly well suited for many of these applications. While most studies are performed using conventional far-field set-ups, the fundamental interactions occur in the vicinity of the particles and are therefore governed by the near-field response of the particles. To gain an understanding of these interactions, several groups are using scanning near-field optical microscopy (SNOM) [1, 2] .This technique has been developed in the past ten years to overcome the spatial resolution limitations of conventional optical microscopes. These microscopes, classified as scanning probe microscopes, have since proven their utility in various nanoscopic applications.

In this paper, we study theoretically the system of silver (Ag) nanoparticles on various substrate surfaces for nanomachining of the substrate using an apertureless SNOM [3]. The calculations are performed on the basis of the Differential Formalism. Metal (Ag), semiconductor (Si) and dielectric (SiO2*)* substrate materials are investigated.

The numerical work is performed by the FM method. This method is well known by the authors working in the diffraction gratings field [4]. The details of FM method have been reported

elsewhere [5]. This method is more adapted for periodical structure. The optical properties (refractive index) of the investigated substrate materials are introduced in the model by using data taken from [6, 7].

Figure 1 represents calculated distributions of the electric field around the silver nanoparticle placed on the Si surface with a period, *d* =600 nm, *dx* = 100 nm, h= 50 nm, lighted in TM polarization (the case where the electric field vector oscillates in a sectional plane that is perpendicular to the surface of the edge structure). As in seen in figure 1, the strongly local-field enhancement appears at vicinity of silver nanoparticle due to surface plasmons excitation. These localized surface plasmons of silver nanoparticle are the interaction between incident electromagnetic waves and induced charge in metallic particles. In this region the electric field is strongly enhanced and the enhancement value is about 10 times higher than the incident one.

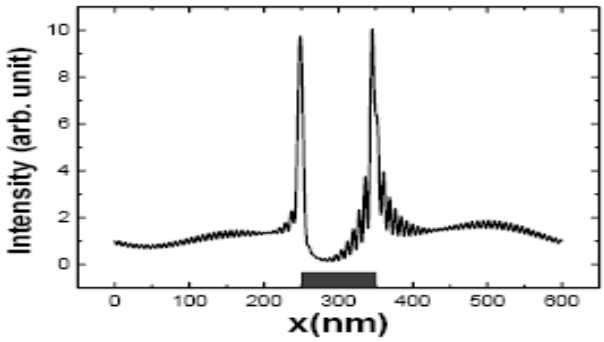

Fig. 1. Calculated distribution of the electric field in TM polarization around the silver particle with a period d of 600nm placed on Si substrate at a wavelength of 800nm. Particle size and angle of incidence are 100×50 nm^2, $\theta=60^0$ respectively at the distance z=0nm

In order to estimate the ability of the presented method of nanostructuring of different materials, numerical simulations are performed using with dielectric and metal substrates.

Figure 2 shows the calculated depth distributions of the electric field in different substrate materials. The results clearly indicate that the substrate material strongly influences the electric field enhancement properties. The electric field drops rapidly to the initial incident value as the decay depth is in the order of tens of nanometres.

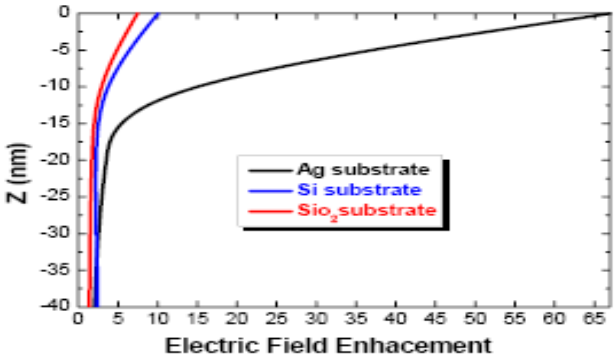

Fig. 2. Depth distributions of the electric field for three different substrate materials at the distance z=0nm

The parameters of the electric field enhancement are also found to depend on the lateral size of the nanoparticle. This dependence is investigated for Si substrate. The results clearly show that the size variation of silver nanoparticles may yield different field enhancement. In Figure 3a, the field enhancement at different particle diameters exhibited multiple peaks which were the points of surface plasmon resonance occurred around 20nm, 30nm, 50nm, 60nm and 90nm. This indicates that the particle diameter of 20nm, 30nm, 50nm, 60nm and 90nm provide a major contribution to plasmon coupling with the dipole radiation between particle to particle is the evanescent field of near-field photons.

Figure 3b represents the electric field enhancement for silver nanoparticles on Si substrate at 800nm excitation wavelength with particle diameter of 30, 60, 80 and 100nm.

The FM results clearly indicate that the increase of the particle size results in the decrease of the electric field enhancement. The field maxima were reached at dx = 30nm. As dx increases further, the enhancement drops quickly. At $z \geq 5$ nm, almost no enhancement exists for all cases. As shown in figure 3b, single peak profiles were observed for all particle sizes with a minimum for dx = 100 nm. The electric field enhancement is extremely sensitive when the lateral size of silver nanoparticle is within a few tens of nanometers. A sudden increase of the field enhancement occurs for the 1-nm distance variation. This effect is related to the strong confinement of near field in the vicinity of the particle surface. An electric field enhancement of ~ 930 can be seen for dx = 30 nm as compared with dx = 100nm. The estimated enhanced field is several times greater than the particle diameter. This result it indicates that both the field enhancement and the spatial confinement are precisely controllable by the particle size.

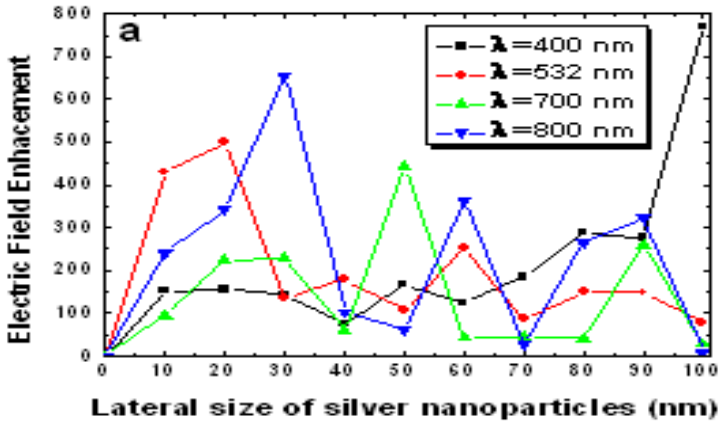

Fig. 3a. Electric field enhancement as a function of the lateral size of silver nanoparticles from 0 nm (no particle) to 100nm with increment of 10nm at the distance z=0nm in TM polarisation

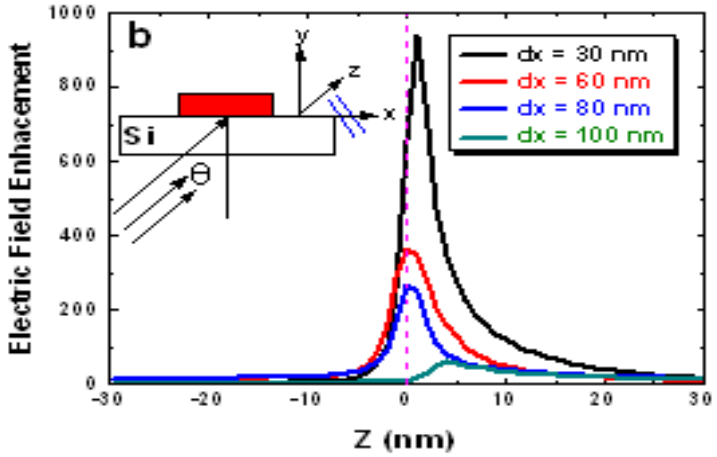

Fig. 3b. Depth distribution of the electric field for different lateral sizes. The particle has a period of 600 nm and is placed on the Si substrate at the distance z=0nm in TM polarization. The parameters are the same as in figure 2

This research has been supported by the Minister of Higher Education and Scientific Research

References

[10] E.D. Palik (ed) 1998 Handbook of Optical Constants of Solids (San Diego, CA: Academic)
[11] A. Sentenac, J-J. Greffet, Ultramicroscopy 57 (1995) 246.
[12] S. Goumri-Said, L. Salomon, J.P. Dufour, F. De. Fornel, A.V. Zayats , Opt. Commun. 244 (2005) 245.
[13] N. Nedyalkov , H. Takada, M. Obara, Appl. Phys A. 85 (2006) 163.
[14] N. Nedyalkov, T. Sakai1, A.P. Atanasov, M. Obara, Chin Opt. Lett. 5 (2007) 122.
[20] N. Nedyalkov , H. Takada, M. Obara, J. Phys. D: Appl. Phys. 39 (2006) 5037.
[21] Y.-F. Chau, D.P. Tsai, Optics Communications 269 (2007) 389–394.

P2.

COMPORTEMENT MICELLAIRE ET VESICULAIRE D'UN TENSIOACTIF CATIONIQUE DIBRANCHE EN PRESENCE D'UN NON IONIQUE FLUORE

A.SARDI[1], F. BOUANANI[1], D. BENDEDOUCH[1] ET C. ZELMAT[1]

[1]laboratoire de Chimie Physique Macromoléculaire, Faculté des Sciences, Département de Chimie, B.P.1524 Université d'Oran, Es- Senia, 31100, Oran. E-mail:mimisar25@yahoo.fr

Ce travail présente les résultats de travaux traitant par tensiométrie d'un système tensioactif mixte de type cationique dibranché / non-ionique fluoré constitué du bromure de didodecyldiméthylammonium (DDAB), et d'un nouveau composé le undécafluoro n-pentyl décaoxyéthylène éther (FSO 100), en vue de déterminer les concentrations micellaires critiques (cmc) et vésiculaires (cvc) pour différentes proportions en DDAB. Les donnés expérimentales sont ensuite analysées sur la base de deux modèles thermodynamiques de formation micellaire mixte. Les résultats obtenus montrent qu'il existe des interactions intra -micellaires de type attractif, et que la composition micellaire en DDAB augmente avec la fraction molaire totale du mélange en DDAB.

L'étude des propriétés physico-chimiques de mélanges de surfactants en solution aqueuse constitue un domaine d'intérêt toujours d'actualité aussi bien académique que technologique. En effet, il s'avère qu'un système mixte tensioactif développe généralement de meilleures performances qu'un tensioactif seul[5],ce qui rend ces systèmes plus efficaces dans divers domaines comme le secteur biologique pour la séparation des protéines[6]ou dans l'industrie comme stabilisateur. Les systèmes mixtes ont été également le sujet d'une attention considérable d'un point de vue théorique[7,8].

Le but du travail présenté ici est de déterminer et d'analyser quelques propriétés physico-chimiques de mélanges de DDAB et de FSO-100 à différentes proportions en DDAB. L'analyse des mesures expérimentales de tensiométrie à 25°C à l'aide de deux modèles thermodynamiques permettra de décrire quelques aspects majeurs du comportement micellaire de ce système mixte.

Ce modèle suppose un comportement de mélange idéal et se base sur le modèle de pseudo-phase. Il établit une relation entre la cmc du mélange, les cmc des deux surfactants purs (cmc_1,cmc_2) et la fraction molaire (X_i) d'un surfactant dans le mélange : $\frac{1}{CMC} = \frac{X_1}{CMC_1} + \frac{1-X_1}{CMC_2}$ (1)

La composition micellaire du surfactant 1 dans la micelle mixte formée est alors donnée par :

$$x_1^m = \frac{x_1\, cmc_2}{cmc_1 + x_1 (cmc_2 - cmc_1)} \qquad (2)$$

La non idéalité des systèmes mixtes peut être appréhendée selon une approche simple basée sur la notion de solution régulière. La cmc du mélange est exprimée en introduisant les coefficients d'activité des deux surfactants dans l'équation de Clint :

$$\frac{1}{CMC} = \frac{X_1}{f_1 CMC_1} + \frac{1-X_1}{f_2 CMC_2} \qquad (3)$$

avec $\ln f_i^m = \beta^m (1 - X_i^m)^2$ et $\beta^m = \ln\left[\frac{X_2\, cmc}{cmc_2\, X_2^m}\right] \Big/ \left[1 - X_2^m\right]^2$

β^m est le paramètre d'interaction intra- micellaire. La conservation de la masse permet d'aboutir à l'équation transcendantale suivante qui peut être résolue de manière itérative pour X_1^m :

$$\left(\frac{X_1^m}{1-X_1^m}\right)^2 \ln\left(\frac{X_1\, CMC}{X_1^m\, CMC_1}\right) = \ln\left(\frac{(1-X_1)\, CMC}{(1-X_1^m)\, CMC_2}\right)$$

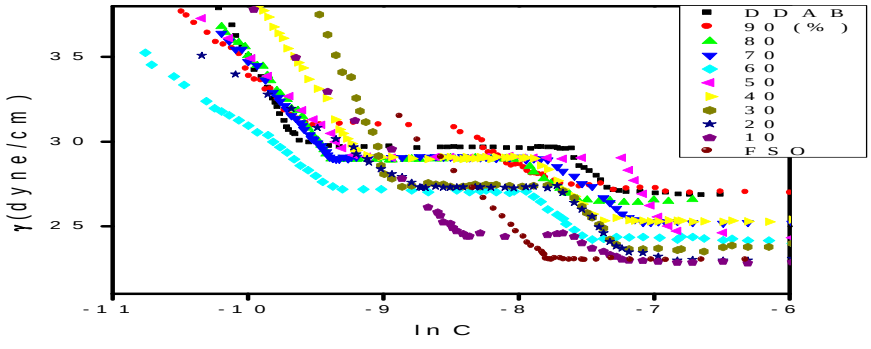

Fig. 1. Variation de la tension superficielle en fonction du logarithme de la concentration totale en surfactant [mM] pour le système DDAB/FSO- 100 à différentes fractions molaires en DDAB

On observe sur la figure 1que toutes les courbes sauf celle correspondant au FSO-100 ont le même comportement que celle correspondant au DDAB pur : une décroissance linéaire aux faibles concentrations suivie d'une stabilité de γ , puis de nouveau une décroissance de γ , et enfin une stabilité pour les concentrations les plus élevée. Le premier changement pour les concentrations faibles correspond à la cmc et le deuxième est la concentration vésiculaire critique (cvc)[9]. Ainsi, même les mélanges pauvres en DDAB forment des vésicules alors que le FSO-100 ne forme que des micelles

La figure 2 montre que les cmc expérimentales sont systématiquement inférieures aux cmc théoriques d'après le modèle de Clint, ce qui indique l'existence d'interactions intra- micellaires de type attractif.

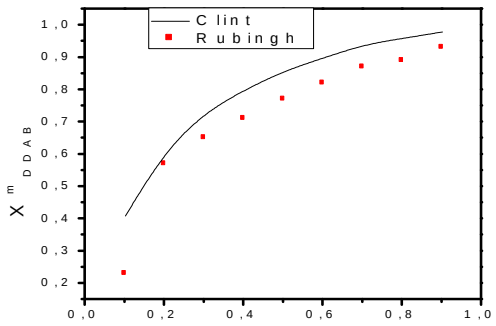

Fig. 3. Variation de la composition micellaire de DDAB en fonction de X_{DDAB}.

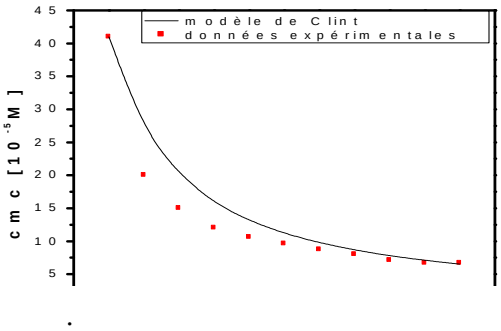

Fig. 2. cmc en fonction de X_{DDAB}

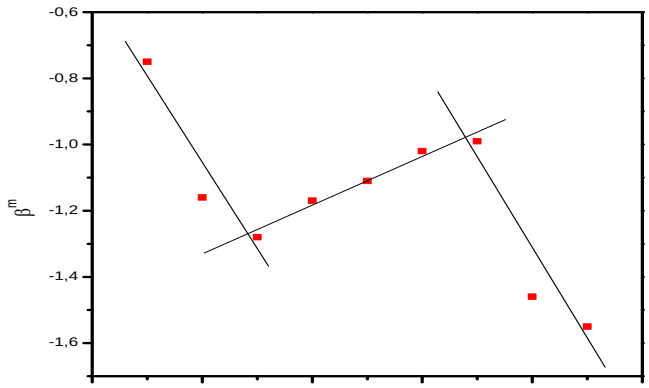

Fig. 4. Variation du paramètre d'interaction

Les droites sont des ajustements linéaires comportement de X^{m}_{DDAB} en fonction de X_{DDAB} indique que les micelles mixtes dans les différents mélanges sont plus riches en DDAB que dans l'hypothèse de mélange idéal.

Les valeurs de β^{m} sont toutes négatives comme la figure 4 le montre, ce qui est cohérent avec la présence d'interactions attractives.

Cette caractérisation physico-chimique des mélanges aqueux (cationique dibranché DDAB et non ionique fluoré FSO-100) à différentes proportions en DDAB a permis de conclure à la réalisation effective d'un système mixte performant.

Des interactions intra- micellaires attractives entre les molécules de DDAB et FSO ont pu être mises en évidence.

P3.

Etude du profil du champ électrique maximum des diodes n+p-p+ à base de SiC et Si

AZZI Ouarda[1]

[1]UNIVERSITE ABOU-BAKR BELKAID. Tlemcen 13000.ALGERIE, e-mail : azi.wrda@yahoo.fr

Ce travail s'inscrit dans le cadre de la conception des diodes. Nous avons étudié l'effet de la concentration de la base sur le profil du champ électrique maximum E_{MAX} qui règne dans la région d'épuisement des diodes, et ainsi l'étude de l'effet de l'épaisseur de la couche active (base P^-) sur E_{MAX}. Nous avons fait cette étude dans le cas où les diodes sont polarisées en inverse. Cependant, nous déterminons la relation entre le champ électrique maximum et la tension de claquage. Nos résultats sont obtenus à l'aide du simulateur électronique PC1D5.

Le claquage d'une diode est la brutale augmentation de son courant inverse lorsqu'on augmente la polarisation en inverse au-delà de la tension de claquage, dans ce cas il apparaît un siège de champ électrique très intense qui devient capable de briser des liaisons de valence entre les atomes de semi-conducteur : libérant un électron et un trou qui sont balayés par le champ électrique, ce qui provoque une augmentation du courant inverse. D'autre part il existe quelque porteurs responsables de courant de fuite dans la zone de charge d'espace, le porteur est capable d'ioniser en donnant un électron dans la bande de conduction et un trou dans la bande de valence.

Dans ce travail [4] nous avons utilisé une diode $n^+p^-p^+$: est réalisé en empilant une couche N^+ (émetteur : $10^{17}cm^{-3}$ /0.6µm) et une couche P^- (base : $10^{14}cm^{-3}$ / 8µm) et une troisième couche P^+($5.10^{16}cm^{-3}$ /300µm), P^+ est appelée le substrat de diode.

On polarise la diode en inverse par une source connectée à la base, et on fait varier la tension inverse V_{INV} ensuite nous avons relevés les valeurs du champ électrique maximum correspondantes.

On note que le champ électrique maximum croit avec l'augmentation de V_{INV} (**Figure1a et 1b**), et aussi il augmente en fonction de la concentration de la base p- (N_A), ceci signifie que, plus le dopage de la base est élevée, plus la résistivité de la base est décroît, et ainsi la mobilité des porteurs est élevée.

On constate, également, que le champ électrique maximum d'une diode à base de SiC est plus élevé que ce d'une diode à base de Silicium, ceci explique que, dans le Silicium tous les dopants sont généralement ionisés à température ambiante, par contre, dans le cas du carbure de silicium, les niveaux des donneurs et accepteurs de l'azote et de l'aluminium, respectivement, sont relativement profonds comparés à l'énergie thermique (k_bT/q) à température ambiante. De ce fait, il faut compte de l'ionisation incomplète des atomes d'impuretés (donneurs et accepteurs), donné par les expressions suivantes [1] [3]:

$$N_a^+ = \frac{N_a}{1 + g_v \exp\left(\frac{E_a - E_{F-P}}{k_B T}\right)} \qquad N_d^+ = \frac{N_d}{1 + g_c \exp\left(\frac{E_{F-n} - E_d}{k_B T}\right)}$$

Figure 1a

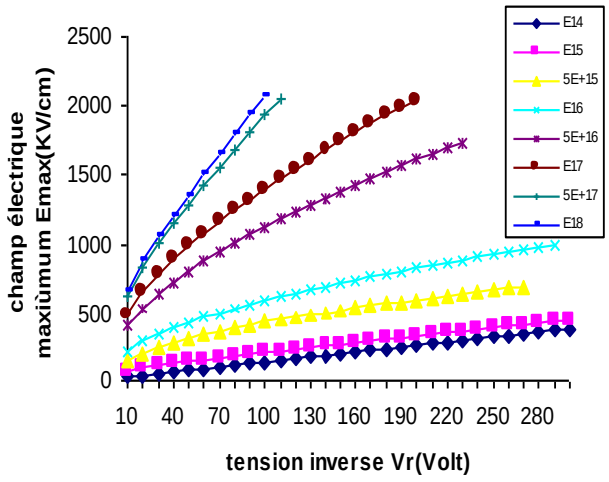

variation du champ électrique maximum en fonction de la tension inverse pour différente valeurs de dopage de la base (n+p-p+) (SiC)

Figure 1b

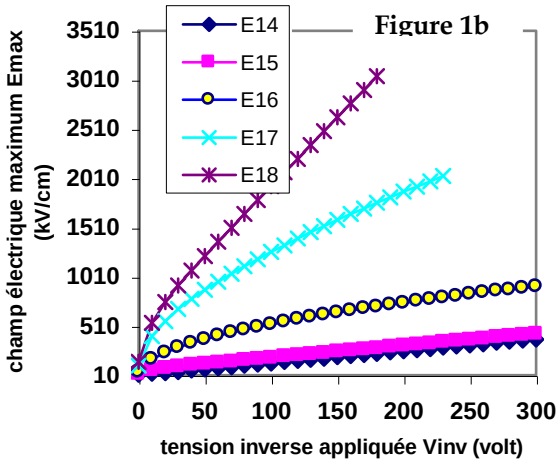

variation du champ électrique en fonction de la tension inverse appliquée pour différentes concentration de la base (Na) n+p-p+ (Si)

Dans une base courte (2µm) d'une diode n+p-p+ polarisée en inverse, le champ électrique maximum est plus élevée que ce dans une base longue (20µm), ceci explique que, plus l'épaisseur de la base est croit, plus la résistance de la base est diminue, par conséquent le champ électrique est augmente.

L'expression donnant R la résistance de la base par unité de surface en fonction de l'épaisseur w_b est :

$$R = \frac{w_b}{q\mu N_b}$$

µ : la mobilité des électrons (minoritaire de base)

La résistance est reliée à l'épaisseur et la concentration de la base, et à la durée de vie des porteurs minoritaires.

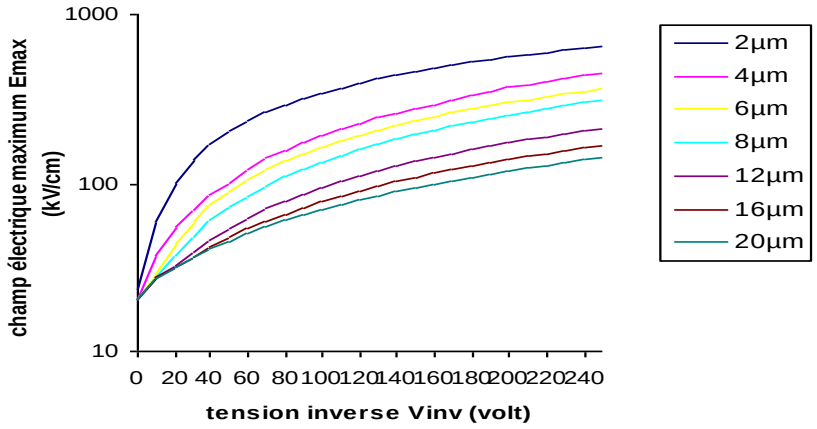

Fig. 2. **variation du champ électrique maximum en fonction de la tension inverse pour différentes valeurs de l'épaisseur de la base**

L'expression théorique [2] donnant la tension de claquage en fonction de la concentration et de l'épaisseur de la base s'écrit pour une diode n+p-p+

$$V_b = E_c w_b - \frac{qN_b w_b^2}{2\varepsilon\varepsilon_0}$$

N_b : la concentration du coté moins dopée (la base p-).

La figure 3 [4] illustre la tension de claquage en fonction de la concentration de la base (N_A).

D'une manière générale, les diodes n+p-p+ présente une meilleur tenue en tension comparée aux diodes n+p-. On voit nettement le rôle bénéfique de la base limité par un substrat et en plus une amélioration de la tenue en tension en augmentant l'épaisseur de la base.

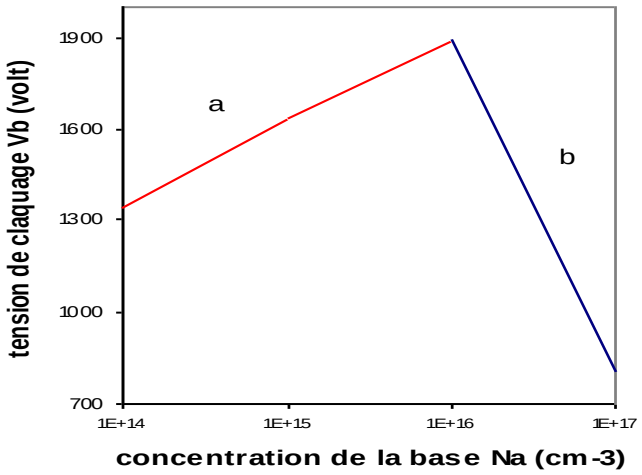

Fig. 3. **tension de claquage en fonction de la concentration e la base Na**

La réalisation des diodes n+p-p+ en SiC a permis de valider l'étude de l'influence de la concentration et l'épaisseur de la base sur le champ électrique maximum en polarisation inverse, et ainsi l'étude de la tenue en tension.

Les dispositifs bipolaires qui ont une couche active large et moins dopée sont plus performants que ceux qui ont une couche active mince et fortement dopées. A partir de cette étude, on peut comparer les caractéristiques de la base (p-) dans une diode n+p-p+ de celles des poches (p) d'une diode JTE.

References

[1] Naji Arssi : conception d'un thyristor 5KV en Carbure de Silicium pour assurer la génération d'impulsion de forte énergie. Thèse Insa de Lyon- Cegely.
[2] W.Fulop, ''Calculation of avalanche breakdown of silicon p-n junctions,'' Solid-State Electron, vol. 10, pp.39-43, 1967.
[3] Mihai Bogdan LAZAR. Etude du Dopage par Implantation Ionique d'Aluminium dans le Carbure de Silicium pour la Réalisation de Composants de Puissance. Thèse Insa de Lyon-CEGELY.
[4].Azzi.O '' Etude de la Tenue en Tension des Dispositifs A Structure JTE à Base de SiC'' thèse de magister. Université de Tlemcen (2003).

P4.

Classical, Quantum and semiclassical Mechanics

N. Baghli[1] and A. Zanoun[2]

[1] Département des Sciences de la Terre. Université d'Oran Es-sénia. Algérie
[2] Département de Méchanique. ENSET d'Oran. Algérie

First one our aim is to give a slight flavor of the process that has led physicists to change completely their conception of reality by passing from classical mechanics to quantum mechanics. We present also some basic notions of quantum mechanics : selfadjoint perators or quantum observables « P », energy « E », wave functions « f », …..

The mathematical study of Schrödinger operators can be very difficult in general, as a consequence one would like to dispose of any kind of approximations physically resonable allow us to predict some of the quantum properties of a system.

The so called Bohr correspondence principe asserts that quantum mechanics is a kind of generalization of classical mechanics, in the sense that one should be able to recover the classical properties of a system by making some approximation of its quantum properties.

The goal of the semiclassical mechanics is to study the quantum behavior when the mass of the particle becomes big with respect to the Planck constant « h », in this case « h » tends to 0, that is to say when the mass of the particle becomes thick enough to leave the quantum regime and to return to the classical regime.

So in the semiclassical mechanics the quantities : « P(h) », « E(h) », « f(h) »,….. depend all on the parameter « h » and one wants to know how they evolve when « h » tends to 0.

As a consequence semiclassical mechanics is a method of using classic mechanics to solve problems of quantum mechanics, it has been used extensively by phisicists and physical chimists to analyze atomic and molecular collisions. It also has been used to treat bound state or eigenvalue problems.

In this paper we shall describe the development of semiclassical mechanics for eingenvalues problems, we construct asymptotique solution of the the Schrödinger equation by the WKB method. We can also introduce the phenomena of resonances in the semiclassical regime.

P5.

Detection of the size and the position of dielectric in thin metal-dielectric composite by the impedance spectroscopy technical.

G. Benabdellah* and N. Zekri

[1]Laboratoire d'Etude Physique des Matériaux, USTO, département de Physique, LEPM, BP 1505 El M'Naouar, Oran, Algeria .* E-mail : abedgh20@yahoo.fr

In our numerical study, we used the impedance spectroscopy technical as a mean of detecting the size and the position of dielectric in thin metal–dielectric composite by analyzing the frequency of relaxation, the real and imaginary parts of the complex impedance of this composite. Such systems are modelled as RC networks, the effective conductivity are determined by using an exact resolution of the Kirchhoff equations. We show a relation between the frequency of relaxation and the size of the impurity and its position.

Dans cette étude, on considère une couche mince à deux dimensions composées d'un matériau conducteur, puis on introduit à la surface une impureté isolante d'une certaine taille et pour différente position par rapport aux électrodes. Chaque grain du matériau est présenté par une impédance qui simule son comportement physique tel que la variation de sa conductivité électrique en fonction de la fréquence, quand il est soumis à un champ électrique qui varie dans le temps. Pour notre cas, Les grains conducteurs sont représenté par une résistance R qui est l'inverse de leurs conductivité électrique $\sigma_c=1/R$, et les grains isolants par une capacité, avec une conductivité électrique $\sigma_i=iC\omega$. Les impédances sont connectées entre elles à travers un réseau électrique carré. L'impédance totale équivalente est calculée par la méthode exacte [1]. L'impédance équivalente caractérise le matériau d'un point de vue macroscopique et qui sera analysée en fonction de la fréquence et de la taille de l'impureté.

Nous avons pris un échantillon à deux dimensions de taille (100X100) nœuds, chaque noeud se compose de quatre impédances afin de reproduire la configuration de réseau carré. On étudiera l'effet de la taille de l'amas isolant sur l'impédance effective, la taille de l'amas allant de 1% à 10% de la taille totale du système, nous avons pris des valeurs unité de R et C (R=C=1) cela correspond à une fréquence de relaxation $\omega_0=1$ *rad/sec,* ce calcul est fait dans une gamme de fréquence qui varie de *1mHz à 1KHz..*

Nous avons calculé pour chaque proportion de l'amas isolant l'impédance complexe du matériau, nous avons tracé la courbe dans la ***fig.1*** qui représente la variation du module de l'impédance complexe de l'échantillon pour des tailles d'impureté allant de 1% à 10%.

On remarque dans cette figure que l'impédance effective du système varie en fonction de la fréquence et surtout en fonction de la proportion de l'amas isolant. Cela veut dire que la proportion de l'amas isolant influe sur le comportement de l'impédance effectif du système. L'impédance passe d'un état constant en fonction de la fréquence (caractère résistif), à un état qui varie en fonction de la fréquence, ce ci traduit la présence de composant capacitif (impureté), dans le matériau. Cette présence est d'autant plus grande quand la proportion de l'amas augmente, ceci nous indique l'existence d'une corrélation entre l'impédance effectif et la proportion de l'amas isolant.

Pour voir la corrélation qui existe entre l'impédance effective et la taille de l'amas isolant, nous avons analysé la partie imaginaire de l'impédance complexe. Dans la **fig. 2**, on représente la variation de la partie imaginaire en fonction de la fréquence et cela pour les différentes proportions de l'amas. On remarque la présence d'un pic qui correspond le minimum de la partie imaginaire à la fréquence de relaxation du système. La aussi on remarque que la partie imaginaire varie de façon très claire en fonction de la proportion de l'amas.

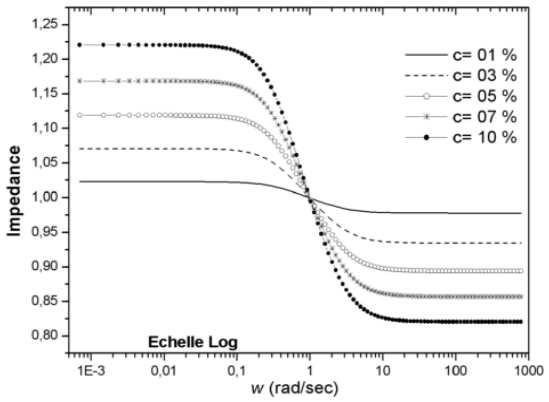

Fig. 1. Impédance effective en fonction de la fréquence pour plusieurs tailles de l'amas isolant au centre de système

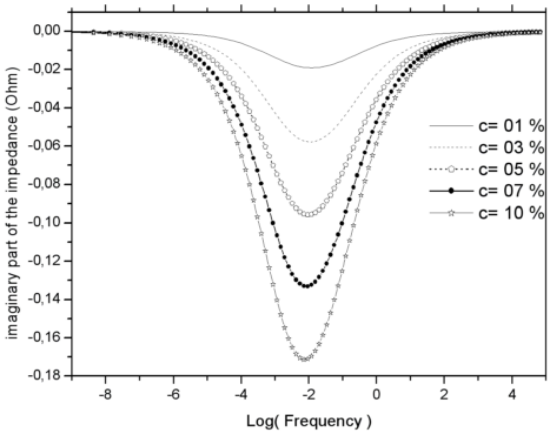

Fig. 2. La partie imaginaire de l'impédance effective en fonction de la fréquence pour plusieurs tailles de l'amas isolant au centre de système

Nous avons tracé l'amplitude de pic en fonction de la proportion de l'amas isolant dans la ***fig.3*** , on remarque la dépendance linéaire de minimum de la partie imaginaire de l'impédance effective complexe du matériau avec la taille de l'amas isolant, d'après l'ajustement :

min(imagZ)=0.002 – 1.96 C .

Telle que *C* la proportion de l'amas isolant par rapport la taille total du système. Ce résultat de point de vu est très important, car la connaissance de l'amplitude de pic de la partie imaginaire à la fréquence de relaxation nous permet de connaître la taille de l'impureté qui se trouve dans le matériau composite.

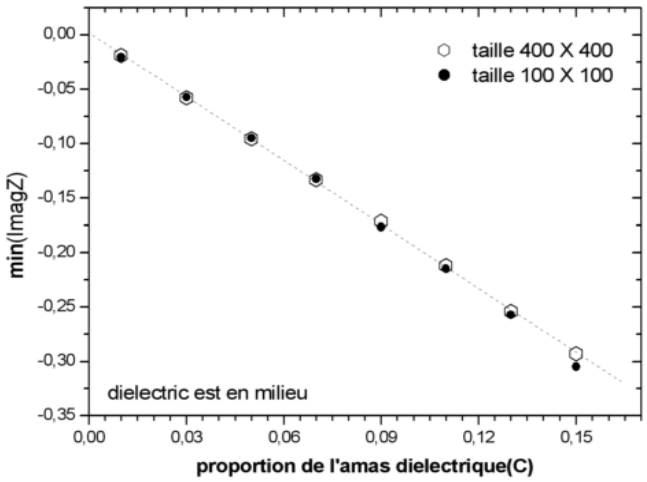

Fig. 3. Amplitude de pic en fonction de la proportion de l'amas isolant.

Maintenant, nous examinons l'effet de la position de l'amas isolant par rapport aux électrodes sur l'impédance effective complexe, nous avons pris une proportion de 6.25% de l'amas isolant, on va déplacer cet amas à partir de la première électrode vers la deuxième électrode (suivant l'axe oy) avec une position fixe suivant l'axe ox (de la coté gauche et la coté droite).

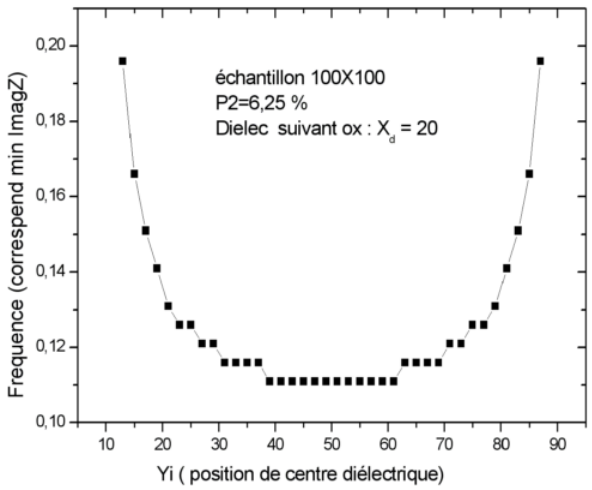

Fig. 4. la variation de la fréquence de relaxation en fonction de la position de diélectrique

Le changement de la position de diélectrique dans le système influe sur la fréquence de relaxation, la ***fig 4*** montre la variation de la fréquence de relaxation en fonction de la position de diélectrique dans le système, nous avons remarqué que lorsque le diélectrique se trouve proche aux bords de système la fréquence de relaxation est maximale et elle diminue rapidement lorsque le diélectrique s'approche au centre de système. Ce résultat est très important, car la connaissance de la fréquence de relaxation permet de bien localiser la position de diélectrique dans une composite métal-diélectrique.

Nous avons modélisé la technique de spectroscopie d'impédance pour détecter la taille de l'amas diélectrique dans une surface métallique et ainsi leur position par rapport aux électrodes. Nous avons trouvé une relation linéaire entre la proportion d'amas diélectrique et le minimum de la partie imaginaire de l'impédance effective de système à la fréquence de relaxation, et d'autre part, l'influence de la position de diélectrique sur la fréquence de relaxation.

L'application de cette méthode s'entend de l'industrie dans différents domaines, on peut l'appliquer par exemple pour détecter les fuites dans les réseaux d'eau. Il s'agit des appareils de plus en plus perfectionnés permettront de localiser les fuites de moyenne importance. Le principe est "d'écouter chanter" le tuyau métallique qui fuit. Le passage de l'eau au travers de la fissure fait vibrer le tuyau. Les choses se compliqueront fortement ensuite avec l'apparition du tuyau en matière plastique, car lui, "il ne chante pas" [2] , dans ce cas là, nous pensons que on peut utiliser la spectroscopie d'impédance pour détecter les fuites, en considérant que les fuites ont un coefficient diélectrique diffèrent que celui de tuyau et comme ça on peut simuler comme une composite de deux composantes.

References

[1] L. Zekri, R. Bouamrane and N. Zekri. J. Phys. A: Math. Gen. **33** (2000) 649 656.

[2] J Osama Hunaidi and Wing T. Chu "Acousticai Characteristics of Leak Signais in Piastic Water Distribution Pipes": AppliedAcoustics, vol **58** (1999), pp 235-254

P6.

Electronic Band Structure of Ternary Alloy CdSexTe1-x

K. Benkabou [1], F. Z. Aoumeur[1] and N. Amrane[2]

1Physics Department, University of Sidi Bel Abbès , Sidi Bel Abbes, 2000 ALGERIA Kbenkabou@yahoo.fr
2Physics Department, , Al-Ain University United Arab Emirates, namranen@yahoo.com

Semiconductor alloys provide a natural means of tuning the magnitude of the forbidden gap and other material parameters so as to optimize and widen the application of semiconductor devices. The ternary alloys systems open new possibilities for materials engineering as they enable control of two basic parameters : the band gap energy and the lattice constant, this procedure is very important in opto-electronic engineering. There is much current interest in II/VI ternary compounds semiconductors for use in a variety of solid-state devices [1, 2].

Studies of the electronic structure of substitutional semiconductor alloys along with their closely related applications have become an important part of semiconductor physics. The fundamental difficulty in the study of alloys band structure is that no exact solution of the Schrödinger equation for the disordered alloy system is obtainable. This has motivated an interest in approximate theories [3, 4].

It is well known that the band gap energy of the alloys shows a nonlinear variation with composition. The present method can be used to explain qualitatively some part of the electronic structure of the ternary alloys ABxC1-x. Our approach is based on the TB Hamiltonian in a nearest neighbors description with an orthogonal basis of five atomic orbital per band (sp3 s*) [5] taking into account the compositional disorder, also called the disorder Hamiltonian. In order to clarify the bowing effect in the ternary alloys of the form ABxC1-x, we form the VCA Hamiltonian matrix (HVCA) and calculate the fluctuations (Hdis) about the VCA using the formalism due to Lee et al [6,7], this model is using to compute energy band gap and band structure of ternary system CdSexTe1-x . A model, calculating the relaxation of bonds for the ternary alloys is used .

The electronic band structure of CdSexTe1-x is showed on fig(1) . The band structure of figure (1) is representative of a semiconductor compound. The alloy exhibits a direct gap for the given composition, which is expected since CdSe and CdTe are both direct-gap compounds. It is well known that the TBM describes quite well the dispersion of the valence bands as the lower conduction band in the high symmetry points .(after the inclusion of the s* states) of the binary semiconductors [8,9]. The band gap energy fig (2) of the ternary alloy considered are calculated as function of x composition. Very good agreement is obtained between the available experimental bowing (0.75) [10] and our calculated bowing with improved VCA (0.79). The band gap is one of the most useful aspects of the band structure, as it strongly influences the electrical and optical properties of the material. Electrons can transfer from the higher valence band to the lowest conduction band by means of carrier generation and recombination processes. The band gap and

defect created in the band gap by doping can be used to create semiconductor devices such as solar cells, diodes, laser diodes and others.

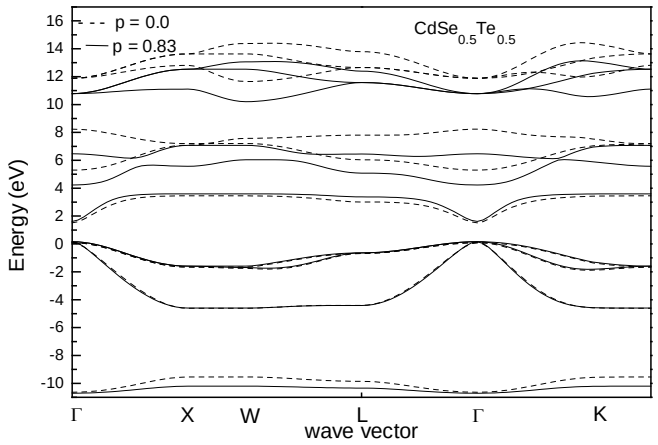

Fig 1 : Band structure of $CdSe_{0.5}Te_{0.5}$

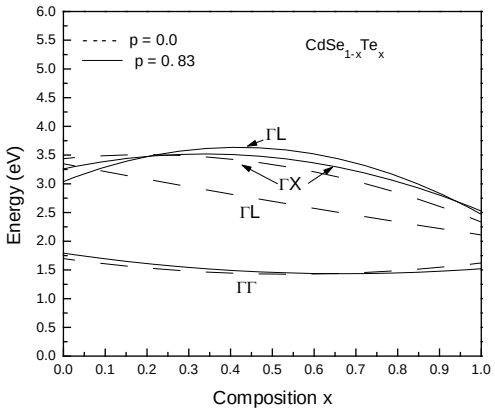

Fig 2 : energy band gap of CdSeTe

References

[1] J. M. Gaines et al. Appl. Phys. Lett. 62 2462 (1993).
[2] H. J. Chen et al. Chinese Journal of Physics 36 533 (1998).
[3] A. Goni, G.M. Stocks , and W.H. Butler, Phys. Rev. B 29 555 (1984).
[4] Z. Q. Li and W Pötz, Phys. Rev. B 43 12670 (1991).
[5] P. Vogl, H. P. Hjalmarson, and J. D. Dow, J.Phys.Chem. Solids 44, 365 (1983).
[6] S. J. Lee et al. Phys.:Condens. Matter 2, 3253 (1990).
[7] S. J. Lee et al. Phys. Rev. B 42, 1452 (1990).
[8] W. A. Harrison, Electronic structure and the properties of solids, Dover publications, Inc. New York (1989).
[9] Y. P. Feng et al. J. Appl. Phys. 74 3948 (1993).
[10] M.J.S.P. Brasil et al. Appl. Phys. Lett. 59, 1206 (1991)

P7.

Structures et énergies du néocarrabiose et du néocarrabiose bisulfaté par la méthode de DFT

N. Berrekhchi-Berrahma –Bestaoui[1]), A.Sayede, N.Yousfi[2], and M. Sekkal-Rahal .

[1]Lboratoire de microscopie, microanalyse de la matière et de spectroscopie *1*
L2MSM), Faculté des sciences, Université de Sidi Bel Abbes ALGERIE Sidi Bel Abbes *22000*
[2] LPCIA,F,R,E, 2485 CNRS , Faculté des Sciences Jean Perrin Université d'Artois
62307 Lens Cedex FRANCE

La molécule (3-O-(3,6-Anhydro-α-D-galactopyranosyl)-β-D-galactopyranose) ou β-D-néocarrabiose est l'une des deux unités répétées des carraghénanes.

Les carraghénanes sont des galactanes sulfatés éxtraits d'algues rouges, utilisés comme épaississants et agents gélifiants en industrie alimentaire. Ces galactanes ont des structures à base de chaines linéaires altérnant des résidus de liaison – 4 α-D-galactopyranose avec des résidus de la liaison -3 β-D-galactopyranose. Habituellement sulfatés en différentes positions et ont souvent une unité α-D-galactose remplacée 3,6- anhydrogalactose.

Dans ce travail des cartes énergétiques utilisant la méthode de Ramachandran [1] de type B3Lyp/6-31g(d) du disaccharide β-D-néocarrabiose [2-4] dans le vide et du bisulfaté dans la vide et dans l'eau ont été réalisées.

Les plus importants paramètres géométriques pour définir la structure tri-dimentionnelle du

disaccharide sont les angles dièdres de la liaison glycosidique fi et psi définis par O5-C1-O1-C3' et C1-O1-C3'-C4' respectivement.

Ces cartes conformationnelles ont été construites par la méthode de French et al. [5] par interpolation de 144 valeurs d'énergie, en faisant varier les angles dièdres Φ et ψ par augmentation de 30°, et en les gardant fixés pendant l'optimisation.

Dans ce travail, l'étude du phénomène de solvatation a utilisé une constante diélectrique pour traiter l'effet du solvant [6-9], ε = 78.39.

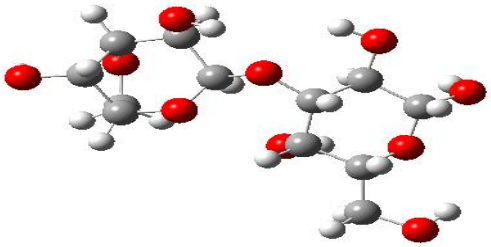

gure 2: Néocarrabiose bisulfaté

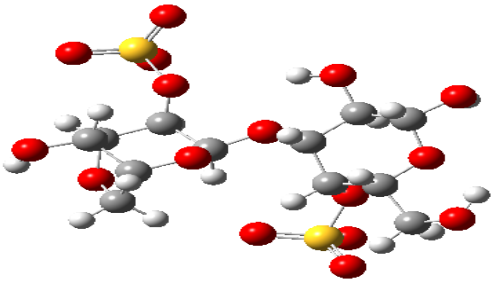

Figure 1: Néocarabiose

1/ Néocarrabiose bisulfate dans le vide:

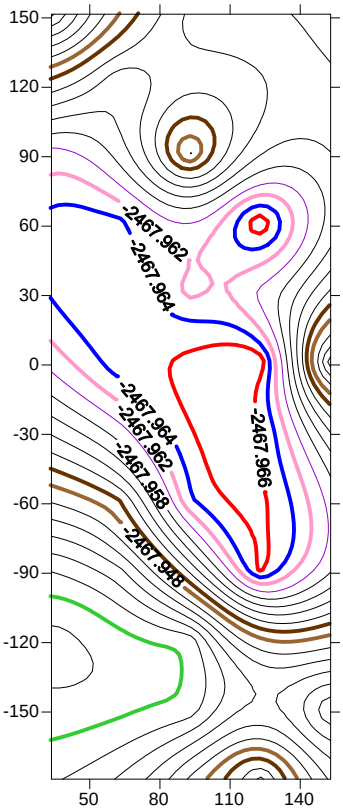

Eau

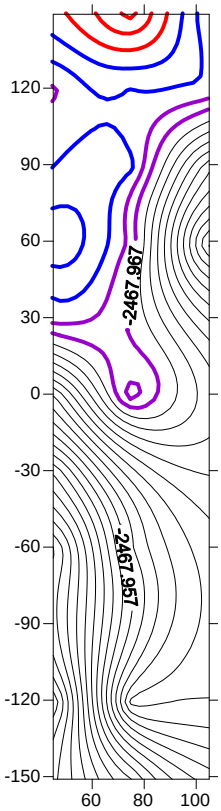

Vide

Fig. 3. Carte du Néocarrabiose bisulfaté dans le vide et dans l'eau

Tableau 1. Les angles dièdres Φ et ψ (en degrès) et les énergies relatives (en Hartrees), dans le vide.

Minima	Ψ	Φ	Energie(Hartrees)
A	61	123	-2467.96761871
B	-59	123	-2467.96639740
C	-29	123	-2467.96639693

Structures des conformères après optimisation:

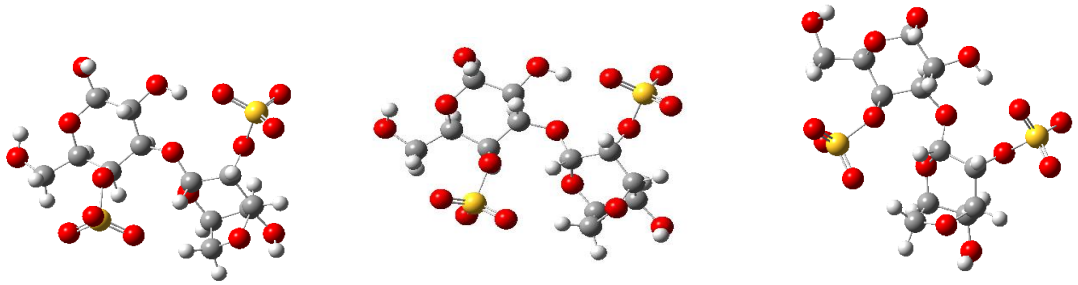

A **B** **C**

Les points A, B et C définissent les paires de valeurs (Φ et ψ données dans le tableau 1) associées aux structures de plus basses énergies.

2/ Néocarrabiose bisulfaté dans l eau:

Tableau 2. Les angles dièdres Φ et ψ (en degrès) et les énergies relatives (en Hartrees)

Minima	Ψ	Φ	Energie(Hartrees)
A	149	75	-2467.97336554
B	59	45	-2467.97078200
C	89	75	-2467.96934448

Structures des conformères après optimisation:

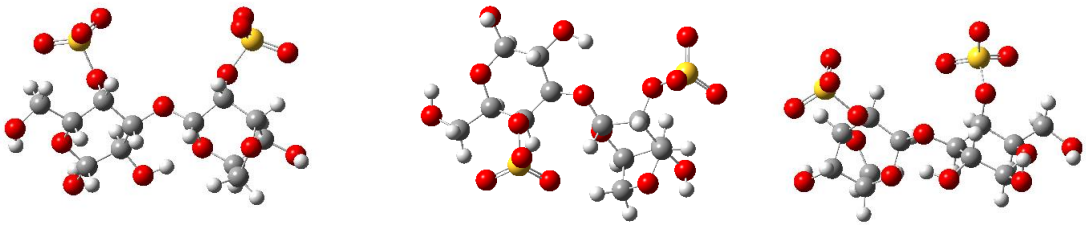

A **B** **C**

Les points A, B et C définissent les paires de valeurs (Φ et ψ données dans le tableau 2) associées aux structures de plus basses énergies.Les cartes énergétiques ont été construites pour deux dimères du β-D-néocarrabiose (non sulfaté) dans le vide et du bisulfaté dans le vide et dans l'eau avec b3lyp/6-31g*. Dans chaque cas on a obtenu trois minima correspondant aux plus basses énergies . Dans l'eau la molécule est plus stable et l'énergie est plus faible.

Réferénces:

[1] Michelle M. Kuttel, Kevin J. Naidoo, Carbohydr res 340, 875 (2005).
[2] Ueda , K. Ochia , H. Imamura ,A. Natagawa , S. Bull Chem. Soc .Jpn 68 ,95 (1995).
[3] Ueda , K. Brady , J. W. Biopolymers .38 ,461(1996).
[4] Stortz . C.A., Cerezo, A.S.J. Carbohydr Chem . 19,1115 (2000).
[5] A.D. French , A.M. Kelterer , G.P. Johnson , M.K. Dowd , C.J. Cramer , J. Comput Chem . 22, 65 (2001).
[6] Goncalves , P.F.B., Stassen , H.J. Comput Chem . 22 ,706 (2002).
[7] Langella , E. Rega , N. Crescenzi , O. Barone , B.J. Comput Chem. 23, 650 (2002).
[8] Curutchet.C. ,Cramer.CJ , Truhlar , D.G. Ruiz-Lopez , M.F. Rinaldi , D. Orozco , M. Luque , F.J.J. Comput Chem . 24, 284 (2003).
[9] Fattebert , J.L, Gygi, F.J. Comput Chem .22,662 (2002).

P8.

Synthesis and Characterization of Nanocrystalline Fe64Ni36 Powders

N. Boudinar1, A. Djekoun[1], A. Chabli1, A. Otmani[1], B. Bouzabata[1], J. M. Greneche[2]

[1]Laboratoire de Magnétisme et de Spectroscopie des Solides Université Badji Mokhtar
Faculté des sciences B. P: 12 (23000) ANNABA –Algérie
[2]Laboratoire de Physique de l'Etat Condensé, UMR CNRS 6087 Université du Maine Faculté des Sciences
72085 LeMANS Cedex 9 –France

In recent years, nanopowders Fe-Ni materials have attracted much attention, because of their potential applications, including sensors, composites and catalysts [1]. Therefore, various physical and chemical methods are developed such as ball milling, electrodeposition, laser ablation, chemical vapor deposition, sputtering, and chemical reduction method can all be used to produce fine metal powders [2, 3]. Fe-Ni alloys with concentration of around 35 at.% Ni and fcc crystal lattice structure, which are called ''invar alloys'' [4], show a very small (almost zero) thermal expansion over a wide range around the room temperature [5]. Ball milling is regarded as an effective way to obtaining nanocrystalline materials. However, decreasing of crystallite size during ball milling of Fe-Ni powders is usually accompanied by phase transformations of the material studied.

Nanostructed $Fe_{64}Ni_{36}$ alloy was prepared by high energy ball milling of elemental iron, and nickel powders in a vibratory ball mill type Spex 8000M under an argon atmosphere for various times. The main structural analysis was carried out via X-ray diffraction (XRD). The results showed the existence of single phase solid solution (fcc) for samples during the first 3h of milling and a grain size was found about 12 nm.

The formation of the nanocrystalline structure during mechanical alloying was followed by X-ray diffraction. The XRD patterns of $Fe_{64}Ni_{36}$ powders for various times are shown in Fig. 1.

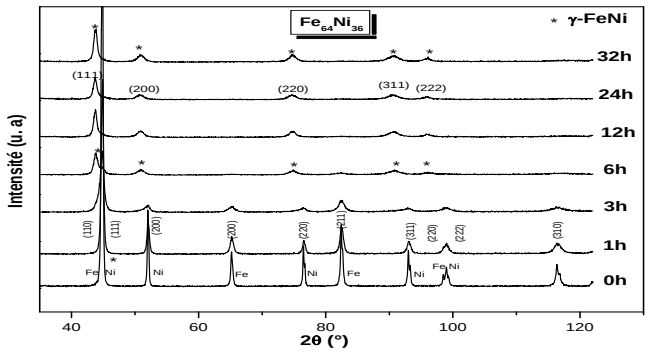

Fig. 1. X-ray diffraction patterns of $Fe_{64}Ni_{36}$ powder synthesised in high-energy mill for various milling times

The XRD results showed that fcc Fe–Ni solid solution is the main product of mechanical alloying and that Fe–Ni fcc solid solution formed after 3 h of milling. The intensities of Bragg peaks for all elemental powders decreased rapidly with the increase of milling time. The nickel peak disappears when the milling time exceeds 3 h. Pekala [6] reported that the structure of the product after ball milling depended on the alloy composition, in the $Fe_{80}Ni_{20}$ alloy it was the bcc structure while for $Fe_{50}Ni_{50}$ alloys it was the fcc structure. From Fig. 1, it can be seen that the drastic reduction in the peak intensities for the powders may be due to a high impact energy, which is applied to powder particles. Peak broadening was also observed in the XRD pattern due to reduction in crystallite size and stresses in the powder particles.

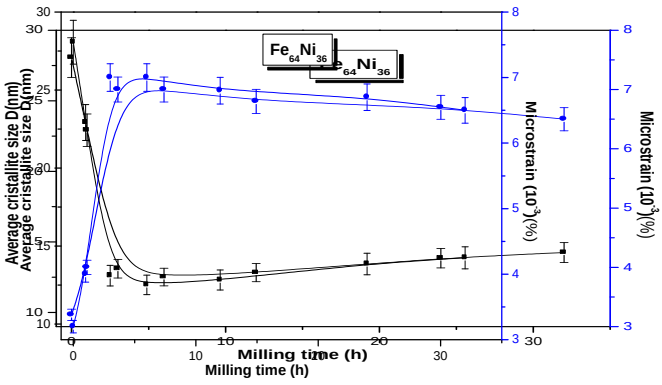

Fig. 2. Crystallite size and Microstrain of Fe_{64} Ni_{36} powders for various milling times

In Figs. 2, the evolution of the crystallite size and of the lattice strain as a function as the milling time are shown for the mechanically alloyed Fe_{64} Ni_{36}. The crystallite size was calculated from the line broadening using the Scherrer's formula. The value of crystallite size D decreases from D = 28 nm to 12 nm for 12 h of milling and lattice strain varied from 0.3 % to 0.89% when the milling time increases. Pekala et al. [6] have found that the value of crystallite size and lattice strain reached 10 nm and 0.46%, respectively after 40 h of milling using high energy ball milled. Using low-energy milling, the same authors [7] have found that these parameters reach 9 nm and 0.47 % after 400 h of milling. Djekoun et al. [8] have found that the value of crystallite size and lattice strain reached 8 nm and 0.21% after 48 h of milling using planetary ball mill high-energy (Fritsch Pulverisette 7).

Fig. 3 gives the lattice parameter for different milling times of the samples. Lattice parameter values were calculated from the high angle peak positions. The abrupt increases in the lattice observed for the sample milled 12 h shows the formation of the FeNi alloy. Furthermore, the lattice parameter increases with increasing milling time.

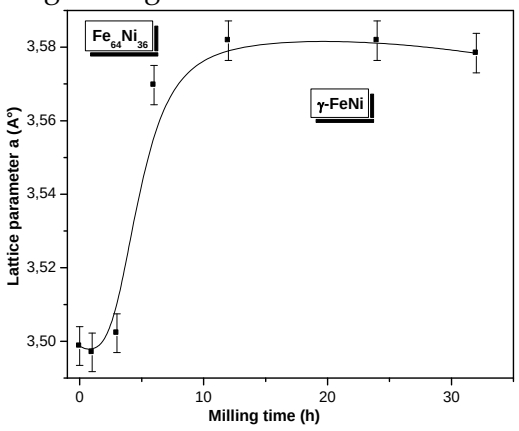

Fig. 3. Lattice parameter of γ - (Fe, Ni) powders for various milling times.

Mechanical alloying of $Fe_{64}Ni_{36}$ led to formation of solid solution fcc-phase. The as-milled powder seemed to have a disordered structure according to our XRD. The results presented in this work clearly show the great potential of this technique. High-energy ball milling of Fe and Ni powders results in the solid solution formation accompanied by a grain refinement.

References

[1] D. J. Sellmgher, M. Yu, R. D. Kirby, Nanostruct. Mater. 12 (1999) 1021.
[2] M. Moreno-Manas, R. Pleixates, Acc. Chem. Res. 36 (2003) 638.
[3] V. Kesavan, P. S. Sivananad, S. Candrasekharan, Y. Kolypin, A. Gedankan, Angew. Chem. Int. Ed. 38 (1999) 3521.
[4] M. M. Abd. Elmeguid, B. Schleede, H. Micklitz, J. Magn. Magn. Mater. 72 (1988) 253.
[5] S. Kumar, K. Roy, K. Maity, T. P. Sinha, D. Banerjee, K. C. Das, R. Bhattacharya, Phys. Statut Solid. A 167 (1998) 175.
[6] M. Pekala, D. Oleszak, E. Jartych, J.K. Zurawicz, Nanostruct. Mater. 11 (1999) 789.
[7] M. Pekala, D. Oleszak, E. Jartych, J.K. Zurawicz, J. Non-Cryst. Sol. 250_/252 (1999) 757.
[8] A. Djekoune, B. Bouzabata, A. Otmani, J. M. Greneche. Catalysis Today 89 (2004) 319-323.

P9.

Les fonctions de correlation pour l'étude du verre silicaté

N. Nehaoua[1], Y. Chergui[2], B. Telrhemti[3], N. Deradji[4] and H. Belkhir[4]

[1] Université Baji-Mokhtar, Annaba, 23000, Algérie, *chergui_nehaoua@yahoo.com*
[2] Université Baji-Mokhtar, Annaba, 23000, Algérie
[3] Université Baji-Mokhtar, Annaba, 23000, Algérie
4 Université Badji-Mokhtar, Annaba, 23000, Algerie

Le but de la simulation d'un système moléculaire sur ordinateur est de calculer le comportement macroscopique à partir des interactions microscopiques. Les méthodes de simulation sont classées habituellement en deux méthodes [1] : Méthodes classiques (Dynamique moléculaire classique, Monte-Carlo) et Méthodes quantiques (ab-intio). La dynamique moléculaire se base sur la résolution des équations du mouvement. Le point de départ de nos calculs est une configuration atomique aléatoire, mais néanmoins réaliste, représentant un verre de forme cubique. La dynamique moléculaire consiste à connaître à chaque instant les forces (et donc les potentiels d'interactions) qui s'exercent sur tous les atomes de la boîte de simulation ainsi que leurs positions et vitesses [2].

Le composé Titanosilicaté n'existe pas dans la nature, il existe sous forme synthétique. Vu son importance technologique ; il a fait l'objet de plusieurs études concernant ces propriétés physiques, parmi elles, nous citons les propriétés optiques. Ces dernières s'avèrent plus intéressantes par un dopage au titane. Bien que la structure de la silice a été bien étudiée, néanmoins le titane reste moins connus, c'est pour cette raison que nous nous sommes intéressé à cette étude pour connaître la structure où cristallise notre composé.

En utilisant la technique de la dynamique moléculaire, implémenter dans le code Dl-poly, nous nous sommes fixé à l'étude des propriétés structurales, en déterminant les distances interatomiques et les angles formés entre divers atomes. Lesquelles pourrons nous être utile pour la détermination de la structure du Titanosilicaté. Les résultats obtenus dans ce travail sont en bon accord avec les résultats théoriques et expérimentaux.

References

[1] P. D. Bristowe, Materials Modelling (Lectures1-9), Part III University of Cambridge Department of Materials Science and Metallurgy 2006.
[2] J.M. Goodman, Chemical Applications of Molecular Modeling, (RSC, 1998).

P10.

Simulation de l'élaboration de Verres Métalliques en couches minces par Melt Spinning

O. chettouh[1], M. Saadi[2], S. H. Abaidia[3]

[1] Université M'hamed Bougerra,Boumerdès.
[2] Université M'hamed Bougerra,Boumerdès.
[3]Laboratoire LMMC, université M'hamed Bouguerra, Boumerdès.Algérie

Les propriétés structurales et thermodynamiques de l'état vitreux de l'alliage binaire l'$Al_{80}Ni_{20}$ exprimées en termes de fonctions de corrélation des paires partielles *g(r)* et par l'entropie, nous ont permis de suivre l'évolution des positions atomiques dans la recherche de leurs métastabilités et de comparer nos résultats à 1000K, donc l'état solide, aux résultats trouvés à 1525K[8] à l'état liquide. La simulation a été effectuée par la dynamique moléculaire en considérant des hypertrempes à des vitesses supérieures à 10^{12} K/s. Les interactions atomiques ont été modélisées par un potentiel du type « Embedded Atom ». Nous sommes partis d'une température supérieure à celle du liquidus, afin d'assurer l'homogénéité du liquide, et d'une structure cristalline du type Cubique à faces centrées.

La modélisation de l'état amorphe dans les solides repose principalement sur deux modèles : le premier dit « modèle microcristallin » et le second est appelé « modèle des sphères dures » Dans le premier modèle, on considère que les atomes sont arrangés dans de très petits cristaux dont la périodicité structurale à longue distance est absente, à cause de l'orientation aléatoire de ces microstructures [1]. Le deuxième modèle considère que les atomes forment une agglomération dense et aléatoire de sphères dures. C'est-à-dire ne contiennent pas de cavités internes pouvant accepter d'autres sphères (modèle de Bernal) [2].Ces agglomérations aléatoires sont caractérisées par leur compacité et leurs fonctions de distribution radiale [3] *g(r)*. Pour un système binaire A_xB_{1-x}, la structure moyenne, peut être exprimée par essentiellement, la fonction de corrélation concentration-concentration $S_{CC}(k)$ [4], qui est reliée à l'ordre ou la tendance à l'agrégation dans l'alliage ce qui la rend apte à y décrire l'ordre chimique ainsi que sa transformée de Fourier $g_{CC}(r)$. Remarquons que la relaxation structurale commence sur la distance des plus proches voisins ce qui est visible au maximum de facteurs de structure.

Pour l'alliage *Al-Ni, B2* Le rayon cut-off, où les interactions tendent vers zéro est de 5.954A°, la portée de l'interaction est au 6ème voisin, mais la contribution du 6ème voisin est négligeable [5].Le code de simulation utilisé pour l'analyse de la dynamique moléculaire est le XMD de Jon Rifk ; jon.rifkin@uconn.edu à l'université du Connecticut.Au départ une équilibration du système a été effectuée dans les conditions standards de pression et de température. La simulation classique par la dynamique moléculaire traite le système dans l'approche microcanonique (NVE). Cependant pour notre cas, pour le contrôle du processus de thermalisation et du phénomène de l'hypertrempe il est nécessaire d'ajouter un paramètre de contrôle de la quantité de chaleur du système. Pour cet effet, on considère l'ensemble canonique (NVT) avec un thermostat de contrôle

de la température [6,7] du type Nosé-Hoover.La structure et les propriétés physico-chimiques des liquides à l'équilibre peuvent être décrits en termes de fonction de distribution des paires *g(r)*. L'analyse des fonctions de corrélation des paires partielles (fig1)et des facteurs de structures à l'état liquide à 1525K [8], comparée aux résultats que nous avons trouvé à 1000K (fig2). Ont permis de conclure que à *T=1000K*, g_{NiNi} est particulièrement intense, ce qui traduit que la couche des 1ers voisins est relativement bien définie et peu étalée, et donc peut être un ordre à courte distance.

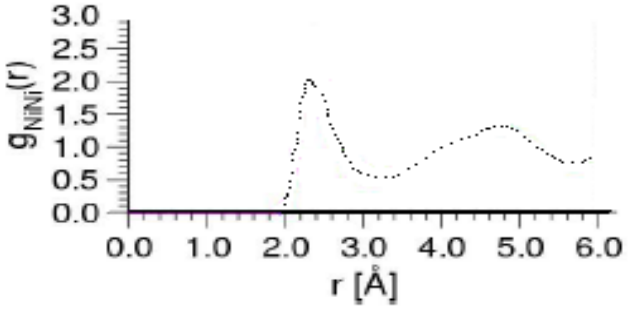

Fig. 1. Fonction de corrélation des paires $g_{Ni\text{-}Ni}(r)$ à T=1525K [13]

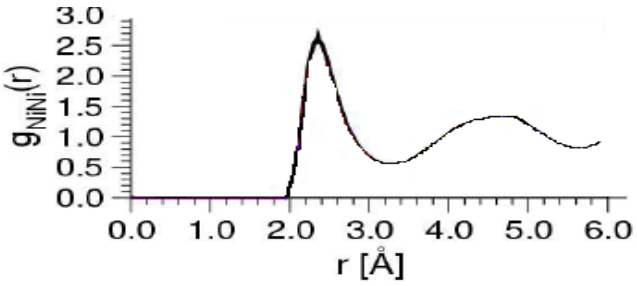

Fig. 2. Fonction de corrélation des paires $g_{Ni\text{-}Ni}$ (r) à T=1000K

En plus la présence d'un prépic dans S_{NiNi} vient appuyer la présence d'un ordre chimique à courte distance et moyenne distance dont la longueur de corrélation est $d=5.43Å$. Nous remarquerons l'ébauche d'un prépic à *T=1525K* ce qui prouve que l'ordre à courte distance existe même dans les liquides et la longueur de corrélation dans les liquides donnée par James d=1.23 (2 Π/q) est vérifiée.

La fonction g_{AlNi} (fig3) à T=1000K est plus intense que g_{AlAl} ou encore g_{NiNi} à la même température, la distance Al-Ni est plus petite que celle d'Al-Al et de Ni-Ni, ce qui montre que les atomes d'*Al* ont tendance à se faire entourer d'atomes *Ni.* Ceci est appuyé par le prépic à amplitude négative (preminimum) dans S_{AlNi} (fig4) et qui est la traduction de la formation d'unités structurales composées d'atomes de natures différentes sur une longueur de $d_{prépic}$ *(corrigée) = 4.65Å*.

L'entropie de configuration associée à l'alliage fondu et à la phase métastable obtenue par la dynamique moléculaire à T=1000K est dans la figure 5.

Son analyse, nous permet plusieurs conclusions.

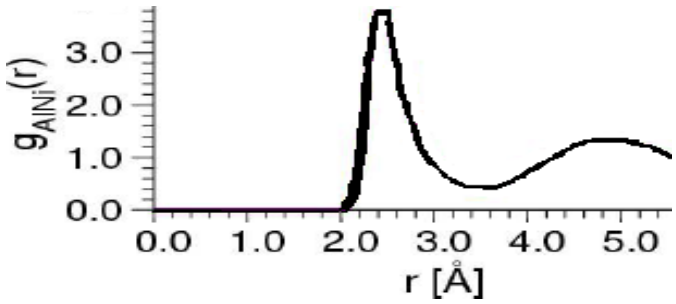

Fig. 3. Facteur de corrélation des paires $g_{Al\text{-}Ni}(r)$ à T=1000K

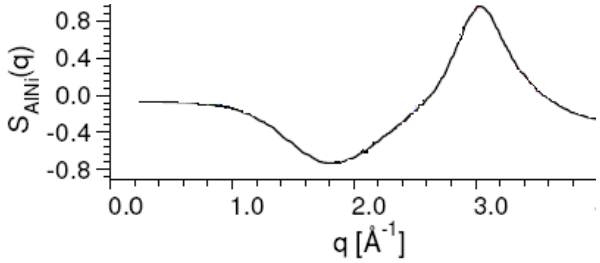

Fig. 4. Facteur de structure $S_{AL\text{-}Ni}$ (q) à T=1000K

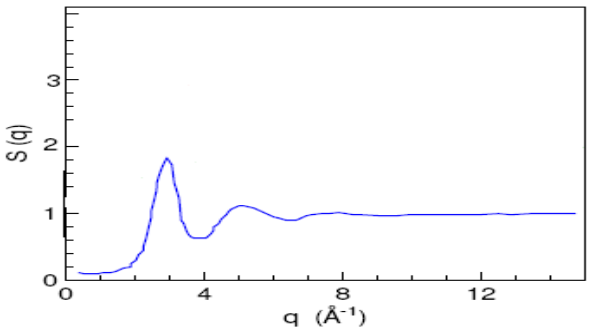

Fig. 5. Entropie S(q) de $Al_{80}Ni_{20}$ à T=1000K.

Après le refroidissement rapide de l'alliage $Al_{80}Ni_{20}$ liquide l'analyse structurale ainsi que thermodynamique, a confirmé son obtention sous forme d'un verre métallique c'est-à-dire la présence de nanocristaux d'AlNi3 dans une matrice amorphe. Ceci car il y a présence de prépics aussi bien dans le facteur de structure S_{NiNi} que S_{AlAl} et donc ordre chimique et topologique à courte distance, mais surtout la présence d'un préminimum dans le facteur de structure dans $S_{Al\text{-}Ni}$ qui est la signature de la forte interaction *Al-Ni.*

L'entropie de configuration confirme la métastabilité de ces composés ainsi que la théorie du volume libre. Cette composition n'est pas proche d'un eutectique profond, cet alliage est binaire, la différence de taille des composants est >12%, et la chaleur du mélange à l'état liquide largement négative ΔH mélange ($Al_{80}Ni_{20}$)= - 25.2KJ/mole**,** permet de le classer avec les alliages décrits dans la théorie, ¨**verre marginal**¨.

REFERENCES

[1]. Solid state physics; Editors: Henry Ehrenreich, Frederick seitz, and David Turnbull. Editors:G.S.Cargill, Robert Gomer, P274-299, 1975.
[2]. Physics of amorphous materials, S.R.Elliott, P325, 1984.
[3]. Models of disorder J.M.Ziman, P69, 1979.
[4]. Order and disorder in liquid alloys, Bernard Pieter Alblas, P22, 23; 1983.
[5]. Embedded atom potential for B2 Ni-Al, Y.Mishin, M.J.Mehl and D.A.Papaconstantopoulos, 2002.

P11.

Complexation of Uranyl with Acetate Ligands: A Density Functional Study

S. N. Derrar[1], S. Krüger[1] and N. Rösch[1]

[1]Theoretische Chemie, Department Chemie, Technische Universität München, 85747 Garching, Germany

The study of the distribution and migration of radioactive and toxic actinide ions in the environment is of general concern and of specific importance for long-term risk assessment of potential nuclear waste repositories. The complexation of the uranyl dication UO_2^{2+} by various anionic ligands in solution has been the subject of a variety of studies because solubility and mobility of these complexes play a crucial role in the migration of actinides in groundwaters.[1] Besides various inorganic anions occurring in natural waters, carboxylic acids are regarded as interesting model ligands because carboxylic groups are considered to be the main functional groups of humic substances which show a strong complexing ability for metal ions[2] and thus influence their The complexation of actinide ions by humic substances and the corresponding small organic model compounds has mainly been examined experimentally;[3-5] only a few theoretical studies have been performed.[6-8] We present a computational model study on uranyl (VI) acetate complexes $[UO_2(OOCCH_3)_n]^{(2-n)}$, n = 0–3. This ligand has been frequently studied experimentally[4,9,10] and also an earlier computational study applying a gas-phase pseudopotential (PP) density functional approach[8] is available, allowing methodological comparison. Here we extent this earlier work by using a scalar-relativistic all-electron density functional approach[11]; we optimized the geometry of the complexes without symmetry constraints, and approximated solvation effects by means of a polarizable continuum model (PCM).[12] Uranyl mono-, bi, and triacetate complexes with the favourable bidentate acetate complexation mode (Fig. 1) have been preoptimized under appropriate symmetry constraints (C_s, C_{2v}, C_{3v}, respectively). Subsequently, the symmetry constraints were released. Optimizations in the gas phase and in aqueous solution (by means of the COSMO[13] PCM model) were carried out, using an LDA density functional (VWN). Subsequently, energetic parameters were determined in a single-point fashion with a GGA functional (BP86). For all calculations the LCGTO-FF-DF (linear distribution.

combination of Gaussian-type orbitals fitting function density functional) method as implemented in the parallel program ParaGauss[14,15] was applied; for further computational details see our earlier in the parallel program ParaGauss[14,15] was applied; for further computational details see our earlier study on uranyl monocarboxylate.[16] Comparison to experiment should only be done for the triacetate species, as effects of explicit aqua ligands, not included in this study, are anticipated.The optimized structures and symmetric and asymmetric uranyl stretching frequencies for $[UO_2(OOCCH_3)_n]^{(2-n)}$, n = 0–3, are collected in Table 1. Uranyl monoacetate exhibits C_s symmetry and the diacetate C_{2v} symmetry, thus results without symmetry constraints are identical. Deviations for uranyl triacetate from C_{3v} symmetry are small (Table 1). Relaxation of symmetry for that complex results in a marginal stabilization of the complex by 2 kJ/mol, accompanied by a slight elongation of the uranyl bond (0.3 pm) and a similar shortening of the ligand bond. In the

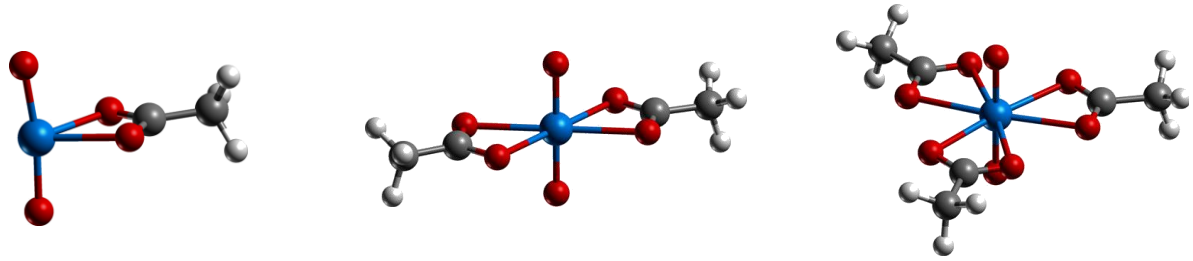

Fig. 1. Optimized structures of $[UO_2(OOCCH_3)_n]^{(2-n)}$, n = 1–3, in solution

Table 1. Average binding energies (kJ/mol) per acetate ligand for $[UO_2(OOCCH_3)_n]^{2-n}$ for n=1–3, Eq. (1), and ligand addition energy, Eq. (2), in the gas phase (GP) and in solution (SOL)[a]

Eq.	n	GP	GP[b]	SOL
1	1	-1575	-1521	-378
	2	-1193	-1158	-311
	3	-882	-854	-263
2	1	-1575	-1521	-378
	2	-812	-794	-245
	3	-259	-246	-165

overall structure of uranyl triacetate this is reflected by a bending of one of the acetate ligands by about 10° out of the equatorial plane of uranyl. Due to the coordination of acetate ligands, the uranyl bond of the triacetate elongates by 9 pm compared to free uranyl. The elongation is largest for the first ligand (4.4 pm) and smallest for the last (1.9 pm), indicating a pronounced bond weakening with increasing number of ligands. Accordingly, the uranyl-ligand bond U-O_c increases from 222 pm for the monoacetate to 245 pm for the triacetate. Also the U-C distance to the carbon atom of acetate increases with the number of ligands. These strong effects on the geometry are mainly due to the decreasing charge of the complex from +1 for mono- to -1 for triacetate, which goes along with a strong charge donation to the uranyl ion. A Mulliken population analysis yields the following charges on uranyl: 0.90, 0.47, and -0.03 e for n = 1–3, respectively. The geometrical results obtained are in very good agreement with those of an earlier PP VWN DFT study[8], which yielded shorter bond lengths by at most 1 pm.

Also in solution, the increasing number of acetate ligands leads to a weakening of the uranyl bond which decreases from 3.7 pm for the first ligand to 2.2 pm to the last one. For each species the uranyl bond is elongated by about 1 pm due to solvation effects. Also the U-O_c bond of the monoacetate is elongated in solution by 4 pm. As the lengthening of the average U-O_c distance with increasing number of ligands is slightly reduced in solution, the solvation effect for the triacetate on U-O_c turns out to be negative, by 2.5 pm, in contrast to all other parameters inspected. The charge of uranyl in the solvated complexes is very similar to the gas phase, going from 1.02 to 0.47 to -0.02 for uranyl mono-, bi- and tri-acetate, respectively.

As reported earlier,[16] GGA functionals yield uranyl bond lengths slightly longer and U-O_c bond lengths considerably longer, for the triacetate by up to 8 pm in the gas phase and in solution, compared to the present LDA results (Table 1).

Our results are in good agreement with an extended x-ray absorption fine structure spectroscopy (EXAFS) determination of U=O_t and U-O_c for uranyl triacetate.[10] Another EXAFS investigation of the same species has been interpreted to show two bidentate and one monodentate acetate ligand.[19] As the values of that latter study, U=O_t = 178±1 pm, the average equatorial U-O distance of 243±2 pm, and U-C = 287 pm, also are compatible with our results, this structure variant of uranyl triacetate needs to be taken into account.

The frequency of the symmetric uranyl stretching mode of uranyl triacetate, calculated at 810 cm^{-1}, agrees with the experimental determination[18] of 823 cm^{-1} better than the result for the diacetate of 853 cm^{-1}. Jones et al. reported vibrational modes for the carboxyl group in solid $Na[UO_2(OOCCH_3)_3]$.[20] For bidentate acetate ligand coordination, they assigned a mode of 1537 cm^{-1} to $\nu(CO_2)_{as}$ and a mode of 1472 cm^{-1} to $\nu(CO_2)_s$. Our results of 1535 cm^{-1} and 1479 cm^{-1} for the corresponding vibrations are in surprisingly good agreement, which must be regarded as somewhat fortuitous because the calculated triacetate complex is compared to a compound in the solid state.

Binding energies of acetate ligands to uranyl have been calculated according to the following equations,

$[UO_2]^{2+} + n\,(OOCCH_3)^- \rightarrow [UO_2(OOCCH_3)_n]^{2-n}$ (1)

$[UO_2(OOCCH_3)_{n-1}]^{3-n} + OOCCH_3^- \rightarrow [UO_2(OOCCH_3)_n]^{2-n}$ (2)

where Eq. (1) yields the average binding energy per ligand and Eq. (2) the binding energy per ligand when consecutively added to uranyl. The corresponding results are collected in Table 2. In the gas phase the average binding energy per ligand decreases strongly from about 1600 kJ/mol to 900 kJ/mol, on going from the mono- to the triacetate. These large binding energies are due to the strong electrostatic attraction of the anionic ligands to the uranyl cation. Even the addition of the third acetate ligand to the diacetate is exothermic, by 259 kJ/mol, although the diacetate is not charged. Earlier B3LYP/PP calculations[8] showed slightly lower binding energies, by up to 50 kJ/mol for the monoacetate. This is in contrast to slightly shorter U-ligand bonds calculated in that study (Table 1). Solvation considerably stabilizes the uranyl ion and charged species, leading to much smaller ligand binding energies (Table 2). For uranyl triacetate we calculated an average binding energy of 263 kJ/mol, which amounts to about one third of the value in the gas phase. Nevertheless, also in solution the addition of the third acetate ligand is exothermic, but only by 165 kJ/mol.

We have carried out relativistic density functional calculations for the uranyl acetates $[UO_2(OOCCH_3)_n]^{2-n}$, n = 1–3. For uranyl triacetate, good agreement with experimental results has been achieved for geometry parameters and the symmetric uranyl stretching vibration. While solvation often leads to an elongation of ionic bonds due to screening effects, an opposite result was calculated for the uranyl-acetate bond in the triacetate. This effect can be traced back to a slightly smaller increase of U-ligand bond lengths with growing number of ligands in solution compared to the gas phase. Earlier calculations employing pseudopotentials yield marginally shorter bond lengths but slightly lower ligand binding energies, nevertheless, in good agreement with our all-electron scalar-relativistic calculations. As uranyl acetate is an important benchmark system, further studies are desirable; they shall include explicit modelling of the first solvation shell as well as an investigation of different coordination modes of acetate ligands.

This work has been supported by the Bundesministerium für Wirtschaft und Arbeit, Germany (Grant 02E10186), and Fonds der Chemischen Industrie (Germany).

References

[1] M. Dozol, R. Hagemann, Pure and Appl. Chem. **65** (1993), 1081–1102.
[2] K. L. Nash, J. M. Cleveland, T. F. Rees, J. Environ. Radioact. **7** (1988), 131-157.
[3] K. Schmeide, S. Sachs, M. Bubner, T. Reich, K. H. Heise, G. Bernhard, Inorg. Chim. Acta **351** (2003), 133-140.
[4] E. H. Bailey, J. F. Mosselmans, and P. F. Schofield, Geochim. et Cosmochim. Acta **68** (2004), 1711-1722.
[5] M. Gál, P.L. Goggin, J. Mink, Spectrochim. Acta **48**A (1992), 121-132.
[6] V. Vallet , H. Moll, U. Wahlgren, Z, Szabó, I. Grenthe, Inorg. Chem. **42** (2003), 1982-1993.
[7] S. Tsuchima, Y. Uchida, T. Reich, Chem. Phys. Letters **357** (2002), 73-77.
[8] W. A. de Jong, E. Aprà, T. L. Windus, J. A. Nichols, R. J. Harrison, K. E. Gutowski, D. A. Dixon, J. Phys. Chem. A **109** (2005), 11568-11577.
[9] L. Rao, P.L. Zanonato, P. Di Bernardo, J. Nucl. Radiochem. Sciences **6** (2005), 31-37.
[10] H. Nitsche, R. J. Silva, V. Brendler, G. Geipel, T. Reich, Y. A. Teterin, M. Thieme, L. Baraniak, G. Bernhard, in: Actinide Speciation in High Ionic Strenght Media, D. T. Reed, S. B. Clark, L. Rao, Eds.; Kluwer Academic/Plenum Publishers: New York (1999), 11-38.
[11] N. Rösch, S. Krüger, M. Mayer, V. A. Nasluzov, in Recent Developments and Applications of Modern Density Functional Theory, J. Seminario, Ed., Theoretical and Computational Chemistry serires vol. 4, Elsevier, Amsterdam (1996), 497-566.
[12] M. Fuchs, A. Shor, N. Rösch, Int. J. Quantum Chem. **86** (2002), 487-501.
[13] A. Klamt, G. J. Schüürmann, J. Chem. Soc., Perkin Trans. **2** (1993), 799-805.

P12.

ETUDE DE COMPORTEMENT DE LA LONGUEUR DE LOCALISATION DES SYSTEMES A 2D

M. Djelloul[1], N. Zekri and A. Djeraba

[1]Laboratoire d'Etude physique des Matériaux (LEPM), Département de Physique, Faculté des Sciences, Université des Sciences et de la Technologie d'Oran M.Boudiaf, BP 1505 El-M'naouer 31045 Oran, Algérie.

Tél-Fax : +213 41 56 03 53, E-mail : djelloul_mokhtar@yahoo.fr

Dans ce travail nous avons utilisé le modèle d'Anderson (Tight-binding) à l'aide de la méthode de la matrice de transfert (MMT) pour examiner les effets du désordre pour différentes énergies et tailles du système. Ceci afin de voir le comportement de la longueur de localisation d'un système bidimensionnel sans interactions en présence d'un désordre diagonal.

Quand le désordre est introduit dans les systèmes ordonnés la symétrie du réseau est brisée et le théorème de Bloch [1] n'est plus valable. La fonction d'onde doit être calculée pour plusieurs échantillons et les quantités physiques sont évaluées en prenant les moyennes.

Anderson [2] montra que la présence du désordre dans un système électronique conduit à la présence d'états énergétiques localisés, c'est-à-dire la fonction d'onde des états est restreinte à une région donnée de l'espace. Il existe un désordre critique au-delà duquel tous les états deviennent localisés. D'après la théorie d'échelle, a une et deux dimensions, pour le moindre désordre tous les états sont la localisés; où, d'après Mott ces systèmes sont des isolants. Dans ce cas les particules sont piégées dans des régions bien déterminées et la probabilité de les trouver en dehors décroît à 1D exponentiellement en s'éloignement de ces régions (états fortement localisés : $\psi(x) \approx \exp(-L/\xi)$ où ξ est la longueur de localisation), alors qu'à 2D, cette probabilité décroît en puissance $\psi(x) \approx L^{-\alpha}$ (états faiblement localisés).

Dans ce travail nous étudions l'effet du désordre diagonal sur la nature des états. La partie 2 sera consacrée à la description du modèle et de la méthode utilisés en donnant la définition de l'exposant de Lyapunov. Dans la partie 3 nous présentons les résultats obtenus et particulièrement l'effet du désordre sur le minimum de l'exposant de Lyapunov qui représente l'inverse de la longueur de localisation λ du système pour différentes énergies et tailles du système, finalement nous concluons dans la partie 4.

Le modèle d'Anderson est décrit par l'hamiltonien des liaisons fortes :

$$H = \sum_i \varepsilon_i |i\rangle\langle i| + \sum_{i,j} t_{ij} |i\rangle\langle j| \qquad (1)$$

Les sites (i,j) forment un réseau de taille $N = L \times L$, ε_i sont les énergies de sites, sont distribuées aléatoirement sur $[-W/2, W/2]$ où W est le degré du désordre diagonal.

Les t_{ij} sont les termes d'échange (énergies cinétiques) distribués aléatoirement sur $[c/w/2, c+w/2]$ où c et w sont le degré et le centre du désordre non diagonal respectivement.

Notre approche numérique a ce modèle est basé sur la récurrence de l'équation de Schrödinger correspond à l'hamiltonien (1), ceci fournit le point de départ la méthode de la matrice de transfert

(TMM) en prenant les conditions aux limites périodiques dans la direction transversale du système.

En utilisant la méthode de la matrice de transfert, nous avons calculé la longueur de localisation d'un système quasi 1D de taille M en présence d'un désordre diagonal W (c=1,2 et w=0), avec un nombre d'itérations de 50000 et une précision de 1%.

La figure2 montre le comportement de la longueur de localisation ξ en fonction du désordre diagonal W pour deux tailles de systèmes M=20 figure2 (a) et M=32 figure2 (b) aux énergies E=0 , +1,+2, nous remarquons que ξ décroît quand le désordre W augmente pour les deux tailles ,ayant des valeurs plus grandes que la taille du système ce qui caractérise un état étendu ceci pour $W \leq 2$ .Au delà de cette valeur ξ devient plus petite que la taille du système ce qui caractérise un état localisé . Notons qu'à l'énergie E=1 et W=1 pour M=20,32 la longueur de localisation ξ >M.

Dans la figure3, nous voyons l'effet du désordre non diagonale c en plus du désordre diagonal W sur ξ , on remarque que pour M=20 figure3 (a) et M=32 figure3(b) à l'énergie E=0 la longueur de localisation ξ pour c=2 est supérieur à ξ pour c=1, donc quand le centre du désordre non diagonal (c'est-à-dire l'énergie de saut entres sites voisins) augmente et en présence d'un désordre diagonal (W faible) on a un système ordonné avec ξ >> M.

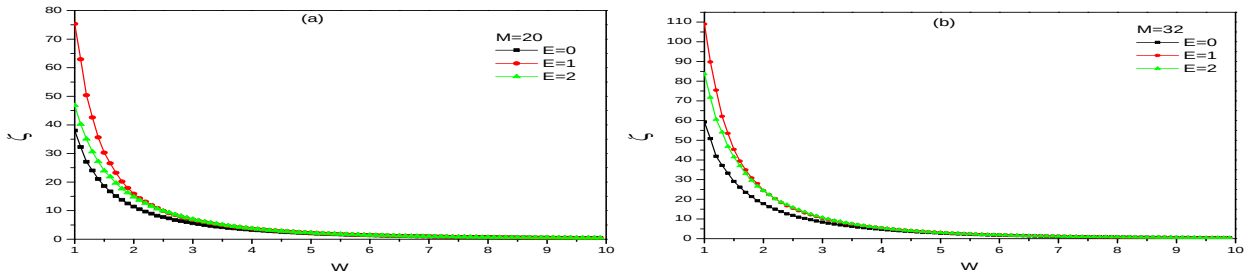

Fig.2 . Longueur de localisation ζ en fonction du désordre diagonal w (tij=1) pour la taille du système M=20 (a) et M=32(b) aux énergies E=0, 1,2

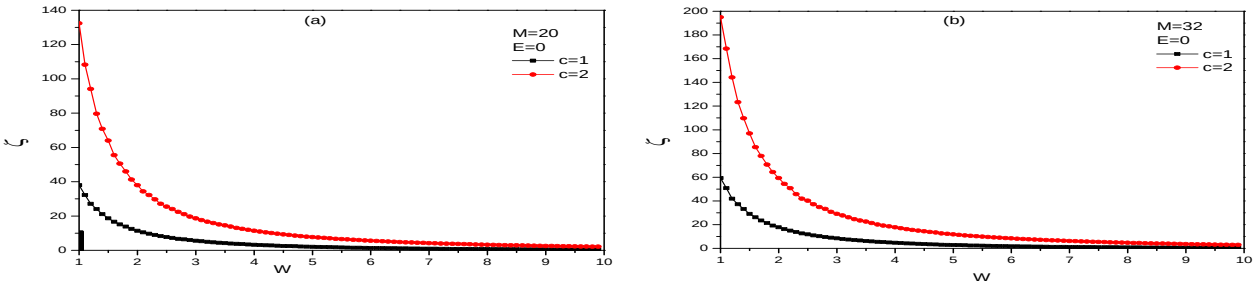

Fig. 3. Longueur de localisation ζ en fonction du désordre diagonal w pour la taille du système M=20 (a) et M=32 (b) à l'énergie E=0 avec tij=1,2

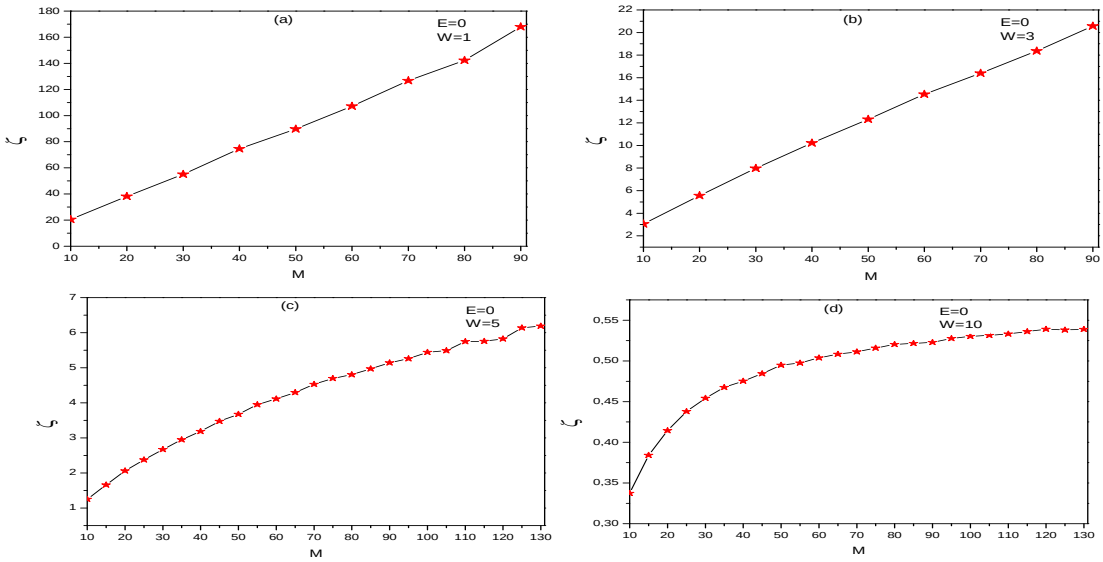

Fig. 4. Longueur de localisation ζ en fonction de la taille du système M pour un désordre diagonal W=1(a), W=3 (b), W=5 (c), W=10 (d) à l'énergie E=0

La figure4 montre l'effet de la taille du système M pour un désordre W croissant (c=1) sur ξ à l'énergie E=0, on remarque que ξ augmente quand la taille du système devient grande ceci pour de faible valeurs de W (W=1) mais ξ diminue quand le désordre est fort.

Notre étude nous a permis de voir que les états d'un système 2D en présence d'un désordre diagonal sont délocalisés pour un faible désordre et localisés pour un désordre fort contrairement aux prédictions de la théorie d'échelle. Notons que les résultats trouvés ne présente pas un comportement particulier pour une certaine valeur du désordre c'est-à-dire l'existence d'un désordre critique pour une transition métal isolant proprement dite mais plutôt une délocalisation des états pour des désordres faibles ceci bien sure en comparant la longueur de localisation à la taille du système.

References:

[1] F.Bloch:Z.Phys. **52**, 555 (1928).
[2] P.W.Anderson: Phys.Rev. **109**, 1492 (1958).
[3] E.Abrahams, P.W.Anderson, D.C.Licciardello et Ramakrishnan: Phys.Rev.Lett. **42**, 673 (1979).
[4] K.Slevin et Y.Asada :Phys.Rev.B **70**, 054201 (2004).
[5] A.Mackinnon et B.Kramer: Z.Phys.B-Condensed Matter, **53**, 1 (1983).

P13.

POLY (METHACRYLIC ACID-g-ETHYLENE GLYCOL) HYDROGELS:

SYNTHESIS AND CHARACTERIZATION

A.FASLA[1,2,3], Z.SEGHIER[1], S.OULD KADA[1] and A. Périchaud[3]

[1]Macromolecular Physical Chemistry Laboratory, Faculty of Sciences,
University of Oran, BP1524, El Mnaouer 31000, Oran, Algeria Email: afasla2005@yahoo.fr
[2]Department of Industrial Chemistry, Faculty of Sciences, Sciences and Technology University of Oran, BP1505, El Mnaouer, Oran, Algeria
[3]Macromolecular Chemistry Laboratory, University of Provence, Case55,
[3]PI.V.Hugo, 13331, Cedex 03, Marseille, France

In recent years, considerable efforts have been made to use environmentally or physiologically responsive hydrogels for biochemical and biomedical applications (carriers for insulin to diabetic patients [1-3]. This process is shown in figure 1) . The complexes of poly (MAA-g-EG) hydrgels are prepared by polycondensation in acid medium.

Initially the polymethacrylic acid were prepared by free-radical polymerization, then added the polyethylene glycol with a different molecular weights. Molecular and structural changes of the P(MAA-g-EG) hydrogels were investigated in their hydrated state using the ATR-FTIR spectroscopy and potentiometry studies identified the formation of interpolymer complexes at low pH. The electrostatique repulsion are not affected by the molecular weights of graft PEG in the hydrogel [4].

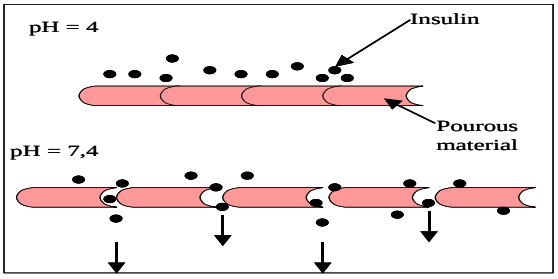

Fig. 1. Delevering insulin by molecular gates with environment changes [5]

We are grateful to Professor Kadjima Munenski (LCO, university of Tlemcen, Algeria) and Dr Amine Addou (LCP, university of Oran, Algeria) for the FTIR analysis of hydrogels.

References

[1] K.Bumsang, A.N.Peppas, Polymer 44 (2003) 3701–3707.
[2] C.L.Bell, A.N.Peppas, Advenced Polymer Science 122 (1995), 125-75.
[3] A.M.Lowman, A.N Peppas, Journal of Biomaterials Science, Polymer Edition 10 (1990), 999-1009.
[4] B.Kim, A.N. Peppas, Polymer 44 (2003) 3708-3710.
[5] C.M.Dorski, F.J.Doyle, A.N.Peppas, Polymer Materials Science Engineering Proceed 76 (1997), 281–282.

P14.

Reversible Transformation between Acetaldehyde and Cyclic Trimer

At Highly Selectivity

I. Safir[1], I.Mrah[2], N.Salhi[2] and M. Belbachir[2]

[1]Laboratoire de Chimie des polymères Département de Chimie ; Faculté des Sciences B.P. 1524 Menaouar. [3]1000 Oran – Algérie
[2]Laboratoire de Physique des Couches Minces et Matériaux pour l'Electronique Département de PhysiqueFaculté des Sciences B.P. 1524 Menaouar. 31000 Oran - Algérie

Acetaldehyde is shown to undergo a reversible Bronsted acid-catalyzed cyclotrimerization reaction, with 100% selectivity, at ambient temperature within the Maghnite-$H^+$is a montmorillonite sheet silicate clay which exchanged with proton to produce Maghnite-H^+ , It is shown by in situ ^1H and ^{13}C NMR spectroscopy and other techniques that the cyclic trimer is the only product formed in this reaction. The equilibrium proportions of acetaldehyde and the cyclic trimer at ambient temperature correspond to a conversion greater than 90%. In contrast, in the corresponding acid catalyzed transformation of acetaldehyde in the liquid state, a broad distribution of products is obtained The reversibility of the cyclotrimerization reaction in Maghnite-H^+, a reaction occurs to produce acetaldehyde as the only product with the same equilibrium distribution of the cyclic trimer and acetaldehyde as that obtained from the reaction of acetaldehyde in Maghnite-H^+ The role of Bronsted acid catalysis in the transformation between acetaldehyde and the cyclic trimer in Maghnite-$H^+$is confirmed from the fact that no reaction occurs on adsorption of acetaldehyde within sodium exchanged Maghnite-H^+.

2,4,6-trimethyl-1, 3.5 Trioxane was obtained by cyclotrimerisation of acetaldehyde in the presence of a Bronsted acid, hydrochloric acid, a paratoluènesulfonique room temperature and with the zeolite fererrite Na3Mg2 ($Al_6 Si_{30} O_{72}$) . In this chapter we describe the results obtained in the cyclotrimerisation of acetaldehyde initiated by the maghnite type montmorillonite clay, activated by 0.23 M sulfuric acid, used as a catalyst, and study the effect of different synthesis parameters depending on the performance and mass viscosimetrique.

The polymers obtained were characterized by different methods of analysis: including the RMN 13C-1H NMR, infra red, Viscometry.

It was chosen for the sample ME1 characterization by NMR - ^{1}**H** (300MHz) contained in the table below,t he solvent is chloroform deuterated ($CDCl_3$) .
The analysis by ^1H -NMR indicates the presence of key protons corresponding to paraldehyde

NMR analysis - ^{13}C:

Displacement of various chemicals present in the carbon paraldehyde.

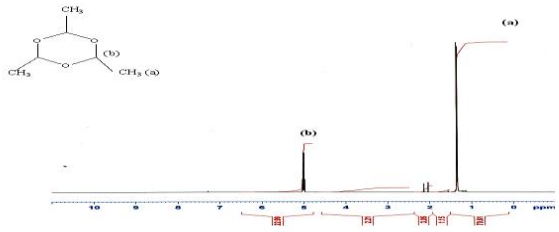

Fig. 1. 1H RMN spectrum paraldehyde (solvent CdCl3)

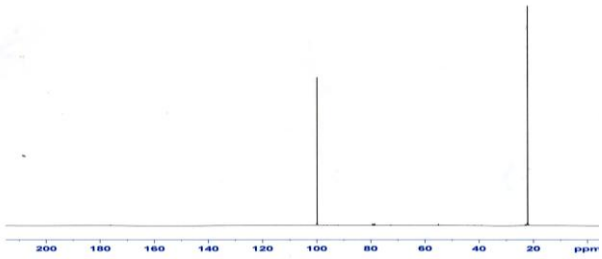

Fig.2. 1H RMN spectrum paraldehyde (solvent CDCl3) to (300MHz)

The formation of 2, 4, 6 - trimethyl - 1, 3, 5 Trioxane was made using the maghnite activated as a catalyst, monomer in the presence of the acetic aldehyde. The study of cyclotrimerisation of acetaldehyde reached the following conclusions: The cyclotrimerisation is possible mass and solution. Yields of mass reactions are high.

Te yields increase with time, which means that the number of active centers increases over time. The values of the molecular weight viscometric increase as the temperature decreases. This indicates the presence of strong interactions (intracellular compounds).

The performance variation depending on the quantity of catalyst maghnite - H + undergoes two phenomena:

The yield increases with increasing the quantity of catalyst to a point where performance is inversely proportional to increases in the amount of catalyst maghnite - H +.

Aprotiques apolar solvents, which are medium dielectric constants promote cyclotrimerisation - The kinetic study of acetaldehyde - Maghnite H + shows that the number of active centers increases over time. The existence of transfer reaction.

P15.

Optical and thermoluminescence properties of chromium Cr in magnesium oxide MgO

A. Kadari[1] and D. Kadri[1]

[1] Department of Physics, Electronic Microscopy and Materials Science laboratory (L.M.E.S.M)
Sciences and Technology University of Oran Mohamed Boudiaf (USTO), BP 1505 M'NAOUAR Oran, 31000, Algeria, kadariahmed_14@yahoo.fr

The presence of the point defects in a material, act directly on the optical and thermoluminescence properties. To control these properties, it is thus necessary to vary the concentration of these impurities (in our study it is the chromium impurity). In this work, we carried out a series of analysis and characterizations of MgO un-doped and MgO doped chromium. This will enable us to analyze the thermoluminescence properties of chromium in magnesium oxide, and its influence on the intrinsic defects (F centers).

The samples analyzed in this work are single crystals MgO and MgO:Cr (MgO doped chromium). The first is polished from Soekawa Chemicals Japan of orientation (001), dimensions are 10×10×1 mm² and mass equalizes with 0.365g. It is known that the MgO crystal have the NaCl structure with a cubic-face-centred (CFC) Bravais lattice with a cubic lattice constant of 4.21 Å. A micro probe analysis of this crystal showed an impurity content of Cr (0.0011%massMgO), Ni, Fe, Ca and K in small quantities. The second sample is MgO doped chromium (MgO:Cr); this last is obtained by thermal diffusion of 31×10^{-4} %MgO (% mass) of chromium in the shape of the powder. This operation requires a thermal diffusion process of 12 hours at the temperature of 1100°C. Firstly the samples were irradiated by an UV Hg source lamp (4.8 eV for 10 minute in air) at low temperature -100°C (170K). Secondly the crystals were thermally heated in a furnace to a temperature between 170 and 500K. These experiments were carried out at liquid nitrogen temperature (73K). [1-2].

In the literature review, we find several works experimental, which identified the emission and absorption bands of defects (impurities), exist in our sample MgO such as Cr, Ni, Fe, K and Ca. The table.1, give the values of absorption and emission energies of chromium impurity in magnesium oxide.

Impurity	Absorption energy (eV)	References	Emission energy (eV)	References
Cr	2.00 2.78	[3-4] [5]	1.70 1.72 1.77	[4-6] [7] [9-3-9]

Table.1. Emission and absorption bands of chromium impurity in MgO

Our experimental results concerning these impurities are in a good agreement with the results advanced in the literature review (table.1). The superposition of absorption coefficients of MgO and MgO:Cr show the increasing in the coefficient absorption following the increasing in the chromium concentration in MgO, this increasing is significant (see Fig.1).

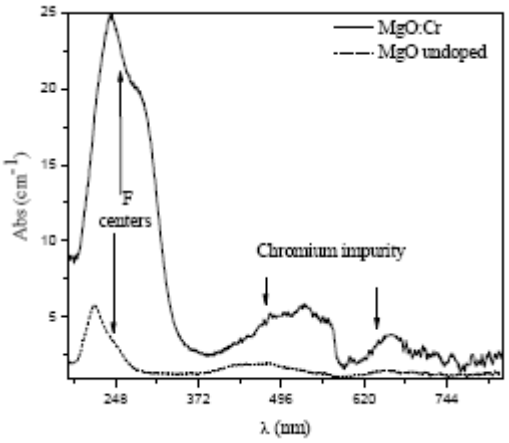

Fig.1. Optical absorption spectrum in MgO un-doped (….) and MgO doped chromium (----)

The chromium Cr can be detected in MgO un-doped even in very weak quantity. It has a band of emission made up of a line duplicated around 720 nm (1.27 eV). The deconvolution of the two spectra in Fig.2 (a) is represented in Fig.2 (b). This figure shows the appearance of three bands around 698, 720 and 745 nm. The band 720 nm (1.72 eV) is attributed to the Cr3+ ions in cubic sites and that the tow other peaks correspond to the vibrations sides bands.

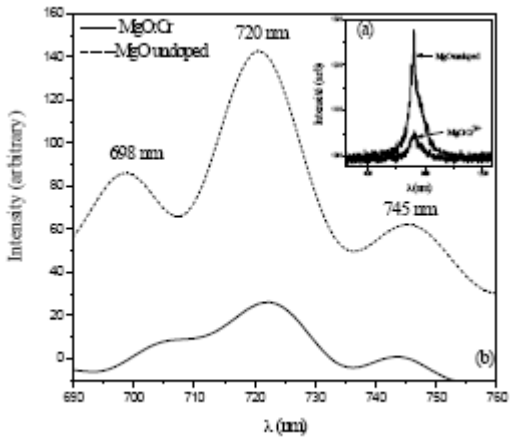

Fig.2. Sub region 690-760 deconvolution of the spectrum Fig.2. (a): MgO un-doped (…) and MgO:Cr (---)

After the thermal diffusion of 31×10-4 %MgO of chromium in MgO, the light intensity decreased as the concentrations of chromium increased. This decreasing is represented by I-TL curves Fig.3.

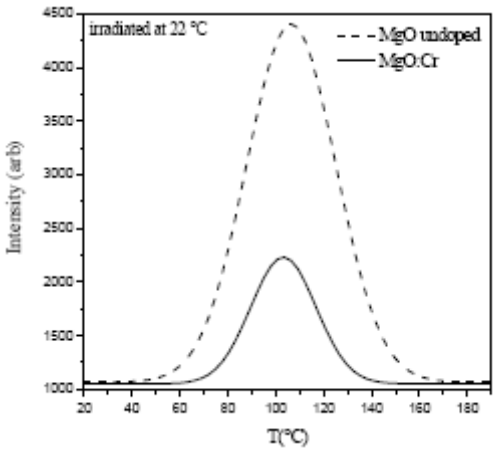

Fig.3. TL intensities curves of chromium impurity in: MgO un-doped (….) and MgO:Cr (----)

In our experimental work the decreasing in the luminescence intensity (I-TL intensity) with the increasing in the chromium concentration (Cr %) can be explained by the considerable increasing in the oxygen vacancies (see Fig.1). The absorption coefficient of chromium impurity has increased by 4 times, whereas the absorption coefficient of F and F+ centers has increased by 8 times. This doubling in the absorption coefficient justifies the assumption that the introduction of chromium Cr into magnesium oxide supported the creation of the oxygen vacancies (F and F+ centers). Nevertheless the assumption of the formation of chromium oxides CrxOy [10] (the reconciliation between defects) rest probable.

References

[1] D. Kadri and A. Mokaddem, J. of Applied Sci., **5** (2005), 1345-1349.
[2] D. Kadri, S. Hiadsi and S. Hamzaoui, J of Applied Sci **7** (6) (2007), 810-814.
[3] L. N. Kantorovich and A. L. Shluger, Phys. Rev. B. Vol **63**, (2001), 184111
[4] M.Jimenez de Castro. J. Phys. C: Solid State Phys. **18**, (1985), 4863-4872
[5] J. P. Larkin and G. F. Imbusch, Phys. Rev. B. (1973), Vol **7**, No 1
[6] Y. Kawaguchi, Solid State Com. **117** (2001) p17-20
[7] P. R. Flecher and C. Leach, J of European Ceramic Soc (1995), pp. 15 859-865.
[8] C.C. Chao, J. Phys. Chem. Solids, **32** (1971), 2517-2528
[9] T. Karner, S. Dogov and N. Mironova, Radition Measurements **33** (2001) 625-628.
[10] Jian-Cheng Chen, Spectroscopic Study on the Fluorescence of Cr ions in double-clad Cr:Yag crystal Fiber. These National Sun Yat Sen University.

P16.

Etude d'une plaque composite à matrice organique Époxy/bore

D. kamli[1], D. Hannachi[2] and A. Djebaili[3]

1 laboratoire de chimie et chimie de l'environnement, université de Batna, Algerie, Kamli_dalila@yahoo.fr
2 laboratoire de chimie et chimie de l'environnement, université de Batna, Algerie.
3 laboratoire de chimie et chimie de l'environnement, université de Batna, Algerie.

Les résines époxy possèdent de meilleures propriétés mécaniques,chimique et électrique ,mais leur coût est supérieure ,employées à grande échelle en aéraulique ,ces résine permettent de fabriquer des matériaux composites dont les propriétés mécanique sont bonnes et qu'on peut utiliser jusqu'à 150 ou 200°C.. Dans ce travail, on va présenter un exemple de calcule des déformations et contraintes d'une plaque stratifiée. Considérons un matériau composites multicouche [+45°/0°/-45°] constitué de trois plis a base d'une matrice époxy.

Pour ce matériau composite le plis à 45° présente une épaisseur de 2mm, le plis central présente une épaisseur de 4mm, la plaque et soumise suivant son axe principal à une sollicitation de 1000N/mm. Le calcul des contraintes apparaissant dans la plaque Se fera suivant le schéma suivant :

-calcul des matrices de rigidité de chaque pli dans le repère du stratifié,

-calcul des matrices A, B et D du stratifié.

-calcul des contraintes.

Caractéristique mécanique	**Matériaux bore/époxy**
Teneur en volume de renfort %	0.5
Masse volumique ρ (g/cm^3)	2.1
Module d'Young sens long E_1 (Mpa)	210000
Module d'Young sens transverse E_2 (Mpa)	19000
Module de cisaillement G_{12} (Mpa)	4800
Coefficient de poisson ν_{12}	0.21

Tableau. 1. .caractéristique mécanique du composites utilisé

La matrice de rigidité des couche dans leur repère propre est définis par :

$$\begin{Bmatrix}\sigma_1\\ \sigma_2\\ \tau_{12}\end{Bmatrix} = \begin{bmatrix}Q_{11} & Q_{12} & 0\\ Q_{21} & Q_{22} & 0\\ 0 & 0 & Q_{66}\end{bmatrix}\begin{Bmatrix}\varepsilon_1\\ \varepsilon_2\\ \gamma_{12}\end{Bmatrix}$$

Avec :

$$Q_{11}=\frac{E_1}{1-\nu_{12}\nu_{21}}\ ; Q_{22}=\frac{E_2}{1-\nu_{12}\nu_{21}}\ ;$$

$$Q_{12}=\frac{\nu_{12}E_2}{1-\nu_{12}\nu_{21}}\ =\ \frac{\nu_{21}E_1}{1-\nu_{12}\nu_{21}}\ ; Q_{66}=G_{12}.$$

Et : $\frac{\nu_{12}}{E_1}=\frac{\nu_{21}}{E_2}$ donc : $\nu_{21}= 0.019$

Donc : la matrice de rigidité des couche dans leur repère propre s'exprime, en gigapascals (GPa), par :

$$\left[C_{ij}\right]=\begin{bmatrix}210.84 & 4.00 & 0\\ 4.00 & 19.08 & 0\\ 0 & 0 & 4.8\end{bmatrix}$$

Les matrices de rigidité des couches dans le repère du stratifié s'obtiennent par application directe des formules :

	θ =45°	θ =0°	θ =-45°
C_{11}	64.28	210.84	64.28
C_{22}	64.28	19.08	64.28
C_{12}	54.68	4.00	54.68
C_{66}	55.48	4.80	55.48
C_{16}	47.94	0	-48.04
C_{26}	47.94	0	-47.94

Tableau 2. Les valeurs de la matrice de rigidité des couches dans le repère du stratif

$C_{11} = Q_{11}\cos^4 + 2(Q_{12} + 2Q_{66})\sin^2\theta\cos^2\theta + Q_{22}\sin^4\theta$

$C_{12} = (Q_{11} + Q_{22} - 4_{66})\sin^2\theta\cos^2\theta + Q_{12}(\sin^4\theta + \cos^4\theta)$

$C_{22} = Q_{11}\sin^4\theta + 2(Q_{12} + 2Q_{66})\sin^2\theta\cos^2\theta + Q_{22}\cos^4\theta$

$C_{16} = (Q_{11} - Q_{12} - 2_{66})\sin\theta\cos^3\theta + (Q_{12} - Q_{22} + 2Q_{66})\sin^3\theta\cos\theta$

$C_{26} = (Q_{11} - Q_{12} - 2Q_{66})\sin^3\theta\cos\theta + (Q_{12} - Q_{22} + 2Q_{66})\sin\theta\cos^3\theta$

$C_{66} = (Q_{11} + Q_{22} - 2Q_{12} - 2Q_{66})\sin^2\theta\cos^2\theta + Q_{66}(\sin^4\theta + \cos^4)\theta$

Les valeurs sont exprimées en GPa dans le tableau 2 :

Le plan moyen du multicouche ne comporte donc que trois déformations :

-un allongement relatif de 0.11% suivant la direction de la charge.Une contraction relative de -0.005% suivant la direction perpendiculaire à la charge.

Une torsion de surface caractérisée par un rayon de torsion de 5000mm, cette torsion est due au phénomène de couplage extension flexion. Dans la couche à 45° les contraintes maximales induites dans le monocouche composites (z = -4mm). Dans la couche à -45° les contraintes maximales induites dans le monocouche composites (z = 4mm).

Références

[1] O.O.Ochoa and J.N.Reddy, Finite element analysis of composite laminate, Kluer academic publishers.
[2] Pierre ODRU, calcul et conception des structures composites, Technique de l'ingénieur, traité plastiques et composites A 7792.
[3] Valery V.Vasiliev, 2001, Mechanics and analysis of composite materials. Elsevier.

P17.

Etude ab initio des propriétés électroniques des composés base de nitrures de terres rares EuN et TbN : application de LDA et LDA+U

N. Kanoun-Bouayed[1] et A. E. Merad[1,2]

[1] Equipe Physique de l'Etat Solide, LPT, Département de Physique, Faculté des Sciences Université de Tlemcen, Algérie
[2] ICTP, Strada Costiera 11 34014 Trieste Italy.a na_kanounbouayed@yahoo.fr

Les nitrures de terres rares couvrent une large gamme de comportements : métallique ou semimetallique au semi-conducteur. Leurs propriétés magnétiques sont particulièrement intéressantes dues à leurs orbitales 4f non remplies et qui sont fortement localisées. L'apparition du domaine du spintronics a donné un nouvel élan et suscité un grand intérêt pour cette classe de matériaux, notamment pour leurs propriétés magnétiques et électroniques uniques [1,2]. L'arrangement de la classe entière des nitrures de terres rares est essentiel afin de comprendre comment les propriétés désirées peuvent être optimisées.

Nos résultats ont été obtenus en utilisant la méthode tous électrons et à potentiel total à base de la mixture entre les ondes planes augmentées lineairisées et les ondes planes augmentées plus les orbitales locales (FL/APW+lo) avec la théorie de la fonctionnelle de la densité. Cette méthode est implimentée dans le code Wien2k [3]. L'influence du potentiel d'échange et de corrélation a été examinée en utilisant LDA, LDA+U, GGA (PBE et WC), et GGA+U (PBE et WC). Le non-chevauchement des sphéres atomiques est aussi vérifié. En outre, les calculs spin polarisés sont réalisés avec deux différentes densités de spin haut et de spin bas et deux séries d'équations de Kohn-Sham d'une particule simple sont résolus de façon auto-cohérente. Tous nos calculs ont été effectués en distinguant les noyaux de gaz rares des électrons de valence, et par consequent, nous avons considéré la configuration électronique suivante ; [Xe] 4f75s2 pour l'Europium, [Xe] 4f95s2 pour Terbium, et [He] 2s22p3 pour l'Azote. D'après les tests de convergence, qu'il suffit de prendre RKmax égal à 9. Cette valeur représente l'expansion des ondes planes, les fonctions d'ondes de valence à l'intérieur des sphéres sont étendues à lmax = 10. Nous allons prendre aussi le nombre des points spéciaux pris dans la zone de Brillouin irréductible est égal à 20. Cet échantillonnage de la zone de Brillouin assure une précision sur l'énergie totale de 1 (mRyd). Il est important de noter le choix judicieux du rapport entre les rayons muffin tin de l'atome terre rare et celui de l'azote. Les rayons muffin-tin sont considérés comme égaux à 2.45, 2.4, 1.7 u.a. (unités de Bohr) pour des atomes Eu, Tb et N, respectivement.

Nous avons calculé la structure de bande des composés EuN et TbN dans l'état ferromagnétique en utilisant les approximations LDA et LDA+U. Les figures 1 et 2 représentent les structures de bande de spin haut (spin majoritaire) et spin bas (spin minoritaire), suivant les directions de hautes symétries de la zone de Brillouin. Comme on peut le voir sur la figure 1, l'application de l'approche LDA + U apporte des modifications aux niveaux des états f dans la structure de bande par rapport à la LDA pour EuN, notamment sur les niveaux d'énergies des états 4f occupés et inoccupés. En effet, dans la structure de bande calculée par la LDA (voir Fig 1), les états Eu-4f occupés sont placés à environ 0.4

eV au-dessous du niveau de Fermi (EF) en hybridation avec les états N-2p, alors que les états 4f inoccupés sont situés près de 4 eV au-dessus du EF, en hybridation avec les états de Eu-5d. D'autre part, le calcul de LDA ne donne pas les énergies de liaison correctes des niveaux d'énergies de 4f. Ce problème est résolu par l'application de la LDA+U (Fig.1). En fait, les états 4f inoccupés demeurent autour 9 eV au-dessus du EF, et les états 4f occupés sont près de 1.44 eV au-dessous du niveau de Fermi. Ce résultat est en bon accord avec les récents calculs théoriques [4].

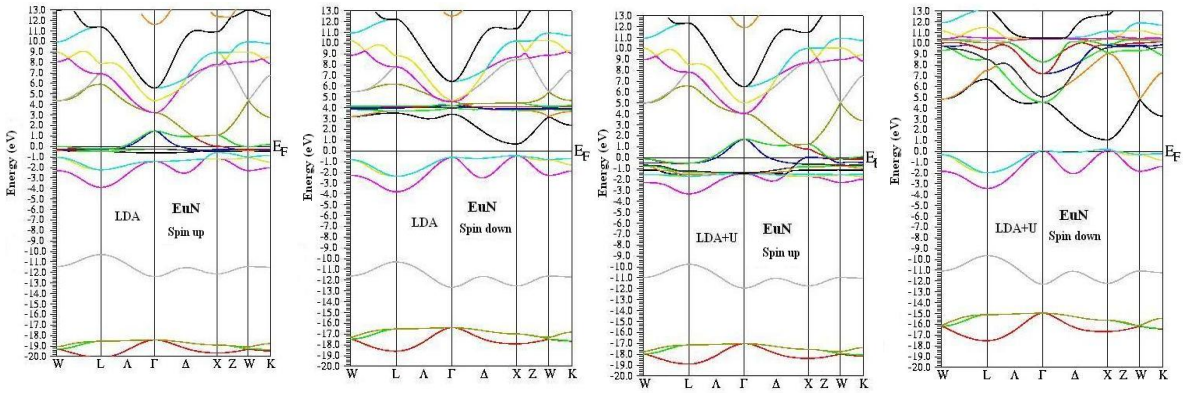

Fig. 1. Structure de bande des spins majoritaires et minoritaires du EuN avec LDA et LDA+U

Comme nous pouvons le voir sur les figures 2, les structures de bande du TbN sont semblables à ceux du EuN. Les grandes différences se situent sur les positions des états 4f occupés et inoccupés trouvés par les calculs LDA+U et de LDA. En effet, dans le calculs LDA, les états Tb-4f occupés sont placés aux environs de 4.4 eV au-dessous du niveau de Fermi, alors que les états Tb-4f inoccupés sont situés près de 0.22 eV au-dessus du EF . Pour les calculs avec LDA+U, les états 4f inoccupés se positionnent autour 5.8 eV au-dessus du EF, et les états 4f occupés sont près de 7 eV au-dessous du EF . Nous pouvons ainsi déduire à partir des structures de bande que les composés EuN et TbN sont semi métalliques avec des énergies de gap égales à 0.9 et 0.37 eV, respectivement, dans la structure de bande des spins minoritaires.

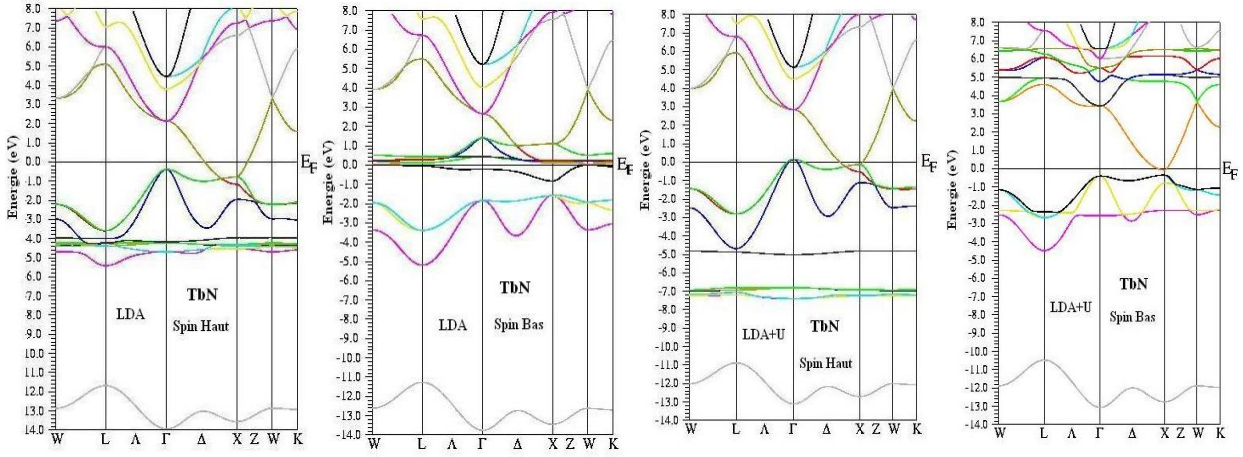

Fig. 2. Structure de bande des spins majoritaires et minoritaires du TbN avec LDA et LDA+U

Dans ce travail, nous nous sommes intéressés à des systèmes de plus en plus controversés, du fait de l'existence des états f dans leurs configurations électroniques (partiellement remplies), les composés à base de nitrures de terres rares EuN et TbN. Nous avons discuté les propriétés structurales et électroniques de ces deux systèmes en fonction de l'approximation quantique utilisée sur le potentiel d'échange et de corrélations: l'approximation de la densité locale (LDA) où/or l'approximation du gradient généralisé (GGA) et LDA+U. L'application de la LDA+U apporte des améliorations considérables à l'interprétation des propriétés électroniques contrairement à la LDA qui n'arrive pas à reproduire la nature électronique de ces systèmes. Enfin, le calcul des moments magnétiques (totaux et relatifs à chaque élément) vient conforter la validité de cette approche à ses systèmes.

Références

[1] S. A. Wolf, D. D. Awschalom, R. A. Buhrman, J. M. Daughton, S. von Molnar, M. L. Roukes, A. Y. Chtchelkanova, et D. M. Treger, Science 294, 1488 2001 .

[2] Y. Ohno, D. K. Young, B. Beschoten, H. Ohno, et D. D. Awschalom, Nature London 402, 709 (1999); H. Ohno, Science 291, 840 (2001).

[3] P. Blaha, K. Schwarz, G.K.H. Madsen, D. Kvasnicka, J. Luitz, WIEN2k, An Augmented- Plane-Wave + Local Orbitals Program for Calculating Crystal Properties, (K. Schwarz, Techn Wien, Austria, 2001), ISBN 3-9501031-1-2.

[4] P. Larson and W.R.L. Lambrecht, A. Chantis et M. van Schilfgaarde, Phys. Rev. B 75, 045114 (1993)

P18.

Calculation of the electrons swarm parameters of N_2 by the Monte Carlo method

B. Liani[1], B. Ardjani[1]

[1] Physics department, Sciences faculty, University of Tlemcen, Algeria. benamarxxm@yahoo.fr

The electron swarm parameters of the nitrogen are calculated in the uniform electric field by the Monte Carlo method. Typically, the transport parameters of the electrons are necessary in any modeling in plasma, and they are the subject of progressive interest in the domain of the high voltage insulation. As tool of simulation the Monte Carlo method is used, generally this method is a probabilistic method use random numbers to find deterministic quantities, the detail of the method in the case of plasma modeling is well described in the Ref[1].

Figure 1 shows that the drift velocity increases if the electric field increases, this is normal since the main role of the electric field is to accelerate the longitudinal velocity of the electrons, also when the electrons are more accelerated arrive at sufficient energies to ionize the gas molecules and consequently the ionization coefficient increase if the electric field increases. The validity of using the Monte Carlo method is shown since the results have good agreement with several calculations of Phelps, *al* [2] and Kunhardt, *al* [3]. The validity is also confirmed by the experimental results find by the pulsed Townsend method [4]. Also the drift velocity has about linear increase what show the validity of the law $W_z=\mu_e E$. The ionization coefficient has about exponential increase what show the validity of the semi-empirical equation [5] $\alpha / N = A \cdot \exp\left(-B/\left(E/N\right)\right)$. where A and B are constants characteristic of the gas.

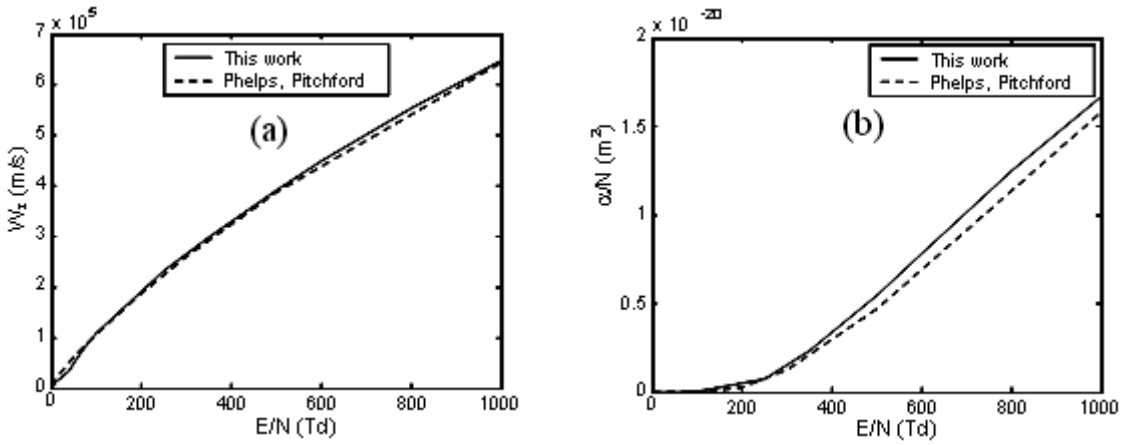

Fig. 1. Electron swarm parameters of the nitrogen (a) drift velocity (b) ionization coefficient

References

[1] Savino Longo Plasma Sources Sci. Technol. **9** (2000) 468–476.
[2] A. V. Phelps and L. C. Pitchford, Phys. Rev. 31, 2932 (1985).
[3] Kunhardt E E, Tzeng Y and Boeuf J P 1986 *Phys. Rev.* A **34** 440–9.

P19.

Route to a correct description of fundamental properties of InN

M. Briki[1], F. Boutaiba[1], A. Zaoui[2] and M. Ferhat[1]

1Département de Physique, Université des Sciences et de la Technologie d'Oran, 31036, mohammed_briki@yahoo.fr,
2L. M. L. (UMR 8107), Polytech'Lille, Université des Sciences et de la Technologie de Lille, Cité Scientifique, Avenue Paul Langevin, 59655 Villeneuve D'Ascq Cedex, France

The main fundamental properties of the cubic InN are studied within the density functional theory.

We used the full-potential augmented plane wave method with two different exchange-correlation potentials, the Perdew-Wang _PW_ and the Engel-Vosko _EV_ approximations, in both cases nonrelativistic and relativistic. We found that the PW and relativistic approximations give a metallic ground state. The use of the EV and nonrelativistic approximations gives, however, a semiconductor phase with a band-gap value of 0.57 eV, which is in fairly good agreement with the recent measurement of 0.61 eV.

The group III-V nitrides AlN, GaN, and InN and theiralloys have recently received big attention for their highefficiency device applications as light emitting diodes (LEDs).[1,2] Among the three materials InN is until now one of the least studied compounds of the III-V nitrides family. This is mainly due to the difficulty in growing high-quality crystals, consequently many of its fundamental parameters are still not well know such as the band gap which is crucial to assess the suitability of indium nitride for various device applications. Earlier measurements established the direct fundamental band gap of wurtzite InN about 1.9 eV.[3] However, recent progress of growth epitaxial hexagonal InN film by molecular beam epitaxy _MBE_ and metal vapor phase epitaxy (MOVPE) has dramatically reduced the band gap of InN to the near infrared value of about 0.7 eV.[4–6] Nevertheless, cubic InN with zinc blende structure is also interesting because it is predicted to possess superior electronic properties for device applications. For instance, the isotropic nature of the zinc blande structure would lower the phonon scattering. Moreover, the cubic InN is expected to have lower band gap energy than the wurtzite phase. Theoretical calculations propose a band gap of 0.6 eV,[7],[8] which would expand the applications of the group III-nitrides more toward the infrared region. These considerations stimulated the research on cubic InN. Recently cubic InN has been grown by MBE with a measured band gap of about 0.61 eV based on photoluminescence experiment.[9] In this letter we present a systematic theoretical study of the fundamental properties of InN in the cubic phase by using the state of the art *ab initio* full potential linearized augmented plane wave method. We use two different exchange-correlation potentials, the Perdew-Wang (PW) and the Engel-Vosko (EV) approximations, both with nonrelativistic and scalar relativistic approximations. The calculations were performed in the framework of density functional theory (DFT). [10] We have employed the full potential linearized augmented plane wave (FLAPW) method as implemented in the WIEN2K code.

[11] The structural parameters were determined using the local density approximation (LDA) based on the Perdew-Wang approximations, [12] in addition to the Engel-Vosvo approximation. [13] We expand the basis function up to *R*MT*K*max=8. The maximum value of partial waves inside atomic sphere is *l*=10. Fully relativistic approximations are used for the core electrons, and scalar relativistic and nonrelativistic approximations are used for valence electrons. Brillouin zone integration is performed on a 8x8x8 Monkhorst-Park mesh, [14] which corresponds to 43 *k* points. Both the *k* points number and the energy cutoff _*R*MT*K*max_ have been tested to be enough for the convergence.

Table I. Structural parameters _lattice constant, bulk modulus, and its pressure derivative_ of cubic InN

	a (Å)	*B (Mbar)*	*B'*
Non-relativistic	4.97	1.48	4.42
Non-relativistic	5.08	1.24	4.60
Scalar relativistic	4.94	1.46	4.98
Scalar relativistic	5.06	1.21	4.63
Theor.	5.00,[a] 4.96,[b]4.98[c]	1.40,[a],1.41[b]	4.38[a],3.75[b]
Exp.	5.00[d]		

[a]Reference 16., [b]Reference 17.

[c]Reference 18., [d]Reference 9.

Table II. Calculated band gaps of cubic InN

	E_g (Γ)	E_g (X)	E_g (L)
Non-relativistic	-0.0023	2.718	3.55
Non-relativistic (EV-	0.573	3.57	4.266
Non-relativistic	-0.184	2.763	3.379
Non-relativistic (EV-	0.364	3.522	3.938
Scalar relativistic	-0.34	2.844	3.112
Scalar relativistic	-0.561	2.90	2.936
Theor.	-0.40,[a]		
Exp.	0.61[e]		

[a]Reference 16., [b]Reference 17. [c]Reference 8., [d]Reference 18. [e]Reference 9.

The calculated structural parameters obtained from a fit to the Murnaghan equation of state [15] are summarized in Table I and compared with previous calculations and experimental data with favorable agreement. Table II gives the calculated band gap of InN with the Perdew-Wang and the Engel-Vosko approximations, and with nonrelativistic and scalar relativistic approximation. In all cases, it is found that the EV approximation increases the band gap from the LDA- GGA-PW (GGA denotes generalized gradient approximation) approximation. However, the decisive correct band of InN is given if nonrelativistic effects are taken into account opening the gap from the LDA-scalar relativistic metallic value of −0.56 eV to the EV value of 0.57 eV. Indeed, relativistic effects are important only for semiconductors with small gap and heaviest atoms like in InAs (Eg=0.4 eV) and InSb (Eg=0.235 eV). Our result support the most recent quasiparticle *GW* calculations of Bechstedt *et al.* [17] and Rinke *et al.* [18] who found, respectively, a band gaps of 0.59 and 0.53 eV. While until now the band gap of InN is not known exactly, our predicted gap of 0.57 eV is in good agreement with the recent experimental value of 0.61 Ev [9]. In Figs. 1 and 2 we present, respectively, the band structure of cubic InN along the high symmetry points of the Brillouin zone, in the GGA-relativistic approximation and the EV with nonrelativistic approximation. The dispersion of the lowest conduction band allows the determination of an effective electron mass m^* near the bottom of the conduction band at Γ point. We derive a value of m^*=0.051, which is in good agreement with the previous calculated values of 0.048 [17] and 0.054. [18] In summary, we have studied the fundamental properties of cubic InN, by using the all-electron FLAPW method. The EV approximation combined with nonrelativistic approximation gives a fundamental band gap of 0.57 eV. This result strongly supports the recent experimental measurement of 0.61 eV.

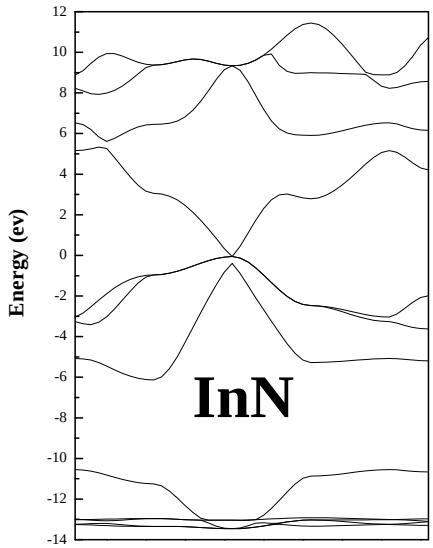

Fig. 1. Band structure of cubic InN in the GGA-Scalar relativistic approximations

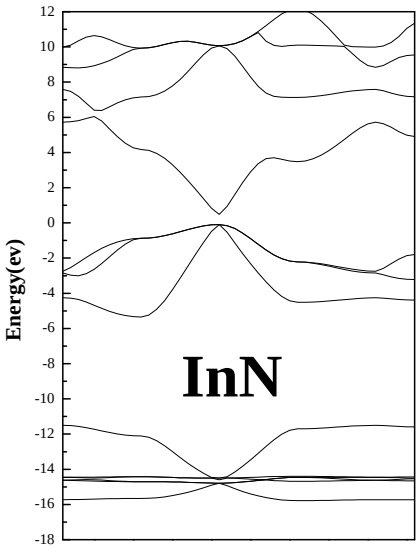

Fig. 2. Band structure of cubic InN in the Engel-Vosko

References

[1] S. Nakamura, M. Senoh, N. Iwasa, and S. Nagahama, Appl. Phys. Lett. 67, 1868 (1995).
[2] S. Nakamura and G. Fasol, The Blue Laser Diode _Springer, Berlin, (1997).
[3] T. L. Tansley and C. P. Foley, J. Appl. Phys. 59, 3241 (1986).
[4]V. Yu Davydov, A. A. Klochikhin, R. P. Seiysan, V. V. Emtsev, S. V. Ivanov, F. Bechstedt, J. Furthmüller, H. Harima, A. V. Mudryi, J. Aderhold, O. Semchinova, and J. Graul, Phys. Status Solidi B 229, R1 (2002).
[5] T. Matsuoka, H. Okamoto, M. Nakao, H. Harima, and E. Kurimoto, Appl. Phys. Lett. 81, 1246 (2002).
[6] J. Wu, W. Walukiewicz, K. M. Yu, J. W. Ager III, E. E. Haller, H. Lu, W. J. Schaff, Y. Saito, and Y. Nanishi, Appl. Phys. Lett. 80, 3967 (2002).
[7] F. Bechstedt, J. Furthmüller, M. Ferhat, L. K. Teles, L. M. R. Scolfaro, J. R. Leite, V. Yu Davydov, O. Amacher, and R. Goldhahn, Phys. Status Solidi A 195, 628 (2002).
[8] A. Qteish, A. I. Al-Sharif, M. Fuchs, M. Scheffler, S. Boeck, and J. Neugebauer, Phys. Rev. B 72, 155317 (2005).
[9] J. Schörmann, D. J. As, K. Lischka, P. Schley, R. Goldhahn, S. F. Li, W. Löffler, M. Hetterich, and H. Kalt, Appl. Phys. Lett. 89 261903 (2006).
[10] P. Hohenberg and W. Kohn, Phys. Rev. 136, 864 (1964).
[11] P. Blaha, K. Schwarz, and J. Luitz, WIEN2K, Vienna, University of Technology 1997 (improved and updated UNIX version of the original copyrighted wien code, which was published by P. Blaha, K. Schwarz, P. Sorantin, and S. B. Trickey, Comput. Phys. Commun. 59, 399 (1990)).
[12] J. P. Perdew and Y. Wang, Phys. Rev. B 45, 13244 (1992).
[13] E. Engel and S. H. Vosko, Phys. Rev. B 47, 13164 (1993.
[14] H. J. Monkhorst and J. D. Park, Phys. Rev. B 13, 5188 (1976).
[15] F. D. Murnaghan, Proc. Natl. Acad. Sci. U.S.A. 30, 244 (1944).
[16] C. Stampfl and C. G. van de Walle, Phys. Rev. B 59, 5521 (1999).
[17] J. Furthmüller, P. H. Hahn, F. Fuchs, and F. Bechstedt, Phys. Rev. B 72, 205106 (2005).
[18] P. Rinke, M. Scheffler, A. Qteish, M. Winkelnkemper, D. Bimberg, and J. Neugebauer, Appl. Phys. Lett. 89, 161919 (2006).

P20.

Extraction des Paramètres d'un Dispositif a Hétérojonction GaSb(n)/GaAlAsSb(p) par des Méthodes de la Littérature après la Quantification des Courants Parasite

K. Mahi[1], K. Zemallach[1], B. Messani[1],

M. Mébarki[1], A. Belasri[1] et H. Aït Kaci[1]

[1] Université des Sciences et de la Technologie d'Oran USTO-MB, Oran, 31000, Algérie.
Université Es Sénia, Oran, 31000, Algérie.

Les paramètres caractéristiques d'un dispositif à jonction p-n, à savoir le coefficient d'idéalité *n* et le courant de saturation *Is*, sont d'une grande importance en se sens où ils donnent une première idée des phénomènes de conduction mis en jeu dans la structure. Ils renseignent aussi sur les performances du dispositif et les possibilités d'optimisation de son fonctionnement. Dans ce travail, nous avons étudie quelques méthodes de la littérature (classique, et Ranuàrez), utilisées pour l'extraction de ces paramètres. Aux faibles polarisations, l'analyse de ces différentes méthodes a montré qu'elles sont, toutes, plus ou moins sensibles aux courants de fuites supplémentaires.

Ces constats nous ont poussés à développer une technique expérimentale simple pour quantifier les courants de fuites et s'en affranchir. Une confrontation des résultats pour *n* et *Is*, obtenus par les méthodes exposées dans ce travail, permettra de trancher sur les résultats et tenter d'exploiter les mesures réalisées sur nos échantillons à hétérojonction p-n. Ce travail préliminaire permettra d'identifier plus facilement les processus de conduction dans notre échantillon de laboratoire.

A partir de la caractéristique courant tension directe de la structure GaSb(p)/ GaAlAsSb(n). Nous avons évalués, par ces méthodes, les paramètres caractéristiques des diodes à géométrie mesa. A peu de choses près, les résultats obtenus pour le coefficient d'idéalité sont très voisins. Ces valeurs proches de 2 suggèrent un mécanisme de recombinaison sous polarisation directe. Les courants de saturations, évalués par la méthode classique sont élevés et peu fiables (entre *1 μA* et *10 μA*). La méthode de Ranuarez donne des résultats raisonnables, entre *200 nA* et *450 nA*.

Références

[1] J. C. Ranuarez , F. J. Garcia Sanchez, A. Ortiz-Conde Procedure for determining diode parameters at very low forward voltage.Sol. Stat. Electron. 43(1999), 2129-2133.

[2] J. H. WernerSchottky Barrier and pn-Junction I/V Plots-Small Signal Evaluation. Appl. Phys. A 47 (1988), 291-300.

P21.

SYNTHESE ET CARACTERISATIONS DU POLYINDANE OBTENU PAR LA POLYMERISATION DE L'INDENE EN UTILISANT LA MAGHNITECOMME CATALYSEUR

MARREF Mohamed [1] , MEGHABAR Rachid [2] , BELBACHIR Mohamed [2]

[1] Département de Chimie Industrielle, faculté des sciences, Université des Sciences et de la Technologie d'Oran, BP1505, Bir El Jir, Oran

[2] Département de Chimie, Faculté des Sciences, Université d'Oran Es-sénia

L'indène est un monomère benzocyclique insaturé. Les polyindanes obtenus par la polymérisation cationique de l'indène, en utilisant la Maghnite-H comme catalyseur sont des polymères thermoplastiques conducteurs. Ces matériaux sont utilisés dans les circuits intégrés notamment pour la protection des puces. La maghnite utilisé comme catalyseur est une argile locale extraite d'un gisement près de Maghnia, cette argile est non polluante et non toxique, et son exploitation est peu coûteuse.Dans ce travail, nous avons décrit la synthèse du matériau (Polyindane) catalysée par la Maghnite-H, ainsi que les caractéristiques et les résultats des analyses du polyindane tels que ; RMN 1H , DSC, IR et la GPC (1-2).De même, nous avons étudié en détail l'effet de la quantité de l'amorceur (Maghnite-H) ; du solvant et de la température sur le taux de conversion du matériau obtenu (Polyindane)

References

[1] O. Nuyken , M. B. Leitner , G. Maier, Makromol. Chem. **192**, 307 (1991)

[2] O. Nuyken , M. B. Leitner , G. Maier, Makromol. Chem. 193 , 487 (1992)

P22.

Lattice dynamics study of bismuth III-V compounds

H. M. A. Mazouz[1], A. Belabbes[1], A. Zaoui[2] and M. Ferhat[1]

[1] Département de Physique, Université des Sciences et de la Technologie d'Oran, Oran, Alegria.
[2] LML (UMR 8107), Polytech'Lille, Université des Sciences et de la Technologie *de Lille, Cité Scientifique, Avenue Paul Langevin, 59655 Villeneuve D'Ascq Cedex, France*

We present first-principles calculations of the structural and lattice-dynamical properties for cubic bismuth III–V compounds: BBi, AlBi and GaBi. The ground-state properties, i.e., the lattice constant and the bulk modulus, are calculated using a plane wave pseudopotential method within density functional theory. A linear-response approach to density functional theory is used to derive the phonon frequencies. The effect of pressure on the dynamical charges and the longitudinal optical–transverse optical splitting is also examined.

Among the III–V semiconductors the bismuth: BBi, AlBi, GaBi, and InBi as well as their alloys have attracted both scientific and technological interest in recent years. It is expected that most of the III–Bi compounds should have a small or even negative gap [1–5]. Thus adding bismuth to III–V semiconductors is of great importance for numerous optical and electronic applications including lasers, solar cells, transistors, and devices based on spintronics. Recent theoretical and experimental works have been devoted to GaAsBi, for which the unusually large band gap reduction [1, 3, 6–8], and giant spin orbit bowing [7], with Bi alloying is a key factor in realizing these applications. These outstanding properties are mainly related to the strong disparity in atomic size between Bi and As, and to the large relativistic effects induced in bismuth. Although considerable progress has been made in theoretical description of the structural and electronic background of bismuth compounds, many of their dynamical properties are still not well established. Recent theoretical studies have addressed similar properties on boron further III–V and II–VI compounds [9–16]. Understanding the dynamical properties of these systems is important for characterization purposes. This requires in turn an accurate knowledge of the bulk phonon dispersion of pure materials. In this paper we investigate the dynamical properties of III-bismuth compounds by employing the plane wave pseudopotential method, density functional theory, and a linear-response technique. The rest of the paper is organized as follows. In section 2, we briefly describe the computational method used in the present work. Results will be presented in section 3. A summary of the work will be given in section 4.

We have applied density functional theory within the local density approximation [17] in a plane wave basis, with ultrasoft Vanderbilt pseudopotentials [18], as implemented in the PWscf code [19]. The many-body electron–electron interaction is described by the Ceperley–Alder functional [20] as parameterized by Perdew and Zunger [21]. The Brillouin zone integrations were performed by summation over 10 special points of the Chadi–Cohen type [22]. The latticedynamical properties are calculated using density functional perturbation theory (DFPT) [23]. In particular, eight dynamical matrices were calculated for $4 \times 4 \times 4$ k-points mesh of

Monkhorst and Pack [24]. These matrices were then Fourier interpolated to obtain the phonon dispersion curves.

The total energy of the zinc-blende phase of III-Bi compounds has been calculated for different volumes of the lattice parameter and fitted to the Murnaghan equation of state [25] in order to obtain the equilibrium lattice constant *a*, and the bulk modulus *B*. The calculated phonon dispersion curves and total phonon density of states are presented in figures 1 for BBi, AlBi, and GaBi, respectively. For GaBi a direct comparison with Raman scattering spectroscopy [28, 29] is only possible for the zone-centre (i.e., at Γ point). The obtained TO (Γ) and LO (Γ) modes give 199 and 205 respectively, which agree well with theexperimental data of 186 [28], 189 [29] for TO (Γ) modes and 214 [28], 196 [29] for LO (Γ) modes. No theoretical calculations exist so far for GaBi. The agreement between our computations and experimental data for GaBi supports our results for BBi and AlBi, where no experimental data are available. Good agreement is noticed for the phonon frequency of BBi compared with recent *ab initio* calculations [22, 23].

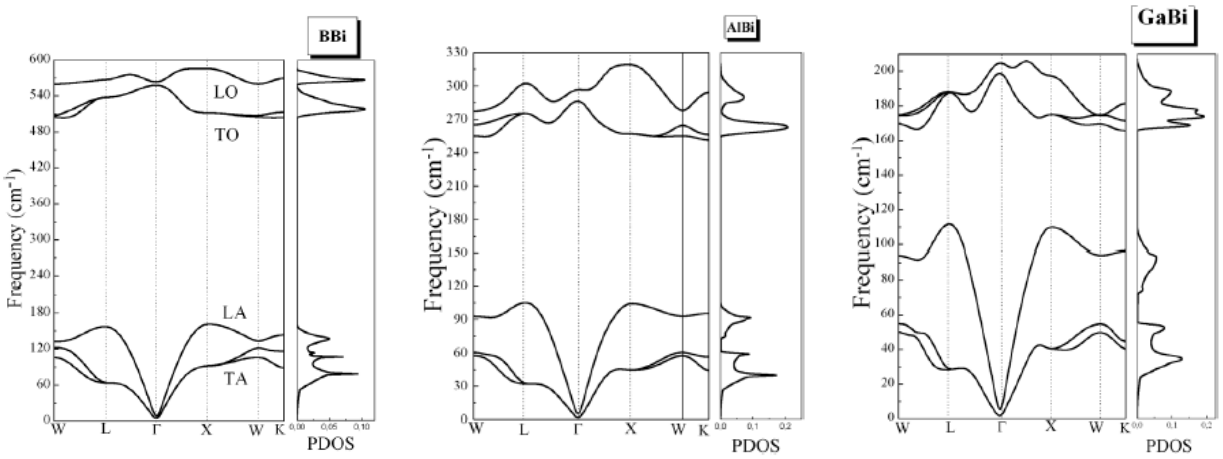

Fig. 1. Calculated phonon dispersion and phonon density of states (PDOS) of BBi, AlBi and GaBi

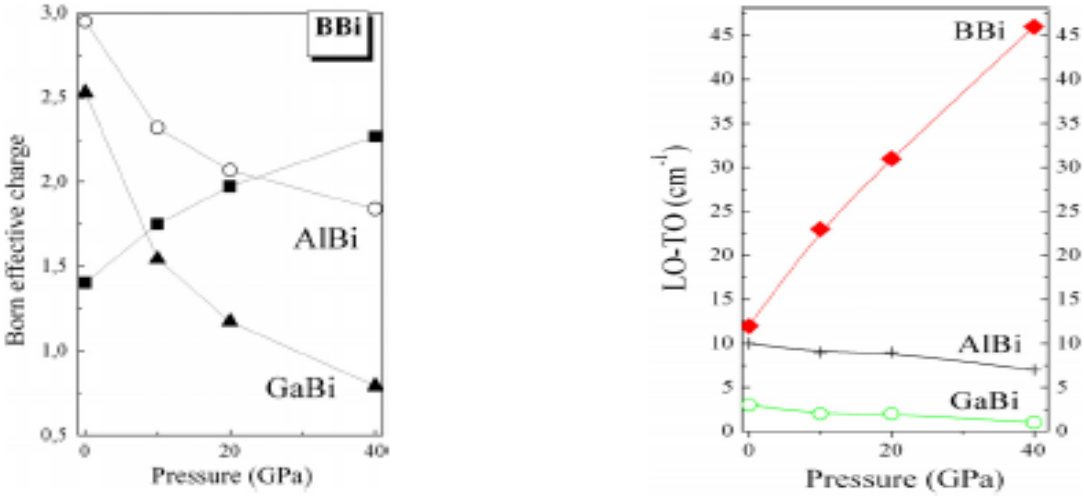

Fig. 2. Born effective charge versus hydrostatic pressure of BBi,AlBi, and GaBi

Fig. 3. Pressure dependence of LO–TO splitting of BBi,AlBi, and GaBi

The change of the Born effective charge under compression of bismuth compounds is presented in figure 4. This is also referred to as the dynamical effective charge, as distinct to the static charge, i.e., the change in electron polarization upon ionic displacement. The Born effective charge decreases with rising pressure for AlBi and GaBi; with opposite behaviour in the case of BBi, where the Born effective charge increases with decreasing volume. This result is in agreement with the recent *ab initio* calculations of BBi [27]. The decrease of the Born effective charge with decreasing volume, is found for most of the III–V and II–VI compounds except for SiC [30], AlN, and GaN [31]. The pressure behaviour of the dynamical charge indicates an electron charge transfer from bismuth to Al(Ga) atoms for AlBi(GaBi) and from boron to bismuth atoms for BBi, i.e., a reduction of the ionicity of the bond (see [32] for additional evidence), in the case of AlBi and GaBi. An increase of the ionicity is observed—however—for BBi. The unusual behaviour of BBi, is due to the anomalous valence charge density, characterized by a charge transfer towards the cation 'B' atom [4, 5].

Finally we now turn to the pressure dependence of the splitting between LO and TO phonon modes of BBi, AlBi and GaBi. Figure 5 shows the increase of the LO–TO splitting of BBi with rising pressure, which is in contrast with the behaviour of most of III–V semiconductors [33, 34]. This is a direct consequence of the net pressure effect discussed above for the boron effective charge. However for AlBi and GaBi we found that the LO–TO splitting decreases with decreasing volume, as found for other III–V semiconductors.

In summary, we have presented *ab initio* calculations of the ground-state and dynamical properties of bismuth III–V compounds BBi, AlBi, and GaBi in the zinc-blende structure.

The results for the lattice constants and phonon frequencies are in good agreement with available theoretical and experimental data. We have highlighted the main differences in the phonon spectra of these materials compared with the other III–V compounds. In contrast to AlBi, GaBi, and other III–V semiconductors, we found that the born effective charge and LO–TO splitting of BBi increases with rising pressure.

References

[1] Janotti A, Wei S-H and Zhang S B 2002 Phys. Rev. B 65 115203
[2] Wang S Q and Ye H Q 2002 Phys. Rev. B 66 235111
[3] Zhang Y, Mascarenhas A and Wang L-W 2005 Phys. Rev. B 71 155201
[4] Madouri D and Ferhat M 2005 Phys. Status Solidi b 242 285
[5] Ferhat M and Zaoui A 2006 Phys. Rev. B 73 115107
[6] Francoeur S, Seong M-J, Mascarenhas A, Tixier S, Adamcyk M and Tiedje T 2003 Appl. Phys. Lett. 82 3874
[7] Fluegel B, Francoeur S, Mascarenhas A, Tixier S, Young E C and Tiedje T 2006 Phys. Rev. Lett. 97 067205
[8] Madouri D, Boukra A, Zaoui A and Ferhat M 2008 Comput. Mater. Sci. at press
[9] Ferhat M, Zaoui A, Certier M and Khelifa B 1996 Phys. Lett. A 216 187
[10] Zaoui A and Ferhat M 2001 Phys. Status Solidi b 225 15
[11] Aouas M R, Sekkal W and Zaoui A 2001 Solid State Commun.120 413
[12] Touat D, Ferhat M and Zaoui A 2006 J. Phys.: Condens.Matter 18 3647
[13] Ferhat M, Zaoui A, Khelifa B and Aourag H 1994 Solid StateCommun. 91 407

[14] Sekkal W and Zaoui A 2002 Physica B 315 201
[15] El haj Hassan F, Zaoui A and Sekkal W 2001 Mater. Sci. Eng.B 87 40
[16] Sekkal W and Zaoui A 2002 New J. Phys. 4 91
[17] Hohenberg P and Kohn W 1964 Phys. Rev. 136 864
[18] Vanderbilt D 1985 Phys. Rev. B 32 8412
[19] Baroni S, Dal Corso A, de Gironcoli S and Giannozzi P http://www.pwscf.org
[20] Ceperley D M and Alder B J 1980 Phys. Rev. Lett. 45 566
[21] Perdew J P and Zunger A 1981 Phys. Rev. B 23 5048
[22] Chadi D J and Cohen M L 1975 Phys. Status Solidi b 68 405
[23] Baroni S, de Gironcoli S, Dal Corso A and Giannozzi P 2001 Rev. Mod. Phys. 73 515
[24] Monkhorst H J and Park J D 1976 Phys. Rev. B 13 5188
[25] Murnaghan F D 1944 Proc. Natl Acad. Sci. USA 30 244
[26] Deligoz E, Colakoglu K, Ciftci Y O and Ozisik H 2007 Comput. Mater.Sci. 39 533
[27] Bouamama K, Djemia P, Lebga N and Kassali K 2007High Pressure Res. 27 269
[28] Seong M J, Francoeur S, Yoon S, Mascarenhas A, Tixier S,Adamcyk M and Tiedje T 2005 Superlatt. Microstruct.37 394
[29] Verma P, Oe K, Yamada H, Harima H, Herms M and Irmer G 2001 J. Appl. Phys. 89 1657
[30] Go˘ni A R, Siegle H, Syassen K, Thomsen C and Wagner J-M 2001 Phys. Rev. B 64 035205

P23.

Mesoporous Cr-MCM-41: An efficient catalyst for selective oxidation of cycloalkanes

L. Mrah[1], A. Bellil[1], M. Adjidir[1]

[1] Laboratoire de Chimie des polymères, Département de Chimie, Université d'Oran Es Senia, Faculté des Sciences, B.P. 1524 Menaouar. 31000 Oran – Algérie, Mrah_houari@yahoo.fr

Highly ordered mesoporous Cr-MCM-41 materials with different Si:Cr mole ratios have been synthesized by using the hydrothermal method and avoiding co-precipitation of chromium oxides

during synthesis. Detailed characterizations of these two-dimensional hexagonal mesoporous Cr-MCM-41 materials were carried out using powder XRD, TEM, SEM-EDS, N2 sorption, FT-IR and UV–vis diffuse reflectance measurements. Cr-MCM-41 materials showed excellent catalytic activity and high selectivity in the direct oxidation of cycloalkanes viz. cyclohexane and cyclooctane to cyclohexanone and cyclooctanone, respectively, using dilute aqueous H2O2 or *tert*-butyl hydroperoxide (TBHP) as oxidant under mild liquid phase reaction conditions.

Open framework microporous and mesoporous metallo- silicates [1–4] have received considerable attention over the last few decades. These materials have found many poten- tial applications in catalysis, separations, coatings and chem- ical sensing. Mesoporous silica-based materials containing different transition elements could be used as catalyst, ex- changer and adsorbent of bulky molecules because of their tunable nanoscale pore opening and exceptionally high in- ternal surface area suitable for the diffusion of bulky organic molecules from the catalytically active sites located inside the pores. Thus, increasing attention has been paid to mesoporous materials with high surface area and narrow pore size distri- bution because of their diverse applications (e.g., adsorbents, catalysts and host materials). Highly dispersed transition metal cations incorporated within the framework of zeolites and mesoporous molecular sieves have unique properties for catalytic reactions [4]. They are also useful for magnetic and electrochemical applications [5,6]. To date, a wide-range of transition as well as non-transition elements have been incorporated in these silica-based mesostructures [4]. The incorporation of a trivalent heteroelement in the SiO2 frame- work could generate a cation exchange or Br¨onsted acid site. The adsorptive and catalytic properties of the other trivalent metal analogs of these microporous and mesoporous metallo- silicates are usually different from their aluminum counter- parts. Besides the modification of acidity, the presence of multivalent transition metal cations in the framework could also create isolated redox centers, which could be suitable for their application as heterogeneous oxidation catalyst in the presence of mild oxidants [7–14]. Crystalline microporous chromium-silicates [7,8] as well as amorphous mesoporous chromium-silicates [9–12] have been found to act as efficient catalysts for oxidation and isomerization reactions. Success- ful incorporation of Cr in the tetrahedral lattice site of meso- porous silica could be achieved through careful preparation of the synthesis gel and its subsequent hydrothermal treat- ment followed by careful calcinations to remove the struc- ture directing surfactants. Here, we have shown that 4.6 wt% Cr could be incorporated successfully preserving the highly ordered mesoporous MCM-41 framework by using a sim- ple hydrothermal method and avoiding the co-precipitation of chromium oxides during synthesis. Detailed characteriza- tions of these two-dimensional (2D) hexagonal mesoporous Cr-MCM-41 materials were carried out using powder XRD, TEM, SEM-EDS, N2 sorption, FT-IR and UV–vis diffuse re- flectance measurements. These mesoporous materials have shown excellent catalytic activity in the liquid phase oxidation of cyclohexane and cyclooctane using peroxide oxidants.

We have prepared mesoporous Cr-MCM-41 samples with Si:Cr mole ratios of 40:1, 20:1 and 10:1 in the synthesis gels. These samples have been designated as samples 1–3, respec- tively. Physico-chemical properties of various chromium- silicate samples synthesized in the present study are given in Table 1. Sample 4, pure silica MCM-41, was synthesized under otherwise identical synthesis conditions except the ad- dition of Cr(III) precursor in the gel. Chemical analysis of these chromium-silicate samples after calcination revealed the absence of any organic SDA. AAS data showed that the Si:Cr mole ratios for samples 1–3 were 37.5, 17.7 and 15.2, respectively. An optimum incorporation of Cr for the ordered chromium-silicate mesophase was observed for sam- ple 2 (4.6 wt% Cr).

Increasing the chromium loading further in the gel resulted in (broadening of the XRD peak) poorly ordered mesoporous structure (sample 3).

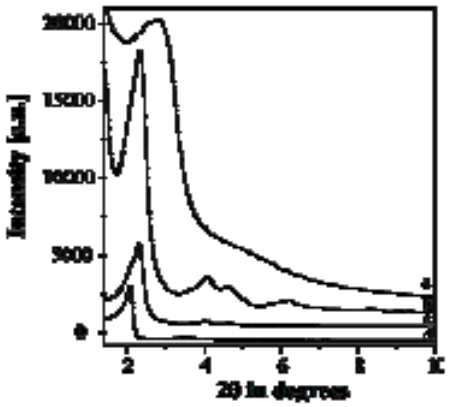

Fig. 1. XRD pattern of calcined sample 3 (a), sample 2 (b), sample 1 (c), and sample 4 (d)

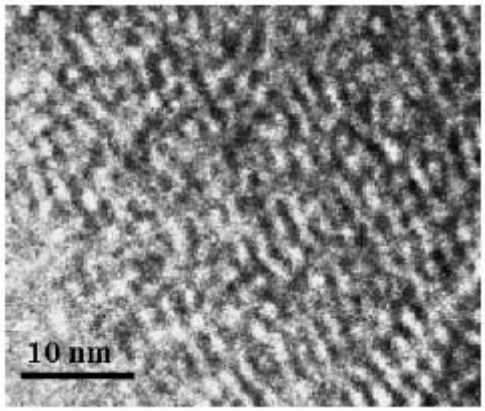

Fig. 2. TEM image of sample 2

XRD pattern of the different mesoporous samples 1–4 are shown in Fig. 1a–d. As seen in Fig. 1b–d, all four small-angle peaks of 1 0 0, 1 1 0, 2 0 0 and 2 1 0 planes, respectively, cor- responding to the 2D hexagonal mesophase of MCM-41 [15] was observed in samples 1, 2 and 4. No distinctive

higher or- der peaks were observed in either of the samples. However, for sample 3, a single broad peak was observed. TEM im- ages of these mesoporous chromium-silicate samples showed the existence of hexagonal arrangement of uniform meso- pores (Fig. 2).

Highly ordered mesoporous chromium-silicate Cr-MCM-41 materials have been synthesized using cationic surfactant as structure directing agent under mild hydrothermal condi- tion and at weakly alkaline pH. Loading of chromium has been found to control the ordering of this mesophase, very high loading leading to disordered mesophase. N2 adsorption measurements indicated medium to high BET-specific sur- face area, uniform mesopore opening and high pore volume in these samples synthesized by using the present hydrother- mal method. UV–vis diffuse reflectance data indicated

that the tetrahedral chromium species has been incorporated into the tetrahedral lattice site of silica. These mesoporous Cr- MCM-41 samples showed excellent catalytic activity in the liquid phase one-pot oxidation of cyclohexane and cyclooc- tane to cyclohexanone and cyclooctanone, respectively using TBHP and H2 O2 as oxidant.

References

[1] R. Szostak, Molecular Sieves: Principles of Synthesis and Identifi- cation, Van Nostrand Reinhold, New York, 1989.
[2] B. Notari, in: D.D. Elley, W.O. Haag, B.C. Gates (Eds.), Advances in Catalysis, 41, Academic Press, San Diego, CA, 1996, p. 253.
[3] X.S. Zhao, G.Q. Lu, G.J. Millar, Ind. Eng. Chem. Res. 35 (1996) 2075.
[4] M.G. Clerici, Top. Catal. 13 (2000) 373.
[5] S. Sundar Manoharan, D. Elefant, G. Reiss, J.B. Goodenough, Appl. Phys. Lett. 72 (1998) 984.
[6] T. Ishihara, M. Nakasu, A. Kawahara, H. Nishiguchi, M. Yoshio, Y. Takita, Electrochemistry 71 (2003) 1105.
[7] B. Jayachandran, M. Sasidharan, A. Sudalai, T. Ravindranathan, J. Chem. Soc. Chem. Commun. (1995) 1523.
[8] Z. Zhu, Z. Chang, L. Kevan, J. Phys. Chem. B 103 (1999) 2680.
[9] R.S. Silva, J.M.S. Arnold, U. Schuchardt, J. Mol. Catal. A: Chem. 171 (2001) 251.
[10] M. Inaba, K. Murata, M. Saito, I. Takahara, N. Mimura, H. Hamada, Y. Kurata, Bull. Chem. Soc. Jpn. 77 (2004) 381.
[11] A.L. Neal, K. Lowe, T.L. Daulton, J. Jones-Meehan, B.J. Little, Appl. Surf. Sci. 202 (2002) 150.
[12] A. Sakthivel, S.K. Badamali, P. Selvam, Catal. Lett. 80 (2002) 73.
[13] R. Noyori, M. Aoki, K. Sato, Chem. Commun. (2003) 1977.
[14] U.R. Pillai, E. Sahle-Demessie, Green Chem. 6 (2004) 161.
[15] C.T. Kresge, M.E. Leonowicz, W.J. Roth, J.C. Vartuli, J.S. Beck, Nature 359 (1992) 710.

P24.

Reactivity indices of some 6 –substituted benzoxazinone derivatives with monochloroacetic acid

S. Bouasla[1], N. Lemouari[1], M.Teguiche[1] et M. Liacha[2]

[1]Laboratoire de Chimie Appliquée (LCA), Faculté des Sciences et de l'Ingénierie, Université 8 Mai 45 Guelma, souad2004_chem@yahoo.fr
[2]Laboratoire de synthèse et de biocatalyse organique, Faculté des science, Universite Badji Mokhtar de annaba, B.P 12 . El-Hadjar annaba, algérie.

In order to gain insights into the reactivity nature and the reactive sites of 6-methyl/6-ethyl/ 6-nitro/ 6-acetyl and 6-benzoyl-1,4-benzoxazin-3-one compounds towards mono-chloro-acetic acid ($ClCH_2COOH$) , we studied in this work the reactivity descriptors of both reagents, thelocal softness sk+ and sk- and the fukui functions f_k^+ and f_k^-. The reactive sites derived from theses calculations are in accordance to the experimental results for a nucleophilic attack on the C-Cl bond by the nitrogen atom , and the reactivity order increases from H >CH_3> C_2H_5 > $COCH_3$> NO_2.

The chemical reactivity of a molecule is often interpreted in terms of charge distribution of its atoms. Atomic charges are used to indicate the preferred direction for a reagent to approach a substrate. Although the chemists have an intuitive feeling for the reactivity based on charge distribution, assigning precise reactivity, from atomic charges failed in several cases [1].

In recent years, reactivity descriptors [2] such as hardness, softness, Fukui functions etc. have emerged as powerful tools in predicting the reactive sites of molecules. These reactivity descriptors are derived from density functional theory. Global hardness and global softness [3] represents the reactivity of a molecule as a whole. On the other hand, the Fukui function defines the reactivity of an atom in a molecule and it is a local property. Fukui function and local softness, which closely related, are suited to describe the relative reactivity for different substrates. Pearson's hard-soft-acid-base (HSAB) [4] Principle Suggested that hard-hard and soft-soft interactions are favourable over hard-soft interactions [5].Again it has been found that soft-soft interactions are preferred in the site of maximum Fukui function [6] . In this paper we have presented the reactivity parameters, the local softness s^+_k and s^-_k, and fukui functions f^+_k and f^-_k of some 1,4-benzoxazin-3-one derivatives namely, 1,4-benzoxazin-3-one, 6-methyl-1,4-benzoxazin-3-one, 6-ethyl-1,4-benzoxazin-3-one, 6-nitro-1,4-benzoxazin-3-one and 6-acyl-1,4-benzoxazin-3-one and the most reactive site in their reaction with monochloro acetic acid were derived. Experimentally it has been found that the methylen group is a subject for a nucleophilic attack by the N-atom of the benzoxazin-3-one ring. Here we have investigated the reactive sites of these benzoxazinonic compounds towards $ClCH_2COOH$ using a local hard-soft-acid-base approach.

Within the frame work of density functional theory (DFT) the global hardness (η)

$$\eta = 1/2\,(d^2E/dN^2)_{v(r)} = 1/2\,(d\mu/dN)_{v(r)} \qquad (1)$$

Where E, N, μ and V(r) are the energy, number of electrons, chemical potential and external potential, respectively. Again, the inverse of global hardness with a factor of ½ is defined asglobal softness (S).

$$S = 1/2\,\eta = (dN/d\mu)V(r) = 1/\,I\text{-}A \qquad (2)$$

Where I and A are the first vertical ionization potential and electron affinity, respectively, of

the chemical species.The local property , Fukui function is f (r) is defined as the derivative of the electron density, ρ(r) with respect to the number of electrons at constant external potential.

$$f(r) = (d\rho(r)\,/\,dN)\,V(r) \qquad (3)$$

Similarly local softness, s(r) is defined as the derivative of electron density ρ(r) with respect to the chemical potential μ at constant external potential.

$$s(\vec{r}) = \left(\frac{\partial \rho(\vec{r})}{\partial N}\right)_{v(\vec{r})} \left(\frac{\partial N}{\partial \mu}\right)_{v(\vec{r})} = f(\vec{r})S = \left(\frac{\partial \mu}{\partial v(\vec{r})}\right)_N S \qquad (4)$$

Applying the finite difference approximation, three types of condensed Fukui functions are found, from electronic population analysis.

$f^+_k = q_k\ (N+1) - q_k(N)$, suited for the nucleophilic attack on the system

$fk = q_k\ (N) - q_k(N-1)$, suited for the electrophilic attack on the system

$f_k^\circ = [q_k\ (N+1) - q_k(N-1)] / 2$, suited for radical attack on the system

Where $q_k(N)$, $q_k\ (N+1)$ and $q_k(N-1)$ are atomic charges for the atom k in the N, N+1, N-1

electron systems.

Muliken charges				
compound	Basis set	N	CH_2 (Cl)	CO (COOH)
Benzoxazinone	STOG	-0.2988	-0.1201	0.2181
6-CH_3-benzoxazinone		-0.2991	-	-
6-C_2H_5-benzoxazinone		-0.2991	-	-
6-NO_2-benzoxazinone		-0.2963	-	-
6-acyl-benzoxazinone		-0.2981	-	-

Table1: MPA derived charges for N atom of benzoxazinone and carbon toms of the C-Clbond

The Fukui functions f^+_k and f_k and local softness s_k^+ and s_k^- are calculated from SFC calculations using minimal STOG basis sets. All the calculations are performed with the hyperchem 7.5 suite of program.The geometries of monochloro-acetic acid and all the 6-X-1,4-benzoxazin-3-one derivatives were optimised using Beck's three parameter hybrid density functional theory B3LYP/ STOG.

The atomic charges derived from Muliken population analysis (MPA) for the benzoxazin-3-one derivatives and monochloro-acetic acid are given in table 1.It is seen from table 1 that that all the charges have negative values for the nitrogen atom N in the heterocycle ring, so an elctrophilic attack should be expected on the N atom of the benzoxazinone. Unexpectedly the methylen group on the acid chloride has a negative charge and the carbonyl CO of hydroxyle group has a positive charge, then the nucleophilic attack takes place at the CO atom. Howeverexperimentally it has been found that the nucleophilic attack occurs on the methylen group of the acid. Hence it is difficult to predict the reactives site from atomic charge values.

The fukui function values for the N atom and carbon atom of CH2 group in the acide chloride are presented in table 2. Considering the MPA derived fukui function. The HSAB principle was applied in order to get insights on the reactivity site in the reaction of 6- substituted 1,4- benzoxazin-3-one towards acid chloride. Strarting form the idea that the interacting atoms should have as close as

possible the values of FF the trend of reactivity observed is for all molecules the reactivity of the N atom electrophilic attacks increases in the order H >CH3> C2H5 > COCH3> NO2.

Table 2: The MPA derived local softness at N atom of the benzoxazinone ring and Carbon of the C-Cl bond

MPA			
Compound	Basis set	N	C (C-Cl)
Benzoxazinone	STOG	-0,0693	-0,0497
6-CH_3-benzoxazinone		-0,2009	-
6-C_2H_5-benzoxazinone		-0,0570	-
6-NO_2-benzoxazinone		-0,0483	-
6-acyl-benzoxazinone		-0,0529	-

The local softness values for all molecules calculated with minimal STOG basis sets are given in table 3.Like fukui functions (FF), local softness values predict the similar trend of reactivity , the reaction is more easy with bearing with drawing group.

Table 3: The MPA derived local softness at N atom of the benzoxazinone ring and carbon atom of C-Cl bond

Compound	Local softness
$ClCH_2COOH$	-0.00020
Benzoxazinone	-0.00030
6-CH_3-benzoxazinone	-0.00034
6-C_2H_5-benzoxazinone	-0.00027
6-NO_2-benzoxazinone	-0.00025
6-acyl-benzoxazinone	-0.00026

Local reactivity descriptors are shown to be more reliable tools in predicting the reactivity site in the nucleophilic displacement reaction of some 6-substituted-1,4-benzoxazin-3-one derivatives with $ClCH_2COOH$. From the fukui functions and local softness values it is concluded that the N-atom of the benzoxazinone ring is the reactive site, and the reactivity increases in the order H >CH3> C_2H_5 > $COCH_3$> NO_2.

References

[1]. W. Lagenaeker, K. Dmel and P. Geerling, J. Mol .Struct (Theochem), 1992,259,317.
[2]. R. K. Roy, S. Krishnan Murty, P. Geerlings and S. Pal, J, Phys. chem, 1998, 102, 3746.
[3]. Chemical Hardness, Structure and bonding, ed. K. D. Sen and D. M. P.Mingos, Springerverlag,Berlin, 1993.
[4]. P. K. Chattaraj, J, Phys.Chem. A, 2001, 105, 511.
[5]. P. K. Chattaraj, G. H. Liuand R. G. Parr, Chem, Phys, Lett, 1995,237, 171.
[6]. K. Fukui, Science, 1982, 217,747.

P25.

Structural, electronic and magnetic properties of the itinerant ferromagnetic SrRuO3 in cubic perovskite phase

N. MOULAY[1], M. RABAH[2], A. ZENATI[1]

[1] Faculté des Sciences, Département de Physique, Université Djillali LIABES de Sidi-Bel-Abbès,), Algérie.

[2] Laboratoire des Matériaux Appliqués, Centre de Recherche (Ex : CFTE), Route de Mascara, Université de Sidi Bel Abbes 22000, Algérie.

The self-consistently calculated values of total energy in the magnetic state of the cubic-perovskite structure were fitted to the Birch equation [21].The ground states properties of SrRuO3 are obtained, the equilibrium lattice constant, bulk modulus and its first derivative values are compared with experiment and previous theoretical results see . The spin-polarized calculation directly gives the magnetic moment μ. the difference between the total numbers of spin-up and spin down electrons which corresponds to the 'saturated magnetic moment', μsat, at T =0. A total Ferromagnetic moment of 0,7 μB was obtained in the idealized cubic structure. This value is compared with others theoretical and experimental results. This is approximately near the results of Singh [16] and P.B Allen and al [9] but less larger then G Santi and al [15].The magnetic moments μ are dominated by the contribution of the Ru 0,42 μB due to its high DoS, with the miner value in Sr 0,026 μB and 0,19 μB in O. there is a weak polarization on O sites mainly through hybridization with the Ru d band. Our total ferromagnetic moment calculated are nearly most quoted values of the experimental for μsat, witch are between 0,8 and 1,6 μB[11-22-23], although these experimental moment results are difficult to obtained because the difficulty in saturating the material. This discrepancy may be due also to finite-temperature effects lowering the magnetization, or, as pointed out by Kanbayashi, to the multidomain structure [24] and the magnetocrystalline anisotropy [10]. It is interesting that our calculated moment is so sensitive to the small distortion of crystal structure from cubic. This accord with the discovery by Kirillov et al [25] that optic phonon modes are affected by the magnetic order. The stoichiometry is another important factor to affect the moment, it's a problem generic to perovskite materials, it would be moderate to affect the moment in a weak ferromagnetic .the magnetism arises from strongly hybridized itinerant Ru–O bands, leading to substantial O contributions to the moment. These will affect the fit of neutron scattering data and should be taken into account. The remaining interstitial magnetization contains both Ru 4d and O 2p contributions, although due to the small O sphere radius and the extended character of O2- p orbitals, the O contribution is probably dominant in this region. In any case, O contributions are large, and reflect the strongly hybridized bands near Ef. Calculations were performed as a function of lattice parameter for the cubic perovskite structure. The moment was found to increase with increasing volume. This trend is confirmed by our cubic calculation for SrRuO3 with a compressed cell(9 per cent) showing a reduction of μ of about 0,024 μB A°-3 not large like calculations of Singh and G Santi[16-15].

This sensitivity can partly be understood in view of the surprisingly large observed influence of the Na doping on SRO which was interpreted in term of volume reduction [26]. This value suggests that the moments are quite robust, although this slope should not be compared with experiment because of the assumed ideal cubic structure.

The calculated density of states (DoS) of perovskite structure SrRuO3 is shown in Figures.2, respectively. We focused our studies only on the region surrounding the Fermi level and that because of the highly complex hybridization that exists in this area. These bands extending from -9 eV to 10 eV show four main peaks in the DOS. The Ru-d is generally responsible on the DoS at Fermi and peak located between -9 and -4 eV except for peak between -4 and -2 where the contribution of p is major. With regard to the region a total domination of Sr-d is registered. This complex narrows to a width of less than 7 eV at the Γ point where p-d mixing is suppressed by symmetry and is broadest along the zone boundaries. These bands originate with a pure Ru 4d eg symmetry state at Γ . This is consistent

with the results of Singh [16] but disagrees with the results of Santi [15]. This peak in the DoS seems to be due mainly to three flat bands: a d_{eg} between Γ and X and two $d_{t_{2g}}$ bands between X and M .The spin splitting at Γ is (0,35 and 0,22) eV in the Ru 4d and O 2p regions, respectively. The peak near the Fermi level is originated of the bands arises from 4d Ru degenerate. This is splitting into t_{2g} triplet (yz, zx and xy) and e_g doublet (x2 − y2), (3z2 − 1) see figure 3. At Γ these bands are at -2,91 eV in t2g and 0,057 eV in eg. For the three orthogonal planes kx=0, ky=0, and kz=0, there is a band of this 4d character showing almost no dispersion in the plane, but dispersing upwards away from it due to 2p-4d mixing. The exchange splitting near Ef reduces the Fermi level DOS to $N\uparrow(Ef) = 24{,}98Ry^{-1}$ and $N\downarrow(Ef) = 23{,}33Ry^{-1}$. At Fermi level this O-p character is mostly from dispersive bands like those dispersing upwards from -2 eV to cross Ef along $\Gamma - R$ in this idealized cubic perovskite structure. Near Ef, approximately one quarter of the projection of these bands is p-like on the O spheres almost the same values than found by Singh. There are several sheets of Fermi surface for this cubic structure. These are flat planar sections of majority spin electrons along the kx=0, ky=0, and kz=0 planes plus additional sections in both spins derived from dispersing p-d hybridized bands. The average velocities $\langle V_{F,x}\rangle \approx \langle V_{F,y}\rangle \approx \langle V_{F,z}\rangle$ are 1,03 x 107 cm/s and 1.71 x 107cm/s for majority and minority spin, respectively. In addition, a gap of 0,4 eV is present in majority spin at Γ below Ef. This difference gap can grow if the magnetic moment is enhanced in the Ru with a value of $2\,\mu_B$/Ru, that will achieve a half metallic behaviour [16]. These results are almost like those obtained by Singh by the difference of 0.1 but this difference is very large in the results achieved by Santi this is due to the sums of the two spin channels showing in table 3. Our calculation for the minority spin is more important than majority spin conversely with the results obtained by Santi. The density of states (DoS) spins polarization, $P_0 = \left[N_\uparrow(E_F) - N_\downarrow(E_F)\right] / \left[N_\uparrow(E_F) + N_\downarrow(E_F)\right]$, where $N_{\uparrow\downarrow}(E_F)$ is the DOS for the majority (minority) bands at the Fermi level. Here in this work, the SrRuO3 bands structure calculations result in almost identical spin-up and spin-down DoS. The ratio of these polarization states is located almost null with $P_0 = 0.25$, even though SrRuO3 has a relatively large magnetic moment. This result is a good agreement with that found by B. Nadgorny and al [27].

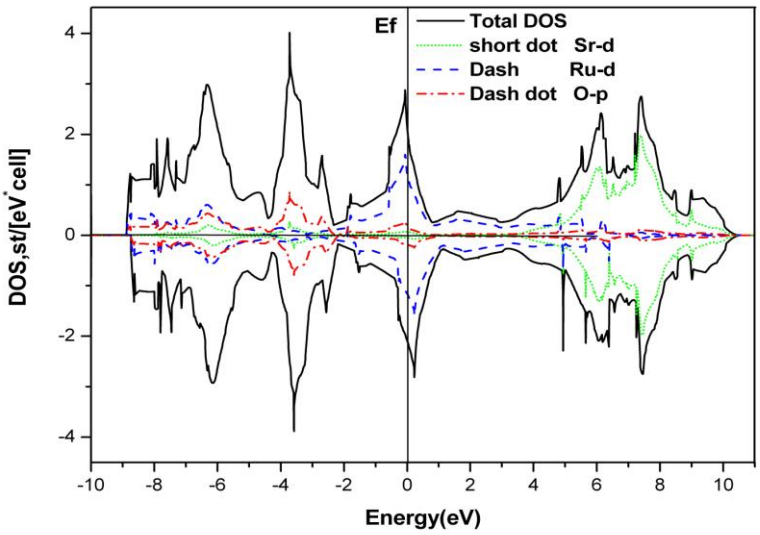

Fig.2. The total and partial DoS in states eV−1/ (f.u spin) for SrRuO3 in the idealized cubic structure for the spin-polarized calculation. The majority-spins electrons' DoS are positives and the minority ones are negatives. The projections are onto FP-LMTO spheres and are on a per atom basis

P26.

Etude *ab initio* des propriétés électroniques du composé ternaire

$(Cu_{1-x}Ni_x)_3Sn$

M.OUSSADOU[1], B. ALLILI[2], A. KELLOU[3], D. BRADAI[4]

[1]Faculté de Physique, USTHB, BP 32 El-Alia, Dar el Beida, Alger, E-mail: oussadou_mezhoura@yahoo.fr
[2]Faculté de Physique, USTHB, BP 32 El-Alia, Dar el Beida, Alger, E-mail : ballili@usthb.dz3Faculté de
[3]Physique, USTHB, BP 32 El-Alia, Dar el Beida, Alger, E-mail : dbradai@usthb.dz
[4]Faculté de Physique, USTHB, BP 32 El-Alia, Dar el Beida, Alger, E-mail : afkel@yahoo.fr

Les composés intermétalliques suscitent à travers le monde de nombreuses recherches et un grand intérêt. La complexité de ces phases en fait une affaire de spécialistes souvent pointus, aussi bien pour ce qui concerne les études expérimentales que la modélisation ou la simulation. Les composés intermétalliques constituent une classe très vaste d'alliages, à l'intérieur de laquelle on met au point des systèmes nouveaux capables de performances améliorées dans des gammes de température aussi élevées que possible : le développement de matériaux à vocation structurale qui conservent leur résistance mécanique et leur rigidité spécifiques à moyenne et haute températures, tout en offrant une bonne résistance à l'oxydation et à la corrosion, constitue un des objectifs du secteur aérospatial.

Dans le cas ou les intermétalliques sont produits par un phénomène de précipitation ou de micro-précipitation, comme c'est le cas de beaucoup d'alliages dits à durcissement structural, leur apparition est suivie d'une amélioration des propriétés mécaniques de la phase mère. Leurs caractéristiques physiques, thermochimiques et métallurgiques sont donc à connaître de manière primordiale.

Recourir à des expérimentations afin de déterminer les paramètres thermochimiques par exemple, s'avère de plus en plus coûteux en moyens de tous genres, c'est pour cela qu'on a de plus en plus recours à des calculs qui dans certains cas donnent des résultats très encourageants.

Dans ce travail nous présentons l'étude *ab initio* des propriétés électroniques du composé intermétallique $(Cu_{1-x}Ni_x)_3Sn$ qui se forme après des traitements thermiques dans l'alliage CuNiSn [1]. Notre étude a été effectuée en utilisant le code WIEN2k [2] conçu pour l'étude des propriétés physique des matériaux, les fondements de ce code sont donnés par Peter Blaha *et al* [2]. L'objectif principal de ce travail est l'étude de l'évolution des propriétés électronique du composé $(Cu_{1-x}Ni_x)_3Sn$ en fonction de la substitution du nickel au cuivre. Les calculs sont faits pour les différentes structures ordonnées dans lesquelles ce composé précipite.Notre travail est une application de la méthode des ondes planes augmentées linéarisées (FP-LAPW) [3] incluse dans le programme [2], qui est la méthode la plus utilisée dans les calculs de structure électronique des solides avec la théorie de la fonctionnelle de la densité (DFT) [4]. L'ensemble de nos études est basé sur l'approximation GGA (P.B.E) [5] associée à la théorie de la fonctionnelle de la densité (DFT).

Comme dans toutes les méthodes de calcul *ab initio* basées sur la DFT, nous n'avons besoin que de quelques données d'entrée pour nos calculs. Nous devons introduire seulement les numéros atomiques des éléments constituants la structure à étudier et leurs arrangements dans l'espace : positions et vecteurs de translation. Après avoir optimisé les paramètres de l'équilibre de la phase (volume de relaxation, la forme de la cellule, les positions des atomes dans la maille) sans aucune autre restriction à part celle imposée par le groupe de symétrie. Nous passons par la suite à l'étude des propriétés électroniques.

Le résultat de notre étude a montrer que la substitution du Ni au Cu dans cette phase $(Cu_{1-x}Ni_x)_3$ Sn modifie profondément ces propriétés électroniques. L'ajout du nickel à pour effet de rapprocher les blocs de la DOS du niveau de Fermi localisé en zéro par une ligne hachurée (voir fig.1). Comme on remarque aussi l'apparition de DOS (anti-liantes) à droite du niveau de Fermi avec la substitution du nickel au cuivre, chose qui nous indique que le nickel affaiblit légèrement la bonne conductivité électrique de l'alliage pour renforcer les liaisons. L'ajout du nickel à pour effet de rapprocher les blocs de la DOS du niveau de Fermi. Comme on remarque aussi l'apparition de DOS (anti-liantes) à droite du niveau de Fermi avec la substitution du nickel au cuivre, chose qui nous indique que le nickel affaiblit légèrement la bonne conductivité électrique de l'alliage pour renforcer les liaisons.

Lorsque le nickel envahit complètement la place du cuivre le niveau de fermi se situe dans un gap. Ce résultat montre que l'ajout du nickel stabilise le composé étudié. Le calcul fait pour l'état magnétique du composé ne montre pas de déséquilibre entre les densités des spins up et des spins down au niveau de fermi. Le moment magnétique est trouvé égal à zéro. On conclut que la substitution du Ni au Cu n'induit de magnétisme au composé $(Cu_{1-x}Ni_x)_3Sn$.

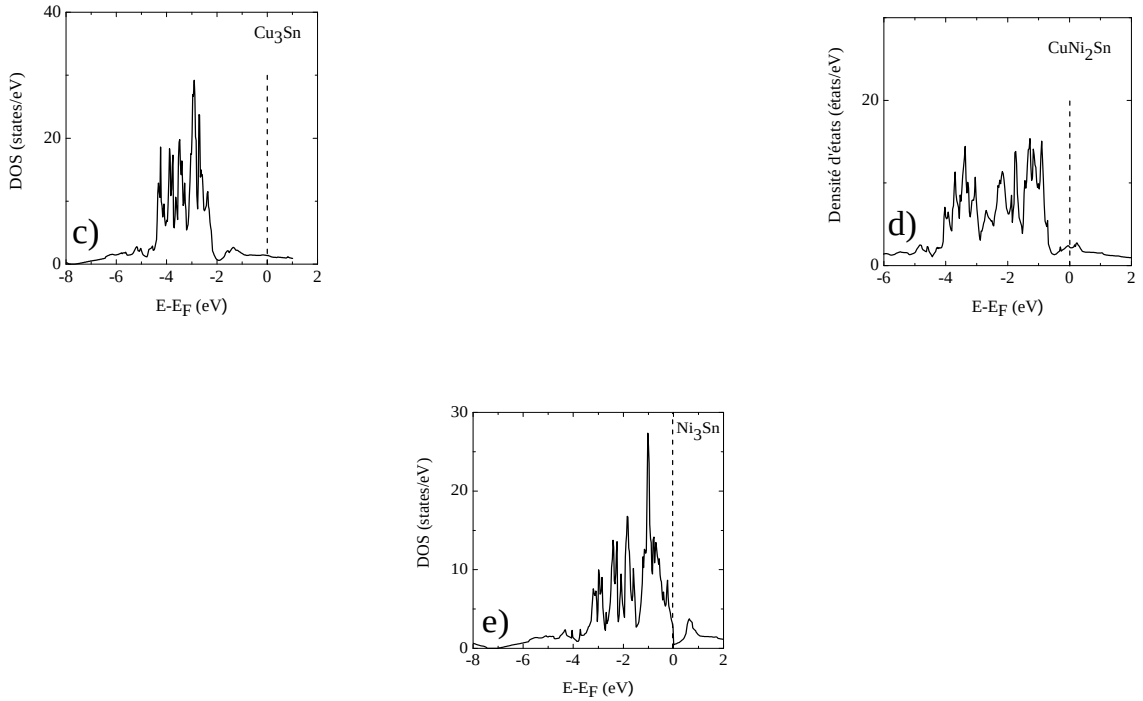

Fig.5. Les densités d'états du composé $(Cu_{1-x}Ni_x)_3Sn$ en fonction de la substitution de Ni

References

[1] J.C. Zhao, M.R. Notis; Acta Mater, **46** (1998), p.4203-4218.
[2] P. Blaha, K. Schwarz, G.K.H. Madsen, D. Kvasnicka, J. Luitz, WIEN2K, An Augmented Plane Wave + Local Orbitals Program for Calculating crystal Properties (Karlheinz Schwarz, Tech.University at Wien, Austria), ISBN. 3-9501031-1-2, 2001.
[3] O.K. Andersen, Phys. Rev. **B 12**, 3060 (1975).
[4] W. Kohn and L.J. Sham, Phys. Rev., B**140** (1965) 1133.
[5] J.P. Perdew, K. Burke and M. Ernzerhof, Phys. Rev. Lett., **77** (1996) 386

P27.

Ab initio study of the structural, electronic and elastic properties of some B2 intermetallic compounds.

A.Sekkal[1], A.Benzair[2], G.Merad[1], H.Aourag[1]

[1] Laboratoire d'Etude et Prédiction de Matériaux, Unité de Recherche Matériaux et Energies Renouvelables, Département de Physique, faculté des Sciences,Université Abou Bekr Belkaid B.P 119, 13000Tlemcen, Algérie
[2] Département de Physique, faculté des sciences, Université Djillali Liabes. 22000 Sidi Bel Abbés, Algérie.

The electronic structure of the intermetallic compounds such as LaMg and YMg which crystallize in the CsCl structure of the B2 type, has attracted the attention of the scientific world because of their anisotropic properties. The advantage of studying these materials is to answer some request industrial in the materials that resist for high temperature, oxidation resistance. However, high ductility has been observed in these compounds at room temperature. In this present work we employed Ab initio calculation methods while basing on the full potential linearized augmented plane wave method (FP-LAPW) within density functional Theory in the Wien-2k code, are used to examine the various properties of the materials (YMg, YRh) like the structural, electronic and mechanical properties. The results obtained are in good agreement with those found in other experimental studies and data.

P28.

Etude théorique du processus d'hydratation d'une chaîne peptidique par dynamique moléculaire

W.Taleb Bendiab, A.Krallafa

Laboratoire de Chimie Physique Macromoléculaire LCPM.
Département de Chimie, Faculté des Sciences,
Université d'Oran Es-Senia .
Email : wafaatb@hotmail.com

Les protéines sont des macromolécules constituées de longues chaînes d'acides aminés, remplissent, au sein de la cellule vivante, des fonctions bien spécifiques définies par leur composition et leur forme tridimensionnelle. Sans la fine couche de molécules d'eau dont elles s'entourent, les protéines solubles ne pourraient accomplir leur fonction biologique.

Nous nous intéressant dans notre étude à identifier comment et pourquoi l'eau interagit avec les protéines.

Notre travail consiste dans un premier temps à étudier le brin peptidique KRFK (Lysine-Arginine-Phenylalanine-Lysine) issue de la thrombospondine qui est une protéine de haut poids moléculaire qui sera analysé sur le plan statique et dynamique de même que son comportement en phase aqueuse.

La méthodologie de calcul envisagée abordera les techniques de modélisations numériques par dynamique moléculaire elle permettra alors de déduire des propriétés physiques, chimiques, thermodynamiques et structurales.

Reference:

[1]Lubert Stryer, Jeremy Mark Berg, John L. Tymoczko (trad. Serge Weinman), Biochimie , Flammarion, « Médecine-Sciences », Paris, 2003, 5 éd. e

P29.

Etude des matériaux organiques chromophormiques synthétiser pour l'optique non linéaire.

M.Boutaleb[1], K.Guemra[2]

[1,2] Laboratoire de chimie organique physique et macromoléculaire
Université Djillali Liabes de Sidi-Bel-Abbès
BP 089 Cité Larbi Ben M'hidi 22000 Sidi-Bel-Abbès.

Le travail présenté consiste en la synthèse et la caractérisation spectroscopique de monomères et copolymères organiques. Ces matériaux ont des bonnes caractéristiques physiques pour l'optique non linéaire. Ils présentent des chromophores, ce qui leur donne un aspect de coloration.

Ces matériaux possèdent dans leurs chaînes latérale des groupements donneurs et attracteurs ce qui rend les électrons de l'unité moléculaire délocalisés sur une grande longueur de conjugaison ; c'est à dire que la molécule est large, plane et conjuguée. L'orientation de ces matériaux par un champ électrique à une température voisine de la température de transition vitreuse, donne naissance à des effets non linéaires du second ordre en optique. La copolymérisation des polymères non actifs avec des molécules à fortes propriétés non linéaires donne des matériaux de choix pour l'optique non linéaire.

L'Optique Non Linéaire est l'ensemble des phénomènes qui résultent de la non linéarité de la réponse d'un milieu matériel à l'action d'une onde électromagnétique du domaine optique. Elle est une conséquence de l'invention du laser, qui permet la génération de champ fort.

La très grande luminance des Lasers permet d'obtenir des champs élevés qui modifient la réponse électromagnétique de la lumière qui ne peut alors plus être décrite par des relations constitutives linéaires. Les propriétés optiques peuvent varier en fonction de la racine carrée, du cube ou des puissances supérieurs du champ électromagnétique incident. [1]. Le développement des nouveaux services de communication optique nécessite la fabrication de matériaux présentant des propriétés optiques non linéaire et fortes hyper polarisabilité pour qu'un matériau ait une forte valeur de l'hyper polarisabilité moléculaire du 1er ordre et de 2ème ordre il faut que la molécule ait une structure non centro-dymétrique et qu'elle possède les caractéristiques suivantes [2, 3] :

a) contenir des électrons délocalisés sur une grande longueur de conjugaison, c'est à dire que la molécule doit être long, plane, et conjuguée.

b) Présenter une structure contenant un groupement donneur d'électrons et un groupement attracteur d'électrons à l'autre extrémité, pour avoir une déformation très dissymétrique du nuage d'électrons et aussi pour assurer un transfert de charge important au sien de l'unité moléculaire.

L'augmentation de l'hyper polarisabilité s'obtient en augmentant la force d'un groupement attracteur ou d'un groupement donneur d'électrons ou les deux au même temps.[4]

Modèle moléculaire

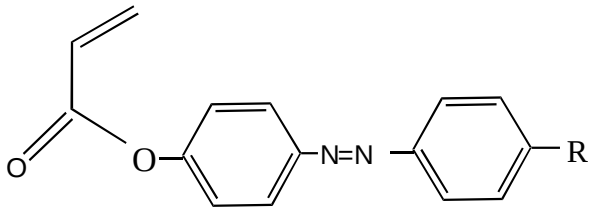

Films polymères et l'ONL :

La technologie de filmeture des polymères est maintenant bien maîtrisée à travers les applications audio-ou vidéo ou les exigences techniques sont également très grandes. Il existe d'ores et déjà plusieurs types de films polymères à propriétés non linéaires [5]

- les polymères dopées
- les polymères cristaux liquide

Le principe consiste à dissoudre des molécules actives dans une matrice thermoplastique amorphe (pour des raisons de diffusion de la lumière) de chauffer le mélange à température au –dessus de la température de transition vitreuse du polymère. D'orienter alors les molécules sous champ électrique, puis de refroidir le matériau en maintenant le champ. La dispersion des colorants azoïques « Redone » dans du poly- méthacrylate de méthyle (PMMA) permet d'obtenir, selon cette technique, des films dopés ayant des activités non linéaires élevées ($\chi(2)$ = 12 . IO-9 e.s.u). $\chi(2)$= l'hyperpolarisabilité quadratique.

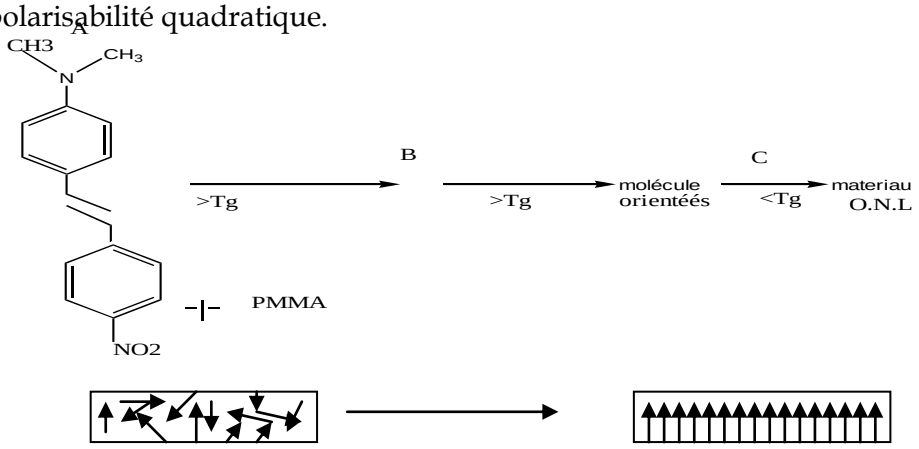

Fig. 7 Principe de réalisation d'un filme polymère à propriétés optiques

A) Dispersion d'une molécule active dans le PMMA.

B) Orientation sous champ électrique des dipôles à θ >Tg
C) Refroidissement sous champ à θ <Tg.

Modification du PVBA par le Benzamide :

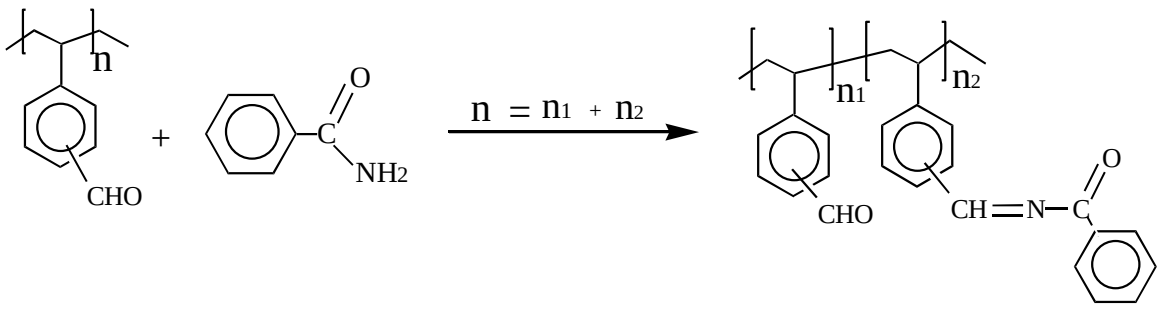

Propriétés des colorants azoïques :

Moments dipolaires en debyes.

R	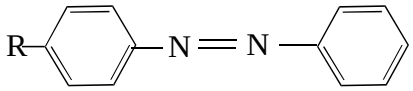	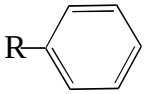	**Δμ**
NH_2	**2.48**	**1.54**	**0.94**
$N(Me)_2$	**3.22**	**1.58**	**1.64**
NO_2	**4.45**	**3.95**	**0.50**

Spectre UV-Visible d'un acrylazophénol :

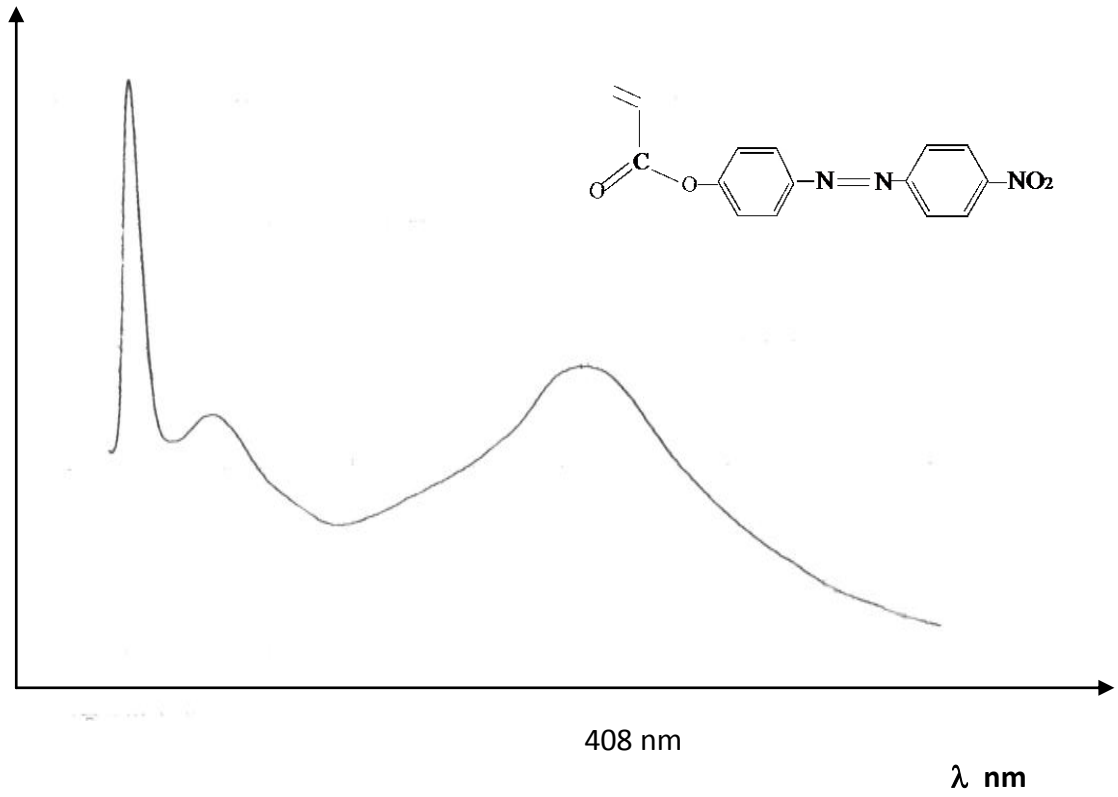

Fig. Spectre d'absorption de le Nitroacrylazophénole en UV-Visible.

Références

[1] : E.P.Raynes, in Electro-optics and Photorefractive materials, Springer Proc. In Phys, 1987, 18,99-109.
[2] : Y.Daoudi, P. Bonifassi. Journal of Molecular Structure (theochem) 451, 1998, 277 – 293.
[3] : A.Fort, M.Barzoukas. Journal of Nonlinear Optical physics and materials. Vol 5.1996, 757 – 765.
[4] : I.Ledoux et Coll, J.Opt.Soc.Am, 1987,B4987.
[5] : C.I.Stegeman et Coll, in Nonlinear Optical Propreities of polymers, M.R.S.Symp. Proc, 1988, 109, 53-64.

P30.

Comportement Micellaire D'un Mélange Binaire De Tensioactifs Non-ionique/Cationique

H. Bélarbi[1], F. Bouanani[1] et D. Bendedouch[1]

[1] Loboratoire de Chimie Physique Macromoléculaire, BP 1524 El Mnaouer, Oran, 31000, Alger,

Quelques propriétés physico-chimiques de mélanges aqueux d'un surfactant cationique, le bromure de dodécyltriméthylammonium (DTAB) et d'un non ionique fluoré, l'undécafluoro n-pentyl décaoxyéthyléne éther (FSO100) ont été déterminées par tensiomètrie à une température fixe de 25°C pour différentes fractions molaires en DTAB. Les résultats expérimentaux obtenus, en particulier les valeurs des concentrations micellaires critiques des mélanges, ont été analysés à l'aide de deux modèles théoriques (Clint [1] et Motomura [2]) qui permettent de déterminer d'une part le comportement de ce mélange, et d'autre part la composition micellaire. Les résultats montrent que l'addition de FSO100 au DTAB permet d'améliorer de manière notable les propriétés micellaires par un effet de synergie. Ce comportement est dû principalement à la réduction des interactions électrostatiques répulsives entre les têtes polaires du surfactant cationique.

References

[1] J.H.Clint, J. Chem. Soc. Faraday Trans 1 71, (1975), 1 327-1334.

[2] K. Motomura, M. Arantono, K .Ogino, M.Abe, Mixed Surfactant Systems, Dekker, New York, vol 46, p99, (1993).

P31.

Etude comparative entre les deux structures GaInAsP/GaAs et GaInAsN/GaAs, Application aux lasers.

M.Berahal , H.Abid

Faculté des Sciences de l'ingénieur, Département d'électronique, laboratoire d'optoélectronique, Université Djillali LIABES de Sidi-Bel-Abbès, 22000, Algérie.

Notre étude est basée sur l'optimisation du laser à base de GaInAsP/GaAs et GaInAsN/GaAs et faire une étude comparative entre les deux structures afin d'aboutir à des résultats permettant à l'expérimentateur de faire le meilleur choix. L'optimisation de ces structures pose cependant un certain nombre de question auxquelles il faut répondre. A travers ce travail, nous répondant à ces questions afin d'aboutir à la maitrise des paramètres clé de la croissance de ces deux matériaux et à la connaissance de ses propriétés physiques intrinsèques. Notre travail se focalise sur deux grands volets qui sont la caractérisation du gain maximal, donc la recherche des valeurs max et la variation de la densité de courant de seuil (la plus importante) qui doit être minimale. L'objectif est donc d'avoir ces deux valeurs en même temps pour les deux dispositifs GaInAsP/GaAs et GaInAsN/GaAs. Pour cela il faut observer leur comportement avec toutes les grandeurs (la température, la largeur de puits, longueur de cavité) intrinsèques et extrinsèques qui permettent un choix convenable. Dans une première étape nous avons fixé la longueur d'onde de fonctionnement à 1.55%µm, afin de pouvoir observer le comportement du gain modal maximal avec les grandeurs physiques pour les deux structures, à miltipuits quantiques (MQW) et à confinement séparé à miltipuits quantiques (SCH). Apres avoir déterminé le facteur de confinement, il s'est avéré que la structure donne des valeurs très élevées par rapport à MQW. Ce facteur de confinement augmente aussi avec la largeur du puits. Le traitement du gain modal maximal nous a permis de donner une idée sur la densité des porteurs de transparence Ntr et donc la densité de porteurs de seuil Nth. Les valeurs du gain modal maximal trouvées permettent de dire que la structure SCH à plusieurs puits quantiques du système est la structure $Ga_{0.7}In_{0.3}As_{0.005}N_{0.005}$/GaAs optimale. Le model entrepris dans le calcul permet de décrire clairement les relations qui existent entre les paramètres de la structure et les caractéristiques du dispositif. Il serait facile alors de procéder à une optimisation graphique qui permet d'aboutir aux cas optimaux. Cette dernière donne les valeurs des paramètres mis en jeu dans le calcule du gain, du facteur de confinement, et du courant de seuil. Notre étude a montré que le candidat le plus prometteur sur substrat GaAs est actuellement l'alliage semi-conducteur quaternaire GaInAsN, qui devrait engendrer la commercialisation d'émetteurs dans les prochaines années.

P32.

SYNTHESE ET CARACTERISATIONS DU POLYINDANE OBTENU PAR LA POLYMERISATION DE L'INDENE EN UTILISANT LA MAGHNITE COMME CATALYSEUR

MARREF Mohamed [1] , MEGHABAR Rachid [2] , BELBACHIR Mohamed [2]

[1] Département de Chimie Industrielle, faculté des sciences, Université des Sciences et de la Technologie d'Oran, BP1505, Bir El Jir, Oran

[2] Département de Chimie, Faculté des Sciences, Université d'Oran Es-sénia

L'indène est un monomère benzocyclique insaturé. Les polyindanes obtenus par la polymérisation cationique de l'indène, en utilisant la Maghnite-H comme catalyseur sont des polymères thermoplastiques conducteurs. Ces matériaux sont utilisés dans les circuits intégrés notamment pour la protection des puces. La maghnite utilisé comme catalyseur est une argile locale extraite d'un gisement près de Maghnia, cette argile est non polluante et non toxique, et son exploitation est peu coûteuse.Dans ce travail, nous avons décrit la synthèse du matériau (Polyindane) catalysée par la Maghnite-H, ainsi que les caractéristiques et les résultats des analyses du polyindane tels que ; RMN 1H , DSC, IR et la GPC (1-2).De même, nous avons étudié en détail l'effet de la quantité de l'amorceur (Maghnite-H) ; du solvant et de la température sur le taux de conversion du matériau obtenu (Polyindane)

References

[1] O. Nuyken , M. B. Leitner , G. Maier, Makromol. Chem. 192, 307 (1991)
[2] O. Nuyken , M. B. Leitner , G. Maier, Makromol. Chem. 193 , 487 (1992)

Theoretical Chemistry

P33.

Pyrolysis of polypropylene over mesoporous MCM-48 material

A.BELLIL, L.MRAH, M.ADJIDIR, F.TOULETTE

[1] Laboratoire de Chimie Matérieux, Faculté des Sciences, Département de Chimie,
*Université d'Oran Es- Senia, 31100, Oran.*Abdelkader.bellil@yahoo.fr

The catalytic performance of mesoporous MCM-48 materials in the degradation of polypropylene (PP) was evaluated using a thermogravimetric analyzer and batch reactor. The activation energy of PP degradation was significantly lowered by the addition of Al-MCM-48. The catalytic conversion was also higher over Al-MCM-48 than over Si-MCM-48. Al-MCM-48 mainly generated C7–C10 hydrocarbons, while Si-MCM-48 exhibited a relatively broader distribution of oil products (C7–C14). Al-MCM-48 showed high catalytic stability for the PP degradation.

At present, most waste plastics in Korea are landfilled or incinerated, despite the high potential for recovering these valuable compounds. Effective methods have been sought for the recycling of waste plastics. Particularly, the recent sharp rising in oil prices may possibly make the pyrolysis of waste plastics economically competitive. The pyrolysis of waste plastics, however, has suffered from the disadvantages of a broad product spectrum and high energy input [1]. Catalytic pyrolysis can improve the product selectivity and reduce the energy input. Most previous studies on the catalytic pyrolysis of waste plastics have used microporous materials, such as zeolites [2–5]. Owing to their large pore openings, mesoporous materials have the advantage of higher accessibility of bulky substances, such as HDPE, to their inner active sites. Recently, MCM-41 [6], which is one of the most common mesoporous catalysts, was reported to allow higher conversion and excellent selectivity for gasoline [7]. However, few studies have been performed on the application of MCM-48, which contains three-dimensional pore openings, to the pyrolysis of polypropylene (PP). As MCM-48 is expected to be resistant to pore blocking, it also would be expected to exhibit much higher activity than MCM-41, which has only onedimensional openings [8,9]. This paper addresses the catalytic performance of MCM-48 on the pyrolysis of PP with regard to the pyrolysis kinetics and product characteristics.

Fig. 1 shows the XRD patterns of Si-MCM-48, Al-MCM-48 (Si/Al ¼ 30) and Al-MCM-48 (Si/Al ¼ 60). The XRD pattern of Si-MCM-48, synthesized using a surfactant blend of CTAB and Brij-30, clearly showed eight peaks, consistent with 211, 220, 321, 400, 420, 332, 422 and 431 planes. The unit cell parameter (a0) calculated from the d-spacing value of the 211 plane was 9.40 nm. The XRD patterns of Al-MCM-48 materials exhibited similar to that of Si-MCM-48, with the exception of a slightly contracted unit cell parameter, which might have been due to the heat treatment at 550 1C following the incorporation of Al. The nitrogen adsorption–desorption isotherm and corresponding pore size distribution obtained for MCM-48 exhibited sharp in□ections characteristic of the sorption of capillary condensation for pores with a diameter of about 2.6 nm. As shown in Table 1, the Si-MCM-48, Al-MCM-48 (Si/Al ¼ 60) and Al-MCM-48 (Si/Al ¼ 30) showed high BET surface areas of 1035, 996 and 994 m2 g 1, and total pore volumes of 1.01, 0.86 and 0.85 cm3 g 1, respectively.From Fig. 2, it could be seen that the incorporation of aluminum into the mesoporous silica material generated higher acid sites which are required for acid-catalyzed reactions, whereas, the pure silica materials did not possess

sufficient intrinsic acidity or reactivity for use as a catalyst. In addition, there are more acid sites in the Al-MCM-48 (Si/Al ¼ 30) than in the Al-MCM-48 (Si/Al ¼ 60). This indicates that the number of acid sites increases with the rise of the aluminium content.

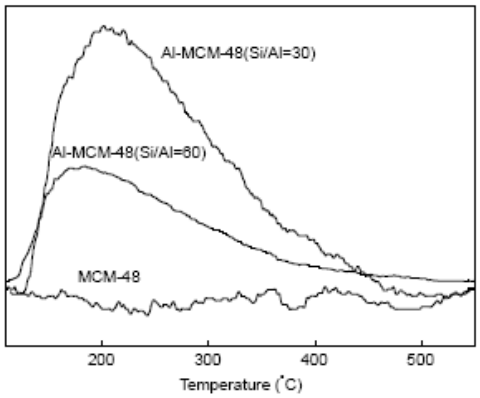

Fig. 2. NH3 TPD of MCM-48 materials

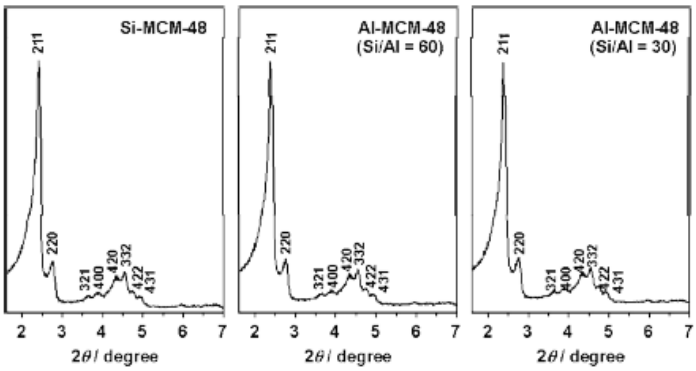

Fig. 1. XRD patterns of calcined

3. Si-MCM-48, Al-MCM-48 (Si/Al ¼ 60) and Al-MCM-48 (Si/Al ¼ 30) materials reduced the temperatures required for the degradation of PP to 440, 335 and 320 1C, respectively, compared to the 475 1C required for thermal degradation alone. Table 2 shows the results of the apparent activation energies for the degradation of PP over these catalysts. The activation energies over Al-MCM-48 materials were much lower than over Si-MCM-48. This result suggests that Al-MCM-48 material may be a promising catalyst for the degradation of PP. Table 3 shows the product distribution obtained for the degradation of PP. The conversion via catalytic degradation was much higher than via thermal degradation. Particularly, Al-MCM-48 (Si/Al ¼ 30) exhibited better activity than Al-MCM-48 (Si/Al ¼ 60) due to the higher amount of acid sites, indicating that the catalytic activity is closely related to the amount of acid sites. Fig. 3 shows the oil product distribution over MCM-48 catalysts. Al-MCM-48 materials mainly generated C7–C10 hydrocarbons, while Si-MCM-48 exhibited a relatively broader distribution of oil products (C7–C14). Table 4 shows that gas product distribution is almost the same irrespective of catalysts. Fig. 4 shows the TG curves obtained from five replicate TGA experiments for the degradation of PP over Al-MCM-48, without any regeneration of the catalyst. During each run, Al-MCM-48 showed similar degradation curves, which was mainly due to the three-dimensional pore structure of Al-MCM-48 that may resist the generation of coke. Furthermore, as shown in Table 5, the catalytic activity of three-dimensional Al-MCM-48 was maintained during the repetitive experiments, while that of one-dimensional Al-MCM-41 was gradually decreased. This suggests that for PP degradation, Al-MCM-48 is the superior catalyst to Al-MCM-41.

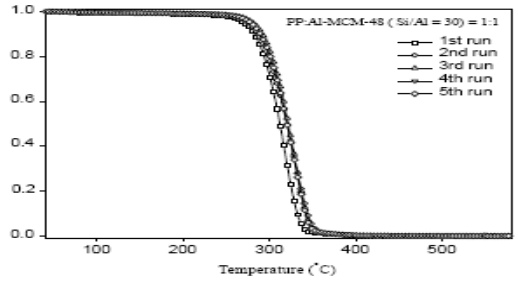

Fig. 4. TG curves of five repetitive c atalytic degradation of PP over Al-

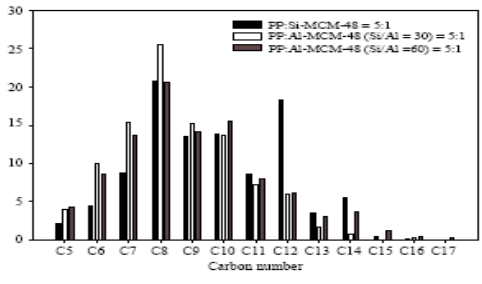

Fig. 3. Product distribution of oil.

Mesoporous MCM-48 materials were employed as catalysts for the degradation of PP. The catalytic activity of Al-MCM-48 was much higher than that of Si-MCM-48. Al-MCM-48 mainly generated C7–C10 hydrocarbons, while Si-MCM-48 exhibited a relatively broader distribution of oil products (C7–C14). Al-MCM-48 showed high catalytic stability for the degradation of PP. In view of these facts, Al-MCM-48 can be considered a promising catalyst for the degradation of other waste plastics.

References

[1] J. Schormer, J.S. Kim, E. Klemm, J. Anal. Appl. Pyrolysis 60 (2001) 205.
[2] R.C. Mordi, R. Fields, J. Dwyer, J. Anal. Appl. Pyrolysis 29 (1994) 45.
[3] G. Manos, A. Garforth, J. Dwyer, Ind. Eng. Chem. Res. 39 (2000) 1198.
[4] J.W. Park, J.H. Kim, G. Seo, Polym. Degrad. Stab. 76 (2002) 495.
[5] R. Bargi, P.T. Williams, J. Anal. Appl. Pyrolysis 63 (2002) 29.
[6] C.T. Kresge, M.E. Leonowicz, W.J. Roth, J.C. Vartuli, J.S. Beck, Nature 359 (1992) 710.
[7] J. Aguado, J.L. Sotelo, D.P. Serrano, J.A. Calles, J.M. Escola, Energy Fuels 11 (1997) 1225.
[8] S.E. Dapurkar, P. Selvam, Appl. Catal. A, Gen. 254 (2003) 239.
[9] P. Selvam, S.E. Dapurkar, Catal. Today 96 (2003) 135.
[10] R. Ryoo, J.M. Kim, J. Chem. Soc., Chem. Commun. (1995) 711.
[11] R. Ryoo, S. Jun, J.M. Kim, Chem. Commun. (1997) 2255.
[12] H.J. Park, Y.K. Park, J.I. Dong, J.K. Jeon, J.H. Yim, K.E. Jeong, Res. Chem. Intermed. (2007) in press.

P34.

DFT study of the reactivity and the aromaticity of simazine using the rotational energy barrier

S. Bitam[1], B. Faycel[2]

[1] Laboratoire C.C.E Faculté des Sciences-Université de Batna 05000, Algérie, bitam_said@yahoo.fr
[2] Laboratoire C.C.E Faculté des Sciences-Université de Batna 05000, Algérie.

Simazine (2-chloro-4, 6-bis (ethylamino)-s-triazine)(**Fig.1**) is in the family of s-triazine herbicides, it is generally considered as non-toxic for most species [1, 2].

The aim of this work is the analysis of the aromaticity and the toxicity of Simazine using the rotational energy barrier as well as some conceptual DFT theory based global reactivity descriptors. Recently it has been shown that local aromaticity my defined strongly on the nature of the topological [3, 4] and chemical environment [5, 6]. The most widely employed method to analyze the aromaticity is the NICS index. This descriptor of aromaticity was proposed by Schleyer et al. [7] as a magnetic index of aromaticity. It is defined as the negative value of the absolute shielding computed at a ring center or at some other interesting point of the system, usually above the ring center. Rings with large negative NICS values are considered aromatic. The more negative the NICS values, the more aromatic the rings are. Non-aromatic species have NICS values close to zero and positive NICS values are indicative of antiaromaticity.

Another method to analyze the aromaticity is the electrophilicity index (ω), it is defined within a density functional theory (DFT) [8] framework, by Parr et al [9] .as a measure of energy lowering due to maximal electron flow between a donor and an acceptor.

All calculations reported in this work were performed by means of the GAUSSIAN 03 [10] computational package. The gas-phase optimized geometries reported here were calculated in the framework of density-functional theory (DFT) using the B3LYP functional [11] which combines the three parameter Becke's exchange non-local functional [12] and the transformed form [13] of Lee–Yang–Parr's correlation non-local functional [14]. NICS values were also computed with the DFT/6-31G (d, p) method through the gauge-including atomic orbital method (GIAO) [15]. The magnetic shielding tensor was calculated for ghost atoms located at the ring critical point (RCP), These values are denoted as NICS (0), according to the practice described by Schleyer et al. who calculated the NICS at the geometrical center (GC) of the ring.

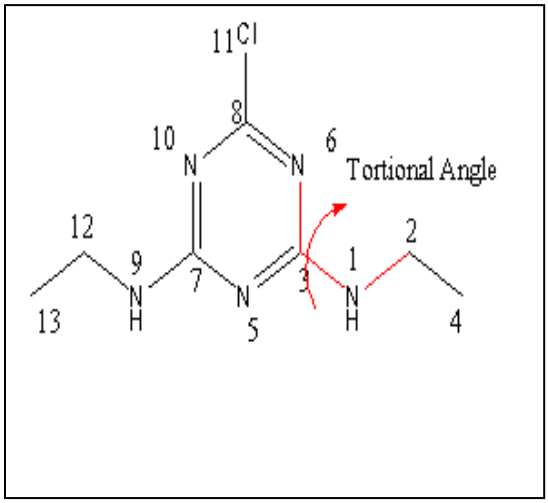

Fig. 1. Simazine structure

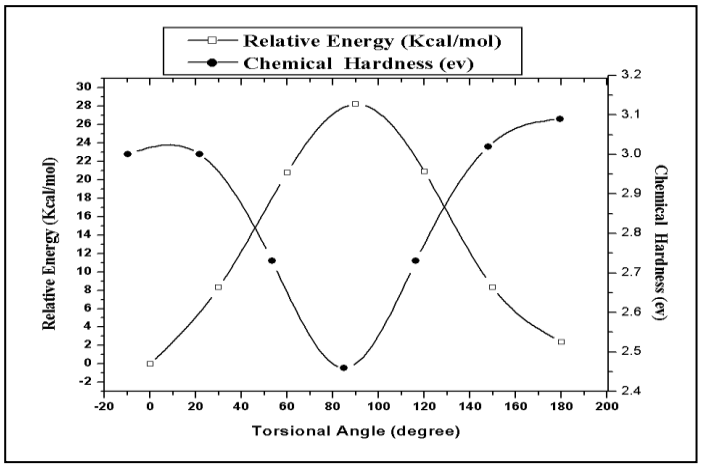

Fig. 2. Relative energy and Chemical Hardness

All calculations that we performed shows that simazine have a non-toxic effect in its stable conformation ($\phi = 0°$). It presents a low electrophilicity value at this state, witch means a low reactivity /toxicity of this molecule, a large gap between HOMO and LUMO mean that the electron distribution resists rearrangement even when the perturbation is moderately strong. It has NICS values close to zero, witch mean that it is non-aromatic molecule. So we can suggest that the toxicity effect of simazine appears after its bio/photo degradability.

References

[1] C.R. Worthing (Ed.), The Pesticide Manual, 8th ed.,British Crop Protection Council, 1987.
[2] N.Frank, Chemicals to control algae. The use of simazine,Aquat. Gard. 1991 4, 190.
[3] Krygowski, T. M.; Ciesielski, A.; Bird, C. W. and Kotschy, A. J. Chem. Inf: Comput. Sci..1995,35, 203.
[4] Krygowski,T.M.; Cyratiski, M.; Ciesielski, A.; Swirska, B.; Leszczyhski, P. J. Chem. Inj Comput. Sci.,1996 in press
[5] Krygowski, T. M. J. Chem. Inj Comput. Sci., 1993,33, 70.
[6] Cyranski, M.; Krygowski, T.M. J. Chem. II$ Comput. Sci., 1996 in press.
[7] P.v.R. Schleyer, C. Maerker, A. Dransfeld, H. Jiao, N.J.R. van Eikema Hommes, J. Am. Chem. Soc. 1996,118, 6317 Press: Oxford UK, 1989.
[8] Parr, R. G.; Yang, W. Density functional Theory of Atoms and Molecules; Oxford University.
[9] Parr ,R. G,;Szentpaly, L. V.;Liu, S. J. Am. Chem. Soc. 1999,121, 1922.
[10] J. Frisch, G.W. Trucks, H.B. Schlegel, G.E. Scuseria, M.A. Robb,J.R. Cheeseman, J.A. Montgomery Jr., T. Vreven, K.N. Kudin, J.C.Burant, J.M. Millam, S.S. Iyengar, J. Tomasi, V. Barone, B.Mennucci, M. Cossi, G. Scalmani, N. Rega, G.A. Petersson,H. Nakatsuji, M. Hada, M. Ehara, K. Toyota, R. Fukuda, J. Hasegawa,M. Ishida, T. Nakajima, Y. Honda, O. Kitao, H. Nakai, M. Klene, X.Li, J.E. Knox, H.P. Hratchian, J.B. Cross, C. Adamo, J. Jaramillo, R.Gomperts, R.E. Stratmann, O. Yazyev, A.J. Austin, R. Cammi,C. Pomelli, J.W. Ochterski, P.Y. Ayala, K. Morokuma, G.A. Voth, P.Salvador, J.J. Dannenberg, V.G. Zakrzewski, S. Dapprich, A.D.Daniels, M.C. Strain, O. Farkas, D.K. Malick, A.D. Rabuck, K.Raghavachari, J.B. Foresman, J.V. Ortiz, Q. Cui, A.G. Baboul,S. Clifford, J. Cioslowski, B.B. Stefanov, G. Liu, A.Liashenko, P.Piskorz, I. Komaromi, R.L. Martin, D.J.Fox,T.Keith,M.A.AlLaham,C.Y.Peng,A.Nanayakkara,M.Challacombe,P.M.W.Gill,B.Johnson,W.Chen,M .W.Wong,C.Gonzalez,J.A.Pople,Gaussian03,RevisionB.05,Gaussian,Inc.,PittsburghPA,2003
[11] P.J. Stephens, F.J. Devlin, C.F. Chabalowski,M.J.

P35.

Etude théorique de la réaction de Diels-Alder par le calcul DFT.

Bouacha Samir, A.H Djerourou*.

Laboratoire de Synthèse et Biocatalyse Organique. BP. 12. 23000. Annaba. Algérie.
Email: bouachasamir10@yahoo.fr

Les réactions de Diels-Alder sont largement utilisées dans la synthèse des composés cycliques et hétérocycliques pentagonaux d'intérêt pharmacologique et d'activité biologique.

Dans ce travail, on se propose d'étudier théoriquement le mécanisme, la régioselectivité et la stéréoselectivité de la réaction de Diels-Alder entre le composé A et B pour former deux stéréoisomères endo et exo respectivement. La réaction est concertée et le produit endo est majoritaire (voir la figure. I).

Les calculs ont été effectuées au niveau B3LYP/6-31G* en phase gazeuse. Nous avons menés une étude théorique en se basant sur les approches théoriques suivantes:

La théorie de l'état de transition, le calcul des barrières d'activation et les indices de réactivité.

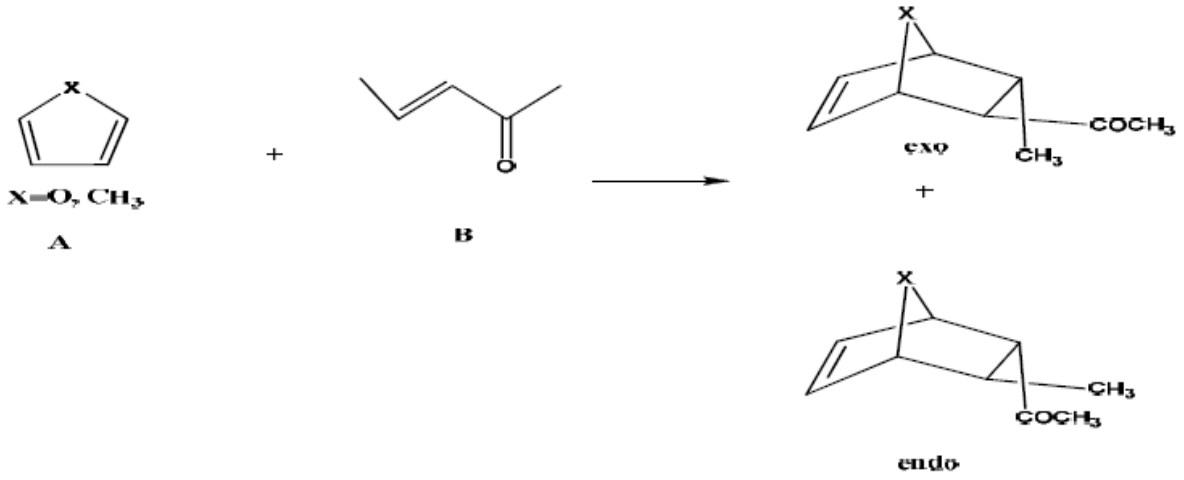

Figure 1.

Références :
[1]Luis R. Domingo* Mini-Reviews in Organic Chemistry, 2005, 2, 47-57.
[2] A.F. Jalbout et al. / Spectrochimica Acta Part A 60 , 2004, 603–609.
[3] J. Chem. Sci., Vol. 117, No. 5, September 2005, pp. 561–571.

P36.

Etude théorique d'un ligand photochrome original à base de dithiényléthène

F. Ibersiene[1], D. Hammoutène[1], A. Boucekkine[2],

V. Guerchais[2], H. Le Bozec[2]

[1] Sciences Chimiques de Rennes, UMR CNRS-Université de Rennes 1 6226, Campus de Beaulieu, 35042 Rennes Cedex, France
[2] Laboratoire de Thermodynamique et Modélisation Moléculaire, Faculté de Chimie, USTHB BP 32, El Alia 16111 Bab Ezzouar, Alger, Algeria

Le photochromisme, changement de couleur sous l'action de la lumière, provient de la propriété que possèdent certaines molécules de commuter de façon réversible sous l'irradiation entre deux formes ayant des spectres d'absorption dans le visible, différents [1,3].

Le photochromisme peut résulter d'une isomérisation cis-trans, d'une électrocyclisation ou d'un transfert de proton.

Les matériaux photochromes jouent un rôle important dans les applications où un changement contrôlé de la couleur est utilisé. Ils peuvent trouver une application dans le domaine de l'affichage, l'imagerie, le stockage et le traitement de l'information, ou les verres optiques.

Dans ce travail, nous présentons l'étude théorique des deux formes, ouverte et fermée, d'un composé photochrome récemment synthétisé [4]. Les calculs menés au niveau TD-DFT [5] et utilisant la fonctionnelle PBE0 et la base LANL2DZ polarisée ont permis une caractérisation complète de ces systèmes. Les résultats obtenus sont utilisés pour expliquer le spectre UV/Visible observé. De plus, il a été montré que, grâce à la propriété de photochromisme de ce composé, ses complexes avec des métaux de transition servent d'interrupteur et sont ainsi de bons candidats pour des applications dans le domaine de la luminescence.

Références

[1] Ting-feng Tan, Pei-li Chen, Hua-ming Huang, Ji-ben Meng, Tetrahedron, 61, 8192, 2005
[2] Xu Li, Zhiyi Song, Yong Chen, Jiben Meng, J.Mol.Struct., 748, 161, 2005
[3] J. Berthet, V. Lokshin, M. Valès, A. Samat, G. Vermeersch, S. Delbaere, Tetrahedron Letters, 46, 6319, 2005
[4] V. Aubert, Thèse de Doctorat de l'Université de Rennes1, 2007.
[5] Gaussian03, voir www.gaussian.com pour plus de détails.

P37.

Etudes théoriques de l'inhibition de la corrosion de l'acier par des dérivés de la thiourée

A. Kheddaoui[1], A. Rahmouni[2] et O. Benali[3]

[1] Laboratoire de modélisation et des méthodes de calcul, Centre universitaire de Saida, B.P. 138, Cité En Nasr, 20002, Algérie

[2] Laboratoire de modélisation et des méthodes de calcul, Centre universitaire de Saida, B.P. 138, Cité En Nasr, 20002, Algérie.

[3] Laboratoire de Spectrochimie et méthodes d'Analyse, Université de Tlemcen, B.P. 119,13000, Algérie.

Les inhibiteurs de la corrosion sont utilisés généralement pour contrôler la dissolution du métal. La plupart de ces inhibiteurs bien connus sont des composés organiques qui contiennent du carbone, l'azote, le soufre et l'oxygène. Parmi ces inhibiteurs on note la thiourée et ses dérivés [1]qui font l'objet de notre travail. Ces composés sont utilisés largement comme inhibiteurs acides dans l'industrie sidérurgique et dans l'industrie pétrolier, pour différentes opérations, tel que conservation, détartrage et nettoyage, des métaux ferrique et alliages [2, 3]. L'étude de processus de la corrosion de l'acier en milieu acide chlorhydrique puis en milieu acide sulfurique et son inhibition par les composés organiques thiourée et ses dérivés est un domaine de recherche très actif, où seules quelques études basées sur les calculs de la chimie quantique ont été réalisées.

Notre travail consiste en la détermination de paramètres quantiques, souvent cités en relation avec le taux d'inhibition de corrosion, de quelques dérivés de la thiourée (Fig 1). Il s'agit de l'énergie de la HOMO, l'énergie de la LUMO, le gaps HOMO-LUMO,le potentiel d'ionisation, le moment dipolaire, les charges atomiques et les indices de Fukui. Différentes méthodes de la chimie quantique telles que : HF, MP2, MNDO, AM1, PM3 et DFT sont utilisées.

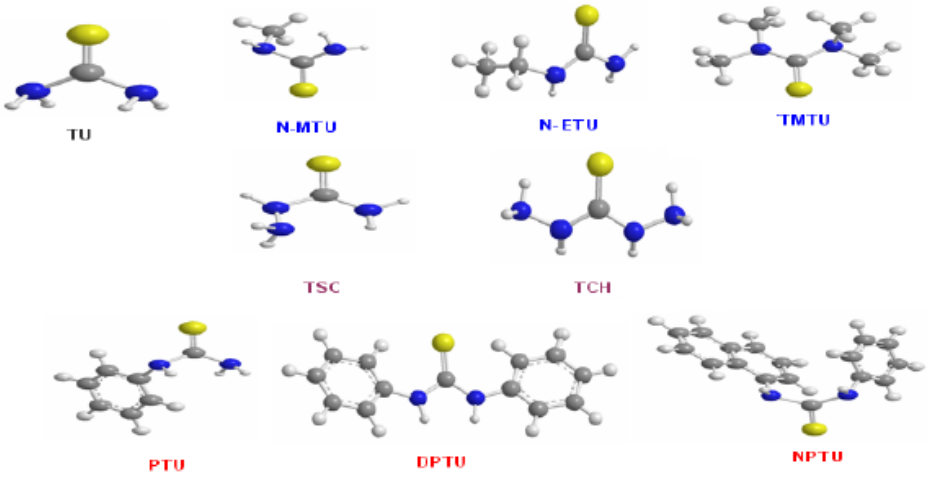

Fig 1 : La structure moléculaire de la thiourée et ses dérivés (**TU**: Thiourée, **N-MTU**: N, methylthiourée **N-ETU**: N-ethylthiourée, **TMTU**:Tetramethylthiourée, **TSC**: Thiosemicarbazide , **TCH**:Thiocarbohydrazide)

Nous avons effectués des calculs d'optimisations de géométrie à différents degré de précision a fin de déterminer de quelques paramètres quantiques, souvent cités en relation avec le taux d'inhibition de corrosion, de quelques dérivés de la thiourée. IL s'agit du moment dipolaire, le potentiel d'ionisation, l'énergie de la HOMO, l'énergie de la LUMO, les gaps énergétiques HOMO-LUMO, les charges des atomes et les indices de Fukui sont également effectuées. Différentes méthodes de la chimie quantique sont utilisées telles que : AM1 , PM3,MNDO qui sont implémentés dans le Mopac 2000 [4],aussi des calculs au niveau HF, MP2 et DFT (avec les deux fonctionnelles B3LYP et B3PW91) par le Gaussian 03 [5] selon la base 6-31g(d).Un essai de corrélation entre le taux d'inhibition de corrosion et des paramètres quantiques sera présenté.

D'après le travail fait, on conclue que:
- L'efficacité inhibitrice de la corrosion de l'acier en milieu acide varié selon les paramètres quantiques suivants: Le moment dipolaire, le potentiel d'ionisation et l'énergie de la HOMO
- L'EI de la corrosion n'est pas corrélé avec l'ELUMO et le gap énergétique.
- Les inhibiteurs thiourée de la corrosion qui portant des forts radicaux donneurs sont plus efficaces contre la corrosion de l'acier en milieu acide Chlorhydrique.
- La charge négative élevé sur l'atome du Soufre des inhibiteurs de la thiourée est confirme leur caractère nucléotidique.
- l'indice de Fukui correspondant à l'atome " S " est plus grand que celui correspondant aux atomes " N ", il en résulte que l'attaque électrophile se fait préférentiellement sur l'atome du Soufre

References

[1] A. E. Stoyanova, S.D.Peyerimhoff, Electrochimica Acta.47,(2002), 1365.
[2] F. Kandemirli, S. Sagdinc, Corr Sci, 49,(2007),2118.
[3] O. Benali , L. Larabi, S. M.Mekalleche ,Y. Harek, J. Mater, Corr. Sci., 41 (2006) 7064.
[4]CS Chemoffice Drawing, Modeling and Information, 100 CambridgePark Drive Cambridge,MA 02140,USA.
[5] M. J. Frisch & Coll,Gaussian 03, Revision C.02, Gaussian, Inc., Wallingford CT, 2004.

P38.

The Study Of Homo Energy For Showing The Basicity And Mülliken Charges On Nitrogen Atoms Obtained By The Semiempirical And Ab Initio Methods In Aniline And Substituted Anilines

N.S. LABIDI1*, A. DJEBAILI2

1Department of chemistry, Faculty of sciences, University of the sciences and technology of Oran (U.S.T.O.MB), BP-1505 ORAN El-M'naouer (31000), Algeria. E-mail : labidi2006@univ-usto.dz
²Department of chemistry, Faculty of sciences, University of BATNA-05000- Algeria

Relationships between the HOMO energy, basicity pKa and Hamett constant $\sigma_{(p)}$ sigma in in aniline and substituted anilines . A linear relationships was found between the HOMO energies obtained by the AM1, HF/3-21G and HF/6-31G methods and pKa was found. The same linear relationships was found between the HOMO energies obtained by these methods and $\sigma_{(p)}$ .Thus, the HOMO energy can adopted instead of pKa and $\sigma_{(p)}$ for choosing the substituents in organic reaction. Mülliken charges on nitrogen atoms were calculated for several aniline and substituted anilines, utilizing the semiempirical and Ab initio methods, relating their values to experimental aromatic amine pKa. Direct relation between pKa and nitrogen charges was found.

Aromatic amines are very important in biological as well as in materials science [1,2]. Particularly, aniline was studied because of its technological application in a vast amount of industrial processes [3,4].In fact, it was used as a precursor for the synthesis of dye and sensitizer molecules, for the synthesis of molecules having potential large non-linear optical Responses, etc [5,6].

Aniline is the classic molecular model for aromatic amines [7]. Several theoretical studies including semiempirical [8–10] and Ab initio calculations [11–13] were carried out to determine the structural and electronic properties of aniline. The inclusion of a substituents groups (–OCH_3, –CH_3, –F, –Cl, –CF_3, –CN, –NO_2) in the aniline leads to the variation of the charge distribution in the molecule, and consequently this greatly affects the structural as well as the electronic parameters [14–15]. There is a very close relationship between the strength of the substituents, the charge of the amine group, the IP, and the basicity of the system [16]. Consequently, the IP, as well as the charge distribution of substituted anilines, should contain a lot of information relevant to practical purposes. Exact quantitative basicity data are very important in applying bases in various fields of chemistry and in designing new bases with desired proprieties. Thus, it is most necessary to discuss a new approach by semiempirical and Ab initio methods for showing pKa of the aromatic primary amines. In this paper, it is reported that the HOMO energies obtained by semi empirical and Ab initio methods [17,18] using Hyperchem (7.0) packages[19] , can be adopted instead of pKa as a new method for showing the basicity of aromatic primary amines. Further more, the relationship between the HOMO energy, pKa and the substituents constant $\sigma_{(p)}$ were reported. Since the Mülliken charges on nitrogen atoms are important as means to investigate the electronic structure of aniline and substituted anilines.

The computations of the aniline and substituted anilines Table1 were performed using Hyperchem packages (Molecular Modelling System) [19] Intel Pentium P4 2002 XP (512 Mb RAM) with the Windows XP operating system. This package can be used to study the electronic structure and energy of ground and excited states of atoms, molecules, ions, first hyperpolarizability etc...

The aniline and substituted anilines structures were initially optimized by Molecular Mechanics calculation with a modified AMBER96 force field [22]. A trial of the electronic calculation method more suitable to our purpose was carried out by single point calculation for the resulting structures using the following Quantum Chemistry methods: a) Semi-empirical: Extended Hückel(EH) [23] and INDO[24] ,MNDO[25] ,PM3and AM1[26] ; b) *Ab initio* procedure with a minimal HF/3-21G, and HF/6-31G[11-13].

Table 1: Aniline and substituted anilines Compounds

Compound	pKa [20]	$\sigma_{(p)}$ [21] Hamett constants
Aniline	30.6	-
p-Toluidine	31.10	-0.17
4-Aminobenzonitrile	25.3	0.66
4-Nitrobenzenamine	20.9	0.78
4-Fluorobenzenamine	30.7	0.06
4-Chlorobenzenamine	29.4	0.23
4-Trifluoromethyl)benzenamine	27.0	0.54
1-(4-aminophenyl)ethanone	25.35	0.50
4-Bromobenzenamine	29.1	0.23

In order to investigate the relationships between the HOMO energy and the degree of electron density in aniline and substituted anilines compounds (1-8), were computed by (AM1, EH, MNDO, INDO, PM3**)** methods. The AM1 method gave a better correlation coefficient (R) for the individual data points in relation to the line fitted to this plot, under linear regression calculation of HOMO= f(pKa) Table 2. These results, summed to the fact that the AM1 method is the more precise semi-empirical Quantum Chemical method available. Linear dependences were found between HOMO energies obtained by the HF/3-21G and HF/6-31G methods methods. From these results, it is clarified that as there are close relationships between pKa, $\sigma_{(p)}$,and HOMO energies obtained by AM1 and HF/3-21G methods. Thus HOMO energies can be used instead of pKa as a new method for considering the electron donation in aniline and substituted anilines compounds (1-8) in organic reactions.

Table2: Correlation coefficients of the regression lines

calculated by different quantum chemical methods

Methods	HOMO= f (pKa)	HOMO= f (σ_p)

	Correlation Coffecient (R)	Correlation Coffecient (R)
AM1	0.89598	0.93344
EH	0.77729	0.70724
MNDO	0.84791	0.86727
INDO	0.18464	0.33168
PM3	0.87805	0.81113
HF/3-21G	0.87124	0.92358
HF/6-31G	0.86267	0.91593

The AM1 method gave a better correlation coefficient (R = 0.95) for the individual data points in relation to the line fitted to this plot, under linear regression calculation of pK_a= f (N charge) Figure 1. The HF/3-21G and MNDO methods show little sensibility to detect aromatic amine nitrogen charge variation in (-NH_2) group. By this point of view, the Ab initio calculation with the small basis set HF/3-21G gave the poorest result, showing very little charge variation and several identical N charge values for different aromatic amine. More sensible methods are EH, AM1 and HF/6-31G.

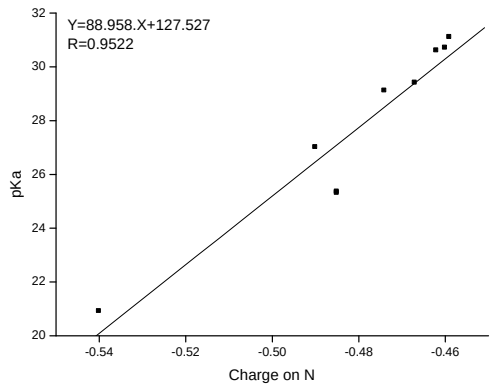

Fig. 1. Relationship between pK_a and (AM1) calculated N Mülliken charges on N of (-NH_2)

In conclusion, it is possible to correlate the calculated HOMO energies obtained by the semi- empirical and Ab initio methods with the aromatic amine basicity. Linear relation ships between pKa and the

HOMO energies obtained by the AM1 and HF/3-21G were found. Linear relationships between the HOMO energies obtained by these methods and $\sigma_{(p)}$ were also found. It is clarified that the HOMO energies in aniline and substituted anilines are useful to elucidate the change of pKa caused by substituents and can be used when choosing donors in various chemical reactions. Furthermore, it is possible to correlate the calculated electronic charge on aromatic amine nitrogen with the aromatic amine basicity. For the studied aniline and substituted anilines, whose pK_a vary little from one to the other, the nitrogen charges also do not show major changes. Hence, although sensibility of the method is not very good, it may be considered as useful for semi-quantitative determination of pKa of donors in organic reactions.

Reference

[1] F.Kippert, D.Lloyd, FEMS Microbial Lett, 132,215 (1994).
[2] L.Olmedo, P.Hourquebie, F.Jousse,in: H.S. Nalwa (Ed.),Handbook of Organic Conductive Molecules and Polymers, 3,Chichester, UK, 1997, pp. 367.
[3] A.G.MacDiarmid, A.J.Epstein, in: Jenekhe,S.A., Wynne K.J., (Eds.), Photonic and Optoelectronic Polymers, American Chemical Society, Washington, DC, 1997, pp. 395.
[4] A.J.Epstein, M.R.S. Bull, 22, 16 (1997).
[5] N. E.Agbor, Cresswell,J. P., Petty,M. C., Monkman,Sensors, A. P., and B.,Actuators: Chemical., 41 :137 (1997).
[6] J.O.Morley, J. Phys. Chem, 99, 1923 (1995).
[7] Y.Wang, S.Saebø, C.U.Pittman, J. Mol. Struct, (Theochem) 281, 91(1993).
[8] W.J.Hehre, L.Radom, J.A. Pople, J. Am. Chem. Soc, 94 ,1496 (1972).
[9] W.J.E.Parr , R.E.Wasylishen, J. Mol.Struct, 38, 272 (1977).
[10] A.D.Gorse, M.Pesquer, J. Mol. Struct, (Theochem), 281,21 (1993).

P39.

A DFT Study of the Competitive Pathways [4+2] vs. [2+2] of the Cycloaddition of 1,3-diazabuta-1,3-diene derivative with Chloroketene

B. Messaoudi and S. M. Mekelleche

Département de Chimie, Faculté des Sciences, Université A. Belkaid, Tlemcen, B.P : 119, Algérie, 13000
b_messaoudi@mail.univ-tlemcen.dz, sm_mekelleche@mail.univ-tlemcen.dz

Cycloaddition reactionsCycloaddition reactions of 1,3-diazadienes are of great importance in heterocyclic synthesis with pharmacological interest. The [2+2] cycloaddition of 1,3-diazadienes with ketenes yields to the formation of azetidinones while the [4+2] cycloaddition yields to the formation of pyrimidinones.

In the present work, we present a theoretical study of the reaction mechanism of the cycloaddition of 1-benzyl-2,4-diphenyl-1,3-diazabuta-1,3-dienes with chloroketene (**Figure 1**). The two possible reaction pathways [2+2]/[4+2] are discussed by the analysis of potential energy surface and DFT-

based reactivity indexes. Our calculations show that this cycloaddition takes place along a stepwise mechanism. The first step, which corresponds to the formation of the zwitterionic intermediate, is rationalized by Domingo's polar model predicting the most favorable electrophile/nucleophile interaction. The second step (ring closure) leading to the formation of either the [2+2] or [4+2] cycloadduct, is rationalized by the electrostatic interaction between the most electrophilic site and the most nucleophilic site of the zwitterionic intermediate. Reaction enthalpies and activation energies have been calculated to predict the thermodynamic and the kinetic controls. Quantum chemistry calculations were carried out at the B3LYP/6-31G* level of theory and are in good agreement with experiment.

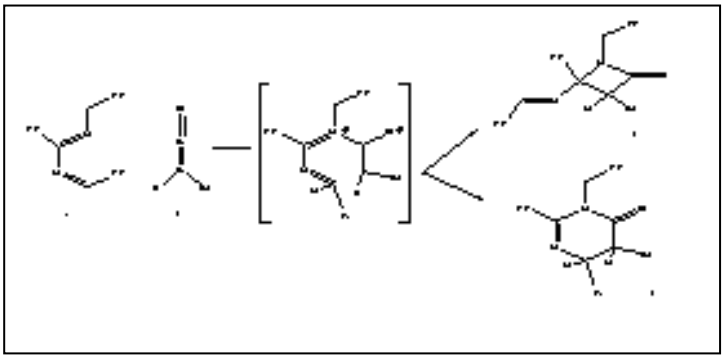

Fig. 1. [4+2]/[2+2] Cycloadditions; Conceptual DFT; Polar Model; Reaction Mechanism.

References

[1] J. Barluenga, M. Tomas, Synthesis of Heterocycles from Azadienes. In Advances from Heterocycles Chemistry, Katritzky, A. RED, Academic Press, Inc: **61** (1993).
[2] E. Rossi, G. Abbiati, E. Pini, Tetrahedron, 53, No. **41** (1997) , 14107.
[3] L. R. Domingo et al, Tetrahedron, **58** (2002) 4417.

P40.

Structural and DFT Studies of

tétra (m-carboxyphenylammonium perchlorate)

S. Farah[1], B. Zouchoune[1, 2]

[1]Laboratoire de Chimie Moléculaire, du contrôle de l'Environnement et des Mesures Physico-Chimique (LACMOM), Université Mentouri de Constantine.

[2]Laboratoire de Chimie Appliquée et Technologie des Matériaux, Centre Universitaire Larbi Ben M'hidi, (04000) Oum-El-Bouaghi, Algérie.

During our investigating on compounds rich in hydrogen bonding [1,2], the title compound tétra (m-carboxyphenylammonium perchlorate) has been isolated. This compound of formula $4C_7H_8NO_2^+$. 4 ClO_4^- crystallizes in P 2_1 space group. The asymmetric unit of this compound is constituted of four monoprotonated cations m-carboxyphenylammonium and four anions perchlorate, of which two present disorders that appears by the thermal agitation of all the entity including the atom of chlorine. The crystalline structure of this compound is formed by an alternation of double cationic and anionic layers that spreads out in the same way to the plan (a,b). The cohesion between the different entities is assured by a three-dimensional network of hydrogen bonding, moderate of type Ô-H…O and N-H...O, and weak of type C-H…O. These hydrogen bondings are established between the cations and between the cations and the anions.

In this work, we have calculated the geometry of m-carboxyphenylammonium cations and perchlorate anions using DFT method (Density functional theory) [3] which showed a relatively strong hydrogen bonds, where NH3 groups highlight significant distortion with respect to the tetrahedral symmetry. The presence of an intermolecular hydrogen bond of type O-H…O, N─H…O and C-H…O leads to the stabilisation of the studied species.

References

[1] L. Bendjeddou, A. Cherouana, F. Berrah, N. Benali-cherif, Acta Crist. **E59** (2003), o576-o570.
[2] A. Cherouana, L. Bendjeddou, N. Benali-Cherif, Acta Crist. **E59** (2003), o1790-o1792.
[3] J.Bernstein, R.E.Davis, L. Shimoni, and N.-L. Chang,Patterns in hydrogen bonding: Functionality and graph set analysis in crystal, Angew chem. int ED Engl **34** (1995), 1555-73.

P41.

Etude théorique de nouveaux composés aromatiques à base de germanium Nitration du 1-Méthyle-Germine

S. Zaater[1], M. Brahimi[1] et A. Rahmouni [2]

1Laboratoire de physico-chimie théorique et de chimie informatique, faculté de Chimie. USTHB. BP N° 32 El Alia, Alger, Algérie.
2Laboratoire de modélisation et méthodes de calcul, Centre Universitaire de Saida, Algérie.

Dans ce travail on étudie l'effet, de la substitution d'un atome de carbone par le germanium dans le cycle benzénique du toluène, sur la régio-sélectivité de la substitution électrophile. A cet effet, on a fait une étude théorique du mécanisme de réaction de nitration du 1-methyle-germine. Celui-ci est comparé à la nitration du toluène. Tous les calculs sont fait au niveau **H**artree-**F**ock (**HF**/6-31G*) de Gaussian03W.

La nitration des composés aromatiques est un procédé industriel très important. L'introduction du groupement NO_2 dans les molécules aromatiques conduit à la formation d'intermédiaires qui jouent un rôle important dans la synthèse des composés pharmaceutiques, des parfums, des pesticides, des explosives, des polymères et des fertilisants.

La nitration du toluène conduit à la formation de trois isomères : l'ortho, le méta et le paranitrotoluène. Expérimentalement, les composés majoritaires sont l'**O**rtho**N**itro**T**oluène (**ONT**) et le **P**ara**N**itro**T**oluène (**PNT**) alors que le **M**éta**N**itro**T**oluène (**MNT**) est obtenu en faible quantité. Cela est du au groupement méthyle qui est ortho et para directeur. Dans le cas des isomères **MNT** et **PNT** le groupement $-NO_2$ est coplanaire au cycle benzénique alors que dans le cas de l'**ONT** le $-NO_2$ présente un écart à la planéité. Cette distorsion est provoquée par une importante répulsion stérique entre les deux groupements $-CH_3$ et $-NO_2$.

Dans ce travail, on s'est intéressé, dans un premier temps, à l'étude du mécanisme réactionnel de la nitration du toluène **[1-4] (figure 1)**.

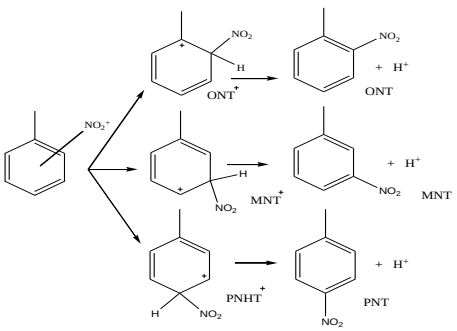

Fig.1. mécanisme de la nitration de toluène

Les résultats obtenus confirment le fait que cette nitration est concertée et que le NO_2^+ se fixe directement donnant lieu à un intermédiaire σ stable.

Selon le site d'attaque de NO_2^+, nous obtenons les complexes suivants: **ONT$^+$**, **MNT$^+$** et le **PNT$^+$,** on obtient le classement, par ordre croissant des énergies HF suivant :

$PNT^+ < ONT^+ < MNT^+$

Cela montre que le **PNT$^+$** est l'intermédiaire le plus stable et que le MNT^+ en est le moins. Nous avons ensuite optimisé la géométrie de **ONT, MNT** et **PNT**. Le classement suivant, au même niveau théorique a été obtenu :

PNT<MNT< ONT

Ce résultat est en accord avec celui obtenu par P.C.Chen et al. **[3]**. Nous remarquons que le complexe **ONT$^+$** est plus stable que le **MNT$^+$** alors que le composé final **MNT** est plus stable que **ONT**.

Nous avons ensuite substitué le carbone lié au groupement méthyle par le germanium et nous avons effectué la nitration de ce composé **(figure 2)**.

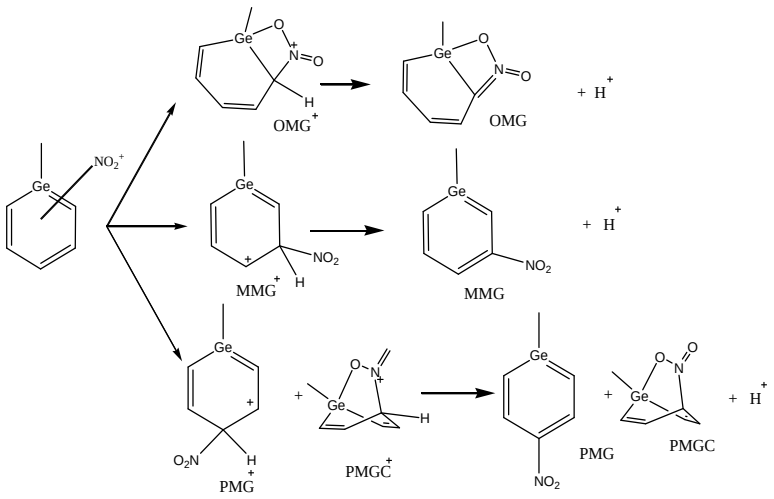

Fig. 2. mécanisme de la nitration du 1-méthyle germine

La nitration du 1-**M**ethyle **G**ermine (**MG**) donne lieu à quatre composés **(figure2)**. Le classement par ordre croissant des énergies HF pour les intermédiaires σ a été obtenu:

$PMGC^+ < OMG^+ < PMG^+ < MMG^+$

Par ailleurs, nous obtenons le classement suivant pour les composés finaux :

PMG < MMG < OMG < PMGC

Comme dans le cas de la nitration du toluène, les énergies des intermédiaires et des composés finaux ne suivent pas la même évolution.

Références

[1] R. Halder, A. Lawal, R. Damavarapu, Catalysis Today 125 (2007) 74-80
[2] M. G. Kuba, R. Prins, G. D. Pirngruber, Applied Catalysis A : General 333 (2007) 78-89
[3] P. C. Chen, S. C. Chen, Computers and Chemistry 26 (2002) 171-178.
[4] P. C. Chen, C. W. Wu, Journal of Molecular Structures (Theochem) 357 (1995) 87-95

P42.

A DFT Study of the Competitive Pathways [4+2] vs. [2+2] of the Cycloaddition of 1,3-diazabuta-1,3-diene derivative with Chloroketene

B. Messaoudi and S. M. Mekelleche

Département de Chimie, Faculté des Sciences, Université A. Belkaid, Tlemcen, B.P : 119, Algérie, 13000 *b_messaoudi@mail.univ-tlemcen.dz*, sm_mekelleche@mail.univ-tlemcen.dz

Cycloaddition reactionsCycloaddition reactions of 1,3-diazadienes are of great importance in heterocyclic synthesis with pharmacological interest. The [2+2] cycloaddition of 1,3-diazadienes with ketenes yields to the formation of azetidinones while the [4+2] cycloaddition yields to the formation of pyrimidinones.

In the present work, we present a theoretical study of the reaction mechanism of the cycloaddition of 1-benzyl-2,4-diphenyl-1,3-diazabuta-1,3-dienes with chloroketene (**Figure 1**). The two possible reaction pathways [2+2]/[4+2] are discussed by the analysis of potential energy surface and DFT-based reactivity indexes. Our calculations show that this cycloaddition takes place along a stepwise mechanism. The first step, which corresponds to the formation of the zwitterionic intermediate, is rationalized by Domingo's polar model predicting the most favorable electrophile/nucleophile interaction. The second step (ring closure) leading to the formation of either the [2+2] or [4+2] cycloadduct, is rationalized by the electrostatic interaction between the most electrophilic site and the most nucleophilic site of the zwitterionic intermediate. Reaction enthalpies and activation energies have been calculated to predict the thermodynamic and the kinetic controls. Quantum chemistry calculations were carried out at the B3LYP/6-31G* level of theory and are in good agreement with experiment.

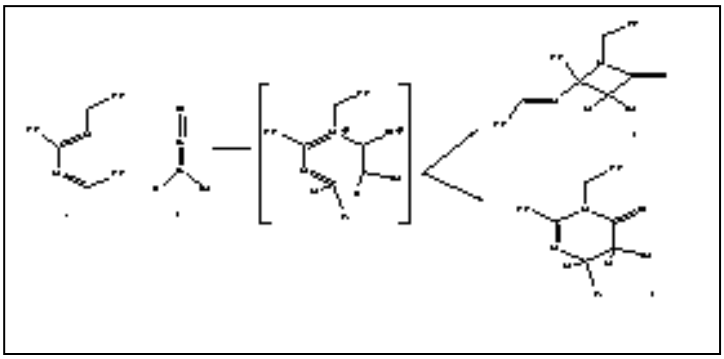

Fig. 1. [4+2]/[2+2] Cycloadditions; Conceptual DFT; Polar Model; Reaction Mechanism.

References

[1] J. Barluenga, M. Tomas, Synthesis of Heterocycles from Azadienes. In Advances from Heterocycles Chemistry, Katritzky, A. RED, Academic Press, Inc: **61** (1993).
[2] E. Rossi, G. Abbiati, E. Pini, Tetrahedron, 53, No. **41** (1997) , 14107.
[3] L. R. Domingo et al, Tetrahedron, **58** (2002) 4417.

Theoretical physics

P43.

Ab-initio calculations of the structural, electronic properties

of CuGaS2 and CuInS2

O. Benhelal[1], A. Chahed[1], S. Laksari[1], B. Abbar[1]and B. Bouhafs[1]

[1]Computational Materials Science Laboratory, Physics Department, University of Sidi Bel-Abbes, 22000 Sidi-Bel-Abbes, Algeria.: e-mail: benhelalomar@yahoo.fr.

The structural, electronic and optical properties of two chalcopyrite crystals: CuGaSe2 and CuInSe2 are studied using the full potential linearized augmented plane waves method within the local density approximation (LDA). Geometrical optimization of the unit cell (equilibrium volume, c/a ratio, internal parameter u, and bulk modulus) is in good agreement with experimental data. The energy gap is found to be direct for both materials and the nature of the gap crucially depends on the manner in which the Cu 3d and (Ga 3d, In 4d) electrons are treated as valence states. Results on band structures and density of states are presented. We report also our results on optical properties like the complex dielectric functions and the refractive index n of the CuGaS2 and CuInS2 crystals. We analyze in detail the structures of the dielectric function observed in the studied energy region.

The Cu-chalcopyrite semiconductors $CuInSe_2$, $CuGaSe_2$, $CuGaS_2$, $CuInS_2$ and their alloys provide absorber materials for the to date most efficient thin-film solar cell technology. Record chalcopyrite solar cells are made from $Cu(In_{1-x}Ga_x)Se_2$ thin-film absorbers with x = 0.15- 0.35, and band gap energy Eg = 1.1-1.2 eV [1]. The usage of $Cu(In_{1-x}Ga_x)(Se_{1-y}S_y)_2$ alloys with higher Ga and / or S content and thus with a wider band gap is desirable when aiming towards high open circuit voltage solar cells based on those wide-gap Cu-chalcopyrites generally deliver a significantly lower device performance compared to the record devices. The main drawback of those wide-gap chalcopyrite devices is the fact that the open circuit voltage V_{oc} does not increase at the same rate as Eg [2]. Thus, it appears that the recombinatio mechanism changes either qualitatively or quantitatively upon alloying CuInSe with high contents of Ga and/or S. It is, however, unclear whether this trend results from lower-grade bulk properties of the wide-gap materials [3,4] or from the less favorable band offset between the CdS buffer layer and the wide-gap chalcopyrite [2].

Theses ternary semiconductors crystallize in the chalcopyrite structure which is related to the zinc blende structure [5]. The equilibrium structural parameters were calculated using the Vienna package WIEN2K [6] We take the Perdew-Wang local density approximation (LDA) [7] for the exchange-correlation potentials.

The equilibrium (c/a) values found were 1.958 and 1.99 for $CuGaS_2$ and $CuInS_2$, respectively. We have obtained a good internal parameters values u which agree well with the experimental values of Shay and Wernick [5] compared with those obtained theoretically by Jaffe [8].

The band structure of $CuGaS_2$ and $CuInS_2$ are calculated and indicated that both compounds are direct band gap semiconductors. The most prominent features of the calculated band structures (bandgaps and crystal-field splitting) of $CuGaS_2$ and $CuInS_2$ are respectively, 0.9 and 0.0095 eV for band gap and 0.001 and 0.0118 eV for crystal-field splitting in agreement with other results of Rashkeev at al [9], who used ASA-LMTO total energy calculations.

The most important quantity is the zero frequency limit epsilon (0) By using the correction scissors, we have corrected our band gap values. With the use the correction scissors, we have obtained a refractive index n_o (0) and n_e(0) which approaches the experimental values of Boyd et al [10] and the calculated values for the n_o (0) given by Xue et al [11,12].

ACKNOWLEDGMENTS: One of us (B. B.) acknowledges the Abdus-Salam International Center for Theoretical Physics (Trieste-Italy).

References

[1]: M. A. Contreras, B. Egaas, K. Ramanathan, J. Hiltner, A. Swartzlander, F. Hasoon, and R. Noufi, Prog. Photovoltaics 7, 311, (1999).
[2]: R. Herberholz, V. Nadenau, U. Ruhle, C. Koble, H. W. Schock, and B. Dimmler, Sol. Energy Mater. Sol. Cells 49, 227, (1997).
[3]: G. Hanna, A. Jasenek, U. Rau, and H. W. Schock, Phys. Status Solidi A 179, R7, (2000).
[4]: J. Reiß, J. Malmstrom, A. Werner, I. Hengel, R. Klenk, and M. C. Lux-Steiner, Mater. Res. Soc. Symp. Proc. 668, H9.4.1, (2001).
[5]: J. L. Shay and J. H. Wernick, Ternary Chalcopyrite Semiconductors : Growth, Electronic Properties and Applications, Perganmon Press, Oxford, (1974).
[6]: P. Blaha, K. Schwarz, G. K. H. Madsen, D. Kvasnicka, and J. Luitz, WIEN2k, An Augmented Plane Wave Plus Local Orbitals Program for Calculating Crystal Properties (Vienna University of Technology, Vienna, Austria, 2001).
[7]: J. P. Perdew and Y. Wang, Phys. Rev. B 45, 13244 (1992).
[8]: J. E. Jaffe, A. Zunger, Phys. Rev. B 29, 1882 (1984).
[9]: S. N. Rashkeev and W. R. L. Lambrecht, Phys. Rev. B 63, 165212 (2001).
[10]: G. D. Boyd, H. Kasper, and J. H. McFee, IEEE J. Quantum Electron. QE-7, 563 (1971).
[11]: D. Xue, K. Betzler, and H. Hesse, Phys. Phys. Rev. B 62, 13546 (2001).
[12]: D. Xue, K. Betzler, and H. Hesse, J. Phys.: Condens. Matter 12, 3113 (2000).

P44.

Effet Electronique Des Acides Sur la Stabilité des Clusters Azaborane et Phosphaborane : Aspect Théorique

N. Bouchakri[1], H.Korichi[1], M.S. Zendaoui[1],

S. Farah[1] and B. Zouchoune[1, 2]

[1]Laboratoire de Chimie Moléculaire, du contrôle de l'environnement et des mesures physico-chimiques Université Mentouri-Constantine, Algérie.
[2]Laboratoire de Chimie Appliquée et Technologie des Matériaux, Centre universitaire larbi Ben M'hidi, (04000) Oum-el-bouaghi, Algérie.

La synthèse, l'étude géométrique et les propriétés électroniques des boranes et leurs différents érivés continuent d'attirer plus d'attention tant sur le plan fondamental que pratique en raison de leurs propriétés électroniques, magnétiques et structurales très intéressantes. Des classes de composés dérivés boranes appelées carboranes, azaboranes et phosphaborane sont connus depuis les années 60, où un ou plusieurs atomes de bore sont remplacés respectivement par des atomes de carbone, azote et phosphore [1].

Notre étude théorique concerne une famille de clusters défini à partir du closo-borane (B12H12-2), du phosphaborane (P2B10H10) et du closo-Azaborane (N2B10H10), nous nous sommes intéressés particulièrement à leur stabilité relative en accord avec les différentes symétries D5d, C2v et C2v. Des calculs des structures électroniques et des analyses des charges nettes de Mulliken nous ont permis de mettre en évidence certaines de leurs propriétés chimiques et les distributions de charge. Ainsi que, les fréquences de vibrationnelles ont été utilisées pour l'identification les différents types de modes de vibrations des liaisons chimiques. Nous avons essayé de classer nos résultats par rapport aux données expérimentales, en utilisant la méthode de fonctionnelle de la densité DFT [2]. Tous les calculs ont été effectués à l'aide du programme Gaussien 98 [3]. Les logiciels GaussView et Molekel ont été utilisés pour la visualisation des structures moléculaires, les orbitales moléculaires et les spectres IR.

Références

[1] B. Stibr, Chem. Rev. 1992, 92, 225-250.
[2] C. Lee, W. Yang, R. G. Parr, Phys. Rev., 1988, B37, 785.
[3] M. J. Frisch et al, GAUSSIAN 98. Revision A. 7, GAUSSIAN Inc, Pittsburgh, PA, 1998.

P45.

First principal study on the electronique structure of ScN

F. BOUTAIBA, M. FERHAT and M. BRIKI

University of Science and Technology of Oran, P.O.Box:1505 El M'Naouer, 31000 Oran, boutaiba_f@yahoo.fr

Scandium nitride (ScN) is emerging as a versatile material for promising technological applications. As part of the transition metal nitride family it initially generated interest for potential applications as wear resistant and optical coatings due to its mechanical strength, high melting point of 2600◦ C [1], and high hardness (H = 21 GPa) with respect to load deformations [2]. ScN crystallizes in the rock-salt phase with a lattice parameter of 4.50 °A3.

The electronic band structure of ScN a key quantity for the design of optoelectronic devices has been difficult to access both experimentally and theoretically [3]. Early experiments were hampered by various complications in growing films with well defined crystalline orientation, stoichometry, low background carrier concentration, and surface roughness [3].

Recent advances in growth techniques have led to a systematic improvement of the material's quality [4]. Employing optical spectroscopy and photoemission, Gall et al. [5] concluded that ScN is a semiconductor with an indirect Γ − X band gap (Eg Γ−X) of 1.3±0.3 eV.

Early Kohn-Sham density functional theory (KS-DFT) calculations employing the local-density (LDA) or Xα approximations predicted ScN to be a semimetal with a small negative band gap between -0.01 and -0.21 eV [6]. In order to overcome the well known underestimation of the LDA band gap, more advanced exact-exchange (OEPx(cLDA)) [5] and screened exchange [7] calculations have been performed, and showed that ScN is a semiconductor with an indirect Γ to X band gap, in accord with experimental evidence [5,8].

However, the calculated band gap of 1.60 eV found in both studies is significantly larger than the most recent experimental value of 0.9±0.1 eV [8]

In order to shed light on this discrepancy we have performed density functional theory. We have employed the full potential linearized augmented plane wave (FP-LAPW) method as implemented in the Wien2K code [9].

In this study we carried out self consistent calculations using Wien2k [9], a full-potential augmented plane wave plus local orbital (APW+lo) method. The calculations are based on the local density approximation LDA [10] and were repeated within the GGA [11] in order to estimate the sensitivity of the results to exchange-correlation. We have considered the cubic structure with experimental lattice constant for ScN (a=4.44 A°). The sphere radii used were 2.1 for Sc and 1.8 for N. Well converged solutions were obtained with RKmax=8.0 (where RMT is the smallest of the muffin-tin radii and Kmax is the plane wave cut-off) and k-point sampling was checked. Fivty six k-points in the irreducible wedge of the simple cubic Brillouin zone was used.

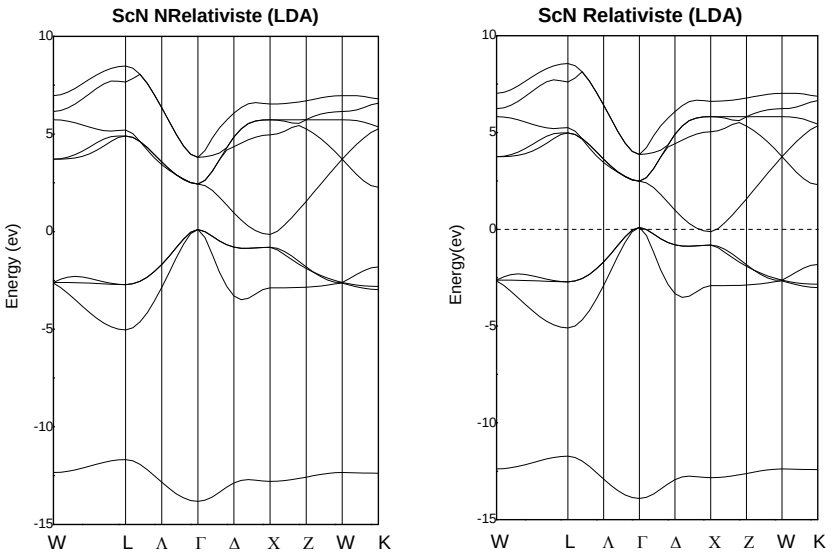

Fig. 1. Band structure calculation of ScN in NRel and Rel cases

References

[1] X. Bai and M. E Kordesch, Appl. Surf. Sci. 175-176, 499 (2001).
[2] D. Gall, I. Petrov, N. Hellgren, L. Hultman, J. E. Sundgren, J. E. Greene, J. Appl. Phys. 84, 6034 (1998).
[3] A. Qteish, cond-mat/0611435 v1 16 Nov 2006.
[4] H. Al-Brithen and A. R. Smith, Appl. Phys. Lett. 77, 2485 (2000).
[5] D. Gall, M. Stadele, K. Jarrendahl, I. Petrov, P. Desjardins, R. T. Haasch, T.-Y. Lee and J. E. Greene, Phys. Rev. B 63, 125119 (2001).
[6] R. Monnier, J. Rhyner, T. M. Rice, and D. D. Koelling, Phys. Rev. B 31, 5554 (1985).
[7] C. Stampfl, W. Mannstadt, R. Asahi, and A. J. Freeman, Phys. Rev. B 63, 155106 (2001).
[8] H. A. Al-Brithen, A. Smith and D. Gall, Phys. Rev. B 70, 045303 (2004).
[9] P. Blaha, K. Schwarz, G.K.H. Madsen, D. Kvasnika, J. Luitz, Wien2k.AnAugmented PlaneWave plus localOrbitals Program for Calculating Crystal Properties, Karlheinz Schwarz, Techn Universitat Wien, Austria, 2001 (ISBN 3-9501031-1-2).
[10]J.P. Perdew, Y. Wang, Phys. Rev. B 45 (1992) 13244.
[11]P.E. Blochl, O. Jepsen, O.K. Anderson, Phys. Rev. B 49 (1994) 16223.

P46.

First-principles calculations of the structural, electronic properties of CuGaSe2 and CuInSe2

A. Chahed[1], O. Benhelal[1], S. Laksari[1], B. Abbar[1] and B. Bouhafs[1]

[1] Computational Materials Science Laboratory, Physices departememtn, University of Sidi Bel-Abbes, Sidi Bel-AbbesFirst Institute, 22000, Algeria, cha_abbes@yahoo.fr

The structural, electronic and optical properties of two chalcopyrite crystals: $CuGaSe_2$ and $CuInSe_2$ are studied using the full potential linearized augmented plane waves method within the local density approximation (LDA). Geometrical optimization of the unit cell (equilibrium volume, c/a ratio, internal parameter *u*, and bulk modulus) is in good agreement with experimental data. The energy gap is found to be direct for both materials and the nature of the gap crucially depends on the manner in which the Cu *3d* and (Ga 3*d*, In 4*d*) electrons are treated as valence states. Results on band structures and density of states are presented. We report also our results on optical properties like the complex dielectric functions and the refractive index *n* of the CuGaSe and $CuInSe_2$ crystals. We analyze in detail the structures of the dielectric function observed in the studied energy region.

The Cu-chalcopyrite semiconductors $CuInSe_2$, $CuGaSe_2$ and their alloys (hereafter referred to as CIGSe) have received considerable attention in recent years. They are analogs of the more common II-VI compound semiconductors. Their physical properties, however, are more complex than those of their binary counterparts because of the metal d-state contribution to the valence band density of states[1-3]. Research on ternary compounds is stimulated by their potential use in optoelectronic devices and have been extensively explored as thin film solar cell absorber material [4-5]. Within the last decade solar cells on the basis of thin film CIGSe could be optimized such that efficiencies have exceeded 17% [6]. Typically CIGSe solar cells are made with p-type ab-sorbermaterial, n-type buffer layers (e.g., CdS), and a combination of intrinsic and highly conducting ZnO window layers.

Theses ternary semiconductors crystallize in the chalcopyrite structure which is related to the zinc blende structure. The equilibrium structural parameters were calculated using the Vienna package WIEN2K [7]. We take the Perdew-Wang local density approximation (LDA) [8] for the exchange-correlation potentials.

The equilibrium (c/a) values found were 1.96 and 1.99 for $CuGaSe_2$ and $CuInSe_2$, respectively. We have obtained a good internal parameters values *u* which agree well with the experimental values of Shay and Wernick [1] compared with those obtained theoretically by Jaffe [2].

The band structure of $CuGaSe_2$ and $CuInSe_2$ are calculated and indicated that both compounds are direct band gap semiconductors. The most prominent features of the calculated band structures (bandgaps and crystal-field splitting) of $CuGaSe_2$ and $CuInSe_2$ are respectively, in agreement with other results of Rashkeev at al [9], who used ASA-LMTO total energy calculations.

The most important quantity is the zero frequency limit epsilon (0) By using the correction scissors, we have corrected our band gap values. With the use the correction scissors, we have obtained a refractive index n_o (0) and n_e(0) which approaches the experimental values of Boyd et al [10] and the calculated values for the n_o (0) given by Xue et al [11,12].

Our present paper reports a systematic study of the structural, electronic and optical properties of two ternary semiconductors $CuGaSe_2$ and $CuGaS_2$ using the APW+lo method within LDA. The ground state properties like equilibrium cell volume, lattice constants, internal parameter and bulk modulus obtained from our calculation agree with the available experimental values. For the electronic properties the calculation provides an excellent description of the band structures for both semiconductors where we found they have a direct band gap. Our results for the real and imaginary parts of the dielectric functions are used to reproduce optical constants, such as the refractive index in good agreement with experimental data.

References

[1]: J. L. Shay and J. H. Wernick, Ternary Chalcopyrite Semiconductors : Growth, Electronic Properties and Applications, Perganmon Press, Oxford, (1974).
[2]: J. E. Jaffe, A. Zunger, Phys. Rev. B **29** (1984), 1882.
[3]: S.-H. Wei and A. Zunger, J. Appl. Phys. **78** (1995), 3846.
[4]: A. Rockett and R. W. Birkmire, J. Appl. Phys. **70**, R81, (1991).
[5]: V. Nadenau, D. Braunger, D. Hariskos, M. Kaiser, C. Koble, A. Ober-acker, M.Ruckh, U. Ru¨hle, R. Scha¨ffler, D. Schmid, T. Walter, S. Zweigart, and H. W. Schock, Prog. Photovoltaics **3** (1995), 363.
[6]: K. Bu¨cher and S. Kunzelmann, *Proceedings of the 14th European Photo-voltaicSolar Energy Conference* ~H. S. Stephens, Bedford, (1997), 363.
[7]: P. Blaha, K. Schwarz, G. K. H. Madsen, D. Kvasnicka, and J. Luitz, WIEN2k, An Augmented Plane Wave Plus Local Orbitals Program for Calculating Crystal Properties (Vienna University of Technology, Vienna, Austria, 2001).
[8]: J. P. Perdew and Y. Wang, Phys. Rev. B **45** (1992), 13244.
[9]: S. N. Rashkeev and W. R. L. Lambrecht, Phys. Rev. B **63** (2001), 165212.
[10]: G. D. Boyd, H. Kasper, and J. H. McFee, IEEE J. Quantum Electron. QE-**7** (1971), 563.
[11]: D. Xue, K. Betzler, and H. Hesse, Phys. Phys. Rev. B **62** (2001), 13546.
[12]: D. Xue, K. Betzler, and H. Hesse, J. Phys.: Condens. Matter **12** (2000), 3113.

P47.

La validité de la prédiction des modèles de transfert de chaleur

par ébullition nucléée en zone bulle isolée

F. Chouarfa[1], M. H. Benhamza

[1]Laboratoire d'Analyses Industrielles et Génie des Matériaux 'Université de Guelma', maissa_anemone@yahoo.fr

Une multitude des corrélations afin de modéliser le phénomène de transfert de chaleur par ébullition nucléée existe. Dans ce travail, une identification des six modèles dans la région des bulles isolées est effectuée afin de reconnaître la dépendance entre les paramètres physiques dominants dans cette zone. Le but de cette analyse est de déterminer l'exactitude de la prédiction de chacun des modèles et en même temps de connaître le phénomène physique le plus dominant du transfert de chaleur par ébullition nucléée et ceci en utilisant une vaste gamme des données expérimentales fiable. A partir de la plus commode corrélation, la densité du site de nucléation la plus importante à l'augmentation du flux de chaleur est déterminée.

La comparaison des différentes corrélations montre que le modèle de Sakashita & Kumada présente le meilleur résultat de transfert de chaleur par ébullition nucléée. Le phénomène physique le plus dominant dans la zone des bulles isolées est la conduction transitoire ayant lieu sous les bulles. L'augmentation de la densité des sites de nucléation diminue le rayon d'activation des cavités ainsi que le diamètre de détachement de la bulle de vapeur. La corrélation choisie peut être aussi extrapolée à la zone de bulles unies.

Cette étude se situe dans le contexte général de l'investigation des phénomènes de transfert de chaleur, son objectif est l'identification des modèles de transfert de chaleur par ébullition concernant les mécanismes élémentaires d'ébullition nucléée (crois-sances, détachement, coalescence, transition, stabilité de l'interface fluide-vapeur, etc.), de niveau de représentation et de complexité permettant ainsi de préciser la relation entre les différents paramètres qui régissant ce phénomène. Ses résultats sont indispen-sables pour comprendre et maîtriser le régime d'ébullition nucléée et pour la validation de nombreuses corrélations numériques concernant les bulles isolées. En se refaire généralement à la courbe d'ébullition pour connaître les régimes d'échange entre un élément chauffant et un fluide caloporteur, parmi ceux-ci l'ébullition nucléée présente le régime le plus favorable. Malheureusement, moins d'études théoriq-ues se sont concentrées sur la physique du processus d'ébullition. En conséquence, des efforts considérables ont été effectués ces années pour pallier à ce problème en utilisant des corrélations qui impliquent plusieurs paramètres réglables. Ce travail se situe dans la continuation des travaux précédemment menés. Son objectif est d'étudier les corrélations proposés et les comparés avec les données expérimentales, afin d'avoir des corrélations fiables.

Chaque modèle est proposée pour un tel phénomène physique qui joue le rôle le plus important dans la contribution au transfert de chaleur, Pour cela on a sélectionné six modèles d'ébullition nucléée

dans la région des bulles isolées puis la validation des ces modèles ont été identifiée d'après l'exactitude des corrélations produites avec une base de données expérimentale fiable.

Ces données fournies par le professeur Sakashita de l'université de HOKKAIDO (Japon).couvrent une large gamme de conditions d'ébullition, y compris plusieurs combinaison surface-fluide.

D'après notre étude on trouve que la conduction est le mode le plus important dans le transfert de chaleur par ébullition nucléée dans la région des bulles isolées, en contraste avec la plupart des modèles qui démontrent que la convection est le mode le plus important comme celle de Rohsenow qui est le modèle le plus publie dans le monde de transfert de chaleur par ébullition.

(q : le flux de chaleur, ΔT : la surchauffe de la surface, Bh : les propriétés physiques des fluides, n : la densité du site de nucléation)

D'après le modèle de Tien, le phénomène physique le plus important qui augmente le taux de transfert de chaleur est la convection naturelle à travers la couche limite thermique(1). Sa corrélation est présentée comme : $q = B_H \Delta T_{sat} n^{1/2}$

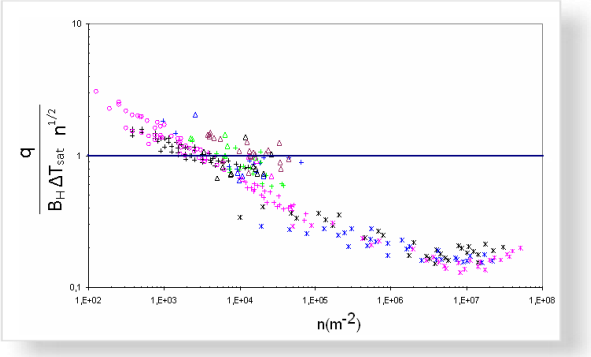

Fig. 1. La corrélation de Tien

D'après ce graphe, on constate que, la corrélation de Tien est très loin des données expérimentales ; à l'exception d'une gamme de donnée très limitée qui présente un accord avec sa corrélation. Soit une erreur maximale de prédiction d'environ 75 % par rapport aux données de Barthau à différentes valeurs de pression (toutes les valeurs sont au dessous de la ligne de l'unité), et une différence inférieur à 30 % pour les données de Nishikawa & Urakawa (toutes les valeurs sont situées au dessus de la ligne de l'unité). Cependant, les données de Kurihara & Meyers sont proches des valeurs exactes d'environ 15%.

Hara suppose que le flux de chaleur est égal à celui transmis par conduction et par évaporation à travers la surface chauffante (2). Sa corrélation est sous la forme : $q = B_H \Delta T_{sat}^{3/2} n^{3/8}$

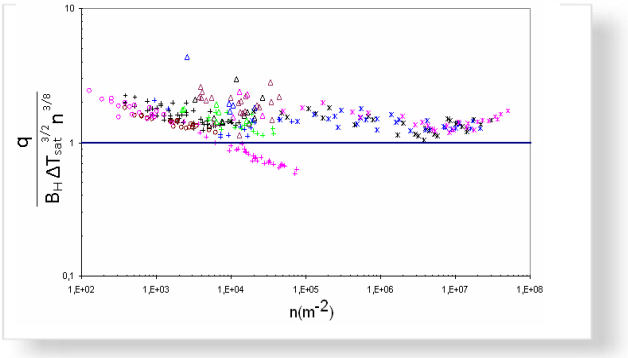

Fig. 2 la corrélation de Hara

Cette corrélation présente des données qui sont plus ou moins proches de l'unité (valeurs exactes), la majorité des ces données sont situés au dessus de ligne de l'unité avec une différence maximale inférieure à 20%, à l'exception de ceux rapportés par Cornwell & Brown qui divergent d'environ 15% au dessous de la ligne de l'unité.

Les corrélations proposées d'après les modèles de Tien, Mikic & Rohsenow, Kurihara & Meyers sont considérées comme loin des données expérimentales. Seulement quelques valeurs sont proches de leurs corrélations.

- Il ressort de la comparaison des différentes corrélations, que le modèle de Hara, Kocamustafaogullari & Ishii, ainsi que celle de Kumada & Sakashita donnent des prédictions de l'ordre de ±10% par rapport aux mesures expérimentales, et que par conséquent, le phénomène physique le plus dominant dans le cas d'un transfert de chaleur par ébullition nucléée dans la zone des bulles isolées est certainement la conduction transitoire de la chaleur ayant lieu sous les bulles à partir de la surface de chauffe.

- On remarquera aussi, que dans ces trois dernières corrélations le paramètre $n^{3/8}$ est présent. Il représente donc l'influence de la densité du site de nucléation.

- Nous aurions pu fignoler pour définir l'existence d'une liaison résistive entre la densité de site de nucléation et le rayon convenable pour l'activation d'une cavité, tel que l'augmentation de la densité

de site de nucléation implique une diminution de ce rayon. Donc l'activation des cavités dépend fortement de la densité de site de nucléation.

- La corrélation de Sakashita & Kumada qui présente une parfaite concordance avec toute la gamme de données, elle représente donc un modèle fiable qui peut être une base pour des futurs recherches dans ce domaine.

Références

[1] C.L.Tien,' A hydrodynamic model for nucleate boiling heat transfer' , Int.J.of heat and mass transfer (1962) 533-540.
[2] A.Hara,' the mechanic of nucleate boiling heat transfer', Int.J.of heat and mass transfer 6 (1963) 959-969.
[3] I.L. Pioro, W. Rohsenow, S.S. Doerffer, 'Nucleate pool-boiling heat transfer: I' Intrenational Journal of heat and Mass transfer 47(2004)5033-5044.
[4] H.Kurihara, J.E.Myers, ' The effects of superheat and surface roughness on boiling coefficients' AICHE.J.6(1960)83-91.
[5] G.Kocamustafaogullari,M.Ishii,'Interfacial area and nucleation site density in boiling system', Int.J.Heat and mass Transfer 26 (1983) 1377-1387.
[6] T.Kumada and H.Sakashita , 'Pool boiling heat transfer-II ', International journal of Heat and Mass Transfer Vol.38, No 6, pp.979-987 (1994).

P48.

Theoretical study of catalytic effects on the Reactivity of five Membered Heterocycles in Elecrophilic Aromatic Substitution

A. Ghomri[1], S. M. Mekelleche[1]

[1] Department of Chemistry, University of Tlemcen, PB 119, Tlemcen, 13000, Algeria. (sm_mekelleche@mail.univ-tlmcen.dz, AM_ghomri@mail.univ-tlemcen.dz)

Substitution reactions on aromatic compounds are the most important methods for the preparation of complex aromatic compounds.

The position selectivity for bromination in substituted five-membered heteroaromatic rings is usually α > β, However, the presence of catalysts can override this directive influence (scheme1).

Our aim in this work is to justify the catalyst effect on the kinetic (or thermodynamic) control of these reactions.

The positional selectivity of the electrophilic attack and the relative reactivity of the three systems are rationalized by means of global and local reactivity indexes derived from DFT .

The quantum chemical calculations reported in this work were performed at the B3LYP/6-311G(d,p) level of theory using GAUSSIAN 98 suite of programs. The atomic electronic populations were calculated using Mulliken (MPA) natural (NPA) and electrostatic (MK, CHELP, and CHELPG algorithms) population analyses.

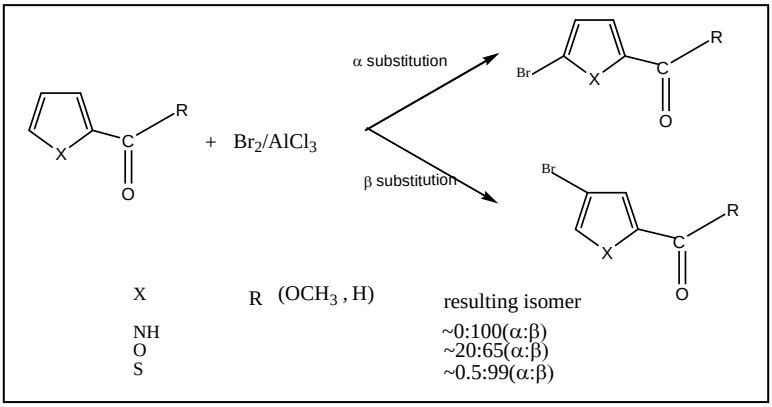

scheme. Reactivity of five Membered Heterocycles in Elecrophilic

References

[1] P. K. Chattaraj, U. Sarkar, D. R. Roy. Chem. Rev. (2007), 107, PR46PR74.
[2] L.I.Belen´kii, T. G. Kim, I. A. Suslov, and N. D. Chuvylkin Russ. Chem. Bull ,Inter. Edition, 54, 4, 853-863, (2005).
[3] H. J. Anderson and L. C. Hopkins, Can. J. Chem., 1964,42, 1279.

P49.

Electronic Structure of cubic ErxGa1-xN using the LSDA+U approach

A. Lazreg[1], Z. Dridi[1], and B. Bouhafs[1]

[1]Modelling and Simulation in Materials Science Laboratory, Physics Department, University of Sidi Bel-Abbes, 22000 Sidi Bel-Abbes, Algeria. Tél: 048-54-43-44 Fax: 048-54-43-44 E-mail aeklazreg@yahoo.fr

Electronic structure calculations were performed for substitutional erbium rare-earth impurity in cubic GaN using density functional theory calculations within the LSDA+*U* approach (local spin density approximation with Hubbard-*U* corrections). The LSDA+*U* method is applied to the rare-earth 4*f* states. The $Er_xGa_{1-x}N$ is found to be a semiconductor, where the filled *f* states are located in the valence bands and the empty ones above the conduction band edge. The filled and empty *f* states are also shown to shift downwards and upwards in the valence and conduction bands, respectively, with increasing the *U* potentials. We show also that the magnetic property of $Er_xGa_{1-x}N$ is drastically different from TM-doped GaN.

The diluted ferromagnetic semiconductors are considered as promising materials for spintronic applications, due to their unique combination of magnetic, semiconducting and optical properties. Most of the materials that have been studied are III-V and II-VI semiconductors doped with Mn and other 3*d* transition metal (TMs), which have been predicted and, in some cases, observed to show hole mediated ferromagnetic behaviour above room temperature **[1-3]**. An accurate description of the electronic structure of solid containing rare-earths is a challenging problem because of their unfilled 4*f* shells **[4]**. In this work, we investigate the nature of magnetic coupling in the Erbium-doped GaN, in the zinc-blende $Er_xGa_{1-x}N$ at x = 0.25 using the LSDA+*U* method. We have reported the spin-polarized band structures, the density of states.

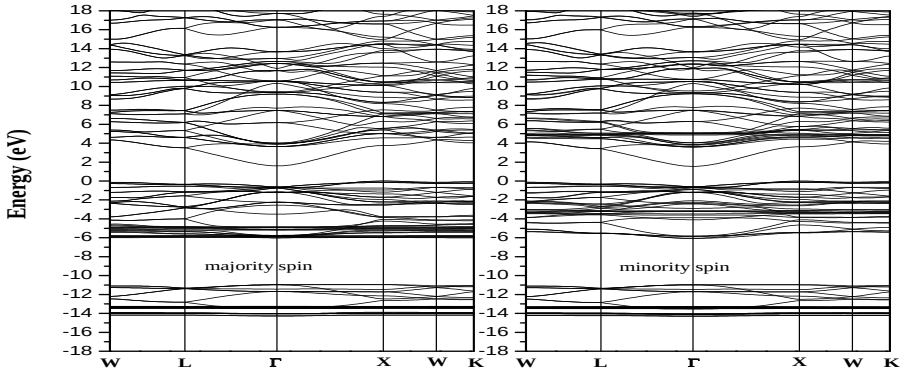

Fig.1. Band structure

Our electronic structure calculations are based on the density-functional theory in the local spin-density approximation (LSDA) with additional Hubbard correlation terms describing on-site electron-electron repulsion associated with the 4*f* narrow bands (LSDA + *U* approach). The first-principles band-structure approach applied in this work is the scalar relativistic full-potential linear-augmented-plane-wave plus local orbital (FPLAPW+lo) method (Wien2k implementation **[5]**). Basis functions

were expanded as combinations of spherical harmonic functions inside non-overlapping spheres around the atomic sites (muffin-tin spheres) and in Fourier series in the interstitial region. In the muffin-tin (MT) spheres, the *l*-expansion of the non-spherical potential and charge density was carried out up to l_{max}=10. In order to achieve energy eingenvalues convergence, the wavefunctions in the interstitial region were expanded in plane waves with a cutoff of $k_{max} = 7/R_{mt}$ (where R_{mt} is the average radius of the MT spheres).

Electronic (figure 1 and 2) and magnetic properties of erbium substituting in cubic GaN have been discussed based on the LSDA+*U* calculations.

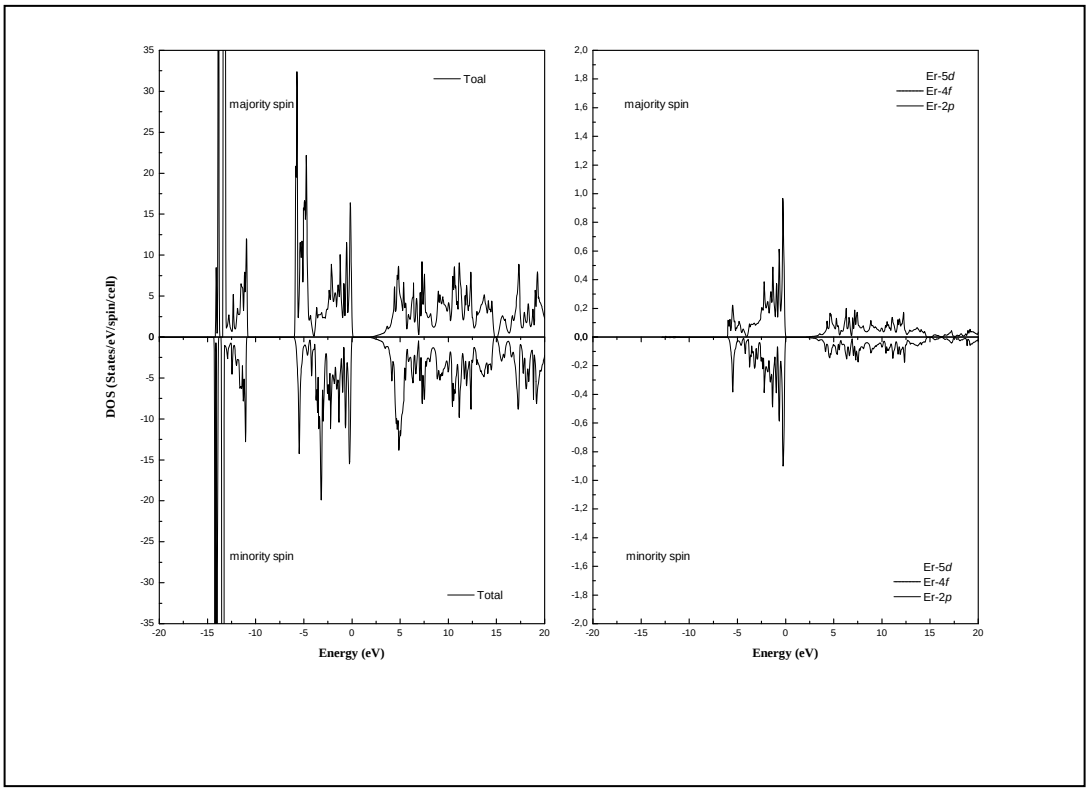

Fig.2. Density of states

The magnetic interaction of the erbium with the host states at the valence and conduction band edges appears to be relatively weak in comparison to that of dilute Mn in GaN. In contrast to LSDA which places the localized *f*-related levels in the middle of the gap, the LSDA+*U* is shown to shift them downwards and upwards on the valence and conduction bands, respectively, leaving the original band gap completely clear, and confirming that the *f* states don't hybridize with the host states.

Reference

[1] I. Zutic, J. Fabian, S. Das Sarma, Rev. Mod. Phys. 76 (2004) 323.
[2] D. D. Awschalom and R. K. Kawakami, Nature (London) 408 (2000) 923.
[3] T. Dietl, H. Ohno, F. Matsukura, J. Cibert, and D. Ferrand, Science 287 (2000) 1019.
[4] I. N. Yakovkin, Takashi Komesu, and P. A. Dowben, Phys. Rev. B 66 (2002) 035406.
[5] P. Blaha, K. Schwarz, G. K. H. Madsen, D. Kvasnicka, and J. Luitz, WIEN2k, An

Augmented Plane Wave + Local Orbitals Program for Calculating Crystal Properties

(Technische Universität Wien, Austria, 2001).

P50.

A Theoretical investigation of ZnOxS1-x alloys band structure

H. Rozale[1], L. Beldi[1], B. Bouhafs[1], and P. Ruterana[2]

[1]Modelling and Simulation in Materials Science Laboratory, Physics Department, University of Sidi Bel-Abbes, 22000 Sidi Bel-Abbes, Algeria.
[2]SIFCOM UMR 6176, CNRS-ENSICAEN, 6 Boulevard Maréchal Juin, 14050 Caen Cedex France.

We report the properties of ordered ZnO_xS_{1-x} alloys calculated in various structures (CuAu-I, Cu_3Au, Luzonite and Famatinite) using a first-principles total-energy formalism based on the hybrid full-potential augmented plane-wave plus local orbitals (APW+*lo*) method, within the local-density approximation (LDA). The calculated band gaps of the alloys are direct and range from 0.49 for O-rich to 1.55 eV for S-rich ZnO_xS_{1-x}. The non linear variation of the band gap energy is related to the large electronegativity difference between O and S.

Group II-O-VI alloys belong to a class of semiconductor alloys in which the anions are partially replaced by the highly electronegative isoelectronic oxygen. As expected these alloys have properties similar to the extensively studies group III-N-V [1–3]. The electronic band structure of such highly mismatched alloys (HMAs) is determined by an anticrossing interaction between localized states of O or N and the extended states of the semiconductor matrix [4,5]. The large modification of the electronic band structure profoundly affects the optical and electrical properties of these alloys. Thus it has been shown that incorporation of a small amount of N leads to a large reduction of the fundamental band gap [6-8], an increase of the electron effective mass [9], an improved donor activation efficiency of the group VI donors [10,11] and to mutual passivation of the group IV donors and the nitrogen [12,13]. Similar large band gap reductions have also been observed recently in group II telluride compounds alloyed with S, O or Se atom [14,15]. Less work has been done on these materials because of the difficulties in the synthesis of the alloys with large enough O content [16,17]. It was speculated that the ZnOS compound system might have bowing parameters as large as GaNP and GaNAs due to the large electronegativity differences between O and S [18]. This would allow tuning the band gap energy over a wide range with only small amounts of sulfur in ZnO, which avoids large lattice mismatch and is highly beneficial for the growth of quantum structures. In addition, the band gap (Eg) engineering might be possible because of larger Eg of ZnS than ZnO. Regardless of these possibilities, S has rarely been doped in ZnO due to problems in fabrication owing to significant difference between S stabilization and high quality ZnO growth temperature windows. For these reasons, there has been no successful report on the S doping in ZnO [19]. Recently, Meyer et al [25] have synthesized ZnO_xS_{1-X} alloys over a wide composition range and measured the respective changes in the lattice parameters and band gap energies as a function of the ZnO_xS_{1-X} composition. The calculations were performed using the non scalar relativistic full potential linearized augmented plane waves (FP-LAPW) method [20] within the framework of the density functional theory (DFT). The exchange-correlation energy of the electrons is described in the local-density approximation (LDA) [21].
For the electronic properties calculation, we treated the O 2s, 2p, S 3s, 3p and the Zn 3d, 4s, 4p orbital's as valence states and all lower-lying state as core. As can be noticed in the figures 1 and 2, both compounds are direct gap materials, with band gap Eg of only 0.8, 2.11 eV, which is much smaller than the experimental values of Eg 3.4, 3.9 eV for ZnO, ZnS respectively[22,23]. Of course this underestimation of the gap energy is another shortcoming of standard LDA. Interestingly, as can be noticed, the ZnO band gap is smaller than that of ZnS. This is a similar trend as other theoretical calculations carried out on CdO and CdS, and between HgO and HgS in the zinc blend phase [24]. This large change in band-gap between ZnO and ZnS has already been explained in terms of the stronger p-d repulsion [25] in ZnO than in ZnS due to the fact that the Zn 3d to O 2p

orbital energy difference is smaller. The larger p-d repulsion pushes the VBM of ZnO more upwards than in ZnS, which leads to a reduction the band gap of ZnO at □ □ point.

Figure 3 shows the variation of the energy band gap for different oxygen concentrations, it can be noticed that there is a reduction of the gap when the concentration of oxygen increases. As may be noticed in the figure, this variation of E_g is not linear, of course, the corresponding bowing is a complex function and, as has been pointed out in many reports, it is due to the volume deformation, charge transfer, as well as bond length relaxation [26,27]. For our purpose, if we have tried to point out the possible contribution from charge transfer between the atoms of the alloy

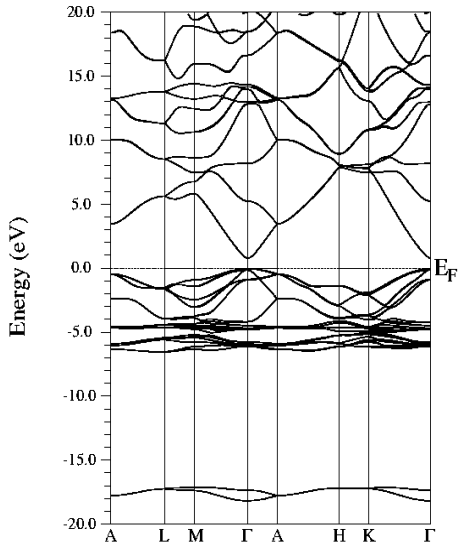

FIG.1. The calculated electronic band structure of ZnO in wurtzite structure with spin orbit included

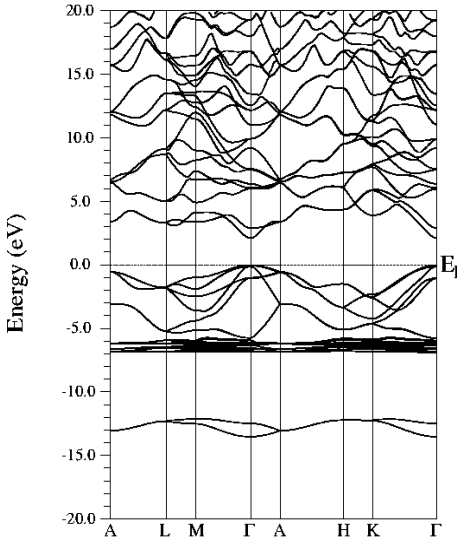

FIG.2. The calculated electronic band structure of ZnS in wurtzite structure with spin orbit included

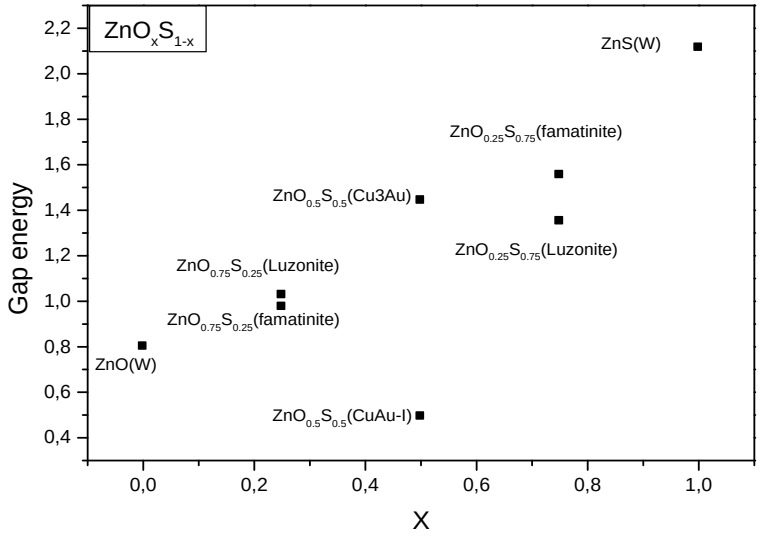

Fig. 3. The electronic band-gap energy as versus the alloy composition in ZnO_xS_{1-x} .

In summary, we have reported an ab-initio study of the ZnO, ZnS compound in wurtzite structure and their ternary ordered alloys ZnO_xS_{1-x} as modeled using Landau-Lifshitz cubic structures. The obtained structural properties are in good agreement with other theoretical results for the binary compounds, which is a support for those of the ternary alloys that we report for the first time. In this instance, the band gaps are shown to vary strongly from ZnO and ZnS in a non linear way. This variation is correlated with the important charge transfer shown to take place on the oxygen atoms.

ACKNOWLEDGMENTS

One of us (B. B.) acknowledges the Abdus-Salam International Center for Theoretical Physics (Trieste-Italy) for financial support and kind hospitality, where part of this work has been carried out.

References

[1] K. M. Yu, W. Walukiewicz, W. Shan, J. Wu, J. W. AgerIII, E. E. Haller, H. P. Xin, and C. W. Tu, Appl. Phys. Lett. 78, 1077 (2001).
[2] J. W. A. III and W. Walukiewicz, Semicond. Sci. Technol. 17, 741 (2002).
[3] C. W. Tu, J. Phys. Condens. Matter. 13, 7169 (2001).
[4] W. Shan, W. Walukiewicz, J. W. A. III, E. E. Haller, J. F. Geisz, D. J. Friedman, J. M. Olson, and S. R. Kurtz, Phys. Rev. Lett. 82, 1221 (1999).
[5] W. Shan, W. Walukiewicz, K. M. Yu, J. W. A. III, E. E. Haller, J. F. Geisz, J. M. Olson, S. R. Kurtz, and C. Nauka, Phys. Rev. B. 62, 4211 (2000).
[6] E. D. Jones, N. A. Modine, A. A. Allerman, S. R. Kurtz, and A. F. Wright, Phys. Rev. B. 60, 4430 (1999).
[7] N. G. Szwacki and P. Boguslawski, Phys. Rev. B. 64, 161201 (2001).
[8] T. Mattila, S.H. Wei, and A. Zunger, Phys. Rev. B. 60, 11245 (1999).
[9] C. Skierbiszewski et al., Appl. Phys. Lett. 76, 2409 (2000).
[10] K. M. Yu, W. Walukiewicz, W. Shan, J. W. A. III, J. Wu, E. E. Haller, J. F.Geisz, D. J. Friedman, J. M. Olson, and S. R. Kurtz, Phys. Rev. B 61, 13337 (2000).
[11] K. M. Yu, W. Walukiewicz, W. Shan, J. Wu, J. W. A. III, E. E. Haller, J. F. Geisz, and M. C. Ridgway, Appl. Phys. Lett. 77, 2858 (2000).
[12] K. M. Yu, W. Walukiewicz, J. Wu, D.Mars, D. Chamberlin, M. A. Scarpulla, O. D. Dubon, and J. F. Geisz, Nat. Mater. 1, 185 (2002).
[13] Y. G. Hong, A. Nishikawa, and C. W. Tu, Appl. Phys. Lett. 83, 5446 (2003).
[14] W. Walukiewicz, W. Shan, K. M. Yu, J. W. A. III, E. E. Haller, I. Miotkowski, M. J. Seong, H. Alawadhi, and A. K. Ramdas, Phys. Rev. Lett. 85, 1552 (2000).
[15] K. M. Yu, W. Walukiewicz, J. Wu, J. W. Beeman, J. W. A. III, E. E. Haller, I. Miotkowski, A. K. . Ramdas, and P. Becla, Appl. Phys. Lett. 80, 1571 (2002).
[16] Y. Nabetani, Mater. Res. Soc. Symp. Proc. M3, 744 (2003).
[17] W. Shan, W. Walukiewicz, J. W. AgerIII, K. M. Yu, J. Wu, E. E. Haller, Y. Nabetani, T. Mukawa, Y. Ito, and T. Matsumoto, Appl. Phys. Lett. 83, 299 (2003).
[18] B. K. Meyer, A. Polity, B. Farangis, Y. He, D. Hasselkamp, T. Kramer, C. Wang, U. Haboeck, and A. Hoffmann, phys. stat. sol. (c) 1, 694 (2004).
[19] Y. Z. Yoo, Z. W. Jin, T. Chikyow, T. Fukumura, M. Kawasaki, and H. Koinuma, Appl. Phys. Lett. 81, 3798 (2002).
[20] O. K. Andersen, Phys. Rev. B. 12, 3060 (1975).
[21] Y. W. J. P. Perdew, Phys. Rev. B. 45, 13244 (1992).
[22] Semiconductors Physics of Group IV Elements and III-V Compounds, K. H. Hellwege, O. Madelung, and Landolt-Bornstein, eds., (1982), Vol. 17.
[23] Semiconductors. Intrinsic Properties of Group IV Elements and III-V-II-VI and I-VII Compounds, K. H. Hellwege, O. Madelung, and Landolt-Bornstein, eds., (1987), Vol. 22.
[24] I. G. Su-Huai Wei, Xiliang Nie and S. B. Zhang, Phys. Rev. B. 67, 165209 (2003).
[25] J. E. Jaffe and A. Zunger, Phys. Rev. B. 29, 1881 (1983).
[26] A. Zunger, S.H. Wei, L.G. Fereira, and J.E. Bernard, Phys. Rev. Lett. 65, 353(1990)

P51.

Electronic properties of the materials AlN, GaN calculation with the Empirical Pseudo-Potential method (EPM)

BENCHERIF Kaddour[1] ,
LOUHIBI Mohamed Elhadi[1], ABID Hamza[2]

[1]ICEPS Intilligent Control & Electrical Power System Laboratory ,University of Sidi-Bel-Abbès ,22000, Algeria.E-mail:CHERIFAUT@yahoo.fr
2Applied Materials Laboratory ,University of Sidi Bel Abbes ,22000, Algeria

The electronic structure of the binary compounds AlN and GaN are presented. We have used the empirical pseudo-potential method. Good agreement between the calculated results and experiment is obtained. The charge densities are presented for the sum of the four valence bands of both AlN and GaN.

The wide-energy gap III–V nitride semiconductors GaN and AlN have received considerable attention in both experiment [1-2] and theory [3-4] for their device applications in the blue and ultraviolet wavelengths. A number of reviews on GaN and AlN were given by Strite and Morkoc [5], P.Kung and M. Razegui [6] and Pankove [7]. The vast majority of research on III–V nitride has been focused on the wurtzite crystal phase. The reason is that most of III–V nitrides have been grown on sapphire substrates which generally transfer their hexagonal symmetry to the nitride film. Nevertheless, interest in zincblende nitride has been growing recently. The zinc-blende GaN has a higher saturated electron drift velocity and a somewhat lower energy band than wurtzite GaN. Mizuta [8] first reported bulk zinc-blende GaN grown on (001) GaAs. There have been several recent studies of the zinc-blende GaN [9-10-11] AlN in zinc-blende structure has an indirect gap at X point with the value of 5.11 eV [12] while zinc-blende GaN with direct gap give us the value of 3.5 eV reported by Bloom.

The empirical pseudo-potential method is simple and expected to give quick and reasonably reliable results. However, in the literature, there is a lack of zinc-blende GaN and AlN experimental data regarding the band structures and it is hard to extract empirical form factor parameters for the EPM calculation.In our work, we adjust the EPM parameters by fitting the band energies of AlN and GaN, obtained using the quasi-particle calculation. Then we use these EPM parameters and the method in Ref [13-14] to calculate the band structure of zinc-blende GaN and AlN.

The final form of EPM. [15]

$$\mathrm{H}_{G',G} = \frac{\hbar^2}{2m_0}\left|G+k\right|^2 \delta_{G,G'} + V_f^S(q)\cos\left(G-G'\right)T + iV_f^A(q)\sin\left(G-G'\right)T$$

The charge densities from EPM are calculated for the sum of the four valence bands [16]:

$$\psi_{n,\vec{k}}(\vec{r}) = \sum_{\vec{G}} a_{n,\vec{k}}(\vec{G}) e^{i(\vec{G}+\vec{k}).\vec{r}}$$

$$\rho(\vec{r}) = \sum_{n,\vec{k}} \psi^{*}_{n,\vec{k}}(\vec{r}) \psi_{n,\vec{k}}(\vec{r})$$

The EPM method is used in the calculation of the zinc-blende GaN and AlN band structures. The experimental measured and calculated energy gap of zinc-blende GaN and AlN using the EPM method are listed in Table I. We adjust the symmetric and antisymmetric pseudo-potential form factors by fitting the band energies of AlN and GaN obtained by Rubio et al [17] quasiparticle calculation. The lattice constants *a* of GaN and AlN used in our calculation are 4.48 and 4.34 Å, respectively. The final adjusted symmetric and antisymmetric form factors of GaN and AlN are resumed in Table II. The band structures of GaN and AlN are shown in Figures 1 and 2, respectively. The results show that GaN is a direct-gap semiconductor with the minimum of conduction band at Γ point, and AlN has an indirect gap with the minimum of conduction band at *X* point. The calculated energy gaps of GaN E_g^{Γ} and AlN E_g^{X} are 3.38 and 5.10 eV, respectively, which are in good agreement with the experimental results . The charge densities from EPM are calculated for the sum of the four valence bands are shown in Figures 3 and 4.

1-Tables:

Table 1. The calculated and experimental energy gap for the binary compounds AlN and GaN[18][19]

	AlN		**GaN**		
$E_{\Gamma\Gamma}$ (eV)	5.94	6.0 [18]	3.38	3.1 [18]	3.2[19]
$E_{\Gamma X}$ (eV)	5.1	4.9 [18]	4.57	4.7[19]	
$E_{\Gamma L}$ (eV)	9.42	9.3 [18]	5.64	6.2[19]	

Table 2. Symmetric and antisymmetric form factors and lattice constants of zinc-blende AlNand GaN [18]

$G\|^2(2\pi/a)^2$	3	4	8	11
V^s_{AlN}	-.0.300 [18]		0.080 [18]	0.110 [18]
V^a_{AlN}	0.280 [18]	0.330 [18]		0.015 [18]
V^s_{GaN}	-0.300 [18]		0.060 [18]	0.070 [18]
V^a_{GaN}	0.280 [18]	0.200 [18]		0.040 [18]

Figures:

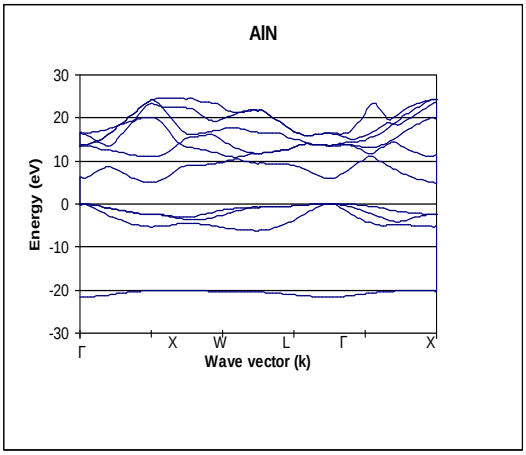

Fig. 1. The band structure of zinc-blende **AlN**

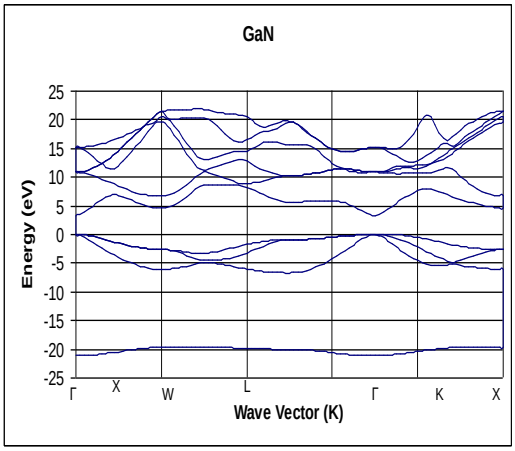

Fig. 2. The band structure of zinc-blende **GaN**

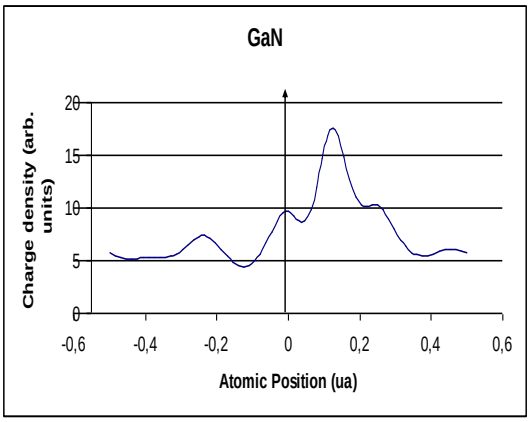

Fig. 3. The charge density of zinc-blende **GaN**

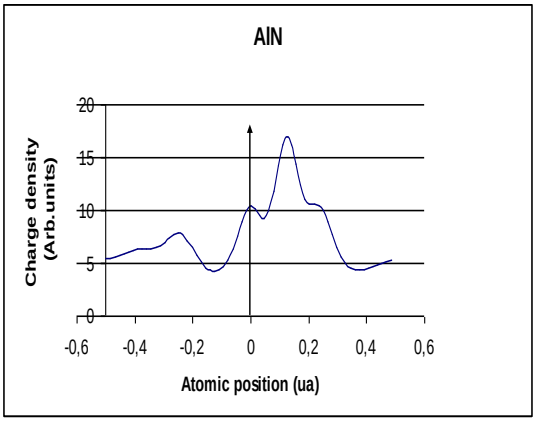

Fig. 4. The charge density of zinc-blende **AlN**

The electronic band structure and the charge density of zinc-blende AlN, GaN, are calculated using an empirical pseudo potential method. It is shown that GaN is a direct-gap semiconductor, with energy gap 3.38 eV. AlN has an indirect, with energy gap 5.10 eV. The charge densities are calculated for the sum of the four valence bands**.**

References

[1] Band parameter for III-V compound semiconductors and their alloy, R.L. Ram-Mohan, Phys Rev., Vol., 89, (2001), 11.
[2] W. C. Johnson, J. B. Parsons, and M. C. Crew, J. Phys. Chem., 36, (1932), 2561,Sci.Lett,11, (1992), 261.
[3] S. Bloom, G. Harbeke. E. Meier, and I. B. Ortenburger, Phys. Status Solidi., B 66, (1974), 161.
[4] A. F. Wright and J. S. Nelson, Phys. Rev., B 50, (1994), 2159.
[5] S. Strite and H. Morkoc, J. Vac. Sci. Technol., B 10,(1192)1237.
[6] P. Kung and M. Razegui, Opt. Rev., 8, (2000), 201.
[7] J. I. Pankove, Mater. Res. Soc. Symp. Proc., 97,(1987), 409 ; 162,(1990), 515.
[8] M. Mizuta, S. Fujieda, Y. Matsumoto, and T. Kawamara, Jpn. J. Appl. Phys., 25,(1986), L945.
[9] Scanlon, Appl., Phys. Lett,. 95,(1991), 944.M. J. Paisley, Z. Sitar, J. B. Posthill, and R. F. Davis, J. Vac. Sci. Technol., A 7,(1989), 701.
[10] Z. Sitar, M. J. Paisley, B. Yan, and R. F. Davis, Mater. Res. Soc. Symp,. Proc. 162, (1990).537.

[11] T. P. Humphreys, C. A. Sukow, R. J. Nemanich, J. B. Posthill, R. A. Radder, S. V. Hattangady, and R. J. Markunas, Mater. Res. Soc. Symp.Proc., 162, 53,(1990).
[12] W. R. L. Lambrecht and B. Segall, Phys. Rev., B 43,(1991), 7070.
[13] J.C. Phillips ,Bonds and bands in semiconductors, Academic Press, New. York (1973).
[14] D. Brust ,Phys.Rev.,A114,(1964).1357.
[15] M. L. Cohen and T. K. Bergstresser, Phys. Rev., 141,(1966), 789.
[16] D.J. Chadi and M.L. Cohen ,Phys.Rev.,B8,(1973),5747.Phys.Rev.,B7,(1973).692.
[17] A. Rubio, J. L. Corkill, M. L. Cohen, E. L. Shirley, and S. G. Louie, Phys,Rev., B 48,
[18] W. J. Fan, M. F. Li, and T. C. Chong, J. Appl. Phys., Vol. 79, (1996) ,188.
[19]Daniel Fritsch, Heidemarie Schmidt and Marius Grundmann , Phys. Rev., B67, (2003).235205.

P52.

THEORITICAL STUDY OF URANIUM COMPOUNDS

B. Teyar, A. Zaiter, S. Meskaldji, S.-E. Bouaoud, B. Zouchoune et L. Belkhiri

Laboratory of molecular chemistry, environmental control and physico-chemical measures (LACMOM) - Faculty of exact sciences, University of Mentouri-Constantine.

Since the discovery of the first cyclopentadienyl actinide complex Cp3UCl in 1956 by Reynolds and Wilkinson [1], several functionalized related compounds bis- tris and tetra (cyclopentadienyl) ((η5-C5R5)nAnL4-n (An = Th-Cf; n = 2, 3 and 4; R = H or alkyl ; L = X, R, RCO, NR2… etc.) have been characterized [2]. We were interested in a series of uranium bis-cyclopentadienyl compounds of type (η5-C5H5)2U(Eph)2 with functional ligands E = N, S, Se and Te whose crystalline structure are recently determinate [3]. While imido group U-N-ph adopts a linear geometry, the others U-E-ph moieties are rather bend. Among the questions which we were interested, we try to understanding the nature of the metal-ligand bonding and the key role of 5f orbitals in the particular geometry of such uranium compounds. Indeed, a new class of reactive molecules with unique catalytic properties not found in the chemistry of metals nd, is evidenced by the existence of a new mode of metal-ligand bonds devoted to the possible participation of uranium 5f orbitals.

The uranium-ligand σ or π interactions will be thus analyzed by comparing the various calculated structural parameters. We also study the redox properties by calculations of all uranium +3, +4, +5 and +6 species. We carried out relativistic DFT calculations by using the ADF2007.01 [4] code (Amsterdam Density Functional) which is perfectly adapted to the quantum treatment of such heavy elements compounds. The optimized molecular geometries on level ZORA/TZP/BP86 are in good agreement with the experimental structures. The unique linear U-N-ph coordination will be rationalized by electronic structure analysis and MO diagram.

References

[1]L. T. Reynolds, G. Wilkinson, J. Inorg. Nucl. Chem. (1956) 2, 246.
[2](a) A. Zalkin, J. G. Brennan et R. A. Andersen, Acta Crystallogr. Sect. (1988) C44, 2104. (b) W. J. Evans, S. G. Ganzales et J. W. Ziller. J. Amer. Chem. Soc. (1991) 113, 7423.
[3](a) William J. Evans, Kevin A. Miller, Joseph W. Ziller, Antonio G. DiPasquale, Katie J. Heroux, and Arnold L. Rheingold, Organometallics (2007), 26, 4287-4293
[4]ADF2007.01, SCM, Theoretical Chemistry, Vrije University, Amsterdam, The Netherlands; http://www.scm.com.

P53.

Etude par dynamique moléculaire de la pulvérisation d'une cible de Cuivre

par des ions d'Argon.

R. Mostefa, M. Elchikh, S. Hiadsi

Département de Physique, Université Mohamed Boudiaf d'Oran, (ex USTO), BP1505, Oran El Menaouer, Algérie. mostefarabah@yahoo.fr

L'étude de la pulvérisation de la surface d'un solide soumis au bombardement des ions à basse énergie a été très riche ces 3 dernières décades. Ses applications technologiques sont nombreuses, en particulier, dans le domaine des couches minces et l'analyse de surface. Dans ce papier, nous avons traité le cas spécifique du bombardement du Cuivre par l'Argon. Nous avons utilisé un code de calcul basé sur la dynamique moléculaire. Nous avons étudié la variation du rendement de pulvérisation en fonction de : l'énergie de l'ion incident, l'angle incidence, l'orientation du plan cristallographique de la cible. Par ailleurs, nous avons estimé aussi l'influence des différents modèles de pertes d'énergie, qui varient selon les potentiels inter-atomiques utilisés par notre code de simulation, sur le rendement de pulvérisation.

.La simulation de la pulvérisation par la dynamique moléculaire a été effectuée par le code de Kalypso (version 2.1) [1]. Les ions d'Argon arrivent à la direction normale au plan de la cible, ensuite l'angle d'incidence sera varié. Nous avons considéré une cible de Cuivre composée de 4410 atomes. La température de la cible est prise égale à 300 K (température ambiante).

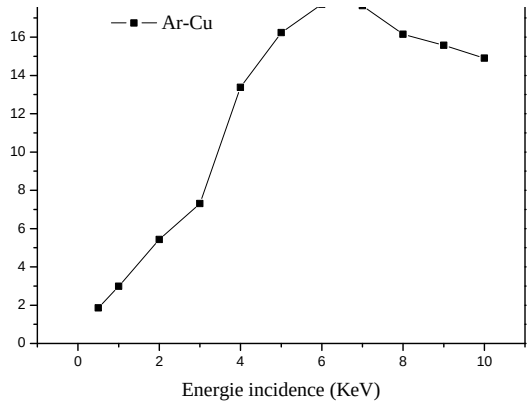

Fig. 1. Variation du rendement de pulvérisation en fonction

de l'énergie incidence (Ar-Cu) plan (111).

Pour tenir compte des effets de la perte d'énergie inélastique (dues aux excitations électroniques), nous avons opté pour les deux modèles suivants : Lindhard–Scharff-Schiott (LSS) et Oen-Robinson (OR) [2]. Nous avons pris un « lot » de 150 projectiles dans chaque simulation dirigés dans une zone de symétrie irréductible en suivant chaque trajectoire durant 3 ps (picosecondes).

A l'incidence normale, et pour une cible orientée selon le plan (111) nous obtenons la figure suivante :

Nous remarquons (voir le figure ci-dessus) que le rendement de pulvérisation noté Y passe par trois phases. La première phase qui correspond à des énergies inférieures à 6KeV, Y augmente linéairement, puis varie très légèrement entre 6 à 7 KeV : c'est la 2ème phase. Au-delà de 7 KeV, on passe à la troisième phase où le rendement décroît. Cette décroissance est due au fait que la cascade de collisions entre différents atomes est de plus en plus en profondeur.

Nous avons exploré l'influence de la structure cristalline de la cible sur le rendement de pulvérisation. C'est ainsi que nous avons choisi les 3 orientations suivantes du Cuivre : (100), (111) et (110) dans la gamme d'énergie allant de 0.5 à 10 KeV (à incidence normale).

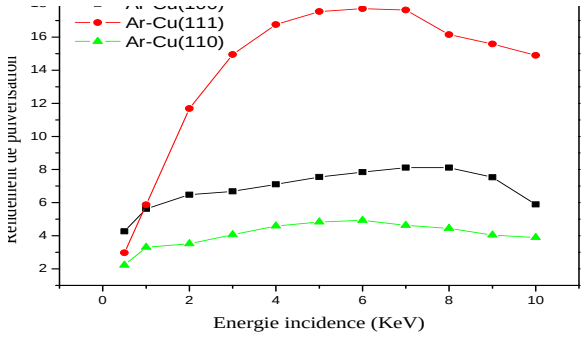

Fig. 2. Variation du rendement de pulvérisation Y en fonction de l'énergie d'incidence pour les 3 plans cristallographiques choisis.

D'après la figure ci-dessus, nous constatons que d'une manière globale, le taux de pulvérisation du plan (111) est nettement supérieur aux deux autres plans pour des énergies d'incidence supérieures à 1 KeV : Y (111)>Y (100)>Y (110). Ceci s'explique par le phénomène de canalisation (channeling) [3]. Mais il faut remarquer que pour une énergie d'incidence inférieure à 1 KeV, on a Y (100) >Y (111). Autrement dit, l'énergie seuil pour la pulvérisation du plan (100) est légèrement inférieure à celle du plan (111) comme on le voit sur la figure où les deux énergies seuils sont proches de 0.5 KeV.

Nous remarquons que le rendement de pulvérisation croît avec l'angle d'incidence θ jusqu'à un maximum de 40°, puis le rendement de pulvérisation décroît jusqu'à 90° (l'angle d'incidence

normale). Par ailleurs, la variation de Y(E) reste la même pour les différents angles d'incidence,et aussi nous remarquons que Y à E=5KeV est supérieur à 2 KeV [4.5].

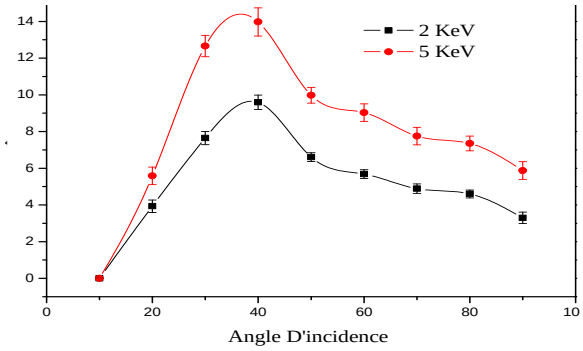

Fig. 3. Variation du rendement de pulvérisation en

fonction de l'angle d'incidence pour le plan (111)

Un but général des efforts de simulation en science des matériaux est intégrer des approches fondamentales telles que DM avec les outils et les modèles de plus haut niveau qui sont employés pour modeler prédictif de technologie et de processus [6,7].Les Simulations de pulvérisation par dynamique moléculaire ont été effectue pour des projectiles de Ar de l'énergie incident entre 0.5-10 KeV sur une cible Cu.

Nous avons confirmé que le code Kalypso se prête bien au phénomène de pulvérisation des cibles métallique pour des projectiles (ion des gaz rare) l'énergie d'incidence allant jusqu'à 10 KeV. C'est ainsi que le choix de la méthode de dynamique moléculaire est justifié par le fait que cette méthode donne des résultats réalistes.

References

[1] M.A. Karolewski, Nucl. Instr. and Meth. B 230 (2005) 402
[2] J. Lindhard, M. Scharff, H.E. Schiott, K. Dan,Vidensk. Selsk. Mat. Phys. Medd. 33 (1966) 14.
[3] J. D. Kress, D. E. Hanson, A. F. Voter, C. L. Liu and X.-Y. Liu, D. G. Coronell. J. Vac. Sci. Technol. A 17.5. Sep/Oct 1999
[4] R. Behrisch (Ed.), Sputtering by Particle Bombardment, Vol. I, Springer, Heidelberg, 1981.
[5] D E. Harrison 1988 Crit. Rev. Solid Stat Mater.Sci.14 SI-78.
[6] S. Hofmann, Phil. Trans. R. Soc. Lond. A 362 (2004) 55.
[7] J.C. Kools, J. Vac. Sci. Technol. A 23 (2005) 85.

Molecular Structure and Spectroscopy

P54.

Dynamique Harmonique et Etude Spectroscopique du

α-D-glucopyranosyl-(1→3)-β-D-fructopyranose

I. Taleb-mokhtari, M. Sekkal-rahal

Laboratoire de Chimie Théorique, Microscopie, Microanalyse de la matière et Spectroscopie Moléculaire, Université Djillali Liabes, 22000, Sidi-Bel-Abbes, Algérie, *il_taleb@yahoo.fr*.

Le but essentiel de la dynamique harmonique est de calculer les modes normaux de vibration d'une molécule. Ce travail à été effectue sur un disaccharide le turanose (α-D-glucopyranosyl-(1→3)-β-D-fructopyranose) (fig.1). C'est un sucre rare car présent pratiquement que dans le miel, et est considéré comme traceur de miel.

Le programme C.V.O.A « **C**ristalline **V**ibration **O**plically **A**ctive », comme son nom l'indique calcule les vibrations optiquement actives des molécules à l'état cristallin. Il permet donc, entre autre, de calculer les fréquences de vibration, la distribution de l'énergie potentielle (PED) qui donne la contribution partielle des coordonnées de symétrie à chaque mode de vibration (la connaissance de cette contribution est fondamentale pour réaliser correctement une analyse des modes normaux de vibration) et le Jacobien qui est utilisé pour faire l'affinement des constantes de forces.

Ces calculs ont été effectués à partir d'un champ de forces provenant de molécules étudiées auparavant [1-2]. Pour faire ces calculs nous avons utilisés dans le cristal le potentiel Urey Bradley Shimanouchi modifié (mUBSFF) intramoléculaire combiné à un potentiel intermoléculaire. Ce dernier fait intervenir les interactions dues à l'existence de la liaison hydrogène, les interactions entre paire d'atomes non liés exprimées à l'aide d'un potentiel de Buckingham et aussi les interactions de type électrostatique.

L'attribution des raies est effectuée, en ajustant les constantes de forces de telle façon que le spectre théorique se reproduise, la distribution de l'énergie potentielle est ainsi obtenue.

Le principe de transférabilité du champ de forces utilisé a été vérifié. Ceci, est du au fait que les constantes de forces utilisées dans le champ de forces, ne subissent pas une forte variation au cours de l'affinement.

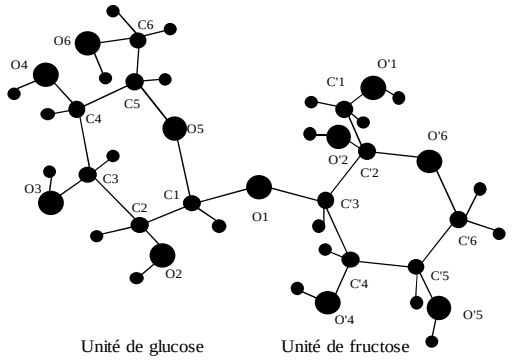

Fig. 1. Le turanose à l'état libre

Bien que cette méthode de détermination des modes normaux de vibration est très fiable et très riche, puisqu'elle permet l'attribution de raies notamment celles dues aux mouvements des groupements CH_2OH des deux unité saccharidiques du turanose, une étude expérimentale de dérivés isotopiques a permis de confirmer cette attribution ; la deutération qui consiste en un remplacement de chaque atome d'hydrogène appartenant aux groupements hydroxyles par son isotope le deutérium (turanose O-D_8), le glissement des bandes (caractéristiques des élongations OH et des déformation COH), nous a permis de rendre l'attribution encore plus exacte (fiable).

Comme dans tous les sucres les spectres sont composés de deux zones distinctes, l'une entre 3600 et 2700 cm^{-1} et l'autre située en dessous de 1500 cm^{-1}.

Dans la première zone on constate, bien évidement, les bandes correspondants au élongations OH et CH. Ces modes sont pratiquement purs. La discussion des résultats a été faite pour chaque type de groupement.

Les groupements CH_2 :

Les modes de cisaillement et de balancement caractéristiques des groupements CH_2 sont situés dans les domaines attendus. Le premier est facilement observable à 1457 cm^{-1} pour le CH_2OH de l'unité glucose et 1450 pour l'unité fructose. Le mode de cisaillement est le plus observable, puisque c'est la bande la plus intense sur la région 1500-1400 cm^{-1}. Le mode de balancement contrairement au cisaillement n'est pas pur il apparaît entre 1380 et 1270 cm^{-1} il est fortement couplé avec des modes de déformation COH. La contribution la plus importante de ce mode (22%) apparaît à 1274 cm^{-1}, il est observé à 1288 cm^{-1} et 1213 cm^{-1} sur le Me-β-D-galactose. Concernant les modes de rotation plane des deux groupements CH_2 (RO et RO') il sont retrouvés en dessous de 900 cm^{-1}, soit par exemple à 899 cm^{-1} (RO' 31%) et 854 cm^{-1} (RO 23%), couplés à des élongation C-O, des déformations CCH et COH.

Les modes de torsion angulaires sont aussi couplés à d'autres modes, ils apparaissent en dessous de 1180 cm^{-1}, pour les anomères du Me-glucose ce mode apparaît respectivement à 1304 et 1200 cm^{-1} et pour le Me-β-galactose à 1203 cm^{-1}. Toutes ces différences de position des fréquences caractérisant le groupement CH_2 sont dues aux différences de géométrie et de configuration du composé.

Les déformations COH :

Les plus fortes contributions des déformations des groupement carbone hydroxyle, se situent entre 1417 et 980 cm^{-1}, et sont en parfait accord avec les attributions faites pour le glucose par Vasko et col. [3]. La distribution de l'énergie potentielle donne une forte contribution de ce mode à la fréquence 1360 cm^{-1} cette bande correspond précisément la déformation $C_{22}O_{10}H_{34}$, ce résultat est confirmé par

les auteurs cités plus haut, en effet ces derniers ont étudiés les spectres Raman et infrarouge en solution dans H_2O est D_2O, du glucose, du cellobiose et du maltose [3,4]. L'étude de ces spectres a permis d'attribuer ce mode aux fréquences 1360 et 1250 cm^{-1}, ce qui est en accord avec nos résultats. Après la deutération nous remarquons que les élongations O-D se déplacent de la région 3600-3270 cm^{-1} vers la région 2964-2431 cm^{-1} voir tableau 32. Les modes de déformation COD apparaissent quant à eux dans la région située entre 1152-871 cm^{-1}.

Les bandes observées à 1407 cm^{-1} ($C_{15}O_{11}H_{23}$), 1203 cm^{-1} ($C_{15}O_{10}H_{23}$), 1125 cm^{-1} ($C_{19}O_7H_{44}$), 1042 cm^{-1} ($C_{21}O_9H_{45}$), 933 cm^{-1} ($C_{13}O_2H_{42}$), disparaissent presque complètement sous l'effet de l'échange isotopique. Cette diminution d'intensité ou disparition des bandes est due au fait que les modes COH correspondants à ces bandes sont couplés à des élongations C-O. Les bandes COH qui ne disparaissent pas au cours de la substitution isotopique du turanose sont dues à des glissements d'autres bandes.

Les groupements carbonés :

Les groupements OCH, HCC, CCH, sont observées dans la région 1388-836 cm^{-1} ce sont des groupement qui mettent en jeu un atome d'hydrogène. Ce résultat est en parfait accord avec ceux obtenus pour des monosaccharides [1,2,5-7], des disaccharides [8] et des polysaccharides [3,4]. Ces modes sont couplés entre eux avec d'autres modes comme les élongations C-O et les déformations COH.

Les déformations d'atomes lourds CCO, CCC, COC et OCO apparaissent dans la région située en dessous de 1000 cm^{-1}. Selon la distribution de l'énergie potentielle, cette région est attribuée aux modes de déformations angulaires endocyclique et exocyclique des atomes lourds (C-C-O, C-O-C ou O-C-O) accouplée à des modes de torsions autour des liaisons C-O et C-C , ceci est en accord avec les travaux précédents.

Les modes dus au groupement réseau :

Dans la région située en dessous de 200 cm^{-1}, apparaissent les modes de translation (Tx,Ty,Tz) et de rotation autour des axes d'inertie (Ra, Rb, Rc), on constate qu'il existe une forte contribution de modes couplés impliquant torsions avec les modes de distorsion CCO, CCC ou COH et avec des modes de rotation et translation. Les bandes de la région en dessous de 160 cm^{-1}, sont également dues aux mouvements du réseau, qui sont essentiellement dues aux modes de translation (Tx, Ty, Tz) et à la rotation autour des axes d'inertie (Ra, Rb, Rc).

Le champ obtenu est donc valide puisqu'il reproduit avec un pourcentage d'erreurs de quelques unités, toutes les fréquences de vibrations moléculaires observées sur les spectres infrarouge et Raman. L'affinement des constantes de forces effectué sur cette molécule a été long et fastidieux du fait qu'elle est constituée de deux unités saccharidiques et par conséquent un grand nombre de fréquences à affiner.

Réferences

[1] M. Dauchez, P. Derreumaux, G. Vergoten, j. Comput. Chem., Vol 14, n°3, (1992) 263.
[2] N. Benbrahim, M. Sekkal-Rahal, G. Vergoten, Spectr. Acta., PartA58, (2002), 3021.

[3] P.d. vasko, j. blakwell, j.l. koenig, Carbohydr. Res., 19 (1971) 297.
[4] P.d. vasko, j. blakwell, j.l. koenig, Carbohydr. Res., 23 (1972) 407.
[5] I. N. Taleb-Mokhtari, M. Sekkal-rahal, g. vergoten, spectr.acta, partA59, (2003) 607.
[6] N. sekkal, I.N. Taleb-mokhtari, m. sekkal-rahal, p.bleckmann, G. vergoten, spectr. acta, PartA59, (2003), 2883.
[7] M. Sekkal, P. Legrand, G. Vergoten, M. Dauchez, Spectr. Acta., PartA48, n°7, (1992) 959.
[8] I. Kouach-Alix, M. Dauchez, M. Sekkal and G.Vergoten, j. Raman spectr., Vol 26, (1995) 223.

P55.

Calcul des modes normaux de vibration des disaccharides dans le cristal

Gafour.M.H, Sekkal-Rahal.M, Youcefi.N, Sellam.M, Bouterfes.M, I.N.Taleb-Mokhtari, Reguieg.C

Laboratoire de microscopie, micro-analyse de la matière et spectroscopie moléculaire,
Faculté des sciences, département de chimie,
Université Djillali Liabes de Sidi Bel Abbes , Algérie

L'α-D-lactose est un disaccharide constitué de deux entités, glucose et galactose lié par une liaison osidique de type (1,3), tendit que l'isomaltulose et aussi un disaccharide se compose de α-D-glucose et β-D-fructose lié l'un par rapport à l'autre par une liaison osidique de type (1,6).

Notre travail consiste à reproduire les données spectroscopiques vibrationnelles de ces molécules utilisant un programme de calcul nommé (C.V.O.A.) [1] (Cristalline Vibration Optically Active). Le calcul a été effectué à partir d'un champ de force de type Urey Bradlay Shimanouchi modifié (mUBSFF)[2]. Après avoir calculé les modes de vibration dans le solide, un calcul supplémentaire a été réalisé dans la solution deuterée dans le but de confirmer les contributions des modes de vibration OH.

Les constantes de force établies pour l'α-D-glucose [3], le β-D-galactose [4] et le β-D-fructose [5] ainsi que les données cristallographiques de l'α-D-lactose [6] monohydrate et l'isomaltulose monohydrate [7] ont été le point de départ de notre calcul.

Nous avons commencé par le calcul des bases fréquences de ces molécules dans le solide (corps rigide), car dans cette région les constantes de force des liaisons hydrogènes interviennent indépendamment des autres, après en passe au calcul des hautes fréquences dans le cristal (corps flexible).Finalement les fréquences calculées sont comparais avec celles observées dans les spectres IR et Raman des molécules et par conséquence on vérifie si la transférabilité du champ de force est fiable.

La région la plus difficile à interprété est celle située entre 500 cm-1 et 1500 cm-1, car dans cet intervalle les bandes sont très couplées, pour cela, les spectres IR et Raman des oligosaccharides qui présentent dans leurs structure les mêmes unités telles que le glucose, le galactose et le fructose ont été accordé dans le but de confirmer les attributions des bandes. Turanose, lactulose, melibiose, gentiobiose, palatinose (isomaltulose), melezitose et stachyose sont les molécules choisies pour enrichie cette étude, ces derniers sont pris dans les deux solutions aqueuse et deutérée. En revanche, les spectres IR et Raman des unités de D-glucose [2], D-galactose [3], L-fructose [8] et rhamnose ont été pris en considération.

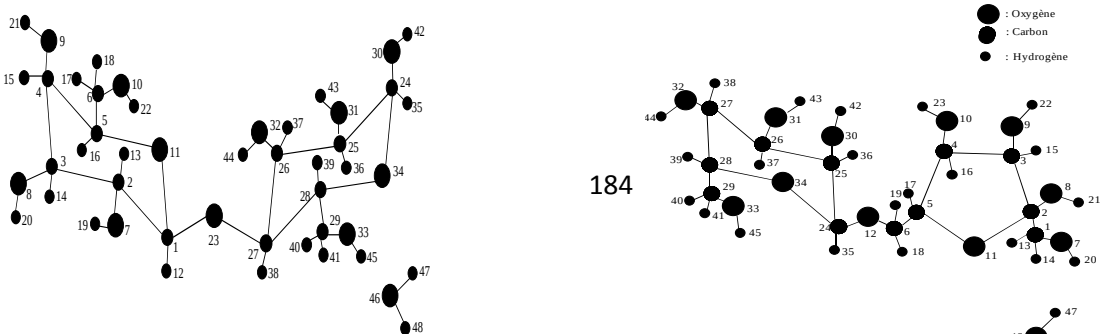

Références
[1] H.Takeuchi, PhD Thesis, Tokyo, Japan. (1975).
[2] T. Shimanoushi. Pure Appl.Chem. 7 (1963) 131.
[3] M. Dauchez, P. Derreumaux et G. Vergoten, J. Comput. Chem. 14 (1992) 263
[4] M. Sekkal, P. Lagant, G. Vergoten et M. Dauchez, Spectrochem. Acta. 48A 9 (1992) 95.
[5] D.C. Fries, ST. Rao et M. Sundarlingam, Acta. Cryst, B27 (1971) 994.
[6] F.S. Parker, Applications of Ifrared, Raman and resonance Raman Spectroscopy in Biochemistry, PleniumPress, New Work (1983).
[7] A.T. Tu, Raman Spectroscopy in Biology, Principe and Applications, Wilay (1982).
[8] M. Kacurakova, M. Mathlouthi, Carbohydrate research, 284 (1996) 145.

P56.

DFT MODELLING OF THE KAPPA CARRAGEENAN IN GAS PHASE AND IN SOLUTION

N. YOUSFI, C. REGUIEG, M. Rahal-Sekkal

Laboratoire de microscopie, micro-analyse de la matière et spectroscopie moléculaire,
Faculté des sciences, département de chimie,
Université Djillali Liabes de Sidi Bel Abbes , Algérie

k-Carrageenan is a linear, negatively charged, sulfated galactan polysaccharide and is one of the three main fractions of the carrageenan family along with iota (i) and lambda (l). The three fractions differ in their degree of sulfation and 3,6-anhydrogalactose content. □-carrageenan is abundantly used in food, chemical and pharmaceutical industries like texturing agent, this is due to its physical property to form thermo-reversible gels1 that is related to its conformation. The structure of one of the two repeating dimers constituting kappa-carrageenan; the 4-O-sulphated-□-D-galactopyranosyl 1,4 anhydro 3,6-□-D-galactopyranose is studied in this work.

DFT optimization studies at B3LYP/6-31G* level of theory2 have been carried out, using the Gaussian 03 program, The main goal is to study the structure and the energy in the whole conformational space of the disaccharide. The role of solvent in the stability of different conformers and the nature of any interactions solvent-disaccharide are very important to underline. We have adopted for the solvent Onsager model.3, our calculations for all conformers of the neutral form give an average volume of 5.50A. and we have considered the value of dielectric constant 78.34 corresponding to polar solvent water

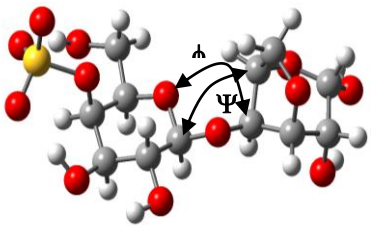

Fig.1. Kappa-carrageenan

for this aim conformational maps4-6 for monosulphated carrabiose (β-D-Galp-4-sulphate-(1→4)-3,6-An-α-D-Galp) (Fig.1) in gas phase and in the solvent have been constructed for the neutral form of the molecule, These conformational maps have been built as suggested by French et al.4

The obtained values of the two dihedral angles are Φ =-74.57° and ψ = 95.71° for the neutral form, for this later form, this optimized structure has been reoptimized in presence of solvent, we have obtained the values of Φ = -73.40 and ψ = 93.28, thereafter these dihedral values was been used as the starting structure to construct the conformational maps in all the calculations,

The results of the gas phase DFT calculations allow us to conclude that a rigid conformational map in full agreement with the relaxed map, is able to predict the regions of the minima in the potential energy surface of k-Carrageenan. The map obtained in the solvent shows regions of minimum energy in the same positions of the regions found in the gas phase.

References
[1] Moir, A.; Smith D. A.; Annu. Rev. Microbiol. 44 (1990) 531-553.
[2] French, A. D. Carbohydr. Res. 1989, 188, 206–211.
[3] Onsager, J. Am. Chem. Soc. 58, 1486 (1936).
[4] French, A. D.; Brady, J. W. ACS Symp. Ser. 1990, 340,1-19.
[5] Tran, V.; Bulèon, A.;Imberty, A.; Pérez S., Biopolymers, 1989, 28, 679-690;Stortz, C. A. Carbohydr Res 1999, 322, 77-86.

P57.

Caracterisation structural et etude spectroscopique des complexes de transfert de charge des N-sulfamoyloxazolidinones avec deux accepteurs.

MESSIAD Hanane[1], Hamouche Karima[2], KADRI Mekki[3]

Département des Génies de Procédies, Université de Guelma 24000, Algérie
[1]messyadhanene@yahoo.fr
[2] libertkarima@yahoo.fr.
[3]mekkikadri@yahoo.fr

Les N-sulfamoyloxazolidinones, dernière génération des sulfamides,comportent deux pharmacophores ce qui leur confère une activité biologique remarquable. La solubilité de ces molécules est nettement améliorée par formation des complexes d'inclusion formés avec la β -cyclodextrine[1,2]. Notre present travail se propose d'étudier l'interaction d'une série de sulfamoyloxazolidinones avec deux accepteurs

d'electron – π connus: le tetracycanoethylene (TCNE) et le 2,3dichloro 5, 6 -dicyano p-benzoquinone (DDQ).

L'interaction a été mise en évidence par spectrophotométrie UV Vis à 20°C. Les résultats montrent que la formation des complexes de stoechiométrie 1 :1. En milieu de chloroforme, Nous discutons des caractéristiques spectrales et des constantes de formation (K_{TC}) et des coefficients d'extinctions molaires (ε_{TC}) en termes de structure de donneur moléculaire, d'affinité d'accepteur d'électron, et d'effets de solvant. Nous avons estimé les potentiels d'ionisation (PI) des donneurs à partir des énergies de transition CT de leurs complexes [3] .

Les paramètres thermodynamiques ΔG^0, ΔH^0 ET ΔS^0 révèlent que la formation du complexe TC des complexes est un phénomène spontané, exothermique se passant avec diminution de l'entropie. [4]

Les résultats obtenus de ces paramètres avec les calculs de la force d'oscillateur (*f*), du moment dipolaire de transition (μ) et du rapport b2/a2 sont en faveur de la mise en jeu d'une forte interaction donneur –accepteur. [5]

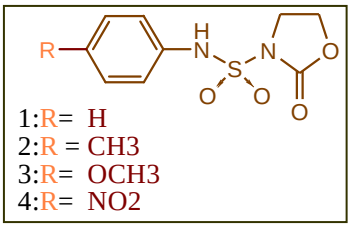

Fig.1. structure des N-sulfamoyloxazolidinones

References:

[1] Mekki KADRI, Nabila Dhaoui , Mohamed Abdaoui , Jean-Yves Winum , Jean –Louis Montero . European Journal of Medicinal Chemistry 39 (2004) 79-84

[2] Mekki KADRI, Rayenne DJEMIL, Mohamed Abdaoui, Jean-Yves Winum ,Frédéric COUTROT, Jean –Louis Montero . Bioorganic & Medicinal Chemistry Letters 15(2005) 889-894.

[3] S. Bhattacharya et al. / Journal of Molecular Structure 784 (2006) 124–13.

P58.

Modified UBSFF calculation of the α-D-allose and β-D-talose

Molecules in the crystalline state

C. Reguieg, M. Sekkal-Rahal; N.Yousfi

Laboratoire de microscopie, micro-analyse de la matière et spectroscopie moléculaire,
Faculté des sciences, département de chimie,
Université Djillali Liabes de Sidi Bel Abbes , Algérie

In this work, we report the force fields obtained for both α-D-talose and β-D-allose. They have been obtained using a modified Urey-Bradely-Shimanouchi Force Field (mUBSFF)[1] involving non-

redundant symmetry coordinates, combined with a complete intermolecular potential energy function taking into account the Van der Waals and the electrostatic interactions and also a contribution of the hydrogen bonds. With these potentials and on the basis of vibrational data (Infrared and Raman spectra of α-D-talose and β-D-allose) and in accordance to previous works made on analogue molecules, we have fitted the set of parameters of both molecules in the crystalline state, they represent the forces fields.

The normal coordinates calculations have been performed using the C.V.O.A (Crystalline Vibrations Optically Active) program that has been written by Takeuchi [2]. The main goal of this program is to calculate the optically active vibrations of the molecule in the crystalline state as well as the frequencies and the normal modes of vibrations. The method here is derived from the Wilson GF method [3], and uses partly local symmetry coordinates developed by Shimanoushi [4].

IR and Raman spectra of β-D allose, α-D-talose and β-D allose O-D5 have been recorded in the 4000-400 cm-1 and in the 4000-20 cm-1 regions.

These spectra constitute the experimental support that allows to reproduce theoretically the vibrational frequencies and to establish a force field for these saccharides through a normal coordinate analysis.

The structure of β-D-allose and the α-D-talose derived from X- ray diffraction and from neutrons diffusion data [5, 6, 7]. In both β-D-allose and α-D-talose molecules, the configuration of the pyranose ring has a 4C1 chair conformation. The exocyclic hydroxymethyl group has a gauche-gauche orientation in the case of □-D-allose and gauche-trans in the case of □-D-taose (Fig. 1, 2)

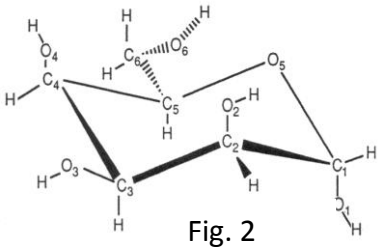

Fig. 2

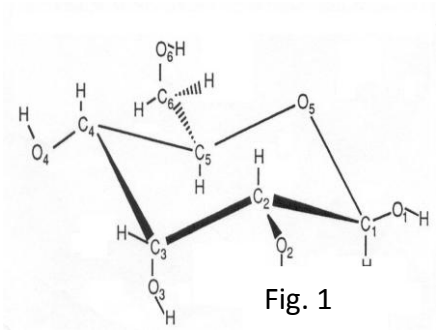

Fig. 1

References:

[1] T. Shimanouchi, Pure Appl. Chem. 71 (1963) 131.
[2] H. Takeuchi, PhD thesis, Tokyo, Japan 1975.
[3] E. wilson, J. Decius and P. Gross McGraw Hill, New York (1958) 54.
[4] T. Shimanouchi, Vibrational Spectroscopy and its Chemical Applications, University of Tokyo, Bunkyoku, Japan, 1977.
[5] L. M. Jkroon-Btenburg, P Van Der Sluis, J. A. Kanters, Acta Cryst, C40 (1984) 1863.
[6] Th. Steiner, cryst. Rev, 6 (1996) 1.
[7] L. K. Hansen, A. Hordvik. Acta Chemica Scandinavica, A31 (1977) 187.

P59.

Elaboration of Hg/InN/InP(100) structures- study by photoelectron spectroscopy ESCA and electrical analysis.

M. A. Benamaraa, A. Talbia, Z. Benamaraa, B. Akkala, N. Chamia, B. Gruzzab, L. Bideuxb, C. Robertb and C. Varenneb .

1Laboratoire de Microélectronique Appliquée Université Djillali Liabès de Sidi Bel Abbès , Algérie.

2Laboratoire des Sciences des Matériaux Pour l'Electronique et d'Automatique, Université Blaise Pascal de Clermont II, Les Cézeaux, 63177 Aubière Cedex, France.

The nitrides of group III metals as InN are very important materials in optoelectronic (light-emitting diodes and laser diodes) and microelectronic areas. It is essential for the realisation of such devices to grow high quality nitride single crystals. In this paper, the nitridation of InP(1 0 0) surfaces has been studied in situ by X-ray photoelectron spectroscopy (XPS) using the Mg Kα radiation (1253.6 eV). After ionic cleaning by Ar+ ions, metallic indium crystallites are created (see figure 1) and the nitridation of the substrates is performed using a plasma glow discharge cell reaction with these indium clusters.

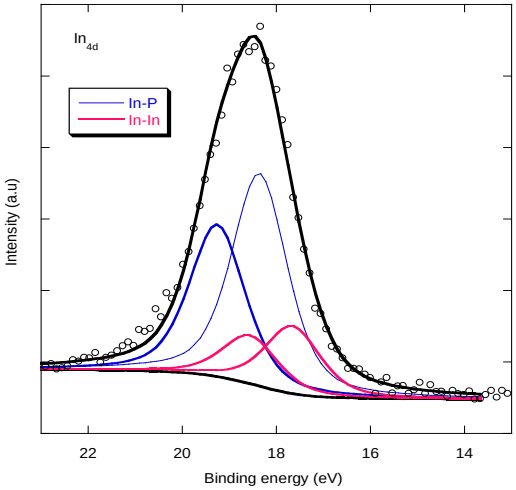

Fig.1. Experimental In_{4d} peak of InP(1 0 0) after ionic cleaning.

We used the In4d and P2p core levels to monitor the chemical state of the surface and the coverage of the present species, figures 2 and 3 shows the evolution of the In4d and the P2p core levels, respectively.

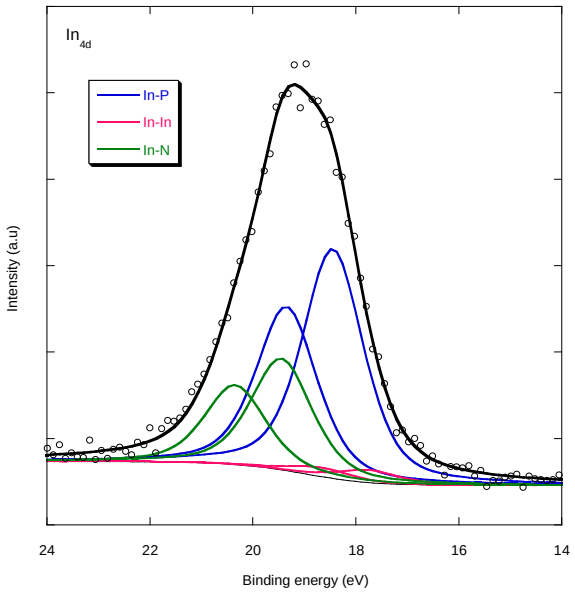

Fig.2. Experimental In_{4d} peak of InP(1 0 0) obtained after nitridation.

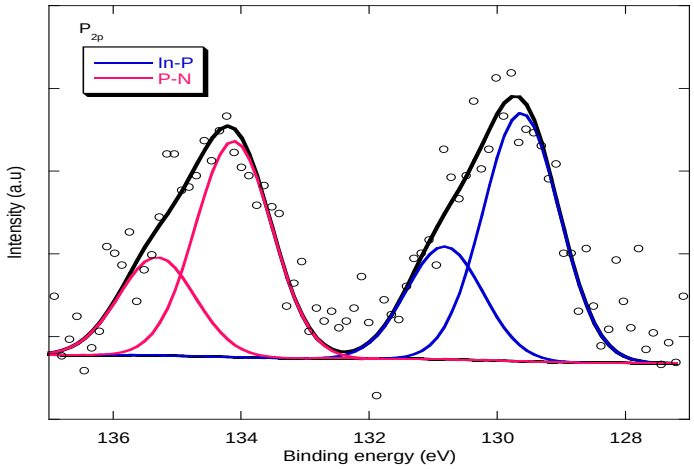

Fig.3. Experimental P_{2p} peak of InP(1 0 0) obtained after nitridation

We observed the creation of InN and PN bonds while the In–In metallic bonds decrease. This confirms the reaction between indium clusters and nitrogen species. A theoretical model based on stacked layers allows us to assert that we have produced almost two monolayers of indium nitride. In order to determine the quality of the elaborated nitride films and the electrical properties of the InN/InP interface, we have used the I(V) electrical method Analysis of the measured characteristics at room temperature (see figure 4) allows the determination of the electrical parameters.

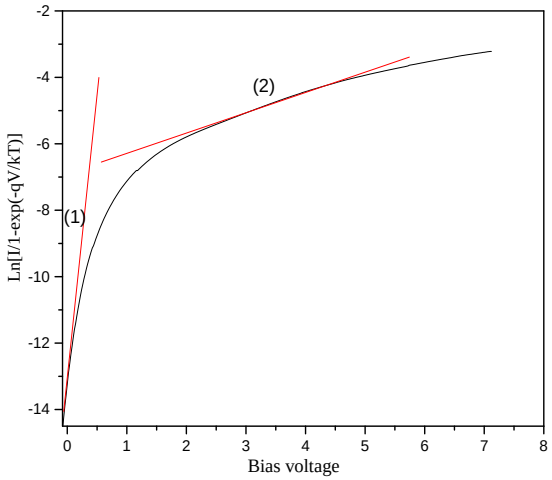

Fig.4. Evolution of ln $[I/(1-\exp(qV/kT))] = f(V)$ vs. bias of the InN/InP structures.

The saturation current Is, the ideality factor η, and the serial resistance Rs are evaluated to 1.92 × 10−6 A, 3.07 and 375 Ω, respectively. The barrier height is determined at room temperature and is equal to 0.547 eV. These results are summarized in table 1.

I_s (A)	1.92×10^{-6}
η	3.07
Φ_{Bn} (eV)	0.547
R_s (Ω)	375

Table1 . Electrical parameters of Hg/InN/InP structures

Simulation and Molecular

Modelling Methods

P60.

Monte Carlo Simulation of the Electron Beam Scattering Under Water Vapor Environment at Very Low Energy

O. Mansour[1], A.Kadoun[1], C.Mathieu[2], K.Aidaoui[1]

[1] Laboratoire de microscopie, microanalyse et spectroscopie moléculaire, Université de Sidi Bel Abbés, faculté des sciences, département de physique.

[2] Centre de calcul et de modélisation, Université de Lens, Université d'Artois, faculté des sciences, France

There are important applications in materials science in witch the role of the environment on a simple are critical. The requirements of SEM, such as a high vacuum and the need for a thin coating if an insulator is being analysed, mean that some types of materials have always proved difficult or impossible to image straightforwardly. The possibility of examining the natural or true surface of practically any specimen has added a new dimension of electron microscopy. ESEM allow even non-conducting, out-gassing, dirty, oily or wet simples to be examined non-destructively in humidified or gaseous environment. With ESEM many experiments may be performed. Low voltage ESEM is promising new technique for morphological characterization. Operating at low voltage has a particular advantage (i) high resolution, (ii) negligible beam damage of the samples. Moreover, an LVESEM equipped with field emission gun (FEG) source witch provide a high brightness, small spot

size and low energy spread in comparison to conventional beam. From the advantage mentioned above, FEG-ESEM at low voltage, offer the capability of being able to perform in situ deformation experiments. The main limitation concerning the use of the ESEMs is the scattering of the electrons of the primary beam with the atoms of the gas. Interactions of the primary beam electrons with the gas molecules in the chamber scatter a fraction of the beam electrons into a broad low intensity skirt around the focused probe. Electrons in the skirt contribute unwanted signals that originate relatively far away from the intended quantitative analysis area. Several authors **(Mathieu, 1999 [1]; Adamiak and Mathieu, 2000[2]; Kadoun et al, 2005[3]; Moncreiff, 1979 [4])** have studied this beam–gas interaction with the influence of the beam energy, working distance, pressure, and gas nature. However, none of these authors has investigated the scattering of electron with gas at very low acceleration voltage. In this paper, we examine, the electron beam profile at very low acceleration voltage, and we discuss this influence on the electrons distribution at the sample level by Monte Carlo simulation. Electron scattering cross sections are also investigated as a function of the energy of electron beam. As primary electrons exit the final PLA of an ESEM and enter the specimen chamber, a certain percentage of them undergo scattering events with water vapor molecules. The fraction of primary electrons scattered depend on the sample chamber pressure (P), primary electrons beam energy (E) and the working distance (W). collision occur when the primary electrons interact with gas particle within an effective area known as the total scattering cross section, witch represent the probability that a scattering event occur. The total scattering cross section is a combination of elastic scattering, were the electron energy before a collision is approximately equal to the electron after a collision and inelastic scattering, were energy from the incident electron is transferred to the gaseous molecule in producing ionization, excitation, molecular dissociation, molecular rotation and molecular vibration. In our simulation, the total collision cross section consists of elastic, total electronic excitation, vibrational excitation, total ionization and attachment cross sections. Here, "total ionization" means the sum of ionization processes producing OH+, O+ and so on including H2O+. The electronic excitation and ionization cross sections can be divided into lots of cross sections of various excitation levels and ionization species since there are numerous data reported to give each cross section. In addition to the electronic excitation and the ionization of water molecules, we also consider the vibrational excitation and electron attachment processes because the cross sections for them are overlying the electronic excitation and ionization cross sections around their threshold energies. These processes are important at the endpoint of the track simulation with low energies decreased from high energy regions of electron because the electrons total penetration depth varies depending on the processes. Two cross sections for the vibrational excitation and three attachment cross sections are taken into account. As the vibration excitation cross sections, two lump modes, (100 + 001), (010), are considered. The set of electron collision cross sections for water vapour used in the simulation is shown in Fig.1.

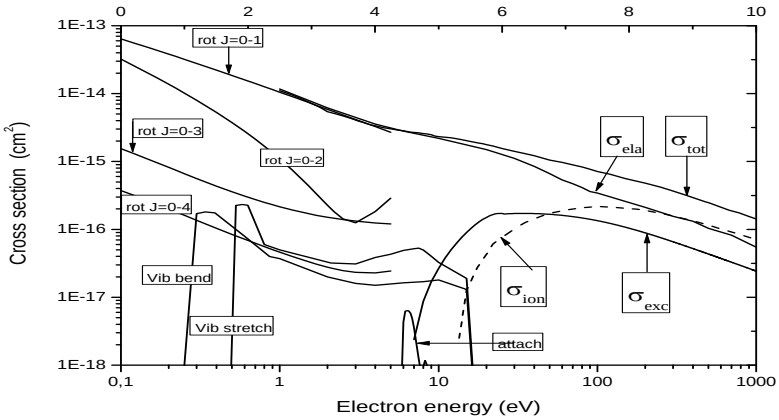

Fig.1. water vapor cross sections vs. energy of electron beam

We have performed Monte Carlo simulations [4,5]of the track of electrons incident on water vapor. The number of the incident electrons is typically 100000 in the present study. Figure 2 shows the energy distributions of electrons just before the ionization and electronic excitation collisions per track history for the incident electron energy from 0.5keV to 1keV. The incident electron starts with initial energy and slows down through the energy loss collisions, i.e., ionization and excitation collisions, to rest. As is shown in Fig.2, the energy distributions exhibit specific patterns for the ionization and excitation processes, where the excitation collisions occur with electron energies mostly below 50eV while the ionization collisions are dominated by high energy electrons around the initial energy and low energy electrons below a few hundred eV.

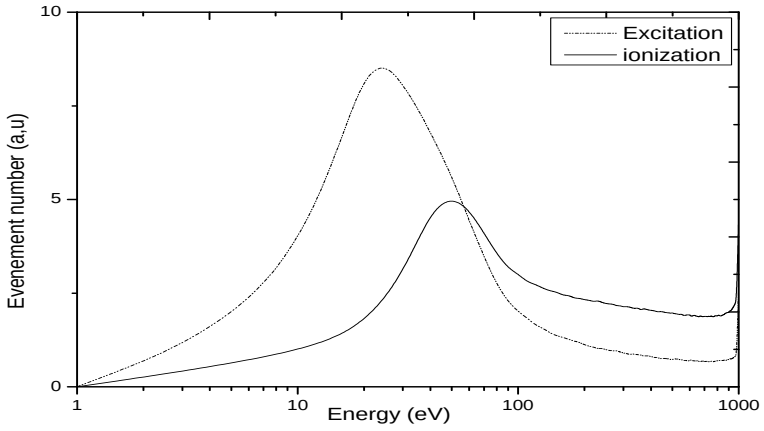

Fig.2. the energy distributions of electrons just before the ionization and electronic excitation collisions

Fig 3 show the electron beam penetration depth in water vapor for the incident energy 0.5keV to 1keV, compared to Bethe range for two pressures (0.5 and 1Torr).

This study on the penetration depth [7] also presents a technological interest. Indeed, one sees on the fig.3 for low energy (1 keV) and a high pressure (1TorrPa for H2O), the depth of penetration is only 8 cm in H2O. It should therefore use a working distance less than that value. The graph below can be

used as a tool to determine the maximum distance to be used for pressure and energy data for water vapor.

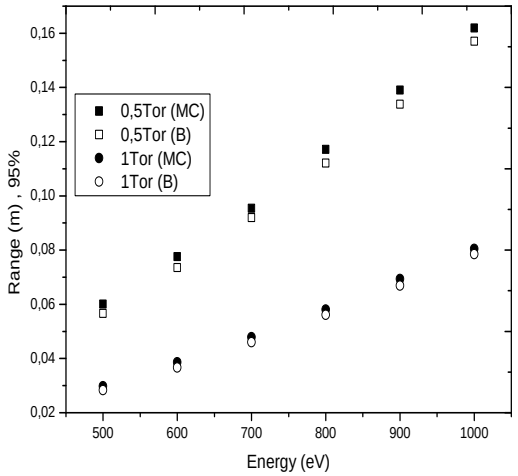

Fig 3. Electron beam Penetration depth in water vapor for various energy and pressure

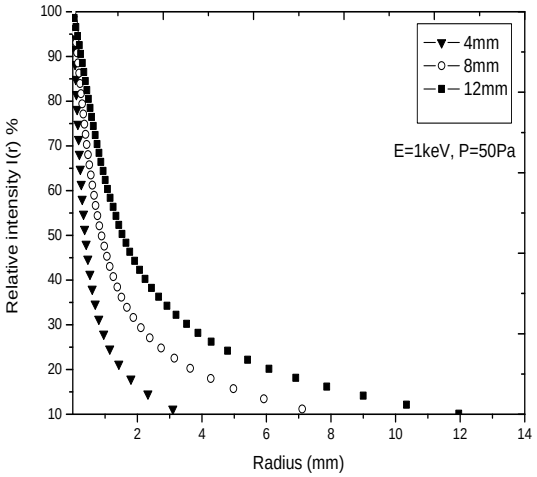

Fig.4.1 Relative intensity profile of 1 keV beam after passing through 4,8,12 mm water vapor at 50Pa pressure

The second part of our calculations deals with the variation of the skirt radius when the analytical distance is varied, Pressure, or energy. At 12 mm the skirt radius is high, of around 12mm at 50 Pa. On the other hand, the skirt extent is drastically reduced for a distance of 4 mm, it seems that the skirt radius remains constant when the pressure increases or energy and that it is in the first approximation only a function of the working distance.

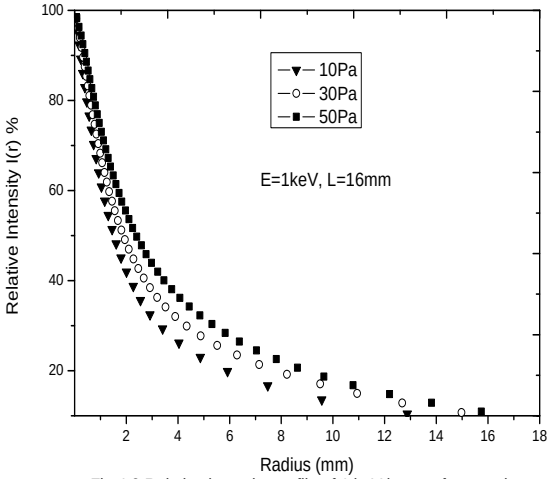

Fig.4.2 Relative intensity profile of 1 keV beam after passing through 16 mm water vapor at differents pressures

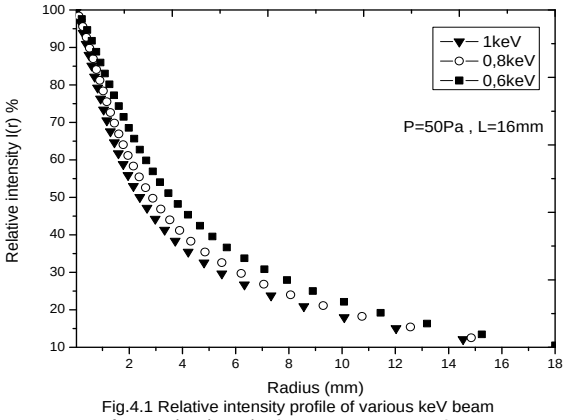

Fig.4.1 Relative intensity profile of various keV beam after passing through 16 mm water vapor at 50Pa pressure

In this study, we have carried out Monte Carlo simulations of electrons in water vapor in order to investigate the beam profile at very low energy in HPSEM. The effect of using very low energy in the low vacuum SEM zone has been compared with Monte Carlo calculations. Results show that lowering

electrons beam energy or pressure has no effect on the skirt extend. Skirt extend is only function with working distance.

References:
[1] Mathieu, C., 1999. The beam gas interaction and the signal gas interaction in the variable pressure SEM. Scanning Electron Microsc. (Scanning Microscopy International. Chicago) 13, 23–41.
[2] Adamiak, B., Mathieu, C., 2000. The reduction of the beam gas interactions in the variable pressure scanning electron microscope with the use of helium gas. Scanning 22, 178–181.
[3] Belkorissat, R., Kadoun, A. , Khelifab,B., Mathieu,C., 2004. The effect of beam diameter on the electron skirt in a high pressure scanning electron microscope. Micron 35, 543–547.
[4] Moncreiff, D.A., Barker, P.R., Robinson, V.N.E., (1979). Electron scattering by gas in the scanning electron microscope. Journal of Physics D: Applied Physics 12, 481–488
[5] Joy, D.C., 1995. Monte Carlo Modeling for Electron Microscopy and Microanalysis. OUP: NY.
[6] Grosswendt B and Waibel E (1978) Transport of low energy electrons in nitrogen and air. Nucl Instr and Meth 155: 145-156
[7]Bethe, H.Z., 1930. Theorie des Durchganges schneller Korpuskulerstrahlen durch Material. Annalen de Phys. (Leipzig), Vol.5, 325-333

P61.

On three dimensions Monte Carlo grain growth simulation

A. Ayad[1] and N. Rouag[2]

[1]Ecole Nationale Supérieure de l'Hydraulique, B P 31, 09000 Blida. Email: abdelhak_ayad@yahoo.com
[2]Laboratoire de microstructure et défauts, Université Mentouri Constantine, route Ain El-Bey, 25000 Constantine. Email : nadrou@wissal.dz

A modified Monte Carlo procedure is applied to studying the kinetics of grain growth in two and three dimensions. This technique involves representing the continuum microstructure on a discrete set of regular space grid. In this paper we investigate the effect of lattice that represents the discrete microstructure by using a square grid for 2D and a simple cubic network for 3D. The grain growth kinetics and grain topology are analyzed both for the 3D domains and for 2D simulated microstructures. The lattice and the number of neighbours have a noticeable influence on the result of simulations. Also the average grain size is a very important parameter because it is closely related with many properties of simulated structures.

In recent years considerable effort and computational resources have been devoted to simulating grain growth in polycrystalline materials. Grain structure is an important microstructural feature of a material. It contributes to strength, ductility, toughness and corrosion resistance and electrical properties. Due to its importance, it has been studied extensively by both theoretical deduction [1,2] and computer simulation in two dimensions (2D) [3,4] but this process represents in fact a three-dimensional (3D) phenomenon[5,6]. It is very difficult to study the 3D grain growth directly by physical experiments. Usually, microstructure studies are performed for cross-sections of experimental specimens, thus providing only 2D microstructure information. Therefore, computer simulation is actually the most effective tool for studying the 3D grain growth process.
The dimensional extension from two-dimensional lattice to three-dimensional lattice or the choice of simulation variables could affect the grain growth characteristics. This contribution shows the simulation passage from 2D to 3D grain growth by the Monte Carlo technique.

The most realistic correspondence between the evolution of real and simulated structures was achieved by Monte Carlo simulations [7]. Monte Carlo simulation of grain growth in a two-dimensional monophase structure starts with the initialization of the simulation lattice. The lattice consists of 100 x 100 square lattice sites that are stored in the computer memory in the form of matrix. Each lattice point is assigned an integer Q_i called orientation or spin where Q_i[1, Q]. A grain is defined by neighbouring lattice points with the same orientation. Then naturally the grain boundary lies between two adjacent lattice points with different orientations. The principle of three-dimensional simulations is the same as in two-dimensional case. The three-dimensional simulations are based on NxNxN spatial grid. The orientation numbers between 1 and Qmax are assigned to each lattice site of the initial microstructure constructed on a 100×100×100 simple cubic sites grid. Qmax is the total number of orientations in the initial microstructure. Lattice sites having an identical Q number are considered as a grain, and a grain boundary segment is defined to lie between sites of unlike Q numbers. Monte Carlo simulation of the grain growth in polycrystalline materials consists in evaluation of potential energy of a lattice point. The energy is determined by interaction of the point with its surrounding lattice points. The Hamiltonian of the interaction is:

$$E = J \sum_{j=1}^{n} \delta_{Q_i Q_j} \quad -1$$

where J is the positive constant which specifying a measure of the interaction of the evaluated i-th point with the neighbouring points, n is the number of nearest neighbours j of site i (n = 4, 8 and 16 for the square lattice in 2D simulation and n = 6, 18 and 26 for the simple cubic lattice in 3D simulation), δ is the Kronecher function with $\delta Q_i Q_j = 1$ if $Q_i = Q_j$ and 0 otherwise. The sum is taken over all n surrounding lattice points [8]. Simulation of grain growth involves the random selection of a site Q_i and its reorientation attempt. The reorientation attempt is restricted to the random site, adjacent to the selected site. Thus the net energy change associated with the reorientation trial can be expressed by:
$Ei = Ei2 - Ei1$
Where Ei1 and Ei2 are boundary energy of site i before and after reorientation trial. The average grain size <R> in 2D microstructure was defined as the square root of the number of lattice points within the grain in the plane, and the average grain size for a cross section $\langle R \rangle_{2D}$ was defined as the square root of the total number of lattice point in the cross-section (i.e. 10 000) divided by the total number of grains in the cross-section.
In 2D simulations, grain growth kinetics are studied by plotting grains number and mean grain size as a function of MCS, as shown in Fig.1 and Fig.2 respectively. Evidently in the square lattice, we have found that the average grain size with consideration of the 2nd and the 3rd neighbours is bigger than the 1st one's consideration. The reason is that in the interaction with bigger number of neighbouring

points the probability of changing orientation is also bigger. As a consequence the average grain size is bigger.

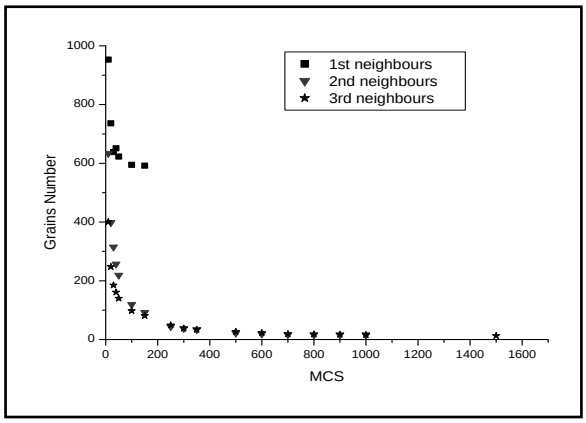

Fig.1. Grains number in 2D as function of MCS with 3rd neighbours consideration

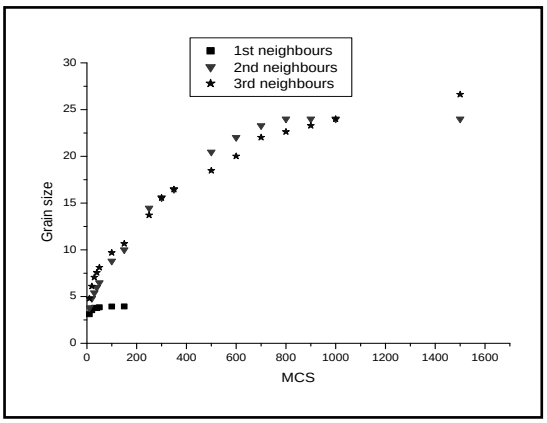

Fig.2. Average grain size in 2D as function of MCS with 3rd neighbours consideration

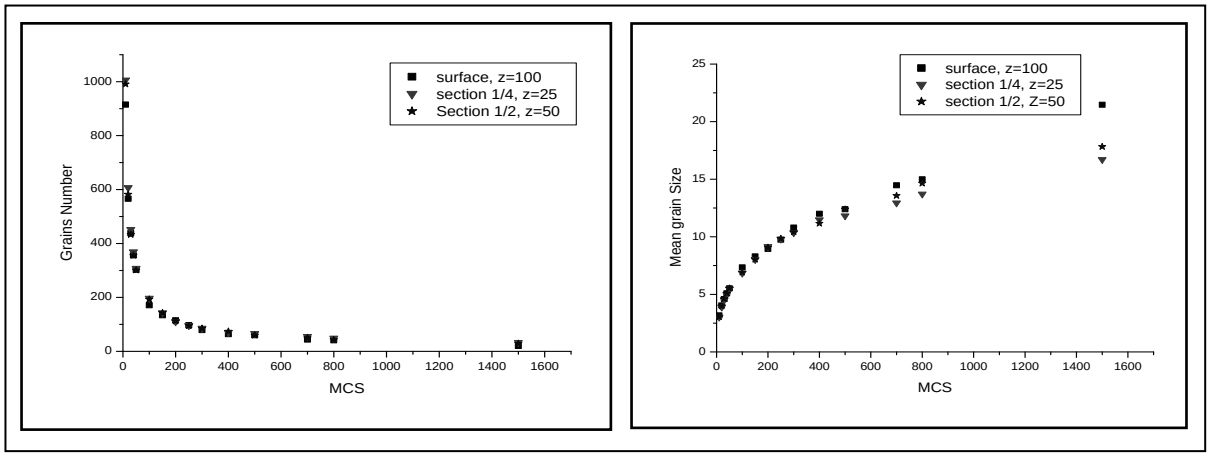

Fig.3. Grains number and mean grain size in 2D as function of MCS for three cross-sectional planes (surface z=100, z=25 and z=50)

Figure 3 shows a power law of the grain growth kinetics for which n was equal to 0.08, 0.44 and 0.35 for 1st , 2nd and 3rd neighbours respectively. During this process, the grain size distribution remains constant, the average radius saturates early for the 1st neighbours (fig.3). The figure (3) shows that the saturation of the growth for the 2nd neighbours is at 800 MCS, on the other hand, for the 3rd one's, the growth does not stagnate ; there is a minority of grains which continue to grow slowly without influencing the full number of grains, this phenomenon corresponds to abnormal grain growth. Below 300 MCS the behaviour is normal i.e. n (3rd neighbours) > n (2nd neighbours) as showed in figure (3) but beyond 300 MCS the grain growth is not uniform (abnormal growth), it is pinned and allows to weakening the growth exponent n. Therefore, the behaviour of the global matrix cannot be justified by the behaviour of a few grains which grows slowly. For this reason we can justify n (0,35 for 3rd neighbours) < n (0,44 for 2nd neighbours). For 3D simulation, in order to facilitate presentations of the simulation results, microstructure was observed in three cross-sectional planes in z direction (at the surface z=100, at the quart depth z=25 and at middle z=50).

Figure (3) shows the evolution of the average grain size $\langle R \rangle_{2D}$ and the grains number for the three cross-sections. Various microstructural features of normal grain growth commonly observed in 2D MC simulations were also seen in the microstructure in the cross-sectional planes. For example, generally large grains grew up while small grains shrank, also 120° angles were found at most grain

corners. These observations are in agreement with the literature. The mean grain size increases as a power law of the time and the grain growth exponent n varied from 0.34 to 0.36 for the three planes. While comparing microstructures obtained on 3D and 2D simulation and the evolution of grain size, we can deduce that the 2D grain growth velocity is greater than the 3D one and the abnormal grain growth takes place early in the case of 2D simulation.

In this paper, three and two dimensional Monte Carlo simulation was conducted to study the isotropic grain growth. Two dimensions grain growth simulation with consideration of the second and the third neighbours seems to give the same grain growth kinetic. In three dimensions grain growth simulation, the study was limited to the evolution of three cross sections and the grain growth exponent was found to be in between 0.34 and 0.36 for the three cross sections. Our first results point out that the study of normal grain growth in 3D cross sections seems to give better results from the direct 2D simulation because the grain growth velocity in the first case is slower and grains grows homogeneously compared to results of 2D simulations.

References

[1] J.E. Burke, D. Turnbull. Prog. Met. Phys. **3** (1952) 220.
[2] J. Von Neumann, Metal Interf. (ASM) (1952) 108.
[3] M.P. Anderson, D.J. Srolovitz, G.S. Grest, P.S. Sahni, Acta Metall. **32** (1984) 783.
[4] E.A. Holm, C.C. Battaile, JOM 53 (2001) 20.
[5] Qiang Yu, Sven K. Esche. Materials Letters **57** (2003) 4622–4626.
[6] Y.J. Kim, S.K. Hwang, M.H. Kim, S.I. Kwun, S.W. Chae. Materials Science and Engineering A **408** (2005) 110–120.
[7] Morhacova, E. Crystal Research and Technology **30** (1995) 4
[8] M. Morhac, E. Morhacova. Cryst. Res. Technol **35** (2000) 117–128.
[9] H. V. Atkinson, Acta Metall. **36** (3), 469 (1988).

P62.

Analyse de L'évolution Spatio-temporelle du Champ Electrique dans Une Microdécharge d'hélium Entre Deux Electrodes Planes et Métalliques

A.K Ferouani[1], M.Lemerini[1], S, Belhou[2] , F. Boudahri[1]

[1] Département de Physique, Laboratoire de Physique Théorique, Université de Tlemcen, Faculté des Sciences, BP 119 Bel Horizon 13000 Tlemcen Algérie.

[2] Departement de Physique, Faculté de Science, Université de Constantine

Ce travail de recherche est consacré à la modélisation de la dynamique des particules chargées, du champ électrique des particules neutres dans les microdécharges générant des plasmas non thermiques. L'étude des microdécharges est fortement motivée par le champ d'application et par la complexité inhérente des phénomènes physiques observés dues aux spécificités de ces décharges de

petite taille. En effet si les particules et la charge d'espace ont un rôle déterminant reconnu, le gaz neutre porteur est souvent assimilé à un milieu passif. Or il peut effectivement participer activement dans la cinématique de la décharge. Le formalisme hydrodynamique du modèle auto cohérent est décrit en soulignant clairement le fort couplage existent entre les dynamiques des espèces chargées, du champ électrique et des neutres, qui nécessite la résolution des équations de transport. La simulation auto cohérente d'une microdécharge dans l'hélium à pression atmosphérique est ensuite étudiée à partir d'un nuage électronique initial jusqu'au passage à l'étincelle. Les différents processus d'ionisation en volume ainsi que les effets de surface entraînant le passage à l'étincelle sont décrits et analysés.

Les expériences qui ont été décrites et modélisées par Novak et Bartnikas [8-9] ont pour but de comprendre la nature microscopique complexe de chaque type de décharge. Dans notre cas, le gaz utilisé est l'hélium de séparation inter-électrodes égale à 0,50 mm, dans les conditions normales de pression (760 Torr) et de température (293 K), soumise à une tension de 480 Volt. Les électrodes sont métalliques et planes et le système possède une symétrie de rotation. Le nuage électronique initial créé à proximité de la cathode se propage vers l'anode à une vitesse fonction du champ électrique appliqué. Ce transit dans une décharge de très petite taille (0,50 mm) a une très courte durée de l'ordre de quelques nanoseconds seulement, impliquant donc une disparition totale du nuage électronique initial après quelques dizaines de nanosecondes.

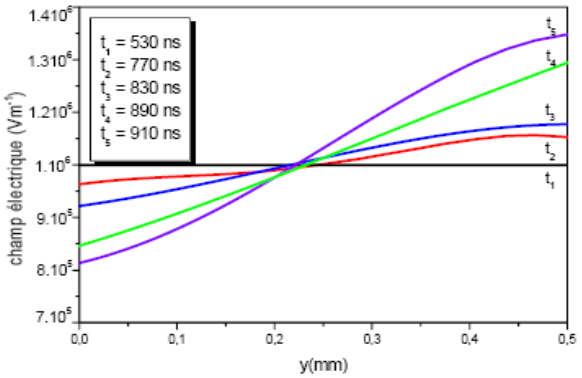

Figure 1 : Evolution du champ électrique sur l'axe pendant les phases initiales de décharge (l'anode est située à y=0 mm et la cathode à y = 0.50 mm)

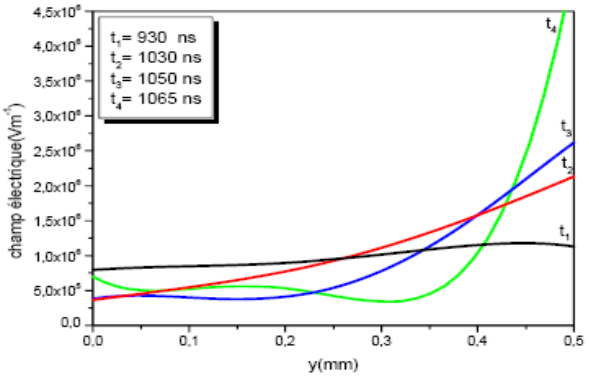

Figure 2 : Evolution du champ électrique sur l'axe pendant la phase de décharge gouvernée par la charge d'espace (l'anode est située à y=0 mm et la cathode à y = 0.50 mm)

La microdécharge à parois métalliques d'hélium étudiée inspire les conclusions suivantes : la dynamique de la décharge n'est donc pas liée à l'hétérogénéité due aux espèces neutres dans ce cas précis. La charge d'espace importante dans la zone cathodique de la micro décharge d'hélium prend naissance due au mode d'émission secondaire des électrons qui manifeste des difficultés à compenser la densité ionique. Il existe ainsi deux ordres de grandeur entre les densités ionique et électronique. Par conséquent, cet écart favorise irrévocablement la dynamique des particules chargées, par le biais d'un champ électrique à croissance très rapide commandant l'évolution de la décharge, et excluant toute participation significative des neutres pendant les phases initiales de la décharge étincelle. Le champ ralentit les électrons à proximité de l'anode et fait basculer le système dans une phase plus dynamique suite à l'emballement de la décharge. Cela a pour conséquence de transiter vers la phase canal ionisé par des phénomènes liés exclusivement aux particules chargées.

References

[1] M.Jugroot, Thèse de Doctorat. N° 2786, Université Paul Sabatier (1997)
[2] M.Cazalens, Thèse de Doctorat de l'université Paul Sabatier, No.425, (1989)
[3] J.p.Boris, D.L.Book, J.Comput.phys.,11, (1973), 38
[4] J.p.Boris, D.L.Book, J.Comput.phys.,20, (1976), 397
[5] J.p.Boris, NRL Memorandum Report.2542, Washington DC, (1972)
[6] J.p.Boris, NRL Memorandum Report.3237, Washington DC, (1976)
[7] J.p.Boris, D.L.Book, 'Methods in computational physics', vol.16, Academic Press, New York, (1976)
[8] J.P Novak, R.Bartnikas, J.Appl.Phys., 64,4, (1988), 1767
[9] J.P Novak, R.Bartnikas, J.Appl.Phys., 62,9, (1987), 3605

P63.

Monte Carlo simulation of surfactant solutions: a modified Larson's lattice model

Ariche Berkane, Rahmouni Ali.

Laboratoire de Modélisation et de Méthodes de Calcul, Centre Universitaire docteur Moulay Taher de Saida, B.P. 138, Cité En-nasr, route de Mascara, 20002 Saida, Algérie. E-mail : ariche_mc@yahoo.fr

Over the last years an extensive studies have been conducted to investigate surfactant solutions and there is an increasing interest in understanding the self assembly proprieties of an amphyphilic molecules, due to their wide spread applications in fabricating various devices and moieties of the nanometer length scales, these systems are very important for a number of technological applications including detergency, catalysis, pharmaceutical, food and cosmetics formulations. The characterization and the behavior of surfactant solutions has been studied extensively using experimental [1-6] and theoretical techniques [7-19]. In the theoretical studies there are tow main classes of simulation models that could be used to study this systems, the detailed atomistic and the coarse-grained models [20,21]. The former approach would be the most rigorous and accurate approach, but the characteristic time for micelles to form in solution and come into equilibrium is generally much larger than the time scales currently accessible by atomistic simulations. In the later models a number of atoms are grouped together, these models are usually able to describe micellization, but they ignore the detailed structural information, these models could be divided in continuum and lattice models, the continuum models [22-24] are more realistic but the lattice models are computationally more efficient. The pioneering studies in this later context were initiated by R. G. Larson [14-19] who examined equilibrium between surfactant microphases using lattice Monte Carlo simulations performed in the canonical ensemble with short-ranged nearest-neighbor interactions.

In our work we consider an NxNxN array of lattice cells completely occupied by tow molecular species, solvent (water) and surfactant chain each water molecule occupying one lattice cell. The surfactant molecule is represented by HiTj, where Hi is a head unit and Tj is a tail unit, the tail and head units each occupy one lattice cell. The unit which occupies a given cell interacts with each of its 26 neighbor units. A periodic boundary conditions are imposed; therefore a unit in the Nth row interacts with units in the first row, and so a unit in the Nth column interacts with units in the first column. The interaction of any pair of neighboring units contributes a specified amount of energy to the total energy of the system.
The simulation methodology that we use is the Monte Carlo technique [25,26], in this technique statistical thermodynamic proprieties of our system are estimated by averaging mechanical proprieties over a large number of configurations or states. From the set of all possible states a starting one is selected. A potential fluctuation or configuration change is then randomly chosen from a specified spectrum of allowed fluctuations. This potential fluctuation is then either realized i.e.The configuration is changed to accommodate the fluctuation, or not realized, i.e. the potential is discarded and the configuration is left unchanged. In the scheme that we use the probability of realizing the potential fluctuation is unity if $\Delta E \leq 0$. i.e. if the potential fluctuation decreases the total energy or leaves it unchanged, whereas the probability of realizing the fluctuation is $\exp(-\Delta E/KBT)$ if $\Delta E > 0$. In the later case, a random number is chosen from the interval [0,1] and the fluctuation is realized if $\exp(-\Delta E/KBT)$ exceeds the random number. Whether or not the fluctuation is realized a new potential fluctuation is then chosen, and another transition occurs, continuing in this manner a Markov chain is generated; the mechanical proprieties of the system such as energy are averaged arithmetically over the states of the Markov chain to give an average value. To generate a new configuration tow different modes of rearrangement are employed: chain twisting and chain reptation. In the chain twisting a unit of a surfactant chain can be exchanged with any neighboring unit, this unit can be a water molecule or a unit of surfactant chain, provided that no chain is severed in the process. In the chain reptation one chain translate but slowly by repeated twisting. Reptation occurs when one end unit of a chain moves to a neighboring site; the second unit, which is attached to that end unit, the third unit moves to the site formerly occupied by the second, etc., so that the chain snakes a unit in distance along the path marked out by the initial chain configuration. The unit originally occupying the site into which the first unit moved in the reptation is placed in the site vacated by the last unit of the chain.

In the common lattice model for surfactant solutions, the descriptions of the interaction energies were often simplified and their quantifications are very rude. These energies were classified into three types: the hydrophobic-hydrophobic interactions, the hydrophilic-hydrophobic and hydrophilic-hydrophilic interactions; however when we investigate the electronic structures of surfactant chains via quantum mechanic calculations we can see that the proprieties of the molecular unit in one tail can change significantly, in other hand the electronic proprieties of solvent molecules and head unit in surfactant molecules are different. In addition the interaction energy depends of neighbouring unit nature due to their structure and the distances that separate them. In our work we studied surfactant solutions with a quantitative way and we specified the interaction energies via analytical potentials. These potentials were evaluated starting from quantum calculations. So the modification brought to the Larson's model is related to the pair interaction energy expression.

During our simulation several proprieties are calculated in order to characterize the micellization process. These proprieties give information about the critical micelle concentration, the size and shape of the micelles; these characteristics were calculated for a series of temperatures, concentrations and surfactant chain length in order to combine all these factors with thermodynamic proprieties.

III.Conclusion

In the work that we develop, we used lattice model and Monte Carlo simulation to investigate the behavior of surfactant solutions, this investigation is a modified version of Larson's lattice model in witch we take into account the electronic and structural details of both surfactant and solvent molecules, in this approach we find a good compromise between the detailed atomistic and the rude lattice models.

References

[1] J. Penfold, E. Staples, P.G. Cummins, Physica B 180A (1992) 537.
[2] A.P. Mikhalkin, Colloid J 56 (1994) 336.
[3] J. Zaho, B.M. Fung, J Phys Chem 97 (1993) 5185.
[4] W.F. Pacynko, J. Yarwood, G.J.T. Tiddy, Liquid Crystals 2 (1987) 201.
[5] B.R. Jennings, M.E. Nash, G.J.T. Tiddy, J Colloid Interface Sci 127 (1989) 537.
[6] M. Carvell, D.G. Hall, I.G. Lyle, G.T.I. Tiddy, Farady Discuss Chem Soc 81 (1986) 223.
[7] K. Shimizu,M. Iwatsuru, Chem Pharm Bull 38 (1990) 1353.
[8] H. Wennesrom, B. Lindman, Phys Rep 52 (1979) 1.
[9] D. Blankschtein, G.M. Thurston, G.B. Benedek, J Chem Phys 85 (1986) 7268.
[10] E. Ruckenstein, R. Nagarajan, J Phys Chem 85 (1981) 3010.
[11] K. Dill, D.E. Kopple, R.S. Cantor, J.D. Dill, Nature 42 (1984) 309.
[12] M. Care, J Chem Soc Faraday Trans 83 (1987) 2905.
[13] M. Care, J.C. Desplat, Molec Phys 87 (1996) 441.
[14] R.G. Larson, J Chem Phys 83 (1985) 2411.

Electrochemisty

P64.

Theoretical Investigation on the Polarization Curve of Solid Polymer Electrolyte Water Electrolysis

B. LAOUN[1], L. SERIR[1]

[1]Applied Research Unit on Renewable Energies, URAER / Zone Industrielle Gaar Taam, P.O. Box 88 – 47000, Ghardaïa, Algeria, Tel. +213 29 87 01 26. Fax. +213 29 87 01 52, E-mail: bralaoun@yahoo.fr

From hydrogen a sustainable source of energy could be produced. In fact, hydrogen may play an important role as an energy carrier of the future [1]. Hydrogen produced from water electrolysis would be the easiest option and the only one currently practical [2]. The chemical process involved in the water electrolysis, split the water molecules to produce hydrogen and oxygen, can be viewed as the reverse process which the proton exchange membrane fuel cells (PEMFC) is based on. From this observation merge the idea to use a solid membrane, like perfluorosulfonic acid polymer (Nafion), as a membrane electrolyzer. The purpose of this study is to analyse the behaviour of the current-potential characteristics of solid polymer electrolysis (SPE) cell via modeling polarization curve of SPE; based on the well known Butler–Volmer kinetics on the electrode surfaces.

One of the new emerging technologies is based on hydrogen. In fact, hydrogen may play an important role as an energy carrier of the future [1].Hydrogen can be produced from many different sources and it looks like that water electrolysis would be the easiest option and the only one currently practical [2].

The chemical process involved in the water electrolysis, split the water molecules to produce hydrogen and oxygen, can be viewed as the reverse process which the proton exchange membrane fuel cells (PEMFC) is based on. From this observation merge the idea to use a solid membrane, like perfluorosulfonic acid polymer (Nafion), as a membrane electrolyzer.

The purpose of this study is to apply a simple, but useful, first-generation theoretical model to explain the current-potential characteristics of solid polymer electrolysis (SPE) cell, based on the well known Butler–Volmer kinetics on the electrode surfaces.In principle, water electrolysis based on conventional electrolyte, like KOH, and based on solid polymer electrolyte are the same device, they can be described almost with the same chemical reaction that takes place at the electrodes.

In case of solid polymer electrolyte water electrolysis, shown in Fig.1, if a potential is applied to the electrodes, the following reaction occurs:

At the anode, water is introduced and dissociated into oxygen, protons and electrons.

$$2H_2O_{(liq.)} + 2e^- \rightarrow H_{2(g)} + 2OH^-_{(aq)} \qquad (1)$$

At the cathode, the protons are driven through the SPE to the cathode under an electric field where they combine with the electrons arriving from the external circuit to form hydrogen gas.

$$2H^+ + 2e^- \rightarrow H_2 \uparrow \quad (2)$$

The net reaction of the entire cell

$$H_2O_{(liq.)} \rightarrow H_{2(g)} + \frac{1}{2}O_{2(g)} \quad (3)$$

Note: the preceding reactions are possible because of the net acidity influence of the solid polymer electrolyte. The preceding electrochemical model is used to simulate the voltage of the solid polymer electrolyte water electrolysis cell. The numerical values are compared with the experimental data published in the literature.

The experimental published parameters are provided on Table 1

Table 1 : Model parameters for water electrolysis for Pt based anode and cathode electrodes on NafionTM electrolyte at 80 °C [4]

Parameters	Values	Dimension
J_a^{ref}, Pt	$10^{-12} - 10^{-9}$	A cm^{-2}
$J_a^{ref}, Pt - Ir$	10^{-7}	A cm^{-2}
J_c^{ref}, Pt	$10^{-4} - 10^{-3}$	A cm^{-2}
L_{PEM}	178	μm

Note: the exchange densities are based on the electrochemically active surface area

Table 2 : Model parameters for water electrolysis for Pt based anode and cathode electrodes on NafionTM electrolyte at 80 °C [8]

Parameters	Values	Dimension	References
p_{O_2}	1	atm	[8]
p_{H_2}	1	atm	[8]
$E_{A,a}$	76	kJ mol^{-1}	[8][6]
$E_{A,c}$	18	kJ mol^{-1}	[8][6]
λ_a	14		[8]
λ_c	10		[8]

The water contents at the anode-membrane and cathode-membrane are taken from Ni & al. [8].

The local ionic conductivity, σ_{PEM}, is estimated by equation (16). For the Nafion™ membrane, the interfacial resistance R_s is assumed to be negligible and hence set equal to zero in this model.

To compare the experimental values with the theoretical model we adopt the following parameters:

- Nafion ™ 117 Membrane, the thickness of the electrolyte is taking L_{PEM} = *50* μm [8], with water content as provided in Table 2
- Temperature set T = 353 K , p = 1 atm
- Electrode catalyst is platinum based, instead to use the values of current exchange of the anode and the cathode provided in Table 1, we use the data giving by Meng Ni & al. [8], at T = 353 K , $J_a^{ref} = 1.0 \times 10^{-5}\ Am^{-2}, J_c^{ref} = 10 Am^{-2}$

We compare data for different contribution of overpotential then for cells voltage versus published experimental data, to show how the model is accurate in simulating both overpotential and overall cells voltage.

For anode overpotential, Fig.3, presents comparison between the simulating and experimental data from [4] of anode overpotential (Pt-IrO_2 anode based), the standard deviation = 0,04667 and the regression coefficient = 0,9540, which indicate the accuracy of the model.

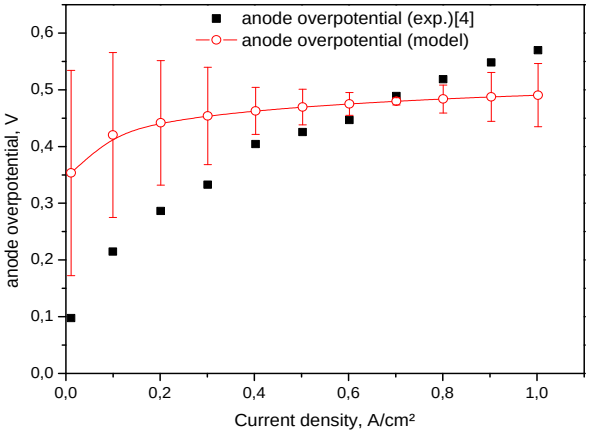

Fig. 3. Comparison between anode overpotential model and experimental data Pt-IrO2 anode based

For cathode overpotential, Fig.4, presents comparison between the simulating and experimental data from [4] of cathode overpotential (Pt cathode based), the standard deviation = 0,01266 and the regression coefficient = 0,97834, which indicate the accuracy of the model.

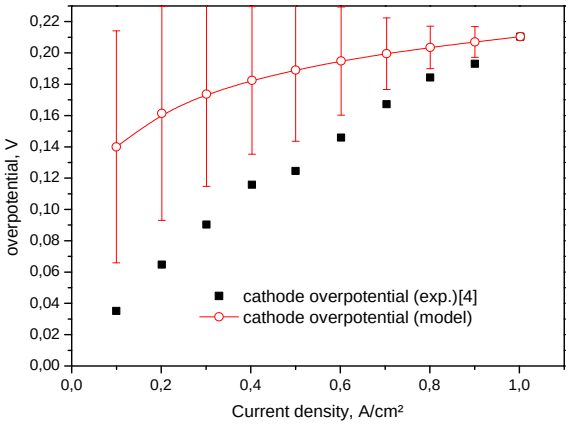

Fig. 4. Comparison between cathode overpotential model and experimental data

This study deals with water electrolysis using a cell with Platinum electrodes and Solid Membrane Electrolyte, Nafion 117. The simulation lead to numerical values that indicates the importance of the current exchange at the anode chambers, the phenomena at the anode-membrane interface is the key point of the entire efficiency of water electrolysis, this is show as overpotential. Finally the result encourage our endeavor to develop a mathematical tool that serve as an expert system to optimize the different parts of SPE water electrolysis

References

[1] Veziroglu T.N., F. Barbir, Solar-hydrogen energy system: the choice of the future. Environ.Conser.**18**, 304-312, 1991.
[2] Barbir F., PEM electrolysis for production of hydrogen from renewable energy sources, Solar Energy **78**, 661-669, 2005.
[3] Bard A.J. & FaulkneL.R., Electrochimie Principes, méthodes et applications, Masson, Paris,1983
[4] Choi Pyoungho, Bessarabov Dmitri G., Datta Ravindra, A simple model for solid polymer electrolyte (SPE) water electrolysis, Solid State Ionics **175**, 535–539, 2004.
[5] Peng Jie, Jae Lee Seung, Numerical simulation of proton exchange membrane fuel cells at high operating
[6] temperature, Journal of Power Sources **162**, 1182-1191,20

P65.

Calcul théorique et numérique des concentrations des espèces eléctroatives par voltammétrie cyclique et semi -integration

F. KESRI[1], Abed.M. AFFOUNE

[1] Laboratoire d'Analyses Industrielles et Génie des Matériaux, Département de Génie des Procédés, Université 08 Mai 45, BP 401, Guelma 24000, Algeria,fatimazi2004@yahoo.fr

L'objectif de ce travail est basé sur la détermination théorique des profiles de concentrations des espèces électro-actives oxydo -réductrices par combinaison de la voltammétrie cyclique et semi intégrale ainsi que la loi de Ficks. La résolution analytique des équations de ficks nécessite une condition initiale et deux conditions aux limites ainsi que l'application de transformation de LAPLACE et le théorème de convolution sur l'expression du courant (I) Eq(1). Le modèle mathématique de profils de concentrations des espèces Ox-Red à l'instant donnée t et à la surface de l'électrode est donnée par Eq (2):

$$m(t)=\frac{1}{\sqrt{\pi}}\int_0^t \frac{I(\tau)}{(t-\tau)^{1/2}}d\tau \qquad (1)$$

$$\begin{cases} C_{Ox}(0,t)=C^*_{Ox}+\dfrac{1}{nFA\sqrt{D}_{Ox}}\dfrac{1}{\sqrt{\pi}}\displaystyle\int_0^t\frac{I(\tau)}{\sqrt{t-\tau}}d\tau \\ C_{Red}(0,t)=-\dfrac{1}{nFA\sqrt{D}_{Red}}\dfrac{1}{\sqrt{\pi}}\displaystyle\int_0^t\frac{I(\tau)}{\sqrt{t-\tau}}d\tau \end{cases} \qquad (2)$$

L'exécution de programme écrit en langage Fortan permit d'établir les profils de concentrations (Fig1)

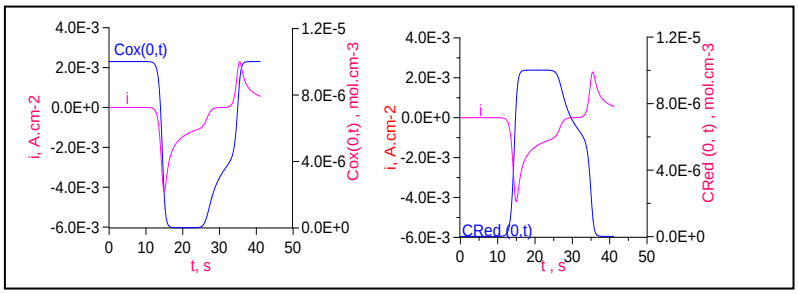

- **Fig. 1.** Évolution du courant et des concentrations des espèces Ox et Red à la surface de l´éléctrode en fonction du temps t.

References :

[1] W. Jin, S.Song et S.Wang, J Electroanal.Chem.,388(1992)73.

[2]S.Martinet, J.Bouteillon et J.P caire, J.App.Electro.Chim.,28(1997) 819.

P66.

Electrical and Electrochemical Analysis of Ternary Compounds

L. Djellal[1], A. Bouguelia[2] and M. Trari[2]

[1] Faculty of Physics (USTHB), Algiers, 16111, Algeria, dlyakout@*hotmail.com*
[2] Faculty of Chemistry (USTHB), Algiers, 16111, Algeria

Ternary compounds belonging to Cu-In-Se system were fabricated by direct reaction in evacuated quartz ampoule. Elaborated $CuInSe_2$ and $CuIn_3Se_5$ ingots are polycrystalline and crystallize respectively in the chalcopyrite and P- chalcopyrite structures. The two compounds are stable in aqueous electrolytes. The flat band potential (V_{fb}) and the doping density were calculated from capacitance measurements. The Nyquist plot allowed obtaining the electrical equivalent circuits of the junction semiconductor/electrolyte.

The ternary semiconductors (SC) of the I-III-VI_2 group have received considerable attention over the last decades due to their potential technological applications such as photo electrochemical (PEC) cells[1]. $CuInSe_2$ and $CuIn_3Se_5$ are stable absorbers with an absorption coefficient (α) exceeding 10^{-4} cm^{-1} [2], this property makes them suitable candidates for photovoltaic applications [3]. The bulk elaboration methods are mainly melting technique like gradient freezing [4] and Bridgman method [5]. In this work, ingots have been prepared by direct reaction of constituents elements in evacuated quartz ampoule. A review on structural, optical and electrochemical characterizations is reported.

Ingots of $CuInSe_2$ and $CuIn_3Se_5$ were synthesized in evacuated quartz ampoule. The starting elements Cu, In and Se all of high purity (5N) were introduced in a silica tube and sealed under vacuum. The tube was submitted to thermal treatments; heating up to 200°C with an isothermal step of 12 hrs to allow the low melting point elements to react together exothermally. The temperature was raised to 450°C and then to the melting point 1150°C. The mixture was maintained 24 hrs at that temperature to ensure homogenization of the melt and complete reaction. The tube was cooled to 665°C and then to room temperature. The as synthesized ingots were identified by X-ray diffractometry (XRD) using filtered Cu Kα radiation. The elemental composition was carried out by the Rutherford Back Scattering (RBS) technique. The diffuse reflectance spectrum has been recorded with a UV VIS Cary 500 De Varian double beam spectrophotometer. The thermopower data (S) were recorded using home built equipment. The standard PEC set up, used for the intensity-potential J(V) characteristics and the capacitance measurements, was composed by a potentiostat Volta lab 201, a 200 W tungsten lamp (Osram) as a light source equipped with reflector and a standard Pyrex electrochemical cell. A Pt sheet (1 cm^2) was used as counter electrode and all the potentials were scaled with respect to a saturated calomel electrode (SCE). The oxygen-free KOH (0.5 M) electrolytic solution, prepared from de-ionized water, was continually bubbled with nitrogen.

The XRD patterns of the powdered samples shows that the elaborated compounds crystallize in the tetragonal structure. For $CuInSe_2$ (SG: $I\bar{4}2d \equiv D_{2d}$), the phase is confirmed by the presence of the peaks (211), (323) and (301), although the characteristic reflection (110) confirms the formation of $CuIn_3Se_5$ (SG: $P\bar{4}2c$). The refined lattice constants (a= 578.2 and c= 1169.1 pm) for $CuInSe_2$ are slightly larger than those for $CuIn_3Se_5$ (*a*= 574 nm and *c*= 1150.1 pm). The chemical composition was evaluated with RBS technique. The values are Cu: 23.39 at%, In: 26.06 at% and Se: 50.55 at% for $CuInSe_2$ and = 13.3 at%, In= 31.5 at% and Se= 55.2 at% for $CuIn_3Se_5$. The diffuse reflectance was converted to $F(R_\infty)$ using the Kubelka-Munk equation ($F(R_\infty) = k/s = (1-R_\infty)/2R_\infty$). R_∞ =

$(I/I_o)_{diffuse}$ being the diffuse reflectivity, k the absorptivity (cm^{-1}) and s the scattering factor. The transition is directly allowed for the two compounds (Fig.1) and the $CuIn_3Se_5$ gap (1.19 eV) is larger than that of $CuInSe_2$ (0.94 eV). This increase is attributed to the generation of periodic V_{Cu}, which reduces the Se:*4p*-Cu:*3d* inter-band repulsion, as compared to $CuInSe_2$, due to a decrease of *d*-character. This effect lowers the maximum of the valence band (V_{BM}) of $CuIn_3Se_5$ thus increasing the gap Eg.

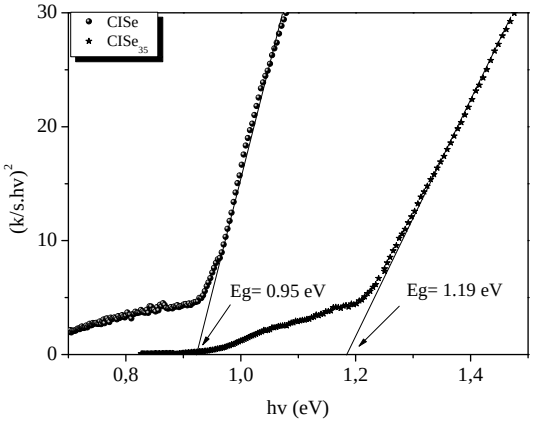

Fig. 1. Direct optical transition obtained by Kubelka-Munk equation.

To establish the conduction mechanism for the two compounds, the variations of the thermopower (S) has been measured up to 740 K. For $CuInSe_2$, the conduction process should be dominated by holes as *S* is positive. The linear increase of S with temperature indicates a hole mobility μ_e thermally activated and a constant doping density N_A. The conduction occurs predominantly by polaron hopping among localized sites. For $CuIn_3Se_5$, S is negative suggesting that the majority carriers are electrons, the relatively large value indicates a low density N_D. The decrease of S with increasing temperature may be attributed to a thermal generation of electrons by impurity ionization (extrinsic process) or to a thermal activation of the mobility.

The chemical stability of the two compounds is attributed to the fact that electronic states of the highest valence band in which the reacting holes are produced, are formed from hybridized Cu: *3d*-Se: 4p wave functions which are bonding states in the theoretical description. Under illumination, the J(V) characteristic clearly exhibits a cathodic photocurrent J_{ph} for $CuInSe_2$ providing unambiguous evidence of *p* type character as expected for the Cu-rich side in the ternary phase diagram. In $CuIn_3Se_5$ J(V) characteristic, the increase of the photo current (J_{ph}) along the positive-going potential is consistent with *n*-type conductivity. V_{fb} was accurately determined from the Mott Schotky plot ($C^{-2} = -(2/e\varepsilon\varepsilon_0 N_A)\{V - V_{fb}\}$). The density, determined from the slope, is $N_A = 3.8\ 10^{17}\ cm^{-3}$ for $CuInSe_2$ and $N_D = 3x10^{16}\ cm^{-3}$ for $CuIn_3Se_5$.

The representation of the imaginary part of the complex impedance ($Z'' = -\omega C_{dl} R_{dl}^2 / (1+\omega^2 C_{dl}^2 R_{dl}^2)$) vs the real ($Z' = R_{el} + R_{dl} / (1+\omega^2 C_{dl}^2 R_{dl}^2)$) part allows to deduce an equivalent electric circuit. R_{el} is the resistance of the solution, R_{dl} the resistance of the semiconductor and C_{dl} the capacitance of SC. In the case of $CuInSe_2$, the plot (Fig.2) shows a semicircular arc which can be fitted to a pure capacitance (1.206 $\mu F/cm^2$). R_{el} (= 2.35 $\Omega\ cm^2$) and R_{dl} (= 329.8 $\Omega\ cm^2$) are evaluated at higher and lower frequencies respectively. For $CuIn_3Se_5$, the plot (Fig.3) shows a semicircle at high frequencies corresponding to a faradic charge transfer. The system is under kinetic control where the resistance R_{dl} (27.9 $\Omega\ cm^2$) is in parallel with the capacitance C_{dl} (900 $\mu F\ cm^{-2}$). We also note a slight offset near the origin indicating a low series resistance attributed to the electrolyte resistance R_{el} (15.3 $\Omega\ cm^2$). The straight line at low frequencies (> $10^3\ s^{-1}$) is due to the diffusion process of

electroactive species in solution known as the Warburg impedance (Z_W) where the ionic diffusion prevails. The electrochemical system, for the two compounds can be assimilated to an equivalent electric circuit (Inset, Fig. 2 and Fig.3).

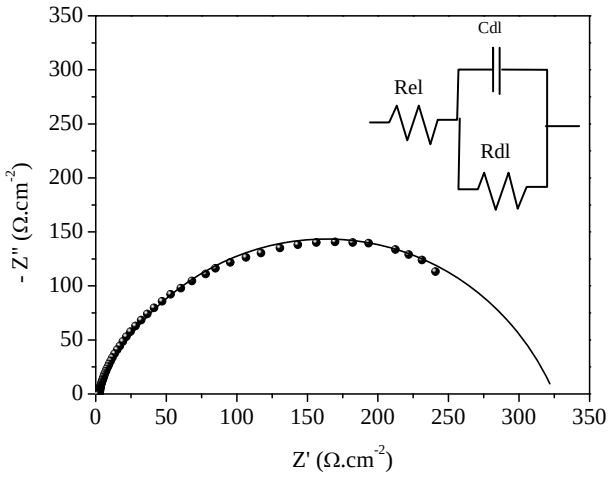

Fig. 2. Nyquist plot and electrical equivalent circuit for $CuInSe_2$.

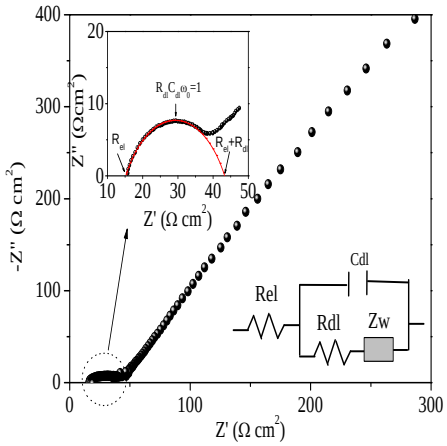

Fig. 3. Nyquist plot and electrical equivalent circuit for $CuIn_2Se_5$.

References

[1] H.T. Shaban, M. Mobarak, M.M. Nassary, Physica B 389 (2007), 351.
[2] R.D.L. Kristensein, S.N. Sahu, D. Haneman, Solar Energy. Mater. 17 (1988), 331.
[3] H. Du, C.H. Champness, I. Shih, T. Cheung, Thin Solid Films 480-481 (2005), 42.
[4] M.A. Arsene, A. Albacete, F. Voillot, J.P. Peyrade, A. Barra, J. Galibert, S.M. Wasim, E. Hemindez, J. Cryst. Growth 158 (1996), 97.
[5] Z.A. Shukri, C.H. Champness, J. Cryst. growth 191 (1998), 97

P67.

Etude électrochimique des dérivés de quinoléines N-oxyde et Nhydroxyquinolone par l'électroréduction sur un électrode de mercure

S. Merzouki[1], F. Z. Issaad[1], N. Mouats1 and C. Mouats

[1] Laboratoire de Chimie Moléculaire, du contrôle de l'Environnement et de Mesures Physico-Chimiques Département de chimie / Faculté des sciences exactes, Université Mentouri, Constantine ,Alger.
*merzoukisoraya@yahoo.fr

Les hétérocycles ont une grande importance dans la chimie organique vue leurs propriétés spécifiques; plusieurs de ces hétérocycles existent dans les produits naturelles et pharmaceutiques. L'électrochimie apparaît comme une méthode de choix pour préparer les différents hétérocycles car l'oxydation anodique et la réduction cathodique est basée sur la préparation sélective d'intermédiaires très actifs (radicaux, cations, anions, les groupes électrophiles et nucléophiles) [1].
La préparation d´hétérocycles azotés par réduction chimique de nitrobenzènes ortho - substitués a fait l'objet de nombreux travaux [2, 3].Cependant, si l'obtention du produit de cyclisation de l'aniline est généralement aisée, les réductions chimiques ne sont pas toujours sélectives [3] et conduisent souvent à des mélanges.
La réduction à potentiel contrôlé de nitrobenzènes ortho substitués conduit à un nombre intéressant d'hétérocycles azotés, par le fait de la cyclisation du groupement hydroxylamine suite à l'attaque susceptible sur un substituant ortho convenablement polarisé (de type carboxyle, carbonyle, nitrile…) [4, 5 ,6].
Des études électrochimiques ont été effectuées dans les solvants EtOH, MeOH et l'acétonitrile en utilisant l'acide sulfurique une fois normale comme électrolyte support.
Les composés étudiés sont: les dérives de l'acide 2-nirobenzylydéne du phényle acétique.

$$ArNO2 + 4e + 4H+ \; ArNHOH \; -H2O$$

$$ArNHOH + 2e + 2H+ \; -H2O$$

$$ArNH2$$

Les polarogrammes enregistrés sur un polarographe à trois électrodes (constitué d'un enregistreur EPL3 et un générateur TACUSSEL PRG5) en milieu acide sulfurique (0,5mole/l, pH=0) et en tampon acétique (pH=4.25).
a)- l'électrolyse effectuée à potentiel correspondant au palier de la première vague polarographique consomme 4 moles d'électrons par mole de substrat, le traitement usuel des solutions donne les dérivés de N-oxyde quinolinone-2 par la transformation de l'hydroxylamine formée.
b)- la réduction à un potentiel plus négatif consomme 6 moles d'électrons par mole de substrat et donne le N hudroxyquinone-2.

Lorsque la fonction hydroxylamine ainsi formée est en position favorable pour se condenser sur un groupement réactif (position cis de ce groupent et du noyau aromatique dans le dérivés éthylénique de départ), la phényl-hydroxylamine ce cyclise rapidement, les hétérocycles correspondants sont alors obtenus avec des rendements quantitatifs.

Lorsque le groupement réactif est en position tans du noyau aromatique, les phénylhydroxylamines
obtenus sont stables, à l'abri de l'air, en milieu peu acide ; en revanche, elles subissent à la transposition de GATTERMAN en milieu acide sulfurique.
Dans tous les cas, l'étude voltammétrique, suivie de l'analyse des produits obtenus par réduction à potentiel peu négatif, permet de préciser la géométrie de l'o-nitrobenzylidéne étudié [8].
L'étude électrochimique des dérivés de l'acide o-nitrobenzylidène phényl acétique nous a permis de savoir les conditions opératoires de préparer le N-oxyde quinolinone-2 avec un bon rendement et une excellente pureté, alors que la méthode classique où on utilise des catalyseurs des métaux de transitions donne le contraire, la même chose est valable pour l'obtention du N-hydroxy quinolinone-2 [7].

Références

[1] C.MOINET, J.B. ALLEN et M.STARATMANN, Organic Electrochemestry 8, 12, (2004).
[2] P.N. PRESTON et G. TENNANT, chem. .Rev.72 (6) ,627 (1972).
[4] A.R. KATRITZKY et J.M. LAGOWSKI, ``Chemistry of the Heterocyclic N-oxides´´, Academic Press, 81 (1971).
[5] H.LUND dans`` Organique Electrochemistry´´, édite par M.BAIZER, M.DEKKER, New York, 3éme édition,
107 (1991).
[6] J.SIECKER, C.MOUATS, , Electrochimica. Acta. 40, 1669 (1995) R.HAZARD, M.JUBAULT, C.MOUATS, A.TALLEC, Electrochimica Acta, N04, 33, p. 1335 (1988).
[7] R.T.COUTTS, D.NOBLE, D.G.WIBBERLEY, J. Pharm. Pharmacol., 16, 773 (1964).
[8] A. CHIBANI R.HAZARD, A.TALLEC Bull. Chim. Fr., 690 (1991).

P68.

Electrical I-V and C-V measurements and electronic transport modelization in the InN/InP hetero-structures

Z. Benamara[1], N. Mecirdi1, B. Akkal[1], M. Chellali[1], A. Talbi[1], M. A. Benamara[1], B. Gruzza[2], S. Benkhalifa[2]

[1] Laboratoire de Microélectronique Appliquée, Université de Sidi bel Abbès, 22000 Sidi Bel Abbès, Algérie.
[2] Laboratoire des Sciences des Matériaux pour l'Electronique et d'Automatique, Université Blaise Pascal de Clermont II, Les Cézeaux, 63400 Aubière Cedex, France.

Developments in the field of III-nitride (InN, GaN, and AlN…) semiconductors have been spectacular due to their highly attractive properties. Many review and papers have been published on the properties of III-nitride semiconductors and on their fabricated devices [1, 2]. In most of these publications the main topics was GaN and its alloys [3] and very few reports exists regarding the InN semiconductor. However, during the last few years, the interest in the indium nitride (InN) semiconductor has been remarkable and the number of papers concerning InN has significantly increased [4]. However, the properties of InN thin films are obscure, since growing high quality InN thin films is still a challenge, due to their stoechiometric instability and low dissociation temperature and the lack of suitable lattice-matched substrates [5, 6, 7]. Related to optical properties of InN, many groups have shown by optical measurements different band gaps for InN: band gap energy of InN is between 0.65 and 1 eV [8, 9, 10], which is smaller than 1.1eV [5] and 1.2 eV [11] and much smaller than 1.89 eV [12].

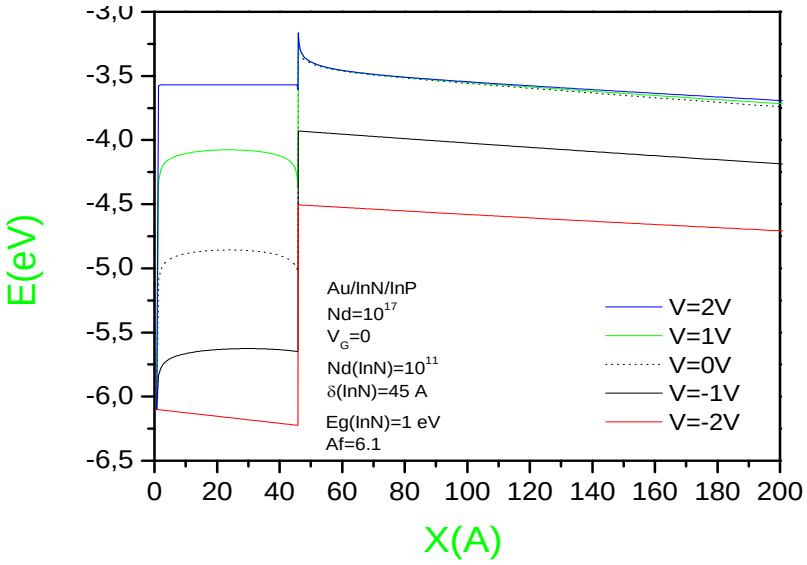

Fig.1. The diagram band (Conduction Band level) of InN/InP structure for different bias voltage.

In this paper, we electrical study thin InN film realized by the nitridation of InP substrates using a Glow Discharge Source (GDS). Then, we have elaborated a metal/InN/InP structures. From I-V curves, we notice a strong tension of threshold and using the C-V curve, we observe a variation around zero Volt (between -0.5Volt and 0.5Volt) and a constant capacitance for positive voltage. This indicates that our structures have different behaviour for Schottky diode and hetero-structure. To explain this phenomenon, we have plotted the variation of the zone of space charge and developed a calculation of diagram bands of InN/InP structures allowing us to understand the phenomena transport in these diodes. In this paper, we show clearly that the InN film play a role of well quantum (see figure 1).

References:

[1] S. C. Jain, M. Willander, J. Narayan,R.V.Overstraeten,
J. Appl. Phys., 87,965(2000).
[2] S. J. Pearton, J. C. Zolper, R. J. Shull, F. Ren,
J. Appl. Phys., 86, 1 (1999).
[3] E. Martinez-Guerrero, C. Adelmann, F. Chabuel, J. Simon, N. T. Pelekanos, Guido Mula, B. Daudin, G. Feuillet, H. Mariette.
Appl. Phys. Lett .,77, 809 (2000).
[4].J. S. Pan, A. T. S. Wee, C. H. A. Huan, H. S. Tan, K. L. Tan.
J. Phys., D 29, 2997 (1996).
[5] T. Inushima, V. V. Mamutin, V. A. Vekshin, S. V. Ivanov, T. Sakon, M. Motokawa, S. Ohoya
J. Crystal Growth, 227-228,481 (2001).
[6] A. G. Bhuiyan, A. Hashimoto, A.Yamamoto.
J. Appl. Phys., 94, 2779 (2003).
[7] Y. Nanishi, Y. Sato, T.Yamaguchi.
Jpn. J. Appl. Phys., Part 1. 42, 2549(2003).
[8] V. Y. Davydov, A. A. Klochikhin, V. V. Emstev, S. V. Ivanov, V. V. Vekshin, F. Bechstedt, J. Furthmuller, H. Harima, A. V. Mudryi, A. Hashimoto, A. Yamamoto, J. Adrhold, J. Graul, and E. E. Haller
Phys. Stat. Sol.(b) 230, R4 (2002).
[9] J. Wu, W. Walukiewicz, K. M. Yu, J. W. Ager III, E. E. Haller, H. Lu, W. J. Schaff, Y. Saito, and Y. Nanishi.
Appl. Phys. Lett., 80, 3967 (2002).
[10] T. Matsuoka, H. Okamoto, M. Nakao, H. Harima, and E. Kurimoto
Appl. Phys. Lett., 81, 1246 (2002).
[11] T. V. Shubina, S. V. Ivanov, V. N. Jmerik, D. D. Solnyshkov, V. A. Vekshin, P. S. Kop'ev, A. Vasson, J. Leymarie, A. Kavokin, H. Amano, K. Shimono, A. Kasic and B. Monemar,
Phys. Rev. Lett., 92, 117407 (2004).
[12] T. L. Tansley and C. P. Foley
J. App. Phys., 59, 3241(1986).

Biological Physics, Drug Design, Bioinformatics and QSAR

P69.

QSAR studies on 2-[4-(thiazole-2-yl)phenyl] propionic acid derivatives as anti-inflammatory agents

Youcef SAIHI[1]; Khaireddine KRAIM [2]; Djameleddin KHATMI[2]

[1]Department of Chemistry, Faculty of Sciences. University of BADJI Mokhtar Annaba, ALGERIA
[2]Department of Industrial Chemistry, Faculty of Sciences and Techniques of Engineer.University of 08 Mai,1945 Guelma – ALGERIA

Non- steroideal anti- inflammatory drugs (NSAID) are still the commonly perscribed drugs world wide for the treatment of inflammatory disease like rheumatoid arthritis, osteoarthritis, orthopedic injuris, post operative pain, acute myalgias etc. 1 In molecule heterocyclic compounds, thiazolidine is a recognized scaffold for potential drugs andcandidates. Anticonvulsant, sedative, antidepressant, anti-inflammatory, antihypertensive, antihistaminic and antiarthritic activities are a few among many other biological responces2 . Recently a series of 2-[4 -(thiazole-2- yl) phenyl] propionic acid derivatives are reported with anti-inflammatory potential.

Quantitative Structure Activity Relationship (QSAR) models are highly effective in describing the structural basis of biological activity3. It is now widely used for prediction of physicochemical properties and biological activity in chemical, environmental and pharmaceutical areas 4. The success of QSAR approach can be explained by the insight offered into the structural determinat ion of chemical properties, and possibility to estimate the properties of new chemical compounds without the need to synthesize and test them5 . Recently we have reported the development of use QSAR models for anti -inflammatory activity6.

In view of above and as a part of our effort to create QSAR models that show substantial predictive promise, in present study we report the QSAR study on anti- inflammatory activity of series of 2-[4-(thiazole-2-yl)phenyl] propionic acid 7 (Table01).

Table 01: Chemical structure and anti-inflammatory potentiel of strucurally similar 2-[4-(thiazole-2-yl)phenyl] propionic acid

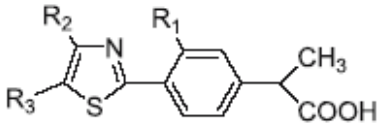

N°	R_1	R_2	R_3	PI_{50}
1	H	H	H	5.56
2	F	H	H	6.60
3	Cl	H	H	6.70
4	Br	H	H	7.00
5	CF_3	H	H	6.52
6	Me	H	H	5.70
7	OMe	H	H	5.28
8	SMe	H	H	6.52
9	OH	H	H	6.22

pI50 = 15.2 + 1.01 nX - 0.205 RDF065m - 0.223 RDF105m - 2.37 Mor08v + 17.6 G1m
- 13.3 Ds + 0.318 Inflammat-50 - 15.8 GGI10 - 55.4 X3A **Equ01**

S = 0.2797 R^2= 94.9% F = 71,64 Q^2= 91.08%

pI50 = - 10.1 - 1.32 GATS4m + 5.49 BEHm3 + 65.9 JGI3 + 0.143 RDF055v + 16.3 G1p
- 0.380 Hy + 0.698 Inflammat-50 - 0.0987 ITH - 11.3 H6p **Equ02**

S = 0.2459 R^2= 96.0% F = 93.83 Q^2 = 93.94%

The Genetic Algorithm performs better than the other approach (Forward stepwise) on the data sets studied. The statistical parameters showed in along with equation (Equ02) for estimate pI50. The model, presented by the(Equ.02) is able to expain 96,0% of the variance in selected data set, moreover, the Genetic Algorithm model represented by (Equ.02) is able to explain almost 2% more variance than the model (Equ.01) obtained by theForward stepwise method.

The results of this study suggest that variables like G1m, Ds, GGI10, X3A play an important role in defining inhibitory activity of 2 -[4-(thiazole -2-yl)phenyl] propionic acid derivatives against cyclooxygenase(COX).The QSAR models obtained using Genetic lgorithm as the variable selection procedure (Equ.02) displays the beststatistical parameters, there by indicating the superiority of GA with respect to Forward stepwise for modeling tne anti inflammatory of 45 2-[4 -(thiazole-2-yl)phenyl] propionic acid derivatives.

References:

[1] S.Prasanna, E. Manivannan, S. C. Chaturvedi, Bioorg. Med. Chem. Lett. 15, (2005), , 131-147.
[2] M.Negwer, Organic-Chemical Drugs and Their Synonyms, (1994),7th edn. Akademie Verlag, VCH Publishers, New York.
[3] B.Debnath, S. P.Vishnoi, B. Sa,T. Jha, Internet Electron. J. Mol. Des. 2, (2003), 128- 131.
[4] X. J.Yao, A. Panaye, J. P.Doucet, R. S. Zhang,. H. F. Chen, M.C. Liu, Z.D. Hu, B.T. Fan, J. Chem. Inf. Compnt. Sci. 44, (2004), , 1257-1269.
[5] O. Ivanciuc, T. Ivanciuc, A. T. Balaban, Internet Electron J. Mol. Des. 1, (2002), 559-586.
[6] N. A. Gangwal, B. Narasimhan, V. K. Mourya, A. S. Dhake, Indian J. Het. Chem. 12, (2003), , 201-213.
[7] Y. Naito, T. Goto, F. Akahoshi, S. Ono, H. Yoshitomi, T. Okada N. Sugiyama Abe S, S. Hanada, M. Hirata, M. Watanabe, C. Fukaya, K. Yokoyama, T. Fujita, Chem. Pharm. Bull. 39, (1991), , 2323 -2339

P70.

QSAR studies about cytotoxicity and anti HIV of flavonoid compounds and statistical considerations about variable selection

K. Kraim[1*], Dj. Khatmi[1] and Y. Saihi[2]

[1] Department of Industrial Chemistry, Faculty of Sciences and Techniques of Engineer
University of 08 Mai 1945, Guelma, 24000, ALGERIA, kkhchem@gmail.com
[2] Department of Industrial Chemistry, Faculty of Sciences and Techniques of Engineer
University of 08 Mai 1945, Guelma, 24000, ALGERIA
[3] Department of Chemistry, Faculty of Sciences, University of Badji Mokhtar,
Annaba, 23000, ALGERIA

Flavonoids are a class of naturally occurring phenolic plant compounds that show biological and pharmacological activity coupled with low toxicity. These compounds are widely distributed in the plant kingdom and ingested daily by humans. Therefore, their use as potential therapeutic compounds against a variety of diseases is of interest[2]. The biological activities of flavones have been extensively reviewed. Some of them have demonstrated extensive biological activities such as anti-inflammatory and anti-allergic, mutagenic and carcinogenic. Thus, a series of flavonoid derivatives with substitutions at C-2 to 8 and C-2' to 5' have been studied to examine the relationships between structural modifications and activities against anti HIV and cytotoxicity activities.

QSAR approach has become very useful in the prediction of physical and chemical activities and properties. Recently a quantitative structure–activity relationship (QSAR) study on a data set of flavonoids as positive anti HIV and cytotoxicity activities was reported by means of quantum chemical descriptors with various statistical methods.

The principal aim of the present paper is to obtain a good linear regression equations for predicting the anti-HIV (EC50) and cytotoxicity (IC50) activities of 24 flavonoid compounds, using 0, 1, 2 and 3D molecular descriptors calculated, and two statistical methods for variable selection are used such as Forward stepwise (FS) and Genetic Algorithm (GA).

Before calculating the molecular descriptors, we carried out geometry optimization calculations for each compound of this study using the quantum chemical semi-empirical method AM1 included in HYPERCHEM 7.0 computer software.

Once approximately 1664 descriptors had been generated by the descriptor generation routine, variable selection was used to reduce the number of descriptors per compound. Feature (variable) selection is used to choose a subset of descriptors that are best in encoding the activity of interest, since many of the calculated descriptors carry redundant and highly correlated information or very little useful information. Feature selection includes objective methods and subjective methods. All molecular descriptors are used for building QSAR models by Multiple Regression Analysis, as implemented in the STATISTICA software.

The linear models obtained were validated by calculating Q^2 values, which are calculated from leave-one-out (LOO) and leave –group-out (LGO) test. In summary, good overall quality of the models indicated by large F, small s and R^2 (goodness of fit) and q^2 (predictability) values close to one.

The regression models for predicting EC50 and IC50 of flavonoid compounds obtained by different methods of variable selection are summarized in **(Table 03)** given below.

Table 3. The statistical and validation parameters for the two GA and FS variable selection methods.

	Eq. N°	*variables*	R^2	*s*	*F*	Q^2_{LOO-CV}	s_{LOO-CV}	Q^2_{LGO-CV}	s_{LGO-CV}
EC 50	*01*	*nX; G1m; RDF010v; RDF115e*	*0.80*	*0.271*	*19.6*	*0.715*	*0.2977*	*0.6946*	*0.3084*
	02	***GATS3m; EEig01d; RDF095u; RDF110e***	***0.85***	***0.236***	***27.1***	***0.8069***	***0.2401***	***0.7792***	***0.2622***
IC 50	*03*	*GGI10; RDF085v; nX; G2p*	*0.74*	*0.272*	*13.6*	*0.5988*	*0.3094*	*0.6341*	*0.2946*
	04	***RDF110e;Mor26m; G2u; E1m***	***0.88***	***0.184***	***35.4***	***0.8314***	***0.1959***	***0.8419***	***0.1895***

The GA performs better than the other approach (FS) on the datasets studied. The statistical parameters presented in Table 03, shown in along with Equ.2 and Equ.4 for estimate EC50 and IC50 respectively, really corroborate that statement. The two models, presented by the Equ.2 and Equ.4, are able to explain 85.1% and 88.2% of the experimental variance in selected data set respectively.

The GA model (02) for predicting EC50 activity is able to explain 5% more variance than the model (01) obtained by the FS method. In the case of IC50 models, the model (04) obtained by the GA procedure is able to explain 14% more variance than the FS model (03).

In conclusion, the QSAR models obtained by using GA as the variable selection procedure (Equ.2 and Equ.4) displays the best statistical parameters, there by indicating the superiority of GA with respect to FS for modeling the anti HIV and toxicity of 24 flavonoid compounds. For that reason, these will be the models worked out from now on.

The test that we used to detect the presence of outliers in Eq.2 and Eq.4 was a standard residual higher than (2 x δ), where δ is equivalent to the standard deviation.

- ***The outliers for model 02 [Log (1/EC50]:***

Removal of the compounds **01** and **02** that presents a large standard residual values and subsequence re-analysis of the dataset produced a following QSAR equation (**Equ. 5**):

Log (1/EC50) = 15.7 – 2.17 GATS3m – 2.40 EEig01d – 0.393 RDF110e + 0.129 RDF095u (**Equ. 5**)

N=22 s = 0.163390 R^2= 0.929 F=55.69 P<10^4

s_{CV-LOO}=0.1809 Q^2_{CV-LOO}= 0.8916 s_{CV-LGO}=0.2062 Q^2_{CV-LGO}=0.8470

- ***The outliers for model 04 [Log (1/IC50]:***

Removal of the compound **n°21** and subsequence re-analysis of the dataset yielded a following QSAR equation (**Equ.6**).

Log (1/IC50) = 4.56 – 0.656 RDF110e- 2.81 Mor26m –10.10G2u + 2.57 E1m **(*Equ.6*)**

N=23 s = 0.1667 R^2= 0.908 F=44.37 P<10^4

s_{CV-LOO}=0.1816 Q^2_{CV-LOO}= 0.8604 s_{CV-LGO}= 0.1682 Q^2_{CV-LGO}=0.8802

Herein, we report a QSAR study for a set of 24 flavonoid compounds to predict their anti HIV (EC50) and cytotoxicity (IC50) activities by Multiple Regression Analysis, using two methods of variable selection, namely Forward Stepwise Regression and Genetic Algorithms methods. The QSAR models, obtained by GA showed the best statistical parameters, revealing therefore its superiority with respect to FS for modeling the anti HIV and toxicity activity of the 24 flavonoids. The final attained QSAR models were able to explain more than 92.9% (EC50); 90.80% (IC50) of the experimental variance after the removal of compounds, shown to be outliers.

Other Fileds

P71.

Biochemical assay of polyphenols in dates and honey collected from south Algeria

M. Bendahmane[1], A. Bessas[1], L. Benmoussa[1], M. Kerarma[1] and M. S. Rahal[2]

[1]Dept of Biologie, 2. Dept of Chimistry, UDL of Sidi-Bel-Abbès

The polyphenols are very precious compounds present specifically in plants; they play a powerful antioxydant role. Among these compounds, three large classes are distinguished: phenol acids, flavonoïdes (ie. anthocyanes) and tannins. Because of their nutritional and therapeutic properties, the content of these substances was investigated in two succulent foods (dates and honey) that are much snuffed in Algeria. Our study carried out at Sidi-Bel-Abbès University consists to analyze by colorimetric and spectrometric method the amount of polyphenols in two varieties of dates (Deglet Nour and Hamraia) and in honey (Bayadh) collected from southern area of Algeria. The results showed that the phenolic compounds in particular the C.P.S.T are very hight in Hamraia dates variety (141,5 µg/ml) compared to that of Deglet Nour (81,5µg/ml), whereas the condensed tannins and anthocyanes, are low and no significant difference between these two varieties. It was respectively estimated at 20.3µg/ml and 15µg/ml in Deglet Nour and at 23.5µg/ml and 14µg/ml for the Hamraia variety. For total polyphenols in honey, the amount found was 90µg/ml for the diluted solution to 2.5% and 205µg/ml for a solution at 10%. These results are very encouraging and showed the richness of these two nutrients in phenolic compounds which are known for their anti-oxidant, anti-aging and anti-inflammatory effects.

Polyphenols, Deglet Nour, Hamraia, Honey, Biochemical assay.

P72.

Nonplanar Electrostatic Excitations in a Plasma Containing Degenerate Electrons and Positrons

W. M. Moslem[1], and R. Sabry[2]

[1]Department of Physics, Faculty of Science, Port Said, Suez Canal University, Egypt
[2]Institut für Theoretische Physik IV, Fakultät für Physik und Astronomie, Ruhr-Universität Bochum, Germany

Nonplanar ion-acoustic solitary waves in an unmagnetized collisionless plasma are investigated by using the Thomas-Fermi electron and positron densities distributions, the hydrodynamic equations for ions, and the Poisson equation. The reductive perturbation method is used to derive cylindrical and spherical Kortwege-de Vries equations. Numerical solutions of the latter are presented as well as the pulses characteristics are discussed.

The present study might be helpful to understand the excitation of nonlinear ion-acoustic solitary waves in a degenerate plasma such as in superdense white dwarfs.

An electron-positron (e-p) plasma usually behaves as a fully ionized gas consisting of electrons and positrons, as seen in the solar atmosphere [1] as well as in many astrophysical objects [2] (e.g. neutron stars, near the polar cap of pulsars, in the active galactic nuclei, in the early universe). Since some of the astrophysical plasmas contain ions besides the electrons and positrons [3], it is

∗ Electronic mails: wmmoslem@hotmail.com and wmm@tp4.rub.de †Also at: Theoretical Physics Group, Department of Physics, Faculty of Science, Mansoura University, Damietta Branch, New Damietta 34517, Egypt. Electronic mails: refaatsabry@mans.edu.eg and sabryphys@yahoo.com1

important to study the dynamics of the nonlinear wave motions in an electronpositron- ion (e-p-i) plasma. During the last three decades, e-p and e-p-i plasmashave attracted significant attention among researchers [2 − 8].

The previous investigations dealing with the nonlinear ion-acoustic waves (IAWs) used the Boltzmann-electron/positron density distribution. However, some of the astrophysical observations (such as white dwarfs [9]) are in a state of very high dense electrons/positrons, i.e. they can be considered as a degenerate

ideal Fermi gas. In such environment, one should use the Thomas-Fermi approximation [10, 11] for describing the degenerate gas of free inerialess lighter particles (electrons/positrons). The ion component can be treated as a classical gas. This choice, though seemingly counterintuitive, is motivated by white dwarfs observation, where the electrons follow the degenerate ideal Fermi gas and the ions are the classical gas (see Fig. 1 in Ref. [11]). Our purpose in this paper is to investigate the behavior of the nonplanar IAWs in a Thomas-Fermi plasma. We consider a three-component plasma in which the ions are modeled by hydrodynamic (classical plasma-fluid) equations and the electrons/positrons are assumed to follow a Thomas-Fermi approximation. We shall examine the effects of the ion-to-Fermi electron temperature ratio, positron density, nonplanar geometry on the behavior of nonlinear electrostatic ion-acoustic excitations.

The paper is organized as follows. In Sec. II, we present the governing equations for the electrostatic IAWs in a Thomas-Fermi plasma. The reductive perturbation method is employed to derive the cylindrical/spherical Kortwegede Vries equation for nonplanar geometry. A similar problem is solved for a plasma with hot isothermal ions and adiabatic ions, respectively. Section III displays the analytical solutions and numerical results for the nonplanar electrostatic excitations. Our results are summarized in Sec. IV.

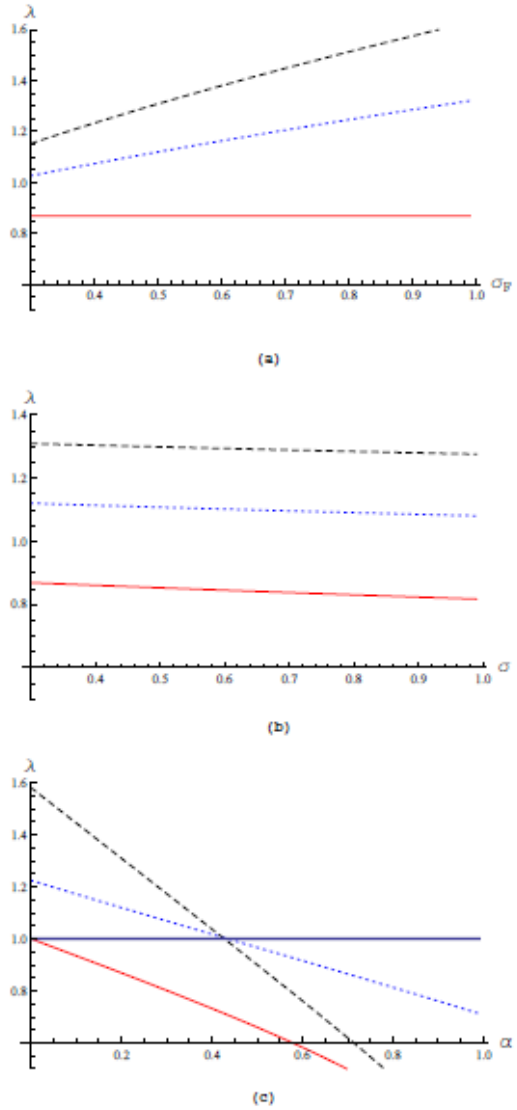

Fig. 1. The phase velocity (λ) is depicted (a) against σF , for α = 0.2 and σ = 0.3, (b) against σ for σF = 0.5 and α = 0.2, (c) against α for σ = 0.3 and σF = 0.5. The solid line corresponds to cold plasma case, the dashed line corresponds to isothermal ions and the dotted line corresponds to adiabatic ion

We have investigated the properties of the nonplanar ion-acoustic solitary waves in an unmagnetized collisionless plasma containing ions and degenerate Fermi electrons. By employing the reductive perturbation method, the cylindrical and spherical KdV equations have been derived and their numerical solutions have been presented. The effects of cold, isothermal and adiabatic ions, as well as the positron density and temperature on the behavior of the propagating pulse have been examined. The present results show that the phase velocity λ can supersonic or subsonic depending on the positron parameters (density and temperature). We have also examined the effect of σF , σ and α on the soliton amplitude and the width. It is found that the localized IAW becomes shorter and narrower with increasing σF , σ and α. Furthermore, the soliton propagation in the nonplanar geometry differs from that in one-dimensional planar geometry. Also, the localized pulse in plasmas having isothermal ions is larger than that with adiabatic ions, but slightly smaller than that with cold ions. It is clear that increasing T leads to an increase of the localized pulse amplitude and the spherical localized pulse moves faster than the cylindrical localized pulse.

Acknowledgement: R.S. acknowledges the financial support from the Egyptian Government under the Postdoctoral Research Program.

References

[1] E. Tandberg-Hansen and A. G. Emslie, The Physics of Solar Flares (Cambridge University Press, Cambridge, 1988), p. 124.
[2] M. Y. Yu, P. K. Shukla and L. Stenflo, Astrophys. J. 309, L63 (1986).
[3] F. B. Rizzato, J. Plasma Phys. 40, 289 (1988); V. I. Bereztiani, D. D Tskhakaya and P. K. Shukla, Phys. Rev. A 46, 6608 (1992); V. I. Bereztiani and S. M. Mahajan, Phys. Rev. Lett. 73, 1110 (1994).
[4] P. K. Shukla, N. N. Rao, M. Y. Yu and N. L. Tsintsadze, Phys. Rep. 138, 1 (1986).
[5] N. Shukla and P. K. Shukla, Phys. Lett. A 362, 221 (2007); S. Ali, W. M. Moslem, P. K. Shukla and R. Schlickeiser, Phys. Plasmas 14, 082307 10 (2007); I. Kourakis, F. Verheest and N. Cramer, Phys. Plasmas, 14, 022306 (2007).
[6] S. I. Popel, S. V. Vladimirov and P. K. Shukla, Phys. Plasmas 2, 716 (1995).
[7] S. Mahmood, A. Mushtaq and H. Saleem, New J. Phys. 5, 28.1 (2003).
[8] W. M. Moslem, I. Kourakis, P. K. Shukla and R. Schlickeiser, Phys. Plasmas 14, 102901 (2007); W. M. Moslem, I. Kourakis, P. K. Shukla and R. Schlickeiser, Phys. Plasmas 15, 019903 (2008).
[9] S. L. Shapiro and S. A. Teukolsky, Black holes, White Dwarfs and Neutron Stars: the Physics of Compact Objects (Mir, Moscow, 1985; Wiley, New York, 1983).
[10] L. A. Girifalco, Statistical Physics of Materials (Wiley, New York, 1973; Mir, Moscow, 1975); N. H. March, in Theory of the Inhomogeneous Electron Gas, Ed. by S. Lundqvist and N. H. March (Plenum, New York, 1983; Mir, Moscow, 1987).
[11] A. E. Dubinov and A. A. Dubinova, Plasma Phys. Reports, 33, 859 (2007).
[12] H. Washimi and T. Taniuti, Phys. Rev. Lett. 17, 996 (1966).
[13] T. Dauxois and M. Peyrard, Physics of Solitons (Cambridge University Press, 2005), p32 and p89. 11

P73.

ETUDE COMPARATIVE DES CARACTERISTIQUES DES DIODES SCHOTTKY A BASE DE GaN NON INTENTIONNELLEMENT

DOPES ET DOPES AU SILICIUM

H. Mazari[1], N. Benseddik[1] , Z. Benamara[1], K. Ameur[1], R. Becharef[2], G. Bassou[2]

1Laboratoire de Microélectronique Appliquée, Département d'électronique, Université Djillali Liabès de Sidi Bel-Abbes, 22000 Sidi Bel-Abbes, Algérie.
2 Laboratoire d'Elaboration et de Caractérisation des Matériaux,Université Djillali Liabès de Sidi Bel-Abbes, 22000 Sidi Bel-Abbes, Algérie

Notre étude a porté sur des substrats GaN Type hexagonale (ou Wurzite) non intentionnellement dopés (n.i.d) et dopés au silicium présentant des paramètres classiques à 300K.

La croissance du GaN a été effectuée par Epitaxie en Phase Vapeur aux Organo Métalliques (EPVOM) sur du saphir. On a déposé des grilles de platine relativement épaisses (1000 Å) pour le contact Schottky et des contacts ohmiques sur la face arrière des échantillons qui sont à base d'aluminium.

L'étude des caractéristiques courant-tension et capacité-tension de la structure Schottky h-GaN/Pt des échantillons n.i.d et dopé Si nous a permis de mettre en évidence les principaux mécanismes de conduction observables. En plus du courant thermoïonique nos structures présentent un courant de génération-recombinaison en surface. En effet les diodes Schottky présentent un facteur d'idéalité élevé et une hauteur de barrière plus faible que celle prévue par la théorie.

Les valeurs des hauteurs de barrière Schottky déduites des courbes C(V) sont de l'ordre de 1.75 eV pour les diodes à base de GaN n.i.d et de 1.33eV pour les diodes à base de GaN dopé Si. Ces diodes présentent une densité d'états d'interface et une fine couche d'oxyde à l'interface, elle est de l'ordre de 14.4 Å pour le GaN n.i.d et 9 Å pour le GaN dopé Si.

La variation des valeurs des hauteurs de barrière observées sur les diodes de même type de dopage, GaN n.i.d et GaN dopé Si, est attribuée à l'inhomogénéité de la surface.

La valeur élevée du facteur d'idéalité et la différence entre les valeurs des hauteurs de barrière déterminées par C(V) et I(V) ont montré aussi qu'à l'effet thermoïonique s'ajoutent d'autres phénomènes comme la recombinaison en surface effet déjà observé par K. Suzue [1, 2, 3].

La valeur élevée de la hauteur de barrière Schottky, effet observé aussi par G. L. Martinez [4] et M. Ambrico [5], a été attribuée à la face gallium présente en surface d'après U. Karrer [6].

Les échantillons GaN n.i.d ont montré la présence d'un dopage résiduel (type donneur) de l'ordre 4.72 1017 cm-3, dû aux lacunes d'azote (N) ou au silicium ou à l'oxygène présents (bâtis de

croissance) lors de la croissance du GaN.

Les échantillons dopés au silicium ont montré la présence d'un dopage au silicium de l'ordre 2.6 1017 cm-3. La présence d'une couche d'oxyde natif plus faible et d'une densité d'états d'interface légèrement plus élevée comparée aux diodes n.i.d lorsque l'on se rapproche de la bande de conduction.

La présence d'une faible couche d'oxyde induit une diminution du courant de saturation thermoïonique donc augmente la hauteur de la barrière Schottky [7].

Mots clés : diodes Schottky, GaN n.i.d, GaN dopé Si, barrière Schottky.

Références:

[1] K. Suzue, S. N. Mohammad, Z. F. Fan, W. Kim, O. Aktas, A. E. Botchkarev, H. Morkoç. J. Appl. Phys.80(8),15 (1996)
[2] G. Parish, R.A. Kennedy, G. A. Umana-Membreno, B. D. Nener Solid Stat. Elec.52, 171-174 (2008)
[3] M. A. Ebeoglu
Physica B 403, 61-66, (2008)
[4] G. L. Martinez, M. R. Curiel, B. J. Skromme and R. J. Molnar.J. of Elec. Mat., Vol26,N°3 (2000)
[5] M. Ambrico, M. Losurdo, P. Capezzuto, G. Bruno, T. Ligonzo, L. Schiavulli, I. Farella, V. Augelli. Solid Stat. Elec.49, 413-419 (2005)
[6] U. Karrer, O. Ambacher and M. Stutzman Appl. Phys. Let., Vol.77, N°13 (2000)
[7] M.K.Hudait, S.B.Krupanidhi Mat. Scu. And Eng. B87,141-147 (2001)

Aknowlegement:

The organizing committee thanks all of the sponsors of this Conference and particulary the main one:
The Alexander Von Humbolt-Stiftung,
Bonn, Germany
www.avh.de

Alexander von Humboldt
Stiftung/Foundation

PHYWE

مجمع شعيعلي
GROUPE CHIALI

ANDRU

We Thank also the head of the Faculty of Sciences and the University of Sidi Bel Abbes